



HAL
open science

Liquid crystal self-organization of colloids in complex environments

Marina Torres Lazaro

► **To cite this version:**

Marina Torres Lazaro. Liquid crystal self-organization of colloids in complex environments. Physics [physics]. Université Paris-Saclay, 2023. English. NNT : 2023UPASP061 . tel-04245987v1

HAL Id: tel-04245987

<https://theses.hal.science/tel-04245987v1>

Submitted on 17 Oct 2023 (v1), last revised 30 Oct 2023 (v2)

HAL is a multi-disciplinary open access archive for the deposit and dissemination of scientific research documents, whether they are published or not. The documents may come from teaching and research institutions in France or abroad, or from public or private research centers.

L'archive ouverte pluridisciplinaire **HAL**, est destinée au dépôt et à la diffusion de documents scientifiques de niveau recherche, publiés ou non, émanant des établissements d'enseignement et de recherche français ou étrangers, des laboratoires publics ou privés.

Liquid crystal self-organization of
colloids in complex environments
*Auto-organisation de cristaux liquides colloïdaux en
milieux complexes*

Thèse de doctorat de l'université Paris-Saclay

École doctorale n° 564, physique de l'Île-de-France (PIF)
Spécialité de doctorat : Physique
Graduate School : GS Physique. Référent : Faculté des sciences d'Orsay

Thèse préparée dans l'unité de recherche **Laboratoire de Physique des Solides (Université Paris-Saclay, CNRS)**, sous la direction de **Rik WENSINK**, Chargé de recherche.

Thèse soutenue à Paris-Saclay, le 30 juin 2023, par

Marina TORRES LÁZARO

Composition du jury

Membres du jury avec voix délibérative

Patrick DAVIDSON

Directeur de recherche, Université Paris-Saclay

Enrique VELASCO CARAVACA

Professeur, Autonomous University of Madrid

Hong XU

Professeure, Université de Lorraine

Anja KUHNHOLD

Docteure, University of Freiburg

Président du jury

Rapporteur & Examinateur

Rapporteur & Examinatrice

Examinatrice

Titre : Auto-organisation de cristaux liquides colloïdaux en milieux complexes

Mots clés : cristal liquide, colloïde, théorie d'Onsager, Hard Particle Monte Carlo

Résumé : Le travail présenté dans cette thèse se concentre sur une étude théorique de l'auto-organisation de cristaux liquides de bâtonnets ou de plaquettes colloïdales dans des milieux complexes. Les explorations sont faites à l'aide d'une théorie statistique basée sur la théorie d'Onsager et la théorie du champ moyen, combinées à des simulations numériques à grande échelle. Le premier cas que nous considérons est celui de disques colloïdaux immergés dans des bâtonnets réversiblement polymérisables où les deux composants sont capables de développer l'ordre nématique. Nous établissons les diagrammes de phase qui présentent un certain nombre de coexistences multiphasiques et discutons le phénomène de polymérisation réversible dans des environnements antinématiques. Le deuxième exemple concerne des bâtonnets et des plaquettes colloïdales immergés dans un cristal liquide thermotrope chiral. Il est démontré que ces

cristaux liquides hybrides moléculaires-colloïdaux présentent un ordre biaxial amélioré, une séparation de phase liquide-liquide médiée par l'ancrage de surface et des organisations colloïdales-moléculaires hybrides bi-hélicoïdales exotiques à forte concentration colloïdale. Le dernier thème aborde l'auto-assemblage mésoscopique de bâtonnets colloïdaux chiraux mélangés à des polymères non absorbants. Selon les conditions, ces mélanges sont connus pour former des tactoïdes, des rideaux liquides en forme de membrane, ainsi que des rubans tordus. En utilisant la simulation par ordinateur semi-grand canonique de Monte Carlo, nous abordons la morphologie et la structure interne de ces gouttelettes LC et nous comparons nos résultats avec des résultats expérimentaux récents sur des bâtonnets de virus fd en forme de fil.

Title : Liquid crystal self-organization of colloids in complex environments

Keywords : liquid crystal, colloid, Onsager theory, Hard Particle Monte Carlo

Abstract : The work presented in this thesis focuses on a theoretical study of liquid crystal (LC) self-organization of colloidal rods or platelets in complex environments. Explorations are made using statistical theory based on Onsager and mean-field theory combined with large-scale computer simulations. The first case we consider are colloidal discs immersed in reversibly polymerizing rods where both components are capable of developing nematic order. We map out the phase diagrams that feature a number of multi-phase coexistences and discuss the phenomenon of reversible polymerization in anti-nematic environments. The second example concerns colloid rods and platelets immersed in a chiral thermotropic liquid crystal.

These so-called hybrid molecular-colloidal liquid crystals are demonstrated to exhibit enhanced biaxial order, surface-anchoring mediated liquid-liquid phase separation, and exotic bi-helical hybrid colloidal-molecular organizations at significant colloid content. The last topic addresses the mesoscopic self-assembly of chiral colloidal rods mixed with non-adsorbing polymers. Depending on the conditions, these mixtures are known to form tactoids, membrane-shaped liquid rafts, as well as twisted ribbons. Using semi-grand canonical Monte Carlo computer simulation, we address the morphology and internal structure of these LC droplets and compare our findings with recent experimental results on filamentous fd virus rods.

*A mi tía Carolina,
por abrirme las puertas
de tantos mundos desconocidos.*

Acknowledgements

I would like to begin by expressing my deepest gratitude to my supervisor, Rik Wensink, for all his support, guidance, and mentorship throughout this journey. His vast knowledge and constant feedback during our countless discussions have been invaluable in shaping this thesis. He also (and more importantly, I would say) has been a great inspiration to me on a human level: his humility, integrity, and patience have certainly influenced my way of doing science. His mentorship extended beyond research, and his genuine care for his students' well-being created a supportive and nurturing environment in which I was able to thrive both academically and personally even during the uncertain and stressful times of the pandemic.

Next, I extend my sincere appreciation to the French National Research Agency (ANR) for the financial support provided under Grant No. ANR-19-CE30-0024 "ViroLego", as well as to the international research consortium INTEGRATE funded by the European Innovation Council. Their support has been instrumental in the successful completion of this work.

I acknowledge the esteemed jury members, Patrick Davidson, Enrique Velasco, Hong Xu, and Anja Kuhnhold, for their time, feedback, and valuable input during the evaluation of this thesis. I am also grateful to the members of my *comité de suivi*, Anniina Salonen and Patrick (again), for their constructive advice and insightful discussions throughout these years.

I would also like to thank the senior members of the Theo-Soft group, Giuseppe Foffi and Frank Smallenburg, whose expertise and interesting discussions during lunch have enriched my understanding of science and academia. I am also thankful to the post-doctoral researchers Andrea Plati, for his unalterable good vibes, and William Fall for trying to introduce me to LAMMPS and high-performance computing in a very short time, and of course for our fun times visiting *préfectures*. Gratitude is also extended to my office mates Saheli, Étienne, and Antoine, whose kind nature has cheered up my days. A special thanks to Étienne who invited me to move to his office when I was feeling lonely on the third floor during the pandemic. Additionally, I would like to acknowledge the valuable initial encouragement I received from a former Ph.D. student in our group, Susana.

I deeply appreciate the hospitality and encouragement I received from the other members of the Theo group. Special mention goes to the *other* Ph.D. students: Mateo, Baptiste, Ansgar, Jean-Baptiste, Lize and Florian with whom I repeatedly shared smiles and tears caused by this journey of tension and excitement in comparable proportions. Their friendship and discussions have been truly rewarding, and the good times we shared around a cup of coffee or a deck of cards will definitely be hard to forget.

I feel grateful to my friends from the undergraduate degree in Physics for sharing those early days when we still did not understand anything, and for staying in touch with me until today: Adri, Martín, Gabriel, Sara, Miguel, Julia, Marta, Álvaro, Isa. I could not have done it without you.

Being in Paris, I have had the opportunity to live with a strange group of fascinating people who are as curious about life in general as I am. I am talking about my friends from the Colegio de España in Paris, and they are too numerous to name them all. But I extend the message to whoever reads this text and knows that I am referring to them: there are no precise words that reflect how grateful I feel to have spent these years by your side, in the kitchen, at breakfast, studying late in the computer room, watching weird movies, sharing music and walls. Thank you a billion times over. And, in particular, thanks to Mateo (again) for offering me his support not only as a work colleague, but also as a neighbour, a playmate, a vegetable provider and a truly caring friend.

None of this would have been possible without the unconditional support of my family and close friends who, despite belonging to fields of expertise far removed from physics, have taken the time to listen to all my mad scientist ramblings. Thanks especially to my aunt Raquel, my aunt Inés, my cousin Clara and my friend Manuelita for coming from Madrid to be at my thesis defense, and to my friend Elba for being at my rehearsals via Zoom. Thanks to my aunt Carolina (to whom this thesis is dedicated) for being my French mother, despite not being French nor my mother; because of you this country always felt like home. And last but not least, Mamá, Papá, Elena, thank you for being the best team I could have ever asked for. Your love, encouragement, and belief in me have been my driving force since the day I was born (well, technically, since Elena was born). Your sacrifices and dedication inspired me to pursue everything I set my mind to, and I am eternally grateful for everything you have done for me. Os quiero muchísimo.

Contents

Acknowledgements	i
1 General introduction	1
1.1 Phenomenological background	1
1.1.1 Entropic phase transitions	4
1.1.2 Mixtures and the depletion effect	5
1.2 Scope of this thesis	7
1.3 Statistical mechanical background	8
1.3.1 Fluids of hard anisometric particles	8
1.3.2 Facing reality	13
1.3.3 Non-uniformity in nematic LCs: nemato-elasticity and surface anchoring	14
1.4 HPMC simulations of colloidal nematics	17
1.4.1 Overlap conditions for hard spherocylinders	18
1.4.2 Semi-grand canonical ensemble	19
1.4.3 Implicit depletants algorithm	21
2 Phase behavior of shape-persistent living polymers templated by discs	25
2.1 Introduction	25
2.2 Model	28
2.3 Second-virial Theory	29
2.3.1 Backbone flexibility	30
2.3.2 Excluded-volume entropy	30
2.4 Molecular weight distribution	31
2.4.1 Isotropic fluid	32
2.4.2 Uniaxial nematic fluid	33
2.5 Isotropic-nematic phase behavior	36
2.5.1 Polymer nematic phase (N^+)	37

2.5.2	Discotic nematic phase (N^-)	39
2.6	Phase diagrams	41
2.7	Quadruple fluid coexistence	43
2.8	Conclusions	45
Appendix 2.A	Renormalized \mathcal{P}_2 approximation for slightly flexible polymers	47
Appendix 2.B	Stability of biaxial nematic order	48
3	Emergent biaxial order in hybrid chiral LCs	52
3.1	Introduction	52
3.2	Surface anchoring of a cylindrical rod	54
3.2.1	Non-interacting rods	56
3.2.2	Non-interacting discs	57
3.2.3	Conically degenerate surface anchoring	58
3.2.4	Order parameters	59
3.3	Model system	60
3.4	Role of elastic distortions	61
3.4.1	Elastic energy of a twisted disclination wrapped around a thin rod	62
3.4.2	Elastic distortions around a rod tilted away from the host director	64
3.4.3	Effective orientational potential of a LC rod	68
3.4.4	Short-pitch cholesteric hosts	69
3.4.5	Elastic distortions around a disc	69
3.5	Conclusions	75
4	Bi-helical order and demixing in hybrid chiral LCs	77
4.1	Introduction	77
4.2	Second-virial density functional	78
4.3	Orthorhombic liquid-liquid phase separation	81
4.4	Effect of colloid-induced elasticity	82
4.4.1	Rods	83
4.4.2	Effect of rod chirality	85
4.4.3	Discs	86
4.5	Conclusions and outlook	87
Appendix 4.A	Twist elastic resistance	88
5	Twisted membranes versus ribbons in colloidal rod-polymer mixtures	90

5.1	Introduction	90
5.2	Simulation model	92
5.2.1	Depletion interactions	93
5.2.2	Chiral interactions	93
5.2.3	Simulation details	94
5.3	Results	95
5.4	Theory for twisted membranes	102
5.4.1	Scaling results for the elastic moduli for a fluid membrane	104
5.4.2	Chiral twist	105
5.4.3	Effect of depletants and twist penetration length	105
5.5	Starfish instability and twisted ribbon	106
5.6	Membrane or ribbon ?	111
5.7	Conclusions and outlook	114
	Appendix 5.A Square well potential	116
	Bibliography	125
	List of Figures	128
	Résumé	129

Chapter 1

General introduction

Abstract

In this chapter, we introduce the concept of lyotropic liquid crystals from both a practical and statistical mechanical perspective. Additionally, we discuss some topics related to Monte Carlo simulations in the semi-grand-canonical ensemble. We also outline the goal of this thesis in relation to recent experimental research on the self-organization of anisotropic colloidal nanoparticles in complex environments.

1.1 Phenomenological background

Soft matter is a term used to describe materials that are distinct from gases and solids, usually excluding simple fluids. A wide range of systems, including soap bubbles, gels, elastomers, liquid crystals, or biological fluids, can be categorized as soft matter. Defining the boundaries of such a vast domain can be challenging due to the diverse topics and segregated nature of researchers, which come from a number of distinct disciplines. Nevertheless, a clear community with a common language exists, and major research topics can be identified that encompass most current studies in this field [1].

Soft matter systems exhibit, in most cases, structural length scales ranging from a nanometer up to a micrometer, and thus are placed within the domain of ‘nanotechnology’. Colloidal systems are well known examples in which this feature is essential to define the range where a very specific type of behavior occurs. Colloids are supramolecular submicron sized substances dispersed in a medium that can be a liquid or a gas. They are much bigger than normal molecules, and hence the medium in a colloidal suspension can often be regarded as ‘background’ with respect to the colloidal size range: this medium may be approximated as a continuum. At the same time, colloids are small enough to present considerable thermal motion in comparison to sedimentation (which is caused by gravitational forces that would become more important for higher-sized particles). Colloids were first discovered by Perrin, who detected Brownian motion as visible manifestation of thermal motion in dispersions of resin colloids in water [2].

When colloidal particles have anisotropic shapes, they can be found in liquid crystalline phases. Liquid crystals are substances that have the appearance of a liquid but possess certain

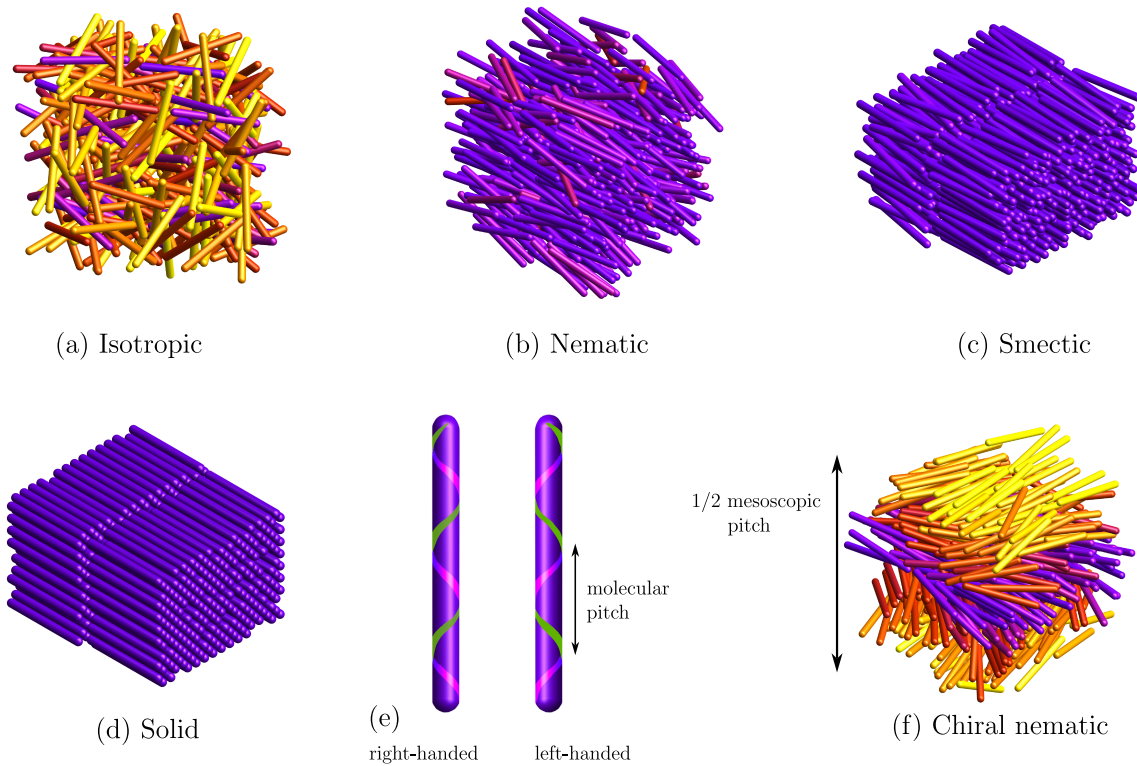


Figure 1.1: (a)-(d) Examples of basic liquid crystals formed by rod-like molecules or nanoparticles. (e) Most molecular chiral features in elongated nano-particles could be described on a coarse-grained level using a rod with an effective chiral electrostatic “patchiness” in terms of a molecular pitch length and handedness (left or right); (f) these particles generate a particular type of nematic phase: the chiral nematic. The implications of molecular chirality on the helical mesostructure (in particular, the mesoscopic pitch) of chiral nematic phases remains a challenging issue.

levels of molecular arrangement similar to crystals. Liquid crystals were first discovered in 1888 by Friedrich Reinitzer, who noticed that a cholesterol-based substance had two melting points at different temperatures, each of them giving way to a liquid-like phase with different optical properties [3]. At the early time of Reinitzer only three phases were known (gas, liquid and solid). Over the years, a big number of substances have been discovered to exhibit many states of matter, including liquid crystal phases that are now widely used in technological advancements such as liquid crystal screens and thermometers [4].

The key difference between a liquid crystal and the commonly observed gas, liquid and solid states is that properties in the first one are anisotropic and vary with direction, even though the substance itself remains fluid. These unique properties emerge due to the elongated shape of its building blocks, which promote collective alignment along a certain direction. In other words, liquid crystalline phases are additional states of matter which are intermediate between the dilute gas and the crystalline solid, and whose existence is related to the additional *orientational* degrees of freedom anisometric particles have compared to spherical ones.

Among the numerous liquid crystalline phases, different degrees of order can be found,

evidenced for instance by diffraction of X-rays and light. Measurements of this kind provide a frame to classify these systems by its similarity to either the gas or the solid phase. Let us consider, among others, the following liquid crystalline phases, depicted in Fig. 1.1:

The *isotropic* (I) fluid phase is very similar to the gas and liquid phases for spherical particles and is characterized by a complete absence of positional and orientational order. At the immediately next stage, we find the *nematic* (N) phase, in which particles are homogeneously distributed without positional order as in a liquid phase, but are ordered in their orientation following an average direction: the *nematic director* $\hat{\mathbf{n}}$. As it will be repeatedly discussed throughout this thesis, in nature one can find particles that, in addition to being anisotropic, present chiral features. This can be due to the arrangement of atoms in a molecular compound, to a (helical) particle shape in some colloidal systems or to a chiral distribution of charges at the surface of the particles, observed for instance in *fd* filamentous bacteriophages viral rods [5]. When chiral particles are in a nematic phase, they arrange themselves into a strongly twisted structure. This special case of a chiral nematic phase is often called *cholesteric*.

The *smectic* (Sm) phase is closer to the solid phase. In smectic liquid crystals, particles are ordered in layers and cannot move freely between them. The smectic phase is, in turn, divided into several sub-phases with slightly different properties. Examples are the smectic A phase (SmA), where particles can move freely inside the layers as in a two-dimensional liquid; or the smectic B phase (SmB), where there is long-ranged positional order: at higher concentrations or lower temperatures, molecules tend to arrange themselves into something more similar to a crystalline lattice.

One sub-classification of liquid crystal materials is based on the mechanism by which they transition from one state to another. *Thermotropic* systems, mainly formed by low molecular weight constituents –and also some polymers–, undergo phase transitions due to changes in temperature, since the thermodynamic properties of these species depend on the attractive forces between the molecules. In this thesis, we focus mostly on *lyotropic* liquid crystals, which form upon increasing the concentration of solute particles. This is the case of systems formed by high-molecular weight synthetic and biological nano-particles [6, 7], polymers such as DNA [8] or surfactants in a solvent [9]. The first case is the one studied in this thesis, where the fact that shape is not subject to fluctuations due to changes in the solvent composition is an advantageous simplification with respect to its amphiphilic and polymeric counterparts.

First experimental reports of nano-particle based lyotropic liquid crystals go back when liquid crystalline behaviour was described for tobacco and tomato mosaic virus (TMV) [10, 11] and vanadium pentoxide (V_2O_5) [12] in the early 20th century. In addition to these rod-like particle systems, colloidal plate-like charged particles and clay particles were discovered to report liquid crystalline behaviour [13]. At present, there are many other examples of lyotropic liquid crystals to be found in a wide variety of dispersions of (mainly rod-like) colloidal particles and solutions of stiff polymers (see e.g. [14] for an overview).

This research work focuses on both theoretical and numerical approaches for the exploration of phase behavior in anisotropic colloidal compounds, with a particular interest in the *entropic* isotropic-nematic phase transition. This transition is well described by Onsager’s theory, pro-

posed in 1949, which assumes a similarity between a gas and a particle solution [15]; and will be used repeatedly throughout this manuscript (more specifically in Chapters 2 and 4) along with other theoretical and numerical tools to study the liquid-crystalline self-organization of colloidal rods or platelets in complex environments. Through our research, we hope to gain a better understanding of the behavior of this kind of systems and contribute to the broader field of liquid crystal research.

1.1.1 Entropic phase transitions

The thermodynamic equilibrium state of a system tends to minimize its Helmholtz free energy:

$$F = U - TS \quad (1.1)$$

where $U = \sum_{i \neq j} u_{ij}$ is the internal energy of the system defined as a pairwise addition of interparticle potentials u_{ij} between particles i and j , T is the temperature and S is the entropy of the system. Clearly, a system at constant temperature can lower its free energy in two ways: either by increasing the entropy or by decreasing the internal energy. Entropy is defined, for an isolated system of N particles in a volume V at an energy U , as follows:

$$S = k_B \log(\# \text{ accessible states}) \quad (1.2)$$

and depends on the total number of states that are accessible to the system under these conditions. Usually, S is interpreted as a measure for the ‘disorder’ in that system. The natural consequence of this interpretation would be that ordering phase transitions can only take place if the loss in entropy is compensated by the decrease in internal energy. These kind of phase transitions are known as *energetic* phase transitions and describe the reality, for example, of the spontaneous phase transition from the regular fluid to the solid crystalline state. In this case, the transition takes place if the freezing lowers the internal energy of the system sufficiently to offset the decrease in the number of accessible configurations and thus the loss in entropy.

However, we can have many ‘ordering’ transitions that are *entropic*. Taking Eq. (1.1) one may consider systems in which the internal energy is a function of temperature alone, S being the only quantity affected by any change in the system at constant temperature. If this is the case, it will be possible to find phase transformations determined exclusively by a change in the entropy. Usually, atomic systems do not fulfill this condition because of the existence of attractive or repulsive interactions u_{ij} whose strength depends on the relative inter-particle distance, and thus, the number density of particles ρ when considering the thermodynamic limit. Temperature is then key to determine the accessibility of an ordered state, following the Boltzmann probability of finding a particle configuration of energy U , $\exp(-U/k_B T)$. Nevertheless, if we limit our attention to hard-core potentials:

$$u_{ij}(r) = \begin{cases} \infty & r < D \text{ (if cores overlap)} \\ 0 & r > D \text{ (if cores do not overlap)} \end{cases} \quad (1.3)$$

where D is the diameter of the hard-core shell (which becomes an orientation-dependent quantity for a pair of anisotropic particles) and r is the distance between their centres of mass, then all the allowed (non-overlapping) configurations at constant temperature will possess the same level of internal energy $U = 0$. Interestingly, T then becomes completely irrelevant and any variation in the Helmholtz free energy will be attributed to changes in entropy, that will be maximized at equilibrium. Ordering phase transitions may occur in systems of this kind considering that different entropic contributions may be competing. In the case of systems formed by elongated uniaxial particles such as rods or platelets, such competition takes place between the following components:

$$S = S_{or} + S_{ex} \quad (1.4)$$

where S_{or} is the *ideal* orientational entropy, associated with the ways in which non-interacting particles can orient or rotate and S_{ex} accounts for the available configurational space for particles interacting through *excluded volume* contributions. The notion that spontaneous ordering of particles corresponds to an increase of the total entropy can be understood under this frame as a competition between these two quantities. When some kind of order emerges, particles lose entropy because the density –in terms of orientations– is no longer uniform. However, this loss is more than offset by the simultaneous gain of available volume, i.e. the number of allowed configurations per particle increases as the particles align. This argument can be extended to higher density phase transformations where positional order is achieved and the available volume each particle is allowed to explore increases if particles are arranged in a more ordered state instead of keeping a homogeneous positional distribution.

The isotropic–nematic phase transition invoked above occurs through a first order transition, as it was probed theoretically by Onsager. He recognized that the transition from an isotropic to a nematic state in solutions containing sufficiently anisometric particles can be described successfully within a virial expansion of the free energy truncated after the second virial term, an approach which could not be used to explain the gas-liquid transition for spherical particles. About a decade after Onsager’s work, Alder Wainwright and others [16, 17] first showed by means of computer simulations that a similar disorder-order transition, albeit of the positional degrees of freedom, occurs in a fluid of hard spheres, where there is a critical packing fraction at which particles will be able to better explore the translational phase space by adopting an (fcc) lattice rather than a disordered arrangement. Much later, computer simulations by Frenkel *et al.* revealed the stability of smectic and columnar liquid crystals which appear upon densifying systems of respectively hard rods [18] and hard platelets [19, 20], without attractive interactions between the particles. All of them consist of transitions driven entirely by *entropic* interactions.

1.1.2 Mixtures and the depletion effect

So far we have implicitly assumed that all particles which build up a gas, liquid (crystal) or solid phase are identical. Many systems in nature are however *mixtures* containing a number of different types of particles or molecules. It is not surprising that the phase behaviour of mixtures is richer than that of pure systems–if only for the additional *entropy of mixing*– and that

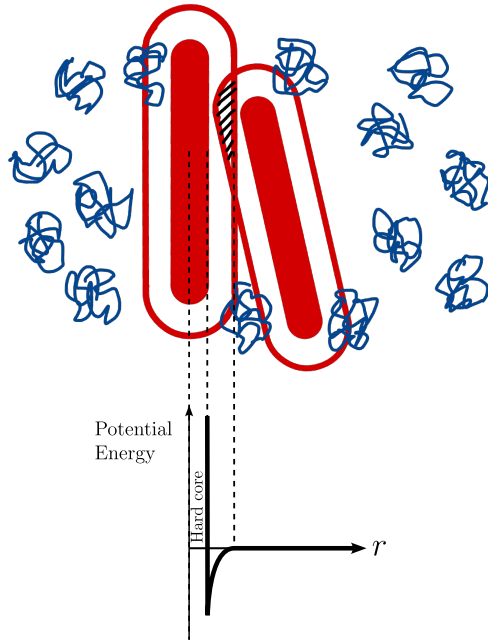


Figure 1.2: The presence of non-adsorbing polymers or other depletion agents (whose size is usually smaller than the colloidal nanoparticles) produces an effective attractive potential between the rods according to the depletion scenario –which depends on the rods relative orientation and distance–. If the rods are at close proximity, the polymers are depleted away from the inner space between the rods in dictated by the overlap of the depletion zones (hatched area). This creates an osmotic imbalance around the cylindrical surfaces pushing the rods together.

mixing different species may lead to phenomena not encountered in one-component systems. An example of a purely entropically-driven self-assembly phenomenon is the ordered arrangement that arises in colloidal mixtures of large particles and smaller particles called depletants, a process known as the depletion effect.

This effect takes place typically when colloidal particles are mixed with non-adsorbing polymers. Fig. 1.2 highlights the ordering transition in this situation by illustrating the effective attractive interaction between large colloidal rods when polymers are added to the system. Negative adsorption results in a region near the colloidal surface, named *depletion layer*, where polymers are less likely to access due to a loss of configurational entropy of the polymer chain. When such regions overlap, there is an increase in the volume available to polymers to explore, thus increasing their entropy and lowering their Helmholtz free energy. Effectively, the addition of depletants to the system generates repulsion between particles of distinct type and, in consequence, attraction between similarly-shaped colloidal particles.

These polymers are often modeled as penetrable hard spheres [21], known as Asakura-Oosawa spheres, in honor of the first theoreticians who proposed a model to describe the depletion effect [22, 23, 24]. By replacing the polymers with spheres of the same radius of gyration, we can obtain the same results in an effective manner. Penetrable hard objects do not interact with each other, i.e. no overlap restrictions are imposed between them, allowing for an ideal gas statistical mechanical treatment; and at the same time they are not allowed to overlap with colloidal particles, causing the emergence of the depletion effect. The main approximations assumed by Asakura and Oosawa are: 1) whereas in reality parts of the polymer chain are unlikely to reside within the depletion layers, in this model polymer access to the depletion zones is strictly prohibited; and 2) polymer chains are assumed not to interact with each other, which is a fair approximation in the regime where the depletant concentration is low.

In this work, depletion-driven demixing caused by strong shape asymmetry in colloidal mixtures emerges in a natural way in Chapter 2 for a system featuring discs and polymerizing rods.

In addition, the consequences of using penetrable hard spheres as a driving agent to stabilize liquid crystalline droplets will be explored in Chapter 5.

1.2 Scope of this thesis

The central aim of this thesis is to theoretically investigate the liquid crystal (LC) self-organization of colloidal particles with different shapes in various contexts. Many of the studies to be described in the remainder of this thesis have been inspired by recent experimental works in systems of colloids with well-controlled shapes and interactions. In particular, we mention the experimental work of [25] on phase behavior and functionalization of complex fluids of filamentous bacteriophages (fd and M13) which display many interesting phenomena left open for theoretical interpretation; as well as recent experimental findings [26, 27] on colloidal dispersion of highly anisotropic particles immersed in molecular LC hosts. One of our primary goals in this work is to account for these experimental observations by constructing simple, yet realistic, models for the colloidal systems under consideration and by scrutinizing relevant aspects of their phase behaviour.

Chapter 1 of this thesis provides an introduction to the background and scope of the research presented. It covers the statistical mechanical background, specifically for fluids of hard anisometric particles. We then discuss the use of hard particle Monte Carlo simulations of colloidal nematics, including some particularities of such simulations for the case of anisometric particles. Overall, the chapter serves as a foundation for the rest of the thesis, laying out the relevant concepts and methods for the research presented in subsequent chapters.

In Chapter 2 a theoretical model is proposed to explore the low-concentration phase behavior of a system consisting of non-covalently bonded, weakly flexible rods treated as living polymers mixed with non-adsorbing rigid colloidal discs. We show that, at large disc mole fractions, the rod nematic phase is disrupted by collective disc alignment in favor of a discotic nematic fluid in which the polymers are dispersed anti-nematically, generating a non-exponential molecular-weight distribution of the resulting polymeric species.

Chapters 3 and 4 address issues related to hybrid molecular liquid crystal nematics. In this part of the work, we consider a system in which molecular cholesteric LCs are doped with thin colloidal particles with large length-to-width aspect ratios. In Chapter 3, single colloid insertions are considered, and we explore the interplay between weak surface anchoring forces, exerted between the colloidal surface and the molecular field, and elastic distortions around the colloid-molecular field interface. In Chapter 4, we use Onsager's theory to account for collective effects in the hypothetical case where multiple colloidal particles are inserted in the hybrid LC.

Finally, in Chapter 5 we introduce a computational model to study the formation of mesoscopic droplets of colloidal rods stabilized by the presence of non-adsorbing polymers. We aim to gain a deeper understanding of the transition between the so-called twisted membranes and twisted ribbons observed experimentally in systems featuring filamentous fd viral rods [28] by performing extensive Monte Carlo simulations in the semi-grand-canonical ensemble. Although twisted ribbons are not observed in our simulations, theoretical descriptions are proposed to

predict the typical geometric features for both droplet morphologies that can in principle be confirmed through experimental verification.

1.3 Statistical mechanical background

In this section we introduce the statistical mechanical framework of Onsager's second virial theory to describe the thermodynamic properties of a spatially homogeneous fluid of hard colloidal rods or platelets. Instead of delving into a technical exposition of Onsager's theory (the reader is referred to Onsager's original paper [15], as well as some enlightening reviews [29, 30] for more detailed information), we will provide an intuitive overview of its main components. As explained in Section 1.1.1, the isotropic-nematic phase transformation results from the competition between two principal quantities, related to orientational and excess contributions. Onsager establishes the formulation of these two quantities and analyzes the transition using entropic arguments alone. We also introduce further modifications that can be applied to the Onsager formalism to account for more complex phenomena.

1.3.1 Fluids of hard anisometric particles

Let us assume an ensemble of slender rigid needles in a fluid state of uniform particle density $\rho = N/V$ at a fixed volume V and temperature T , and focus on the orientational phase space the rods adopt in a fully isotropic and nematic configuration. If we treat each rod orientation on the unit sphere as a separate state we may define an orientational entropy as the ratio of the number of explorable orientational states:

$$\frac{S_{or}}{N} \sim k_B \ln(\# \text{ orientational states}) \quad (1.5)$$

More specifically, the following expression for the ideal orientational free energy can be obtained:

$$\frac{S_{or}}{N} = -k_B \int f(\Omega) \ln [4\pi f(\Omega)] d\Omega. \quad (1.6)$$

where $f(\Omega)$ is the normalized *orientational distribution function* (ODF) that in general depends on a solid angle Ω . This expression is derived by applying the following assumptions:

1. Start from the configurational partition function for an imperfect gas where the total potential energy is expressed as a summation over particle pairwise interactions that are orientation dependent.
2. Assume the analogy between an imperfect gas and a dispersion of colloidal particles in a solvent with fixed chemical potential.
3. Divide the orientational space into s arbitrarily small solid angle sections, consider each rod orientation as a separate species and transform the partition function to account for

a mixture of s species, each one of N_k particles with $k = 1, \dots, s$, such that

$$\sum_{k=1}^s N_k = N. \quad (1.7)$$

4. The partition function then becomes a complicated summation over all possible combinations of $\{N_1, N_2, \dots, N_s\}$ satisfying Eq. (1.7). For large N , however, it is justified to approximate the complete set of summations by its maximum term. Let us define $\{\tilde{N}_1, \tilde{N}_2, \dots, \tilde{N}_s\}$ as the orientation distribution associated to the maximum term of the summation.

5. After some rearranging, the following expression can be obtained for the orientational part of the free energy:

$$\beta F_{\text{or}} = N \left\{ \ln \left[\frac{4\pi}{\Delta\Omega} \right] + \sum_{k=1}^s \frac{\tilde{N}_k}{N} \ln \frac{\tilde{N}_k}{N} \right\}, \quad (1.8)$$

where $\beta = 1/k_B T$, $\Delta\Omega = 4\pi/s$ is the chosen size of the angular bins.

6. Taking the limit $\Delta\Omega \rightarrow 0$ for a *continuous* distribution in Ω we directly obtain Eq. (1.6).

It is clear, following Eq. (1.6), that the orientational entropy is maximized when the ODF is isotropic. In consequence, and since in a nematic phase the needles are strongly aligned along either poles of the unit sphere, we infer that the orientational entropy of a nematic phase is always smaller than that of an isotropic fluid at comparable particle orientation.

Let us focus now on the other competing part of the entropy in this system. The excluded volume free energy of an ensemble of slender rigid needles can be approximated systematically by a virial expansion in terms of the density $\rho = N/V$ [31]. Starting from the law of ideal gases applied to a colloidal solution:

$$\Pi V = N k_B T \quad (1.9)$$

where Π is the osmotic pressure of the system, the virial correction can be applied as follows:

$$\beta \Pi = \rho + B_2 \rho^2 + B_3 \rho^3 + \dots \quad (1.10)$$

where B_2 and B_3 are the second and third virial coefficients, and are calculated by integrating simultaneous interactions between two and three particles respectively¹:

$$B_2 = -\frac{1}{2V} \int \int \Phi_{12} d\mathbf{r}_1 d\mathbf{r}_2 \quad (1.11)$$

$$B_3 = -\frac{1}{3V} \int \int \int \Phi_{12} \Phi_{13} \Phi_{23} d\mathbf{r}_1 d\mathbf{r}_2 d\mathbf{r}_3 \quad (1.12)$$

¹Note that, for non-spherical particles, B_2 and B_3 also need to be integrated through the orientational degrees of freedom, which is not explicitly indicated in Eq. (1.11) and Eq. (1.12) for simplicity.

where $\Phi_{ij} = \exp(-u_{ij}/k_B T) - 1$ are the so-called Mayer functions. Onsager stated by geometrical arguments that the following scaling relation for B_2 and B_3 is fair for long thin rods:

$$\frac{B_3}{(B_2)^2} \sim \frac{D}{L} \left(\ln \frac{L}{D} + cst. \right) \quad (1.13)$$

which vanishes in the limit of infinitely thin needles. The decrease has been verified by means of Monte-Carlo simulations on hard spherocylinders by Frenkel [32, 33] showing that higher order virial coefficients can be neglected only if $L/D \gg 100$. The situation is much different for thin platelets for which Onsager estimated

$$\frac{B_3}{(B_2)^2} \sim \mathcal{O}(1), \quad (1.14)$$

which is also true for spheres. Therefore, virial contributions of order higher than two can be neglected for thin needles, which allows for a simplified analytical treatment of the problem in contrast to the case of non-elongated particles where higher orders must be considered. These higher order contributions in the virial expansion –involving clusters of three, four, etcetera particles– can be derived using other methods, albeit approximately, such as ‘scaled particle’ [34, 35] and density functional theories (see [29, 36] for a review). In this thesis, due to the low density regime regarded in all the analytical works, it is reasonable to stick to the second virial approximation.

What remains now is to integrate the second virial coefficient. For the system presented here, the pairwise interaction between particles u_{ij} is strictly hard and depends on the relative orientation between needles; we can thus deduce

$$\Phi_{ij} = \Phi(\mathbf{r}_{ij}, \Omega_i, \Omega_j) = \begin{cases} -1 & \text{if overlap} \\ 0 & \text{otherwise} \end{cases} \quad (1.15)$$

The interaction between two particles only contributes to the integral in Eq. (1.11) if particles are close enough to overlap, i. e. if they are both contained inside the *excluded volume* generated from their relative orientations:

$$B_2 = \frac{1}{2} \int \int v_{excl}(\Omega_1, \Omega_2) f(\Omega_1) f(\Omega_2) d\Omega_1 d\Omega_2 \quad (1.16)$$

Since we are accounting for possible inhomogeneous angular configurations, the previous reformulation of the integral must be weighted by the ODF $f(\Omega)$.

The meaning of the excluded volume is clarified in Fig. 1.3. Considering long hard rods we immediately infer that the excluded volume is strongly orientation-dependent; it is greatly reduced when the rods align. In consequence, taking Eq. (1.16) one can see that collective alignment of the rods and thus an anisotropic ODF will reduce the value of B_2 with respect to an isotropic state.

Lastly, we recall the free energy formulation of an imperfect gas approximated by the second

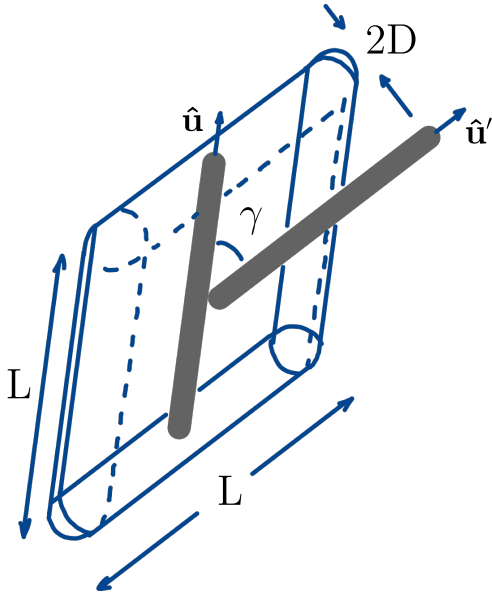


Figure 1.3: Illustration of the excluded volume of two spherocylinders of length L and diameter D at mutual orientation γ . Rod alignment leads to a strong reduction of the excluded volume represented by the lozenge-shaped figure.

virial correction:

$$\frac{\beta F}{N} = \beta \mu_0 + \ln[\Lambda \rho] - 1 + B_2 \rho \quad (1.17)$$

with μ_0 a reference chemical potential of the dispersed particles depending only on the solvent conditions, and Λ the (de Broglie) thermal volume, arising from integrations over the translational and rotational momenta of the anisometric particles. The last term corresponds to the free volume *entropy* in the context of Onsager's formalism, since for hard core interactions it does not depend on temperature, but only on the average over all possible configurations. Collecting the previous results from Eq. (1.6) and Eq. (1.16) we obtain the following expression:

$$\begin{aligned} \frac{\beta F}{N} = & \beta \mu_0 + \ln[\Lambda \rho] - 1 + \int f(\Omega) \ln[4\pi f(\Omega)] d\Omega \\ & + \frac{\rho}{2} \iint d\Omega d\Omega' f(\Omega) f(\Omega') v_{\text{excl}}(\Omega, \Omega'). \end{aligned} \quad (1.18)$$

This is the final recipe to model the phase behavior of a mixture of hard rods, where the most probable orientational state is given by the function $f(\Omega)$ that better minimizes the Helmholtz free energy. The isotropic-nematic transition comes from a competition between the before-last and last terms, which correspond to the orientational and excess entropy respectively. For low concentrations, the orientational entropy dominates and is maximized by an isotropic distribution, whereas for high concentrations the second virial term becomes more important, which favors a nematic distribution at the expense of losing orientational entropy.

The critical packing fraction at which an isotropic-nematic ordering occurs roughly corresponds to the situation when the bare particle volume is of the same order of magnitude as its average excluded volume:

$$\phi_{IN} \propto \frac{\text{volume per particle}}{\text{average excluded volume per particle}} \quad (1.19)$$

The excluded volume for a pair of spherocylinders as sketched in Fig. 1.3 reads

$$v_{excl}(\Omega_1, \Omega_2) = 2L^2D|\sin \gamma| + 2\pi D^2L + \frac{4}{3}\pi D^3 \quad (1.20)$$

An analogous expression was obtained by Onsager for two cylinders with different arbitrary lengths, diameters and mutual orientation [15]. Simple scaling considerations for thin cylinders then prompt us to infer that, whereas the volume per particle scales as $\propto LD^2$, the excluded volume typically goes as $\propto DL^2$. In consequence,

$$\phi_{IN} \propto \frac{D}{L} \quad (1.21)$$

Clearly, the more slender the rods (large L/D) the lower the critical packing fraction at which the I-N phase transformation can be expected. Strictly, in the Onsager limit $L/D \rightarrow \infty$ the transition occurs in the ultra-dilute regime where a pair-interaction-only approximation is entirely justified.

For uniaxial isolated colloidal particles, the nematic phase is axially symmetric about $\hat{\mathbf{n}}$, $f(\Omega) = f(\theta)$ where θ denote the angular deviation of the particle along the polar direction with respect to the global nematic director. The sharpness of this ODF depends on the concentration of the system, and thus we can find different levels of orientational order. The level of order of a nematic phase can be quantified by means of the *uniaxial order parameter* S , defined as follows:

$$S = \langle P_2(\cos \theta) \rangle = \frac{1}{2}(3\langle \cos^2 \theta \rangle - 1) \quad (1.22)$$

in terms of the second Legendre polynomial. The uniaxial order parameter then lies within the interval $-1/2 \leq S \leq 1$, where $S = 1$ indicates perfect ordering (all molecules along $\hat{\mathbf{n}}$) and $S = 0$ indicates maximum disorder, intrinsic to the isotropic phase. The negative limit, $S = -1/2$, signifies the theoretical ordered state along a plane perpendicular to the director (the *anti-nematic* state). An example of the latter type of organization will be discussed in 2.

Mixtures

Chapter 2 will focus on mixtures of anisometric particles consisting of multiple distinct species (e.g., mixtures of discs and polymers with multiple aggregation numbers). Introducing mole fractions $x_j = N_j/N$ for each species j , the free energy of the mixture can be expressed as a straightforward generalization of Eq. (1.18):

$$\begin{aligned} \frac{\beta F}{N} &\sim \ln[\rho\bar{\Lambda}] - 1 + \sum_j x_j \ln x_j + \sum_j x_j \int f_j(\Omega) \ln [4\pi f_j(\Omega)] d\Omega \\ &+ \frac{\rho}{2} \sum_j \sum_k x_j x_k \iint d\Omega d\Omega' f_j(\Omega) f_k(\Omega') v_{excl}^{jk}(\Omega, \Omega'), \end{aligned} \quad (1.23)$$

with $\bar{\Lambda} = \prod_j \Lambda_j^{x_j}$. The contribution $\sum_j x_j \ln x_j$ represents the *entropy of mixing* due to the fact that we are dealing with different species. Although the free energy for mixtures can be easily established, the implications of Eq. (1.23) are quite significant. In particular, each species j

now has its own ODF which must be normalized according to $\int f_j(\Omega)d\Omega \equiv 1$. Moreover, in the case of phase coexistence between an isotropic (I) and a nematic (N) phase, the conditions for mechanical and chemical equilibrium require equal osmotic pressure Π and chemical potentials μ_j for *all* species involved. Thus, the coexistence equations read:

$$\begin{aligned}\Pi^I &= \Pi^N \\ \mu_j^I &= \mu_j^N \quad \text{for all } j,\end{aligned}\tag{1.24}$$

where we must take into account that the composition x_j may differ in each phase due to fractionation effects. These considerations indicate that the calculation of phase transitions in mixtures is generally a challenging task, requiring specific approximations or numerical techniques depending on the physical situation. More details on the particular approaches addressed in this research work can be found in Chapter 2 in which we discuss the case of reversibly polymerizing rods mixed with discs.

1.3.2 Facing reality

Going back to the experimental systems of nanorods and platelets mentioned at the beginning of this chapter it is clear that a simple hard-particle model is often too simple to arrive at a satisfactory description of a typical experimental setup. A number of extensions and modifications of Onsager's theory are then necessary. Some of them involve attempts to account for:

1. Multicomponent mixtures of rod, disks, or living polymers
2. Effect of external aligning fields (e.g. shear and electromagnetic fields)
3. Rod (semi-)flexibility
4. "Soft" interactions (e.g. depletion attraction)
5. Chirality
6. Non-uniform systems (interfaces, effect of solid substrates)

In the main body of this work we will illustrate the rich phenomenology brought about by the topics listed above, most of the time as perturbations to the main entropic hard-core contribution, discussed previously in the context of Onsager's theory. We hope that these examples will convince the reader of the predictive power and versatility of Onsager's second-virial theory even when applied beyond the strict bounds of applicability as formulated in his original paper. In what follows, topics 4 and 5, albeit already introduced, are now very briefly discussed from a more quantitative perspective. Additionally, the effect of non-uniformity in LC systems (topic 6) is discussed in Section 1.3.3

Depletion

While the effective potential induced by (polymer) depletion remains relatively tractable for simple spherical particles, the quantity becomes highly non-trivial for more complex colloidal shapes. This is due to the intrinsic orientation-dependence of the depletion zones and their overlap conditions when generalized to suspensions involving rod or disk-shaped nanoparticles, and also to the non-additive nature of the depletion potential when the size of the depletants is comparable to the width of the colloids. The depletion attraction between non-isotropic particles could be formally expressed as a mean-field correction term:

$$U_{dep} \sim -\frac{1}{2} \frac{N^2}{V} \Pi_{dep} \left\langle \int_{\substack{\text{no core overlap,} \\ \text{depletion zone overlap}}} d\mathbf{r}_{ij} v_{ij}^{dep}(\mathbf{r}_{ij}) \right\rangle_{\text{orientational states of rods } i \text{ and } j} \quad (1.25)$$

where Π_{dep} is the osmotic pressure exerted by the depletants. In arriving at this expression, the depletion agents have been considered to be mutually non-interacting and the effective attraction potential between the nanoparticles is proportional to the overlap volume v_{ij}^{dep} of the depletion zones of particles i and j (see Fig. 1.2) [37].

Chirality

The presence of surface charges (or *soft patches*) residing on the colloid surface in a distinctly *helical* distribution can impart a distinctly chiral signature on to the effective interactions between the nanoparticles. In this case, there is a supplementary soft interaction coupling to the rod orientation vector $\hat{\mathbf{u}}$ of each rod i and j (see Fig. 1.1 (e) and (f)) and their centre-of-mass distance vector \mathbf{r} through the following pseudo-scalar expression [38]:

$$u_{ij} \sim \varepsilon_c g(r) (\hat{\mathbf{u}}_i \cdot \hat{\mathbf{u}}_j) (\hat{\mathbf{u}}_i \times \hat{\mathbf{u}}_j \cdot \mathbf{r}) \quad (1.26)$$

In Chapter 5, we will analyze in detail the implications of this interaction for the chiral features of colloidal mesoscopic compounds, whose microscopic details can be encapsulated into the effective chiral amplitude ε_c and decay function $g(r)$, which expresses the typical range over which chiral forces are transmitted. The effective potential is distinctly chiral and lacks inversion symmetry, meaning that it changes under a parity transformation $\mathbf{r}_{ij} \rightarrow -\mathbf{r}_{ij}$, while preserving basic head-tail symmetry $u_{ij}(\hat{\mathbf{u}}_{i/j}) = u_{ij}(-\hat{\mathbf{u}}_{i/j})$.

1.3.3 Non-uniformity in nematic LCs: nemato-elasticity and surface anchoring

In this section, we discuss how the presence of confining boundaries can significantly alter the overall free energy of the system. This situation arises, for instance, when colloidal particles are immersed in a thermotropic liquid crystal and defects emerge around the colloidal surface, as discussed in Chapter 3 and 4 or when dealing with liquid crystalline droplets such as tactoids and smectic membranes surrounded by an isotropic environment (Chapter 5). First, we focus on the elastic free energy originated from deformations in the bulk director field, described in

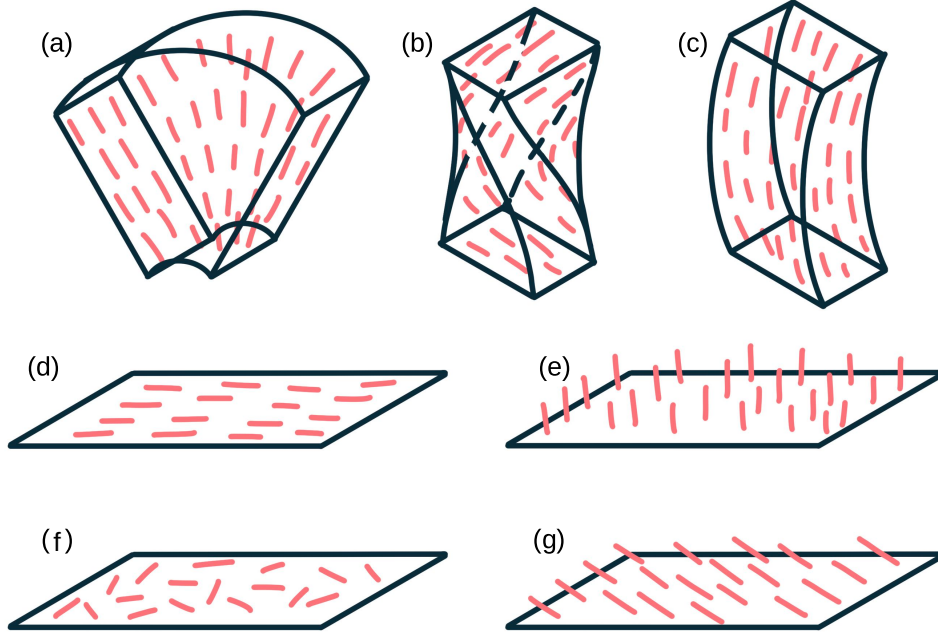


Figure 1.4: Top row: elastic deformations in nematic liquid crystal: (a) splay, (b) twist and (c) bend. Middle and bottom row: surface anchoring situations of a nematic liquid crystal on a surface: (d) uniform planar anchoring, (e) homeotropic anchoring, (f) degenerate planar anchoring and (g) tilted anchoring.

the Frank-Oseen form. Next, a surface term to the free energy is presented that accounts for the order induced by the presence of an interface, an effect commonly known as *surface anchoring*.

Nemato-elasticity

In general, the ordering effect of an external interaction applied to the bulk nematic phase leads to specific elastic deformations in the nematic director. This external influence can be, for example, the presence of an interface with a solid, a liquid or a gas near the bulk nematic phase (as discussed in Chapters 3 and 5) or the interaction between the nematic phase and some external field (e.g. in Chapter 4 we study the immersion of a colloidal nematic into a twist-inducing molecular cholesteric field). The resulting deformations of the nematic director can be described by one or a combination of any of the basic elastic modes: splay, twist and bend. These modes are sketched in Fig. 1.4 (a), (b) and (c), and are often expressed in terms of spatial variations of the nematic director $\hat{\mathbf{n}}$ expressed by the Frank-Oseen free energy for the case of weak deformations [39]:

$$F = \frac{1}{2} \int d\mathbf{r} [K_1(\nabla \cdot \hat{\mathbf{n}})^2 + K_2(\hat{\mathbf{n}} \cdot \nabla \times \hat{\mathbf{n}} + q_0)^2 + K_3(\hat{\mathbf{n}} \times \nabla \times \hat{\mathbf{n}})^2] \quad (1.27)$$

The elastic constants K_i inherently depend on the nematic order parameter (S , defined in Eq. (1.22)). The splay, twist and bend modes are addressed through the constants K_1 , K_2 and K_3 respectively. The constant q_0 appearing in the twist deformation term is relevant only

in chiral phases, and accounts for the inverse cholesteric pitch. Further extensions can be incorporated in the Frank–Oseen free energy that are primarily restricted to the surface of the nematic liquid crystals:

$$F_{13} = K_{13} \int d\mathbf{r} \nabla \cdot [\hat{\mathbf{n}}(\nabla \cdot \hat{\mathbf{n}})] \quad (1.28)$$

$$F_{24} = -K_{24} \int d\mathbf{r} \nabla \cdot [\hat{\mathbf{n}}(\nabla \cdot \hat{\mathbf{n}}) + \hat{\mathbf{n}} \times (\nabla \times \hat{\mathbf{n}})] \quad (1.29)$$

K_{13} and K_{24} are known as the *splay–bend* and the *saddle–splay* mixed constants respectively. In Chapter 5 we demonstrate that saddle-splay elasticity plays an important role in stabilizing chiral tactoids such as double-twisted ribbons observed in mixtures of colloidal rods and non-adsorbing polymer [28].

The Frank elastic energy is often simplified by assuming the *one constant approximation*: $K = K_1 = K_2 = K_3$, in which case Eq. (1.27) reduces to:

$$F = \frac{1}{2} K \int d\mathbf{r} [(\nabla \cdot \hat{\mathbf{n}})^2 + (\nabla \times \hat{\mathbf{n}})^2] \quad (1.30)$$

While this approximation is commonly applied in most LC modelling studies we demonstrate in Chapters 3 and 5) that it may lead to qualitative discrepancies with experimentally observed behavior for complex director deformations such as chiral defects and twisted ribbons we respectively consider in those chapters.

Following Eq. (1.27), the bulk nematic order parameter S is often assumed to be uniform throughout the system volume, a consideration that we consistently apply in our analytical work in Chapters 3 and 4 on colloids immersed in thermotropic LCs. This assumption is justified if the surface anchoring forces are weak and director distortions around the surface are only weakly developed. For the mesoscopic LC membranes discussed in Chapter 5 the assumption of constant bulk nematic order works well as long as the local colloid density is uniform throughout the membrane. We wish to emphasize that the Frank–Oseen theory is a particular case of a more complete LC continuum theory that accounts for changes in the bulk nematic order, known as the Landau–de Gennes theory that we do not use here. We refer the reader to De Gennes’ book [39] for more details on this theory.

Surface anchoring

The presence of a solid, liquid or gas interface in the vicinity of the nematic liquid crystal phase can affect the inherent ordering, leading to a modified equilibrium state. Particles next to the interface tend to follow a surface–induced axis. In general, the director alignment along this axis is determined by the interaction between the liquid crystal and the aligning surface, giving way to a variety of anchoring geometries. Some of them are shown in Fig. 1.4. For uniaxial nematics, the surface contribution to the free energy reads:

$$F_s = -\frac{1}{2} W_0 \oint d\mathcal{S} (\hat{\mathbf{n}}_s \cdot \hat{\mathbf{n}}_0(\mathcal{S}))^2 \quad (1.31)$$

where W_0 represents the strength of anchoring, $\hat{\mathbf{n}}_0$ is the preferred “easy” direction of nematic order at the surface denoted by \mathcal{S} and $\hat{\mathbf{n}}_s$ is the actual nematic director. This contribution is known as the Rapini–Papoular surface anchoring free energy [40] and is a reliable choice to account for anchoring forces between a liquid crystal and a substrate [41].

1.4 Hard-particle Monte Carlo (HPMC) simulations of colloidal nematics: some technical details

In the last half century, the use of molecular simulations has become increasingly widespread across a multitude of scientific disciplines, representing an essential tool in the realm of colloidal and soft matter science. The initial success of these simulations can be traced back to their ability to predict the transition between the fluid and solid phases in a system of hard spheres [16, 17]. Since then, molecular simulations have become a pillar in soft matter research, allowing for the exploration of complex systems at the molecular level with remarkable accuracy and versatility.

Molecular simulations are classified into two principal categories: Molecular Dynamics (MD) and Monte Carlo (MC) simulations. The fundamental aim of both techniques is to acquire macroscopic observables from microscopic properties of the system. While MD simulations focus on time averages, MC simulations rely on ensemble averages. In the thermodynamic limit, these two types of averages become equivalent, according to the ergodic hypothesis, which postulates that a system traverses all possible states in its phase space over a long enough time scale [42]. As a result, the use of molecular simulations has led to significant advances in a variety of fields, ranging from materials science to biophysics and beyond, making them an indispensable tool for contemporary scientific research.

One of the advantages of MC over MD is that it permits to study systems characterized by non-analytical interaction potentials e. g. the hard core interaction invoked in this work. Using Monte Carlo simulations to explore the configurational space of a system at certain conditions, an observable A can be calculated as an average over a big number of accessible configurations. In the canonical ensemble (systems at constant $\{N, V, T\}$) this can be integrated using the Boltzmann probability $\exp(-U/k_B T)$ of finding a particle configuration of energy U :

$$\langle A \rangle = \frac{\int d\mathbf{r}^N A(\mathbf{r}^N) \exp(-\beta U)}{\int d\mathbf{r}^N \exp(-\beta U)} \quad (1.32)$$

A possible way to evaluate Eq. (1.32) is through the Metropolis Monte Carlo algorithm [43], which becomes much simpler for hard core systems due to the fact that, in this case, the Boltzmann factor can only be worth 0 or 1. The basic form of a MC cycle takes then the form of Algorithm 1 In this section we aim to give an overview of the technical peculiarities of Hard Particle Monte Carlo (HPMC) simulations of anisotropic particles, in particular mixtures of elongated rods and depletants, that are used in the computational model studied in Chapter 5.

Algorithm 1: Metropolis Monte Carlo algorithm for hard-core potentials in the canonical ensemble.

```

1 Start from an initial configuration of  $N$  particles;
2 for  $k = 0, \dots, N - 1$  do
3   | Choose a random particle  $i$ ;
4   | Give the particle a random transformation (translation or rotation);
5   | Check for overlaps;
6   | if new configuration generates an overlap then
7     | | Reject: roll back to old configuration;
8   | else
9     | | Accept: update the configuration;
10  | end
11 end

```

1.4.1 Overlap conditions for hard spherocylinders

As shown in Algorithm 1, in HPMC a move is accepted if there is no overlap between two particles. Hence an efficient overlap test is key in this technique. In the case of spherical objects the overlap test is very simple: it is enough to compute the distance between the center of the two spheres r_{ij} and verify that it is less than the sum of their radii: $r_{ij} \leq R_i + R_j$ or, in a computationally cheaper form, $r_{ij}^2 \leq (R_i + R_j)^2$. It is possible to model elongated hard rods that use this simple overlap condition by building particles composed of spherical objects attached in a linear chain. In this case, the overlap test simply consists on evaluating pairs of spherical objects associated to distinct rods. However, the computational expense of this strategy is enormous as it involves the order of N_b^2 operations at each MC move where N_b is the number of spherical beads in one rod. This problem is overcome if each colloidal rod is considered to be a spherocylinder, for which a more efficient overlap test is proposed by Allen *et al.* [30]. The key steps are outlined below.

A spherocylinder i is defined by its cylindrical surface length L , the diameter D of its cylindrical surface and its two hemispheres, the coordinates \mathbf{r}_i of its center of mass and the unit vector $\hat{\mathbf{u}}_i$ indicating its orientation. We want to determine the minimum distance between the cores of two spherocylinders i and j with equal lengths and diameters. We can describe any point of the line segment core of i and j parametrically as

$$\begin{aligned} \mathbf{r}_i(\lambda) &= \mathbf{r}_i + \lambda \hat{\mathbf{u}}_i \\ \mathbf{r}_j(\mu) &= \mathbf{r}_j + \mu \hat{\mathbf{u}}_j \end{aligned} \tag{1.33}$$

In order to calculate the minimum distance between two arbitrarily oriented lines we can take advantage of the fact that the shortest distance vector,

$$\mathbf{r}_{ij}^{min}(\lambda_0, \mu_0) = \mathbf{r}_j(\mu_0) - \mathbf{r}_i(\lambda_0), \tag{1.34}$$

must be perpendicular to both $\hat{\mathbf{u}}_i$ and $\hat{\mathbf{u}}_j$. Assuming $\mathbf{r}_{ij}^{min}(\lambda_0, \mu_0) \cdot \hat{\mathbf{u}}_i = 0$ and $\mathbf{r}_{ij}^{min}(\lambda_0, \mu_0) \cdot \hat{\mathbf{u}}_j = 0$

we obtain a system of equations that we can solve to get the minimizing values λ_0 and μ_0 :

$$\begin{pmatrix} \lambda_0 \\ \mu_0 \end{pmatrix} = \frac{1}{1 - (\hat{\mathbf{u}}_i \cdot \hat{\mathbf{u}}_j)^2} \begin{pmatrix} -\hat{\mathbf{u}}_i \cdot \mathbf{r}_{ij} + (\hat{\mathbf{u}}_i \cdot \hat{\mathbf{u}}_j)(\hat{\mathbf{u}}_j \cdot \mathbf{r}_{ij}) \\ +\hat{\mathbf{u}}_j \cdot \mathbf{r}_{ij} + (\hat{\mathbf{u}}_i \cdot \hat{\mathbf{u}}_j)(\hat{\mathbf{u}}_i \cdot \mathbf{r}_{ij}) \end{pmatrix} \quad (1.35)$$

where $\mathbf{r}_{ij} = \mathbf{r}_j - \mathbf{r}_i$ is the distance between centers of mass. Since for line segments $-\frac{L}{2} \leq (\lambda, \mu) \leq \frac{L}{2}$ we have to truncate the result of Eq. (1.35) if it exceeds this limit. In order to avoid more arithmetical operations than necessary, at this point it is better to compute the square minimal distance

$$\begin{aligned} (\mathbf{r}_{ij}^{min})^2(\lambda_0, \mu_0) &= \mathbf{r}_{ij}^2 + \lambda_0^2 + \mu_0^2 - 2\lambda_0 \hat{\mathbf{u}}_i \cdot \mathbf{r}_{ij} \\ &\quad + 2\mu_0 \hat{\mathbf{u}}_j \cdot \mathbf{r}_{ij} - 2\lambda_0 \mu_0 \hat{\mathbf{u}}_i \cdot \hat{\mathbf{u}}_j \end{aligned} \quad (1.36)$$

from quantities already calculated. All the above scheme works unless spherocylinders are completely parallel to each other, in which case Eq. (1.35) is not well defined. We can add a condition to account for this particular case, where the minimal distance would be simply calculated as the distance between two parallel lines.

There is an overlap between the two spherocylinders if $(\mathbf{r}_{ij}^{min})^2 \leq D^2$. A generalization of this idea can be done for mixtures of two different species of spherocylinders of lengths $L_{1,2}$ and diameters $D_{1,2}$ by simply rewriting

$$\begin{aligned} -\frac{L_i}{2} &\leq \lambda \leq \frac{L_i}{2} \\ -\frac{L_j}{2} &\leq \mu \leq \frac{L_j}{2} \\ (\mathbf{r}_{ij}^{min})^2 &\leq \left(\frac{D_i + D_j}{2} \right)^2 \end{aligned} \quad (1.37)$$

where $i, j = 1$ or 2 if the spherocylinders belong to the first or second species respectively. For mixtures of spherocylinders and spheres, the expressions can also be valid by taking $L = 0$ for spheres.

1.4.2 Semi-grand canonical ensemble

Several theories have been developed that enable calculations of phase transitions in systems with depletion interactions. The free volume theory (FVT) by Lekkerkerker *et al.* [44] for the phase behavior of dispersions of colloids and non-adsorbing polymer was the first one to account for depletant partitioning over the coexisting phases. This theory is based on the osmotic equilibrium between two systems: a hypothetical depletant reservoir and a mixed colloid + depletant system. Because of its affordability in terms of complexity and yet a phenomenologically accurate description of the problem, this theory serves as a standard reference today, both for theoretical and computational models.

The starting point is the *semi-grand* potential density of a system of colloids and polymer in equilibrium with a reservoir containing only the polymer. This semi-grand potential is separated into a hard colloid contribution and a polymer contribution. The colloid part may be

described by known expressions for the colloidal fluid and crystalline phases in the canonical ensemble (fixed volume, temperature and number of colloidal particles $\{N, V, T\}$). The polymer contribution is found from a build-up principle: starting from a system without polymer, chains are added to the system until the final concentration is reached, and the polymer contribution is calculated by integrating along this path. This is the reason why the polymer part is treated in a more natural way by using the grand canonical formalism (fixed volume, temperature and polymer chemical potential $\{\mu_p, V, T\}$). The key assumption of this theory is that thermodynamic quantities can be calculated for both colloids and depletants from their independent ensembles, correlated only by means of an ensemble-averaged free volume for the depletants in the mixed system $\langle V_{free} \rangle$. As a result, we can define the semi-grand canonical potential

$$\Omega(N, V, T, \mu_p) = F_0(N, V, T) - \Pi^R \langle V_{free} \rangle \quad (1.38)$$

where F_0 is the free energy of the colloidal particle system without added depletant, μ_p represents the chemical potential of the polymer depletant and $\langle V_{free} \rangle$ is the available volume for the depletants, i.e. the total volume in the mixed system outside the depletion layers, and it is approximated by the free volume in the pure hard colloid dispersion $\langle V_{free} \rangle_0$. This approximation is valid in the limit of low depletant activity, and starts losing accuracy when increasing it. Π^R is the osmotic pressure in the reservoir, and it can be easily calculated by considering the depletants as penetrable hard spheres, which allows for an ideal gas formulation in terms of van 't Hoff's law

$$\Pi^R = n_p k_B T \quad (1.39)$$

where n_p is the number density of the depletants in the reservoir. We can also write the chemical potential:

$$\mu_p = \text{const} + k_B T \ln n_p \quad (1.40)$$

In order to equate the depletant chemical potentials in both systems, we infer that the average number of depletants in the mixed system N_p must fulfill

$$N_p = n_p \langle V_{free} \rangle \quad (1.41)$$

In what matters to our simulations presented in Chapter 5, the total number of particles in a semi-grand MC scheme is no longer constant, but rather fluctuating towards an optimal value given by $N + N_p$. This allows us to stabilize mesoscopic colloidal systems such as tactoids and colloidal membranes while maintaining a constant depletion pressure. Algorithm 2 describes a modification of Algorithm 1 that accounts for depletants in the semi-grand canonical ensemble. Similar schemes have been performed by Bolhuis and Frenkel [45] and Vink and Horbach [46]. Both of these works employ cluster moves as a strategy to increase the acceptance ratio of these MC simulations, which is otherwise significantly low since trial depletant insertion moves have a high probability of overlapping with the volume occupied by the colloids.

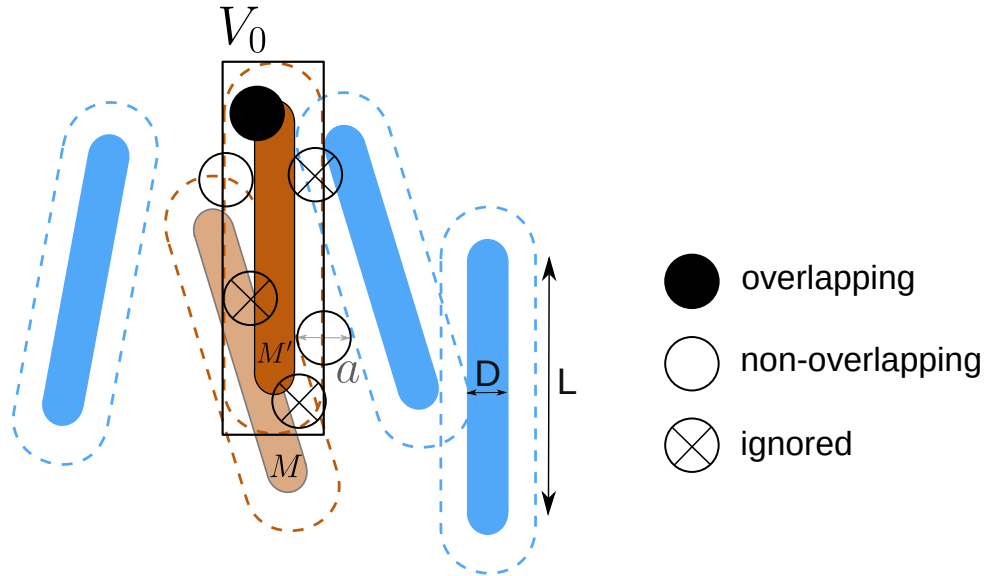


Figure 1.5: Depletant positions (spheres) considered for rejection of a colloid move (orange spherocylinders). When updating the configuration, depletants are randomly inserted into the cylinder (black rectangle) containing the excluded volume between the colloid and the depletants. Overlapping depletants (black spheres) lead to rejection of the trial move. Depletants that overlap with the old position M or with surrounding colloids (blue) are not considered.

1.4.3 Implicit depletants algorithm

In the previous approach, simulation performance can become compromised due to the need to explicitly track all the depletant particles. This is particularly evident in our simulations where a large region of the system volume needs to be kept empty around the mesoscopic colloidal droplets to prevent artifacts induced by system boundaries. As a result, a significant portion of the total volume is completely filled with depletants, which need to be stored and updated during the simulation and yet are not relevant for subsequent statistical analysis.

Some approaches that aim to overcome this issue ([47, 48, 49] to name a few) are based on an effective depletion potential approach, integrated over all the depletant degrees of freedom. However, achieving sufficient accuracy in the pairwise effective potential also comes at the expense of computation time, whereas an overly simplified interaction may hinder the study of arbitrary shapes and size ratios.

Glaser *et al.* [50] proposed a scheme to handle many-body depletion interactions implicitly, avoiding the need to simulate a large number of particles, while maintaining a particle-based approach instead of a more complex effective pairwise potential. The fundamental idea behind this scheme is that depletants can be treated as an ideal gas, assumed to be statistically independent, and therefore, they can be randomly inserted into the excluded volume surrounding a single translated or rotated colloid for each MC step. These depletants are then discarded and re-generated at the following step. The algorithm is particularly efficient for dilute systems of colloids and a large expected number of depletants. It obeys detailed balance and is suitable for multi-core parallel implementations.

In a nutshell, Algorithm 3 conveys the basic idea of this scheme in its most general form. However, this version is computationally impractical since it requires integration of the free volume V_{free} in the entire simulation box for every single colloid move. In the original article [50] several alternative volume choices are considered, and proved to obey detailed balance. It is possible to choose a smaller region $V_0 \subset V$ of the entire volume, containing only the region where modifications are being applied. For simplicity, this volume can also contain regions in principle inaccessible to depletants, i. e. $V_0 \setminus (V_0 \cap V_{free}) \neq \emptyset$; it suffices to ignore the colloid-polymer overlaps occurring in these regions.

For anisotropic colloids with aspect ratios ~ 1 , [50] proposes to choose V_0 as the circumsphere of diameter $D_{colloid} + D_{depletant}$ around the colloid in the new configuration M' , ignoring depletants that overlap with the colloid in the old configuration M . In our case, due to the large aspect ratios that we will be dealing with, we shall rather define V_0 more conveniently as a cylinder at the center of mass of the moved colloid i' , with diameter $D + a$, length $L + D + a$ (with a being the depletant diameter) and orientation $\hat{\mathbf{u}}'_i$. See Fig. 1.5 for a depiction of our approach.

Algorithm 2: Semi-grand canonical Monte Carlo scheme for mixtures of N colloids + depletants at constant chemical potential μ_p .

```

1 Start from an initial configuration of  $N$  colloids and  $N_p$  depletants;
2 for  $k = 0, \dots, N + N_p - 1$  do
3   Choose a random particle type;
4   if type is colloid then
5     Choose a random particle  $i$ ;
6     Give the particle a random transformation (translation or rotation);
7     Check for overlaps;
8     if new configuration generates an overlap then
9       | Reject: roll back to old configuration;
10    else
11      | Accept: update configuration;
12    end
13  end
14  if type is depletant then
15    Choose a random transformation (insertion or deletion);
16    if insertion then
17      Generate random coordinates;
18      Check for overlaps;
19      if new configuration generates an overlap then
20        | Reject: roll back to old configuration;
21      else
22        | Insert with probability
23          |
24          |  $\sim \frac{V}{\Lambda(N_p + 1)} e^{\beta\mu_p}$ 
25        end
26      if deletion then
27        Choose a random particle  $i$ ;
28        Delete with probability
29          |
30          |  $\sim \frac{\Lambda N_p}{V} e^{-\beta\mu_p}$ 
31      end
32    Update  $N_p$  if necessary;
33  end
34 end

```

Algorithm 3: General implicit depletant algorithm proposed by [50].

```

1 Start from an initial configuration  $M$  of  $N$  colloidal particles;
2 for  $k = 0, \dots, N - 1$  do
3   Choose a random particle  $i$ ;
4   Give the particle a random transformation (translation or rotation). Let  $M'$  be the
   new system configuration;
5   Check for overlaps;
6   if overlap in  $M'$  then
7     | Reject: roll back to  $M$ ;
8   else
9     According to the Poisson probability distribution
           
$$\sim \text{Poisson}\left(\frac{V_{free}}{\Lambda} e^{-\beta\mu_p}\right)$$

       of mean and variance  $\frac{V_{free}}{\Lambda} e^{-\beta\mu_p}$ , choose a number of depletants  $N_p$  that will be
       generated;
10    Generate  $N_p$  random depletant positions in  $V_{free}$  the free volume of  $M$ ;
11    Check for overlaps between  $M'$  and the generated depletant positions;
12    if overlap then
13      | Reject: roll back to  $M$ ;
14    else
15      | Accept: update to  $M'$ ;
16    end
17  end
18 end

```

Chapter 2

Phase behavior of shape-persistent living polymers templated by discs

Abstract

This chapter is based on the publication [51]

Living polymers composed of non-covalently bonded building blocks with weak backbone flexibility may self-assemble into thermoresponsive lyotropic liquid crystals. In this chapter we demonstrate that the reversible polymer assembly and phase behavior can be controlled by the addition of (non-adsorbing) rigid colloidal discs which act as an entropic reorienting “template” onto the supramolecular polymers. Using a particle-based second-virial theory that correlates the various entropies associated with the polymers and discs, we demonstrate that small fractions of discotic additives promote the formation of a polymer nematic phase. At larger disc concentrations, however, the phase is disrupted by collective disc alignment in favor of a discotic nematic fluid in which the polymers are dispersed anti-nematically. We show that the anti-nematic arrangement of the polymers generates a non-exponential molecular-weight distribution and stimulates the formation of oligomeric species. At sufficient concentrations the discs facilitate a liquid-liquid phase separation which can be brought into simultaneously coexistence with the two fractionated nematic phases, providing evidence for a four-fluid coexistence in reversible shape-dissimilar hard-core mixtures without cohesive interparticle forces. We stipulate the conditions under which such a phenomenon could be found in experiment.

2.1 Introduction

Supramolecular “living” polymers are composed of aggregating building blocks that are joined together via non-covalent bonds. The polymers can break and recombine reversibly as the typical attraction energy between monomers is comparable to the thermal energy [52, 53]. Elementary (Boltzmann) statistical mechanics then tells us that the polymers must be in equilibrium with their molecular weight distribution which emerges from a balance between the association energy and mixing entropy of the polymers. This results in a wide range of different polymeric species with an exponential size distribution whose shape is governed primarily by temperature and monomer concentration. Reversible polymers are thus distinctly different from

usual “quenched” polymers whose molecular weight distribution is fixed by the conditions present during the synthesis process.

Reversible association is ubiquitous in soft matter. Examples include the formation of various types of micellar structures from block-copolymers [54, 55], hierarchical self-assembly of short-fragment DNA [56, 57], chromonic mesophases [58, 59] composed of non-covalently stacked sheetlike macromolecules, and the assembly of amyloid fibrils from individual proteins [60]. Microtubules, actin and other biofilaments provide essential mechanical functions in the cell and consist of dynamically organizing molecular units that self-organize into highly interconnected structures [61].

A particularly interesting case arises when the monomers associate into shape-persistent, directed polymers [62]. Interpolymer correlations then become strongly orientation-dependent and may drive the formation of liquid crystals. Spontaneous formation of lyotropic liquid crystals has been observed, for example, in long worm-like micelles under shear [63], oligomeric DNA [64] and chromonics [58]. When the monomer concentration exceeds a critical value, the polymers grow into strongly elongated aggregates and an (isotropic) fluid of randomly oriented polymers may spontaneously align into, for instance, a nematic liquid crystal characterized by long-range orientational correlations without structural periodicity [39]. While aggregation-driven nematization has been contemplated also for thermotropic systems [65], our current focus is on lyotropic systems composed of rigid polymers suspended in a fluid host medium, where the isotropic-nematic phase transition can be rationalized on purely entropic grounds in terms of a gain of volume-exclusion entropy upon alignment at the expense of orientational entropy [15, 66, 29]. However, this argument becomes more convoluted in the case of directed, reversible polymers where the trade-off between these two entropic contributions is compromised by a simultaneous maximisation of the mixing entropy and the number of monomer-monomer linkages. In particular, the coupling between orientational order and polymer growth turns out to be a very important one; collective alignment leads to longer polymers, which tend to align even more strongly thus stimulating even further growth [67]. Recent simulation studies have basically corroborated this scenario [68, 69, 70].

An intriguing question in relation to the above is the following: Can the hierarchical organization of reversible polymers be controlled by the addition of non-adsorbing shape-dissimilar components that affect the way they align? Indeed, for chromonics it is known that the presence of additives can bring about condensation or reorientation of the reversible stacks, thereby changing their phase behavior through subtle modifications of the system entropy [71]. Recent experiments on clay nanosheets mixed with reversibly polymerizing tubuline rods have demonstrated that these mixtures remain stable against flocculation and provide a testbed for exploring entropy-driven phase behavior of biopolymer-platelet mixtures [72]. Furthermore, it is well established that mixing prolate (rod-shaped) colloids with their oblate counterparts generates a strong coupling between the orientations of both components leading to organizations with mixed nematic and anti-nematic symmetries. Numerous theoretical studies starting with the early work of Alben [73] have attempted to rationalize the intricate isotropic-nematic phase behavior of these mixtures placing particular emphasis on stabilizing the highly sought-after biaxial nematic phase in which both components are aligned along mutually perpendicular directions

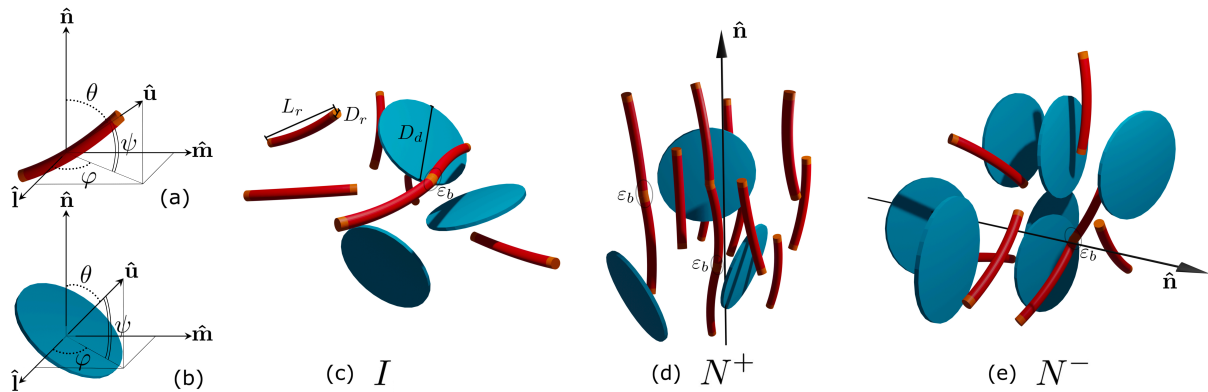


Figure 2.1: Schematic representation of the various liquid crystal phases emerging for discs mixed with polymerizing rods: (a) - and (b) - Principal angles describing the orientation $\hat{\mathbf{u}}$ of a single rod monomer - and disc - with respect to the molecular director $\hat{\mathbf{n}}$ with θ denoting the polar angle, φ the azimuthal angle and $\psi = \frac{\pi}{2} - \theta$ the polar angle. (c) Isotropic phase. (d) polymer uniaxial nematic phase N^+ . (e) discotic uniaxial nematic phase N^- in which the reversibly polymerizing rods are dispersed *anti-nematically*.

thus generating a fluid with an orthorhombic (D_{2h}) symmetry [74, 75, 76, 77, 78, 79, 80, 81, 82, 83, 84]. Similar kinds of anti-nematic or biaxial symmetries could arise when dispersing rod-shaped colloids in a thermotropic liquid crystal under appropriate anchoring conditions [85, 86]. Anti-nematic order has been shown to naturally emerge in porous smectic structures of shape-persistent nanorings [87, 88] or may be realized with the help of external electromagnetic fields as was demonstrated for clay nanosheets [89] and for discs in the presence of associating magnetic beads [90]. In this study we wish to build upon the preceding concepts and explore hierarchical self-organization of reversible polymers in the presence of disc-shaped particles. An example of colloidal discs that could be envisaged are clay nanosheets that consist of nanometer-thick discotic particles with a very high diameter-to-thickness ratio. These particles find widespread use in industrial soft matter and are at the basis of many colloidal-polymer composite materials [91, 92]. The clay sheets on their own, provided they do not gelate in crowded conditions, have a natural tendency to align and form various types of liquid crystals, including nematic phases [93, 94, 95, 96]. When mixed with reversibly polymerizing components in the absence of strong disc-polymer attractions, the discs not only induce orientational "templating" of the supramolecular polymers [97], they also influence the mixing entropy of the system which must have consequences for polymer growth and phase behavior [98, 99]. It is precisely these combined entropic effects that we wish to examine more closely in this work. To this end, we formulate a simple model (Section II) that we subsequently cast into a particle-based theory (Section III) that features reversible association and accounts for all relevant entropic contributions on the approximate second-virial level. The orientation degrees of freedom of the species are treated using a number of simplified variational approaches that render our theory algebraically manageable. We stress that our primary attention in this work goes to mixed-shape nematic phases and we do not consider partially crystallized states that may become stable at elevated packing conditions where our theoretical approach is no longer applicable.

Our study broadly falls into two parts. In the first part (Section IV) we explore the molecular weight distribution in mixtures in which the polymers are organized either nematically

or *anti-nematically*. The latter state can be realized at elevated disc concentrations where correlations between the discs are strong enough to generate nematic order of the discotic subsystem which in turn, enforces the supramolecular rods to align perpendicular to the discotic director in such a way that the overall system retains its uniaxial $D_{\infty h}$ point group symmetry (Fig. 2.1(e)). Whereas reversible polymers in a conventional nematic organization are distributed along a near-exponential form with minor non-exponential corrections at short lengths [69], we argue that *anti-nematic* living polymers may, under certain conditions, exhibit a strong non-exponential weight distribution with the most-probable polymer size being oligomeric rather than monomeric.

In the second part of the chapter (Section V and VI) we explore the isotropic-nematic phase behavior of the mixed systems by focusing on the uniaxial nematic phases, which seems to be the prevailing nematic symmetry for strongly shape-dissimilar mixtures [83, 75, 81, 79, 100]. Our theoretical model is generic and should be applicable to a wide range of different monomer-disc size ratios and temperatures. We discuss the key features for a few exemplary mixtures. One of them is a distinct azeotrope that develops for the isotropic-polymer nematic coexistence, suggesting a strong orientational templating effect imparted by volume-excluded interactions between the polymers and the discs. Furthermore, under certain disc-monomer size constraints, a remarkable four-phase equilibria appears involving a simultaneous coexistence of isotropic gas and liquid phases along with two fractionated uniaxial nematic phases. In Section VII we discuss our findings in relation to recent colloid-polymer models where similar multiphase equilibria have been reported. We end this work with formulating the main conclusions along with some perspectives for further research in Section VIII.

2.2 Model

In this study, we focus on mixtures of tip-associating rod-shaped monomers with limited backbone flexibility mixed with rigid discs. An overview of the basic particle shapes is given in Fig. 2.1. We assume that each rod monomer is equipped with identical attractive patches at either tip such that each rod end can only form a single bond with an adjacent rod tip producing a linear polymer. The rods do not associate into multi-armed or ring-shaped polymers. We further assume that all species retain their basic fluid order such that the respective density distributions remain uniform in positional space (but not necessarily in orientational phase space). We do not account for the possibility of hexagonal columnar phases formed by (pure) polymers at high monomer concentration and low temperature combined with elevated polymer backbone flexibility [98, 101]. In fact, discs too may form columnar structures at packing fraction exceeding typically 40 % [19, 102, 103] which goes beyond the concentration range we consider relevant here. Interactions between the polymer segments and the discs are assumed to be purely hard with the only energy scale featuring in the model being the non-covalent bond energy ε_b between the monomers.

Contrary to previous modelling studies of rod-discs mixture we focus here solely on uniaxial nematic phases and ignore the possibility of biaxial order in which both components align along mutually perpendicular directors. Our focus is motivated by the strong expectation that

excluded-volume interactions between the polymers and the discs, which are the principal entropic forces behind generating nematic order [15], are too disparate to guarantee such orthorhombic nematic symmetry to be stable. Previous theoretical studies [80, 81, 100, 83, 84] as well as experiments [104, 105, 106] and simulations [75, 107, 82] on mixed-shape colloids suggest that strongly unequal excluded volumes indeed favour demixing into strongly fractionated uniaxial nematic phases. In view of the basic symmetry difference between the linear polymer and disc, we then anticipate a rod-based uniaxial phase (denoted N^+ , Fig. 2.1(d)) in which the discs are distributed anti-nematically throughout the uniaxial matrix. Conversely, when the discs outnumber the polymers, a disc-based uniaxial nematic (N^- , Fig. 2.1(e)) is formed in which the aggregating rods adopt anti-nematic order. The onset of biaxial order emerging from these uniaxial reference phases can be estimated from a simple bifurcation analysis discussed in Appendix 2.B.

2.3 Second-virial Theory for Reversible Polymers mixed with rigid discs

We start with formulating the free energy per unit volume V of a mixture of discs with density $\rho_d(\hat{\mathbf{u}})$ and reversibly polymerizing rods. We define $\rho_r(\ell, \hat{\mathbf{u}})$ as the number density of monomer segments aggregated into a polymeric rod with contour length ℓL and orientation described by unit vector $\hat{\mathbf{u}}$. The aggregation number or polymerization degree is specified by the index $\ell = 1, 2, 3, \dots$. Let us write the free energy per unit volume of the mixture as follows [69, 108]:

$$\begin{aligned} \frac{F}{V} \sim & \sum_{\ell} \int d\hat{\mathbf{u}} [\ln(4\pi\Lambda_r\rho_r(\ell, \hat{\mathbf{u}})\ell^{-1}) - 1] \ell^{-1}\rho_r(\ell, \hat{\mathbf{u}}) \\ & + \int d\hat{\mathbf{u}} [\ln(4\pi\Lambda_d\rho_d(\hat{\mathbf{u}})) - 1] \rho_d(\hat{\mathbf{u}}) + \frac{F_{as}}{V} + \frac{F_{wlc}}{V} + \frac{F_{ex}}{V} \end{aligned} \quad (2.1)$$

Without loss of generality, all energies are implicitly expressed in units of thermal energy $k_B T$ (with k_B Boltzmann's constant and T temperature). Furthermore, $\Lambda_{r/d}$ are the thermal volumes of the species which are immaterial for the thermodynamic properties we are about to explore. The factor 4π is included for convenience and equals the unit sphere surface representing the orientational phase space. The total rod monomer concentration ρ_{r0} is a conserved quantity so that $\rho_{r0} = \sum_{\ell} \int d\hat{\mathbf{u}} \rho_r(\ell, \hat{\mathbf{u}})$. Likewise, $\rho_{d0} = \int d\hat{\mathbf{u}} \rho_d(\hat{\mathbf{u}})$ represents the number density of discs. The first two terms are related to the ideal gas or mixing entropy and describe the ideal translation and orientational entropy of each polymer and disc, respectively. The third contribution in Eq. (2.1) represents an association energy that drives end-to-end aggregation of the monomer segments. It reads:

$$\frac{F_{as}}{V} = \varepsilon_b \sum_{\ell} \int d\hat{\mathbf{u}} \ell^{-1} \rho_r(\ell, \hat{\mathbf{u}}) (\ell - 1) \quad (2.2)$$

The free energy per unit volume arising from the polymerized rod segments follows from the bond potential ε_b between two adjacent rod segments and the number density $\rho_a(\ell, \hat{\mathbf{u}}) = (1/\ell)\rho_r(\ell, \hat{\mathbf{u}})$ of polymers with aggregation number ℓ each containing $\ell - 1$ bonds. Being normalized to the thermal energy the potential ε_b serves as an *effective* temperature scale. At strongly reduced temperature ($\varepsilon_b \ll 0$) the association energy is minimised when all monomers join together into a single long polymer, while at high temperature ($\varepsilon_b \gg 0$) polymerization is strongly suppressed. If $-\varepsilon_b$ is of the order of the thermal energy $k_B T$, the single chain configuration is highly unfavorable in view of the mixing entropy that favors a broad distribution of aggregates with strongly disperse contour lengths. This we will explore more systematically in Section IV.

2.3.1 Backbone flexibility

The second last term in Eq. (2.1) represents the effect of polymer flexibility through a correction to the original orientational entropy (first term in Eq. (2.1)) that accounts for the internal configurations of a so-called worm-like chain [29]. This leads to a strongly non-linear term with respect to the segment density [109, 69]:

$$\frac{F_{wlc}}{V} = -\frac{2L_r}{3\ell_p} \sum_{\ell} \int d\hat{\mathbf{u}} [\rho_r(\ell, \hat{\mathbf{u}})]^{1/2} \nabla^2 [\rho_r(\ell, \hat{\mathbf{u}})]^{1/2} \quad (2.3)$$

where ∇^2 denotes the Laplace operator on the unit sphere. The persistence length ℓ_p measures the typical length scale over which local orientational fluctuations of the segments are correlated. In our model we assume that the rod segments are only slightly flexible [109] so that $\ell_p \gg \ell$ suggesting that the main orientational entropy stems from the rigid body contribution that is subsumed into the ideal gas term in Eq. (2.1). The worm-like chain correction vanishes in the somewhat unnatural situation where all polymers, irrespective of their contour length, are perfectly rigid and the persistence length tends to infinity ($\ell_p \rightarrow \infty$).

2.3.2 Excluded-volume entropy

The last contribution in Eq. (2.1) is the excess free energy that incorporates all excluded-volume driven interactions between the stiff polymers and discs. Assuming all interactions to be strictly hard, we write following Ref. [74]:

$$\begin{aligned} \frac{F_{ex}}{V} &= \frac{1}{2} \sum_{\ell, \ell'} \iint d\hat{\mathbf{u}} d\hat{\mathbf{u}}' \rho_r(\ell, \hat{\mathbf{u}}) \rho_r(\ell', \hat{\mathbf{u}}') 2L_r^2 D_r |\sin \gamma| \\ &+ \sum_{\ell} \iint d\hat{\mathbf{u}} d\hat{\mathbf{u}}' \rho_r(\ell, \hat{\mathbf{u}}) \rho_d(\hat{\mathbf{u}}') \frac{\pi}{4} L_r D_d^2 |\cos \gamma| \\ &+ \frac{1}{2} \iint d\hat{\mathbf{u}} d\hat{\mathbf{u}}' \rho_d(\hat{\mathbf{u}}) \rho_d(\hat{\mathbf{u}}') \frac{\pi}{2} D_d^3 |\sin \gamma| \end{aligned} \quad (2.4)$$

where $L_{r,d}$ and $D_{r,d}$ denote the length and diameter of the cylindrical building blocks (see Fig. 2.1(b)). We assume all polymers and discs to be sufficiently slender, i.e., $L_r/D_r \gg 1$ and $D_d/L_d \gg 1$, and we assume monomers and discs to present relative sizes such that $D_d/D_r \gg 1$ so that finite-thickness corrections to the excluded volume terms above can be neglected. Next

we formally minimize the free energy with respect to the polymer segment distribution

$$\frac{\delta}{\delta \rho_r(\ell, \hat{\mathbf{u}})} \left(\frac{F}{V} - \lambda_r \sum_{\ell} \int d\hat{\mathbf{u}} \rho_r(\ell, \hat{\mathbf{u}}) \right) = 0 \quad (2.5)$$

and to the one-body density of the discs

$$\frac{\delta}{\delta \rho_d(\hat{\mathbf{u}})} \left(\frac{F}{V} - \lambda_d \int d\hat{\mathbf{u}} \rho_d(\hat{\mathbf{u}}) \right) = 0 \quad (2.6)$$

The Lagrange multipliers $\lambda_{r,d}$ ensure that the total concentration of each species (monomers and discs) be preserved. The coupled Euler-Lagrange (EL) equations can be rendered tractable by expanding the orientation-dependent kernels that depend on the enclosed angle γ between the main particle orientation axes, as we will show next.

2.4 Molecular weight distribution from second-polynomial approximation

A commonly employed method to cast the free energy in a more tractable form is to express the trigonometric functions featuring in the excluded-volume Eq. (2.4) in terms of a bilinear expansion in Legendre polynomials [110, 111, 112]. Truncating this expansion after the second-order contribution leads to a simplified theory that has been explored previously for rod-plate mixtures [74, 100] as well as in the context of rods with fixed length polydispersity [113]. For the present mixture, the approximation should be adequate if the nematic order of either component is not too strong. Note that if this condition is not sufficiently fulfilled, calculations may lead to quantitative (and, in some cases, even qualitative) differences in the phase diagrams. We write:

$$\begin{aligned} |\sin \gamma| &= \frac{\pi}{4} - \frac{5\pi}{32} \mathcal{P}_2(\cos \theta) \mathcal{P}_2(\cos \theta') + \dots \\ |\cos \gamma| &= \frac{1}{2} + \frac{5}{8} \mathcal{P}_2(\cos \theta) \mathcal{P}_2(\cos \theta') + \dots \end{aligned} \quad (2.7)$$

in terms of the second Legendre polynomials $\mathcal{P}_2(x) = \frac{3}{2}x^2 - \frac{1}{2}$. The orientation of each particle is described by a polar angle θ and azimuthal angle φ defined with respect to the nematic director $\hat{\mathbf{n}}$ (see Fig. 2.1a and b). Let us define a set of *size-specific* nematic order parameters for the polymer:

$$S_{r\ell} = \rho_{r\ell}^{-1} \int d\hat{\mathbf{u}} \rho_r(\ell, \hat{\mathbf{u}}) \mathcal{P}_2(\hat{\mathbf{u}} \cdot \hat{\mathbf{n}}) \quad (2.8)$$

with $\rho_{r\ell} = \int d\hat{\mathbf{u}} \rho_r(\ell, \hat{\mathbf{u}})$ a partial number density of rod segments belonging to polymers of length ℓL . Likewise we find for the discs:

$$S_d = \rho_{d0}^{-1} \int d\hat{\mathbf{u}} \rho_d(\hat{\mathbf{u}}) \mathcal{P}_2(\hat{\mathbf{u}} \cdot \hat{\mathbf{n}}) \quad (2.9)$$

These order parameters allow us to distinguish between an isotropic fluid ($S_{r\ell} = S_d = 0$), a polymer-dominated uniaxial nematic fluid (N^+ : $S_{r\ell} > 0$, $S_d < 0$) and a discotic one (N^- :

$S_r < 0, S_d > 0$), as sketched in Fig. 2.1d and e, respectively. With the aid of these expansions, the excess free energy can be written in terms of a simple bilinear dependence on the nematic order parameter:

$$\begin{aligned} \frac{F_{ex}}{V} \sim & \rho_{r0}^2 \left(1 - \frac{5}{8} \bar{S}_r^2 \right) + 2q\rho_{r0}\rho_d \left(1 + \frac{5}{4} \bar{S}_r S_d \right) \\ & + z\rho_d^2 \left(1 - \frac{5}{8} S_d^2 \right) \end{aligned} \quad (2.10)$$

Here, we have implicitly renormalized the free energy and species densities in terms of the isotropic excluded volume of the monomeric rods $v_{rr} = \frac{\pi}{4} L_r^2 D_r$. The excess free energy thus only depends on the excluded-volume *ratios* $q = v_{rd}/v_{rr}$ and $z = v_{dd}/v_{rr}$ with $v_{rd} = \frac{\pi}{16} L_r D_d^2$ and $v_{dd} = \frac{\pi^2}{16} D_d^3$ denoting the isotropized monomer-disc and disc-disc excluded volumes, respectively. Furthermore, the bar denotes a molecular-weight average of the nematic order parameter associated with the polymers:

$$\bar{S}_r = \rho_{r0}^{-1} \sum_{\ell} \rho_{r\ell} S_{r\ell} \quad (2.11)$$

Similarly, the coupled EL equations may be cast as follows:

$$\begin{aligned} \ell^{-1} \ln[4\pi\rho_r(\ell, \hat{\mathbf{u}})\ell^{-1}] &= \lambda_r + \varepsilon_b \ell^{-1} + a_r \mathcal{P}_2(\hat{\mathbf{u}} \cdot \hat{\mathbf{n}}) \\ &+ \frac{L_r}{3\ell_p} \frac{\nabla^2[\rho_r(\ell, \hat{\mathbf{u}})]^{1/2}}{[\rho_r(\ell, \hat{\mathbf{u}})]^{1/2}} \end{aligned} \quad (2.12)$$

and

$$\ln[4\pi\rho_d(\hat{\mathbf{u}})] = \lambda_d + a_d \mathcal{P}_2(\hat{\mathbf{u}} \cdot \hat{\mathbf{n}}) \quad (2.13)$$

The uniaxial order parameters that feature in the EL equations are specified as follows:

$$\begin{aligned} a_r &= \frac{5}{4} (\rho_{r0} \bar{S}_r - 2q\rho_{d0} S_d) \\ a_d &= \frac{5}{4} (z\rho_{d0} S_d - 2q\rho_{r0} \bar{S}_r) \end{aligned} \quad (2.14)$$

We are now equipped to explore the equilibrium polymer length distribution $\rho_{r\ell} = \int d\hat{\mathbf{u}} \rho_r(\ell, \hat{\mathbf{u}})$ corresponding to the basic fluid symmetries we consider (cf. Fig. 2.1).

2.4.1 Isotropic fluid

In the isotropic phase, all nematic order parameters are strictly zero. Applying conservation of monomers to Eq. (2.12) and performing some algebraic rearrangements we find a geometric distribution (i.e., the discrete analog of the exponential distribution):

$$\begin{aligned} \rho_{r\ell} &= \ell e^{\varepsilon_b + \lambda_r \ell} \\ &= \ell e^{\varepsilon_b} (1 - m_I^{-1})^\ell \end{aligned} \quad (2.15)$$

in terms of the mean aggregation number:

$$m_I = \frac{\sum_{\ell} \rho_a(\ell) \ell}{\sum_{\ell} \rho_a(\ell)} = \frac{1}{2} \left(1 + \sqrt{1 + 4\rho_{r0} e^{-\varepsilon_b}} \right) \quad (2.16)$$

which, as expected, goes up monotonically with increasing monomer concentration ρ_{r0} and also increases when the effective temperatures ε_b grows more negative. Since there is no global particle alignment whatsoever, the presence of the discs does not influence the polymerization process, and the polymer molecular-weight distribution is independent from the disc concentration.

2.4.2 Uniaxial nematic fluid

The decoupling of polymeric rods and discs is no longer valid for a nematic fluid where the alignment direction of one component is strongly affected by the amount of orientational “templating” it experiences from the other component. The polymer density follows from Eq. (2.12) and can be written in an exponential form:

$$4\pi\rho_r(\ell, \hat{\mathbf{u}}) = \ell \exp[\varepsilon_b + \ell\lambda_r + \tilde{a}_r \ell \mathcal{P}_2(t)] \quad (2.17)$$

with $t = \cos\theta$. The three basic contributions affecting the polymer molecular weight distribution in a (uniaxial) nematic fluid are easily identified in the argument; the first denotes monomer-monomer bonding while the second term enforces monomeric mass conservation. The third one is the most interesting one; it encapsulates the templating effect associated with nematization of the discs as per Eq. (2.14). Here, we have introduced a_r as a renormalized version of the one in Eq. (2.14):

$$\tilde{a}_r = a_r + \xi \quad (2.18)$$

The factor ξ depends on both a_r itself and on the polymer persistence length ℓ_p . It accounts for the finite polymer flexibility and vanishes for strictly rigid polymers ($\ell_p \rightarrow \infty$). The corresponding expressions are given in Appendix 2.A. As noted previously, the multiplier λ_r featuring in Eq. (2.17) follows from monomer mass conservation:

$$\sum_{\ell=1}^{\infty} \int d\hat{\mathbf{u}} \rho_r(\ell, \hat{\mathbf{u}}) = \rho_{r0} \quad (2.19)$$

The summation can be resolved analytically and we find:

$$\rho_{r0} = e^{\varepsilon_b} \frac{1}{2} \int_{-1}^1 dt \frac{e^{W(t)}}{(e^{W(t)} - 1)^2} \quad (2.20)$$

The molecular-weight averaged nematic order parameter Eq. (2.11) is then given by:

$$\bar{S}_r = \rho_{r0}^{-1} e^{\varepsilon_b} \frac{1}{2} \int_{-1}^1 dt \frac{\mathcal{P}_2(t) e^{W(t)}}{(e^{W(t)} - 1)^2} \quad (2.21)$$

The two conditions above are intricately coupled given that \tilde{a}_r depends on both \bar{S}_r and S_d via Eq. (2.14). Convergence of the summation Eq. (2.19) requires that the argument be negative:

$$W(t) = \lambda_r + \tilde{a}_r \mathcal{P}_2(t) < 0, \quad \text{all } t \quad (2.22)$$

Noticing that $-1/2 \leq \|\mathcal{P}_2\| \leq 1$ one then finds that λ_r should satisfy:

$$\begin{aligned} -\lambda_r &< |\tilde{a}_r| \quad (N^+) \\ -\lambda_r &< |\tilde{a}_r/2| \quad (N^-) \end{aligned} \quad (2.23)$$

and it is tempting to introduce a rescaled normalization constant λ'_r that is strictly positive ($\lambda'_r > 0$) for both phases. With this, we recast:

$$W(t) = \begin{cases} \frac{3}{2}\tilde{a}_r(t^2 - 1) - \lambda'_r & (N^+) \\ \frac{3}{2}\tilde{a}_r t^2 - \lambda'_r & (N^-) \end{cases} \quad (2.24)$$

Unlike for the isotropic phase, the normalization constant λ'_r can not be resolved in closed form. The molecular-weight distribution of the polymer follows from integrating Eq. (2.17) over all orientations $\hat{\mathbf{u}}$:

$$\rho_{r\ell} = \ell e^{\varepsilon_b} \frac{1}{2} \int_{-1}^1 dt e^{\ell W(t)} \quad (2.25)$$

The uniaxial nematic order parameter $S_{r\ell}$ associated with a polymer of length ℓ is easily found from:

$$S_{r\ell} = -\frac{1}{2} \left\{ 1 + \frac{1}{\tilde{a}_r \ell} - \frac{1}{F\left(\sqrt{3\tilde{a}_r \ell}/2\right) \sqrt{\tilde{a}_r \ell/3}} \right\} \quad (2.26)$$

in terms of Dawson's integral $F(x) = e^{-x^2} \int_0^x e^{y^2} dy$ [114]. The discotic nematic order parameter S_d easily follows from the above expression upon substituting $\tilde{a}_r \ell \rightarrow a_d$. A little reflection of Eq. (2.26) tells us the following; since a_r does not depend explicitly on the aggregation number ℓ , the nematic order parameter $S_{r\ell}$ must be a monotonically increasing function of the polymerization degree ℓ ; the longer the polymers the stronger their nematic ($a_r > 0$) or anti-nematic ($a_r < 0$) alignment in the mixed nematic fluid. This effect becomes systematically weaker for increasingly flexible polymers as can easily be inferred from the above expression by comparing $S_{r\ell}$ versus ℓ for rigid polymers ($\xi = 0$) versus the case of slightly flexible ones (ξ nonzero but small) for any given value for a_r .

Let us now examine a concrete example by picking a dense uniaxial discotic nematic doped with polymerizing rods. The polymers are dispersed anti-nematically within the discotic fluid as indicated in Fig. 2.1(e). In specifying the shape of the rods and discs, we can distinguish between so-called *symmetric* mixtures [74], in which the excluded-volume between two monomers, a monomer and a disc and two discs are all equal, so that $q = 1$ and $z = 1$ and *asymmetric mixtures* composed of species with strongly disparate excluded volumes. Our principal attention goes to the latter systems which arise more naturally in an experimental context when mixing, for instance, tip-associating colloidal rods such as *fd* [115, 7] with clay platelets [116]. The molecular-weight distributions of some mixtures of this nature are shown in Fig. 2.2.

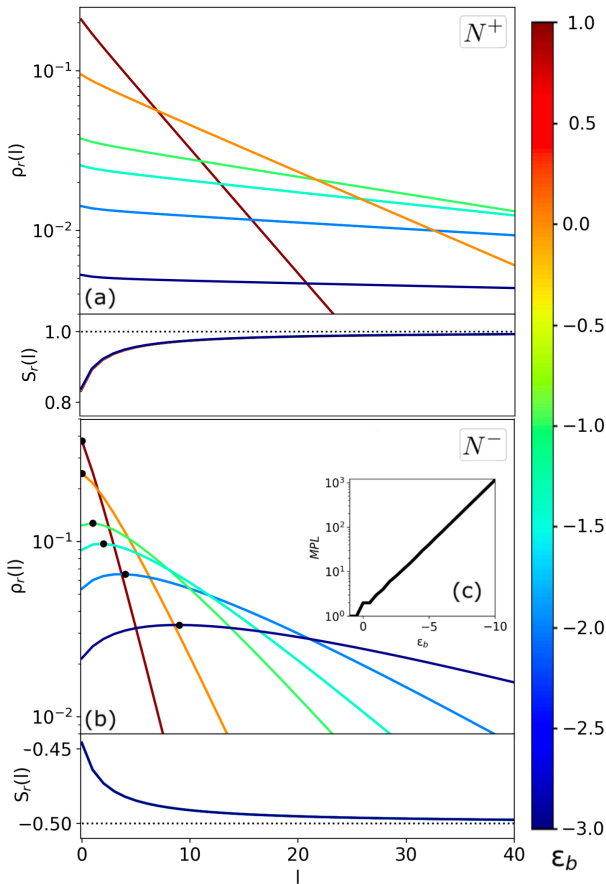


Figure 2.2: Polymer molecular-weight distributions $\rho_{r\ell}$ and corresponding uniaxial nematic order parameter $S_{r\ell}$ as a function of the polymer length ℓ for (a) a typical polymer nematic N^+ and (b) discotic nematic phase N^- . The effective temperature ε_b is color-coded. (c) Most Probable Length (MPL) in terms of the effective temperature ε_b . Fixed parameters: persistence length $\ell_p = 3$, disc mole fraction $x = 0.5$, overall concentration $\rho = 3$, excluded-volume ratios $q = \frac{1}{4} \frac{L_r}{D_r}$ and $z = \pi q$ with monomer aspect ratio $L_r/D_r = 10$.

Fig. 2.2(a) relates to the uniaxial polymer-dominated nematic phase (N^+) and demonstrates an exponential probability distribution whose shape can be tuned by changing the effective temperature of the system. As expected, the tail of the distribution grows upon decreasing the temperature, which would give longer polymers. A more interesting scenario shows up for the discotic nematic phase (N^-) in Fig. 2.2(b), where the distributions are no longer monotonically decreasing. The maximum of the distributions corresponds to the most probable length of the polymers for each system, which depends quite sensitively on the effective temperature as we observe in Fig. 2.2(c). Reversible polymerization within an anti-nematic organization thus leads to a strong manifestation of oligomeric polymers at the expense of its monomeric counterparts. We note that the orientational order associated with the anti-nematic oligomers remains relatively mild (particularly at larger temperature ε_b) so that the second-polynomial truncation should not be too severe.

As we will see during the incoming sections of this chapter, the overall particle concentration and disc molar fraction associated with Fig. 2.2 may correspond to regions of the phase diagram where the uniform nematic system is in fact thermodynamically unstable with respect to some kind of phase separation. The molecular-weight distributions should therefore be interpreted under the caveat that monophasic nematic fluidity is preserved and that any demixing process is somehow suppressed. We wish to add that the non-monotonic features of the anti-nematic polymer molecular-weight distribution are also present at conditions where monophasic anti-nematic order is found to be stable. Next we address the thermodynamic stability of the mixtures within the context of a Gaussian variational theory.

2.5 Isotropic-nematic phase behavior

At conditions where (anti-)nematic order is strong, the previously used polynomial-based expansion truncated after \mathcal{P}_2 [Eq. (2.7)] is no longer appropriate and a cumbersome inclusion of multiple higher-order terms becomes necessary [112, 84]. A more technically expedient route towards exploring the thermodynamics of strongly ordered nematic fluids is to use a simple Gaussian parameterization of the orientational probability [66, 29]. Following [108] we express the polymer molecular-weight distribution in a factorized form:

$$\rho_r(\ell, \hat{\mathbf{u}}) = \rho_{r\ell} f_G(\hat{\mathbf{u}}) \quad (2.27)$$

where f_G is a normalized Gaussian distribution with a variational parameter that is proportional to either the degree of nematic order ($\alpha^{(1)} > 0$) or anti-nematic order ($\alpha^{(2)} > 0$). The corresponding Gaussian distributions for the polar angles corresponding to these different nematic symmetries are given by [83]:

$$f_G(\hat{\mathbf{u}}) \sim \begin{cases} \frac{\alpha^{(1)}}{4\pi} \exp(-\frac{1}{2}\alpha^{(1)}\theta^2), \\ \sqrt{\frac{\alpha^{(2)}}{(2\pi)^3}} \exp(-\frac{1}{2}\alpha^{(2)}\psi^2) \end{cases} \quad (2.28)$$

where $\psi = \frac{\pi}{2} - \theta$ ($-\pi/2 < \psi < \pi/2$) denotes a polar angle (see Fig. 2.1a). The Gaussians operate on the domain $0 < \theta < \pi/2$ and must be complemented by their mirror $f_G(\pi - \theta)$ for $\pi/2 < \theta < \pi$ given that all nematic phases are required to be strictly apolar. The Gaussian representations are appropriate only for strong nematic order ($\alpha \gg 1$). They are clearly inadequate for isotropic systems since the probabilities reduce to zero when $\alpha \rightarrow 0$ instead of reaching a constant. Obviously, we apply the same distributions to the discs with $\alpha_d^{(1)}$ and $\alpha_d^{(2)}$ denoting the variational parameters quantifying the amount of (anti)nematic order of the discs. The disc probability density is then equivalent to Eq. (2.27):

$$\rho_d(\hat{\mathbf{u}}) = \rho_{d0} f_G(\hat{\mathbf{u}}) \quad (2.29)$$

A major advantage of using Gaussian trial functions is that we may apply asymptotic expansion of the various free energy contributions [66] which are valid in the limit $\alpha \rightarrow \infty$. In particular, it can be shown that the double orientational averages over the sine and cosine in Eq. (2.4) up to leading order in α take a simple analytic form [83]. In the general case in which particles with equal nematic signature (nematic or anti-nematic) do not necessarily have the same degree of alignment the asymptotic averages read:

$$\begin{aligned} \langle\langle |\sin \gamma| \rangle\rangle_{11} &\sim \sqrt{\frac{\pi}{2} \left(\frac{1}{\alpha^{(1)}} + \frac{1}{\alpha^{(1')}} \right)} \\ \langle\langle |\cos \gamma| \rangle\rangle_{12} &\sim \sqrt{\frac{2}{\pi} \left(\frac{1}{\alpha^{(1)}} + \frac{1}{\alpha^{(2)}} \right)} \\ \langle\langle |\sin \gamma| \rangle\rangle_{22} &\sim \mathcal{F}(\alpha^{(2)}, \alpha^{(2')}) \end{aligned} \quad (2.30)$$

Here, the double brackets denote the orientational averages featuring in the excess free energy Eq. (2.4) with $\langle \cdot \rangle = \int d\hat{\mathbf{u}} f_G(\hat{\mathbf{u}})$. The symmetry of nematic order clearly matters since the anti-nematic case features a distinct logarithmic dependence. The function \mathcal{F} reads in explicit form:

$$\mathcal{F}(\alpha^{(2)}, \alpha^{(2')}) = \frac{4\alpha^{(2)}Q - 2(1+Q)\operatorname{arctanh}\sqrt{Q} - (1+Q)\ln(1-Q) + (1+Q)\ln(4\alpha^{(2)}Q)}{2\pi\alpha^{(2)}Q} \quad (2.31)$$

in terms of the ratio $Q = \alpha^{(2')}/\alpha^{(2)}$ with $\alpha^{(2)}$ and $\alpha^{(2')}$ quantifying the anti-nematic order parameters of two polymeric species differing in length. Note that generally, $\alpha^{(2)} \neq \alpha^{(2')}$. The expression becomes a lot more manageable if all polymers are assumed to exhibit an equal degree of alignment, irrespective of their length. Then, $Q = 1$ and [117]:

$$\mathcal{F}(\alpha^{(2)}) = \frac{2}{\pi} \left(1 + \frac{\ln \alpha^{(2)}}{2\alpha^{(2)}} \right) \quad (2.32)$$

Similar asymptotic expressions may be obtained for the orientational entropy featuring in the ideal free energy Eq. (2.1). For strong nematic or anti-nematic order we find, respectively [83]:

$$\begin{aligned} \sigma_1 &= \langle \ln 4\pi f_G(\hat{\mathbf{u}}) \rangle_1 \sim \ln \alpha^{(1)} - 1 \\ \sigma_2 &= \langle \ln 4\pi f_G(\hat{\mathbf{u}}) \rangle_2 \sim \frac{1}{2} \left(\ln \alpha^{(2)} + \ln \frac{2}{\pi} - 1 \right) \end{aligned} \quad (2.33)$$

The worm-like chain entropy Eq. (2.3) too can be quantified within the Gaussian limit which leads to:

$$\begin{aligned} \langle f_G^{1/2}(\hat{\mathbf{u}}) \nabla^2 f_G^{1/2}(\hat{\mathbf{u}}) \rangle_1 &\sim -\frac{\alpha^{(1)}}{2} \\ \langle f_G^{1/2}(\hat{\mathbf{u}}) \nabla^2 f_G^{1/2}(\hat{\mathbf{u}}) \rangle_2 &\sim -\frac{\alpha^{(2)}}{4} \end{aligned} \quad (2.34)$$

We infer that the loss of conformational entropy of an *anti-nematic* polymer is half that of a nematic polymer. This suggests that a worm-like chain is able to retain more of its internal configurations when aligned anti-nematically than in a nematic organization of equal strength. With all the orientational averages specified, we now turn to computing the free energy and its derivatives.

2.5.1 Polymer nematic phase (N^+)

We first focus on the case of the polymer-dominated nematic phase which is expected to be stable at elevated monomer concentration and low disc mole fraction. Inserting the asymptotic orientational averages formulated above into the corresponding entropic contributions in Eq. (2.1) we obtain the following algebraic expression for the free energy density (in units thermal

energy $k_B T$ per randomized monomer excluded volume v_{rr}):

$$\begin{aligned}
\frac{F^{N^+}}{V} &\sim \sum_{\ell} \rho_{r\ell} \ell^{-1} [\ln \rho_{r\ell} \ell^{-1} - 1 - \varepsilon_b + \sigma_1(\alpha_{r\ell})] \\
&+ \rho_{d0} [\ln \rho_{d0} - 1 + \sigma_2(\alpha_d)] \\
&+ \frac{1}{3\ell_p} \sum_{\ell} \rho_{r\ell} \alpha_{r\ell} + \sum_{\ell, \ell'} \rho_{r\ell} \rho_{r\ell'} h_{r\ell r\ell'} \\
&+ 2q\rho_{d0} \sum_{\ell} \rho_{r\ell} h_{r\ell d} + z\rho_{d0}^2 \frac{8}{\pi^2} \left(1 + \frac{\ln \alpha_d}{2\alpha_d}\right)
\end{aligned} \tag{2.35}$$

with h_{ij} is short-hand notation for:

$$h_{ij} = \sqrt{\frac{8}{\pi} \left(\frac{1}{\alpha_i} + \frac{1}{\alpha_j} \right)} \tag{2.36}$$

where α_i and α_j should be considered dummy variables for the species-dependent nematic order parameters as specified by the indices i and j . For later reference we also define:

$$g_{ij} = \left(\frac{8}{\pi}\right)^{1/2} \left(1 + \frac{\alpha_i}{\alpha_j}\right)^{-1/2} \tag{2.37}$$

At equilibrium, the species-dependent nematic order parameters $\alpha_{r\ell}$ and α_d follow from the minimum conditions:

$$\frac{\partial F/V}{\partial \alpha_{r\ell, d}} = 0 \tag{2.38}$$

The expressions above can be simplified considerably by noting that a small amount of backbone flexibility causes the nematic alignment to fully decorrelate from the polymer contour length. We then approximate $\alpha_{r\ell} \approx \alpha_{r\ell'} = \alpha_r$, independent from ℓ . Applying Eq. (2.38) we obtain a set of simple algebraic equations:

$$\begin{aligned}
m_{N^+}^{-1} \alpha_r^{1/2} &= -\frac{1}{3\ell_p} \alpha_r^{3/2} + \frac{2}{\sqrt{\pi}} \rho_{r0} + q\rho_{d0} g_{rd} \\
\alpha_d^{1/2} &= z\rho_{d0} \frac{8}{\pi^2} \left(\frac{\ln \alpha_d - 1}{\alpha_d^{1/2}} \right) + 4q\rho_{r0} g_{dr}
\end{aligned} \tag{2.39}$$

with m_{N^+} the mean aggregation number in the polymer nematic phase. The molecular-weight distribution now becomes strictly exponential, as for the isotropic phase. We write:

$$\rho_{r\ell} = \ell e^{\tilde{\varepsilon}_b} (1 - m_{N^+}^{-1})^{\ell} \tag{2.40}$$

with an *effective* potential $\tilde{\varepsilon}_b$ that depends on the orientational entropy:

$$\tilde{\varepsilon}_b = \varepsilon_b - \sigma_1(\alpha_r) \tag{2.41}$$

Given that $\sigma_1 > 0$, the effective temperature is *lower* than the bare one, so that polymerization in the nematic phase is stronger than in the isotropic fluid, as is well established [99, 67]. The mean aggregation number in the nematic phase has an analogous form to Eq. (2.16)):

$$m_{N^+} = \frac{1}{2} \left(1 + \sqrt{1 + 4\rho_{r0}e^{-\tilde{\varepsilon}_b}} \right) \quad (2.42)$$

The chemical potentials are obtained from the standard thermodynamic relations $\mu_{r,d} = \partial(F/V)/\partial\rho_{r0,d0}$. The contribution from the polymers reads:

$$\begin{aligned} \mu_r^{N^+} &\sim \ln(1 - m_{N^+}^{-1}) + \frac{1}{3\ell_p} + m_{N^+}^{-1}\sigma_1(\alpha_r) \\ &+ 2\rho_{r0}\frac{4}{\sqrt{\pi\alpha_r}} + 2q\rho_{d0}h_{rd} + \varepsilon_b \end{aligned} \quad (2.43)$$

while for the discs we find:

$$\mu_d^{N^+} \sim \ln \rho_{d0} + \sigma_2(\alpha_d) + 2q\rho_{r0}h_{rd} + 2z\rho_{d0}\frac{8}{\pi^2} \left(1 + \frac{\ln \alpha_d}{2\alpha_d} \right) \quad (2.44)$$

The osmotic pressure follows from the thermodynamic relation $-P = (F - N\mu)/V$ leading to:

$$\begin{aligned} P^{N^+} &\sim e^{\tilde{\varepsilon}_b}(m_{N^+} - 1) + \rho_{d0} + \rho_{r0}^2\frac{4}{\sqrt{\pi\alpha_r}} \\ &+ 2q\rho_{r0}\rho_{d0}h_{rd} + z\rho_{d0}^2\frac{8}{\pi^2} \left(1 + \frac{\ln \alpha_d}{2\alpha_d} \right) \end{aligned} \quad (2.45)$$

Note that all pressures are implicitly renormalized in units of the thermal energy $k_B T$ per monomer excluded volume v_{rr} .

2.5.2 Discotic nematic phase (N^-)

Repeating the previous steps for the discotic nematic through simple bookkeeping we write for the free energy of the discotic phase:

$$\begin{aligned} \frac{F^{N^-}}{V} &\sim \sum_{\ell} \rho_{r\ell}\ell^{-1} [\ln \rho_{r\ell}\ell^{-1} - 1 - \varepsilon_b + \sigma_2(\alpha_{r\ell})] \\ &+ \rho_{d0}[\ln \rho_{d0} - 1 + \sigma_1(\alpha_d)] + \frac{1}{6\ell_p} \sum_{\ell} \rho_{r\ell}\alpha_{r\ell} \\ &+ \sum_{\ell,\ell'} \rho_{r\ell}\rho_{r\ell'}\frac{4}{\pi}\mathcal{F}(\alpha_{r\ell}, \alpha_{r\ell'}) \\ &+ 2q\rho_{d0} \sum_{\ell} \rho_{r\ell}h_{r\ell d} + z\rho_{d0}^2\frac{4}{\sqrt{\pi\alpha_d}} \end{aligned} \quad (2.46)$$

The corresponding minimum conditions for the variational parameters under the assumption that all polymer species experience the same degree of orientational order ($\alpha_{r\ell} = \alpha_{r\ell'} = \alpha_r$) are

as follows:

$$\begin{aligned}\frac{1}{2}m_{N^-}^{-1}\alpha_r^{1/2} &= -\frac{1}{6\ell_p}\alpha_r^{3/2} + \rho_{r0}\frac{8}{\pi^2}\left(\frac{\ln\alpha_r - 1}{\alpha_r^{1/2}}\right) + q\rho_{d0}g_{rd} \\ \alpha_d^{1/2} &= z\rho_{d0}\frac{2}{\pi^{1/2}} + 2q\rho_{r0}g_{dr}\end{aligned}\quad (2.47)$$

The molecular-weight distribution is analogous to Eq. (2.40) but with the effective temperature now reading:

$$\tilde{\varepsilon}_b = \varepsilon_b - \sigma_2(\alpha_r) \quad (2.48)$$

which, as for the case of the polymer nematic phase suggests that particle alignment facilitates polymer growth, although less so for anti-nematic polymers since generally $\sigma_2 < \sigma_1$ (Eq. (2.33)). The chemical potential of the polymers and the discs are given by, respectively:

$$\begin{aligned}\mu_r^{N^-} &\sim \ln(1 - m_{N^-}^{-1}) + \frac{1}{6\ell_p} + m_{N^-}^{-1}\sigma_2(\alpha_r) \\ &\quad + 2\rho_{r0}\frac{8}{\pi^2}\left(1 + \frac{\ln\alpha_r}{2\alpha_r}\right) + 2q\rho_{d0}h_{rd} + \varepsilon_b \\ \mu_d^{N^-} &\sim \ln\rho_{d0} + \sigma_1(\alpha_d) + 2q\rho_{r0}h_{rd} + 2z\rho_{d0}\frac{4}{\sqrt{\pi\alpha_d}}\end{aligned}\quad (2.49)$$

Finally, the pressure of the N^- phase reads:

$$\begin{aligned}P^{N^-} &\sim e^{\tilde{\varepsilon}_b}(m_{N^-} - 1) + \rho_{d0} + \rho_{r0}^2\frac{8}{\pi^2}\left(1 + \frac{\ln\alpha_r}{2\alpha_r}\right) \\ &\quad + 2q\rho_{r0}\rho_{d0}h_{rd} + z\rho_{d0}^2\frac{4}{\sqrt{\pi\alpha_d}}\end{aligned}\quad (2.50)$$

The thermodynamics of the isotropic phase is easily established from the original free energy Eq. (2.1) because the randomized excluded volumes becomes simple constants, namely $\langle\langle|\sin\gamma|\rangle\rangle = \pi/4$ and $\langle\langle|\cos\gamma|\rangle\rangle = 1/2$. We thus obtain the following expressions for the chemical potentials in the isotropic fluid [108]:

$$\begin{aligned}\mu_r^I &\sim \ln(1 - m_I^{-1}) + 2\rho_{r0} + 2q\rho_{d0} + \varepsilon_b \\ \mu_d^I &\sim \ln\rho_{d0} + 2z\rho_{d0} + 2q\rho_{r0}\end{aligned}\quad (2.51)$$

The osmotic pressure combines the ideal gas and excluded volume contributions and reads:

$$P^I \sim e^{\varepsilon_b}(m_I - 1) + \rho_{d0} + \rho_{r0}^2 + 2q\rho_{r0}\rho_{d0} + z\rho_{d0}^2 \quad (2.52)$$

Binodals denoting coexistence between phases of any symmetry may be established from equating chemical potentials and pressures in conjunction with the minimum conditions for the nematic variational parameters, where relevant. Phase diagrams can be represented in a pressure-composition ($P - x$) plane or, alternatively, in a density-density representation using $\rho_{r0} = c(1 - x)$ and $\rho_{d0} = cx$ in terms of the overall particle concentration c and disc mole fraction ($0 < x < 1$). In order to remain consistent with the Gaussian approximation adopted in our analysis, we will focus on *asymmetric* mixtures characterized by both monomer-disc and disc-

disc excluded volumes being much larger than the monomer-monomer one. The considerable excluded-volume disparity thus ensures that the nematic order of all components be sufficiently strong. Concretely, we impose that $\alpha_{r,d} > 5$ for all numerical results to be self-consistent.

2.6 Phase diagrams

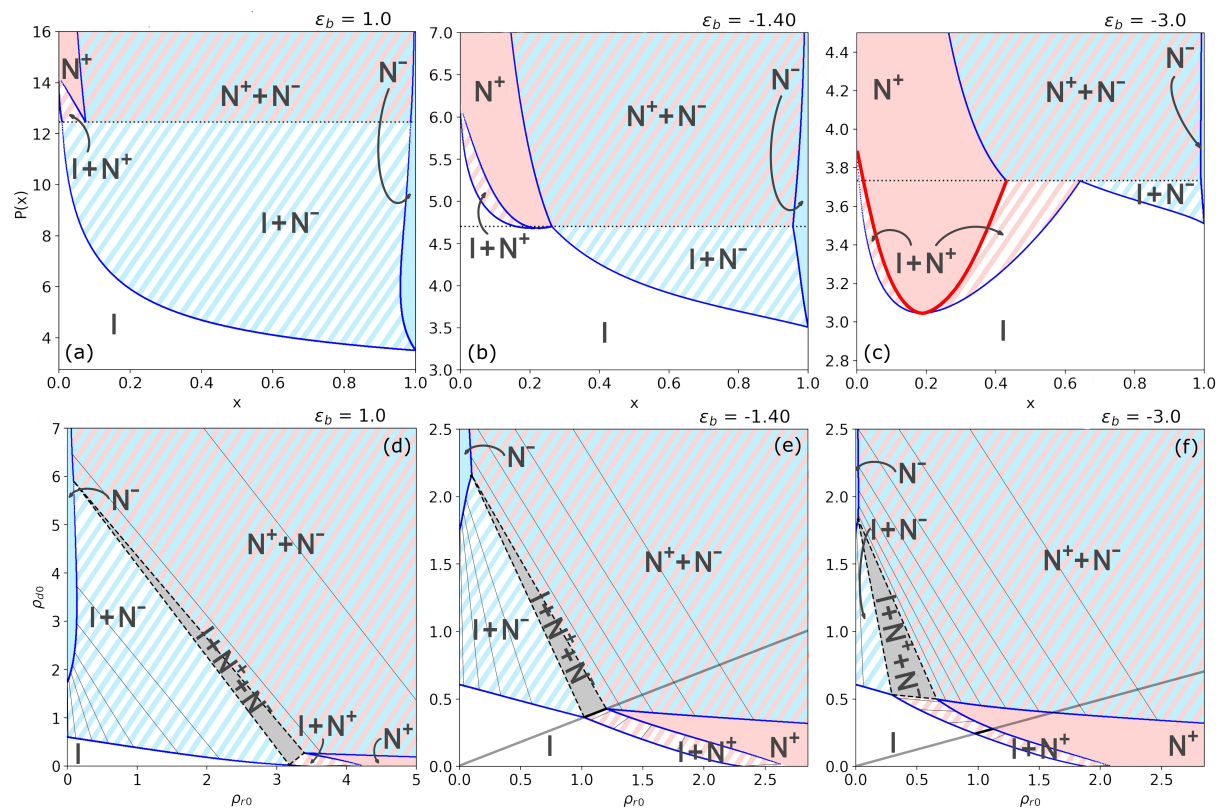


Figure 2.3: Overview of the isotropic I (white) - polymer nematic N^+ (red) - discotic nematic N^- (blue) phase diagrams for a mixture of discs and reversibly polymerizing weakly flexible rods at various effective temperatures ε_b . Two types of phase diagrams are represented: osmotic pressure P versus disc mole fraction x (top panels) and concentration of discs ρ_{d0} versus concentration of rods ρ_{r0} (bottom panels). Fixed parameters: persistence length $\ell_p = 3$, excluded-volume ratios $q = \frac{1}{4} \frac{L_r}{D_r}$ and $z = \pi q$ where $L_r/D_r = 10$. The presence of a negative azeotrope is indicated in panels (e) and (f) as a bold black line, which is shown to be parallel to the dilution line (grey diagonal shown in (e) and (f)).

Fig. 2.3 presents an overview of the isotropic-nematic phase diagram for a mixture of reversibly polymerizing rods and discs at three different temperatures. The choice of excluded-volume parameter q and z is inspired by the typical dimensions of experimentally realizable anisotropic colloids, where the monomeric rods and discs usually have *equal* largest dimensions ($L_r = D_d$). The monomer aspect ratio L_r/D_r can be chosen freely but we fix it here at $L_r/D_r = 10$. The disc aspect ratio is not constrained as long as the discs are sufficiently thin ($D_d/L_d \gg 1$). In this study we keep the persistence length fixed at $\ell_p = 3$. We found that variations up to $\ell_p = 10$ (corresponding to stiffer monomers) did not lead to major changes in

the phase behavior. For practical reasons we refrained from exploring the near-rigid rod limit ($\ell_p \rightarrow \infty$) which is known to cause the polymers to grow to unphysically large lengths [67].

Several key trends in the phase diagrams can be discerned. First of all, Fig. 2.3(a) correspond to high-temperature scenario in which reversible polymerization happens on a very limited scale. The shape-dissimilar nature of the mixture translates into a phase diagram that is highly asymmetric about the equimolar point $x = 0.5$. Second, demixing is prominent given the large range of monomer-disc compositions where the mixture fractionates into strongly segregated uniaxial nematic phases [Fig. 2.3(a)]. Only at very low osmotic pressures, where particle exclusion effects are relatively weak, does the mixture remain miscible throughout the entire composition range. We further observe that the discotic nematic N^- can be stabilized over a relatively broad pressure range, while the polymer nematic (N^+) only features at elevated pressures, where polymerization is strong enough for the long polymers to align into a conventional nematic organization with the discs interspersed anti-nematically. The phase diagram also features a triple $I - N^+ - N^-$ equilibrium in agreement with previous predictions [82, 83] and experiment [104, 106] for discs mixed with *non*-polymerizing rods.

Reducing the temperature stimulates polymer growth and, consequently, enhances the stability window for the polymer-dominated nematic [Fig. 2.3(b) and (c)]. Reversible polymerization thus renders the phase diagrams less asymmetric. At the same time, the osmotic pressure (and concomitantly the particle concentrations) at which nematic order occurs drops significantly as polymerization becomes more prominent. Furthermore, the $I - N^+$ binodals develop a remarkable (negative) *azeotrope* which in Fig. 2.3(b) coincides with the triple pressure. Under these conditions, coexistence occurs between a discotic nematic, a polymer nematic and an isotropic fluid with the latter two having the same monomer-disc composition. At lower temperature the azeotrope comes out more prominently at $x \approx 0.2$ (Fig. 2.3(c)). In the density-density representations shown in the bottom panels, the azeotrope manifests itself at the point where the tie line connecting the monomer and discs concentrations of the coexisting I and N^+ phases coincides with the dilution line. The latter are straight lines emanating from the origin along which the overall particle concentration changes but the monomer-disc composition is preserved. It can be gleaned that upon following a dilution line at, for instance, $x = 0.2$ the sequence of phase transitions encountered depends strongly on temperature. At high temperature [Fig. 2.3(a)] the isotropic fluid first transforms into N^- , then develops a triphasic $I - N^+ - N^-$ equilibrium. At low temperature, however, a polymer nematic is formed first, followed by a binematic $N^+ - N^-$ coexistence while the triphasic equilibrium does not show up at all unless the monomer concentration is significantly increased. Fig. 2.4 provides insight into the change of nematic order of the polymers and discs as well as the mean aggregation number of the N^+ across the azeotrope. In view of their considerable excluded volume, the discs are way more ordered than the polymers ($\alpha_d > \alpha_r$). Increasing the mole fraction of discs reduces the nematic order of both components, though the decrease is much more significant for the discs than the change of α_r for the polymers which in fact develops a minimum at the azeotrope.

We move on to explore a similar mixture featuring more slender rod monomers, namely $L_r/D_r = 25$. The resulting phase diagram is shown in Fig. 2.5. The asymmetry of the mixture is now very strong with the monophasic N^+ and N^- regions being largely unstable except for

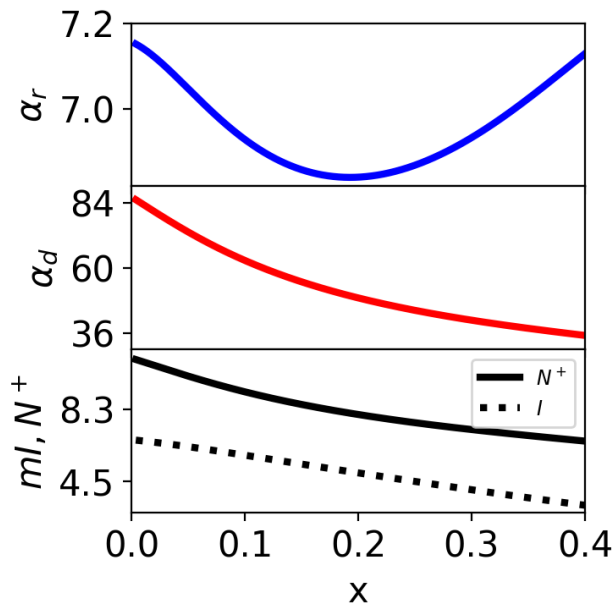


Figure 2.4: Nematic order of the polymers (α_r) and discs (α_d) and polymer mean aggregation number (m) of the nematic N^+ phase in coexistence with the isotropic phase I across the azeotropic region. The corresponding binodal in Fig. 2.3(c) has been indicated in red.

strongly purified systems (x close to 0 or 1) [Fig. 2.5(b)]. Qualitatively, the phase diagram resembles the one in Fig. 2.3(a), but the isotropic fluid undergoes a gas-liquid-type phase separation producing two phases differing in composition. The I_1 -phase may be associated with a discotic colloidal gas, and I_2 with its liquid counterpart. The demixing is driven by the extreme excluded-volume difference between the rod monomers and the discs. This phenomenon has been reported for (non-polymerizing) rod-disc mixtures in Ref. [81], where the effect was ascribed to a *depletion* of discs by the much smaller rods. Isotropic-isotropic demixing has been more generally observed when mixing different shapes dominated by hard-core repulsion [118], including thin and thick rods [119], spheres and discs [120, 121] and discs differing in diameter [122]. It has also been observed in thermotropic LC-solvent mixtures where the effect is primarily of enthalpic origin and is caused by specific interactions between the LC forming molecules and the solvent [123, 124]. It is well known that mixing colloids with non-adsorbing polymer depletants creates an effective attraction between the colloids which is entirely of entropic origin and may drive various types of demixing mechanisms [37]. In our case, the depletion effect is however less clear-cut given that the “depletants” reversibly polymerize into a wide array of different sizes [125] and experience orientation-dependent volume-exclusion interactions which are usually ignored in colloid-polymer models. Moreover the average polymer size depends, via Eq. (2.16), on the monomer concentration which is different in the gas and liquid phases. Fig. 2.5(c) demonstrates that the difference in mean aggregation number between the two isotropic phases is in fact quite small, with the disc-rich fraction harboring slightly longer polymers. Note that the presence of isotropic-isotropic demixing gives rise to a low-pressure triple equilibrium where both phases coexist with a discotic nematic N^- .

2.7 Quadruple fluid coexistence

At this stage, one might wonder whether a mixture could be designed in which the two separate triple equilibria in Fig. 2.5 were to join into a *quadruple* coexistence featuring all fluid

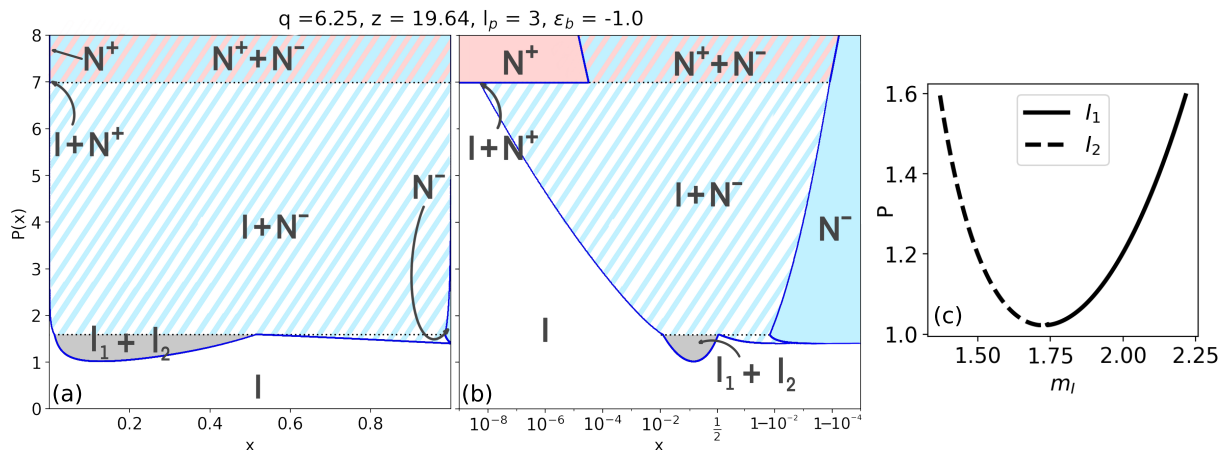


Figure 2.5: Phase diagram in the osmotic pressure-composition ($P - x$) representation with the following parameters: persistence length $\ell_p = 3$, effective temperature $\varepsilon_b = -1$, excluded-volume ratios $q = \frac{1}{4} \frac{L_r}{D_r}$ and $z = \pi q$ corresponding to a monomer aspect ratio $L_r/D_r = 25$. The disc mole fraction x is plotted on a linear scale (a) and on a logarithmic scale (b) to highlight the behavior close to single-component systems (pure polymers $x = 0$, and pure discs $x = 1$). Note the presence of a coexistence between an isotropic gas and fluid phase (I_1 and I_2) with different discs compositions (grey region). (c) Comparison of mean aggregation numbers m_I between I_1 and I_2 for a given pressure. I_1 corresponds to the phase at the lowest disc mole fraction x .

phases. In Fig. 2.6(a) we demonstrate that this scenario is indeed possible. For the particular mixture shown there, the rod monomers and discs no longer have equal largest dimensions ($L_r = D_d$) but the disc diameter is somewhat smaller than the rod length, namely $D_d = 0.7L_r$ while the rods are kept sufficiently slender ($L_r/D_r = 25$). The excluded-volume asymmetry is then sufficiently reduced to make the two triple points coincide and generate a simultaneous coexistence between two isotropic and two nematic phases, each differing in monomer-disc composition and overall particle concentration. This mixture is by no means unique and belongs to a family of monomer-disc size ratios where a remarkable I_1 - I_2 - N^+ - N^- quadruple point could be encountered, as illustrated by the colored manifold in Fig. 2.6(b). This result provides important guidance if one wishes to explore these intricate multi-phase equilibria in real-life mixtures featuring reversibly polymerizing rods mixed with colloidal platelets.

At this point we wish to draw a connection with recent theoretical explorations of polymer depletion on purely monomeric colloidal rods which have revealed similar multi-phase equilibria involving one-dimensional periodic smectic structures as well as fully crystalline states [126]. Similar phenomena involving isotropic-nematic-columnar quadruple points had been reported previously for disc-polymer mixtures [127]. In those studies, the multiphase equilibria emerge from an effective one-component theory based on free-volume theory where polymeric depletants, envisaged as fixed-shape spherical particles that do not interact with one another, are depleted from the surface of the colloidal rod due to volume exclusion as per the original Asakura-Oosawa model [22, 23, 24]. In our work, the depletion effect is strongly convoluted since all components (polymer species and discs alike) are explicitly correlated, albeit on the simplified second-virial level. Furthermore, high-density crystal phases with long-ranged positional order are not considered in the present study since their stability requires strong uniformity in particle shape [128], which is not the case in our mixtures. In fact, even for basic mixtures of non-associating

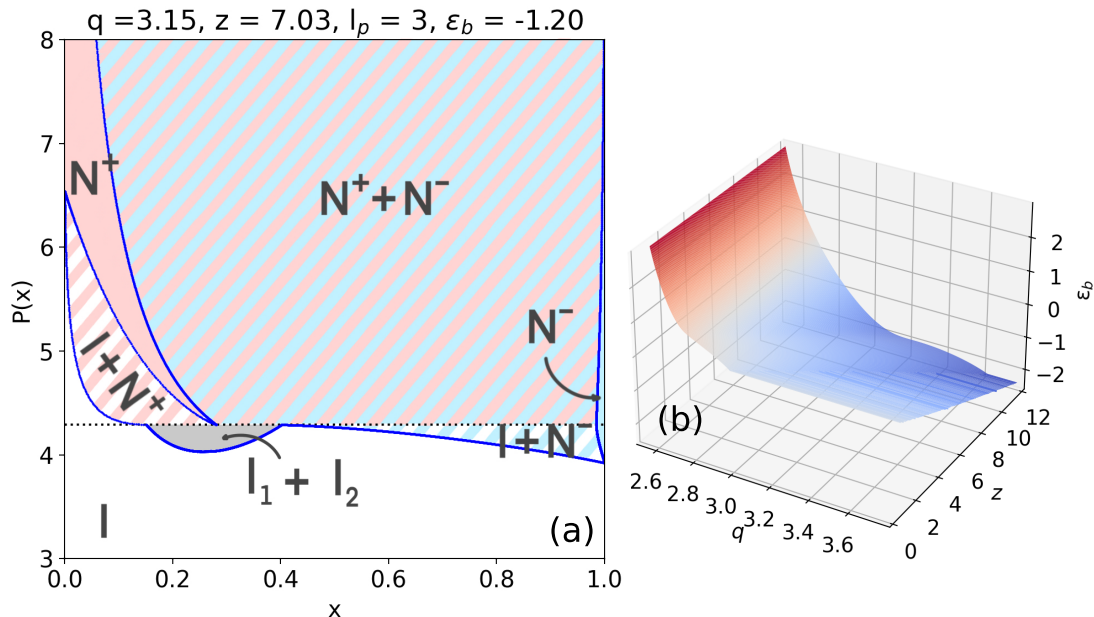


Figure 2.6: (a) Phase diagram in the osmotic pressure-composition ($P - x$) representation showing an I_1 - I_2 - N^+ - N^- quadruple point at $P = 4.29$. For this particular case, $\ell_p = 3$, $\varepsilon_b = -1.2$, $L_r/D_r = 25$ and $D_d/L_r = 0.7$. (b) Visualization of combinations of rod-disc excluded-volume ratio (q and z) and temperature ε_b where an $I_1 - I_2 - N^+ - N^-$ quadruple coexistence is possible.

hard rods mixed with hard discs the full phase behavior at conditions of elevated particle packing remains largely elusive to this day. Large-scale numerical simulations or density-functional computations are needed to overcome the limitations of the simple second-virial approach taken here, but these are technically challenging to implement for dense multi-component systems.

The results gathered in Fig. 2.6 illustrates the possibility of generating four different fluid textures emerging from reversibly changing excluded-volume-driven interactions alone, without the need to invoke attractive interparticle forces. This could bear some relevance on the emergence of functionality through liquid-liquid type phase separation in biological cells which are composed of biomolecules possessing a multitude of different shapes, some of them controlled by reversible association [129, 130].

2.8 Conclusions

We have explored the phase behaviour of a simple model for thermoresponsive supramolecular rods mixed with discotic particles. Possessing attractive tips the rod monomers reversibly associate into polymers that retain their basic slender rod shape and experience only a limited degree of backbone flexibility. The interaction between the species is assumed to be of steric origin such that basic shape differences between the constituents, more specifically the excluded-volume disparity, plays a key role in determining the prevailing liquid crystal symmetry. The principal ones are a polymer nematic (N^+) composed of nematic polymer interspersed with an anti-nematic organization of discs and a discotic nematic (N^-) in which the polymers are dispersed anti-nematically. Lowering temperature stimulates polymer growth which enlarges

the stability window for the N^+ phase. The phase diagram develops a marked *azeotrope* upon increasing the mole fraction of added discs which indicated that the polymer nematic is stabilized by the addition of non-adsorbing rigid discs provided their mole fraction remains small. The polymer-dominated nematic phase eventually becomes destabilized at larger mole fractions where mutual disc alignment disrupts the nematic order of the polymers in favour of the formation of a discotic nematic phase in which the polymers self-organize into an anti-nematic structure. The corresponding molecular weight distribution functions strongly deviates from the usual exponential form and becomes non-monotonic with a maximum probability associated with oligomeric aggregates. Enhancing the shape-asymmetry between the rod monomers and discs we observe a depletion-driven demixing of the isotropic fluid which opens up the possibility of a quadruple existence featuring two isotropic phase along with the fractionated polymer and discotic nematic phases. Such quadruple points occur in a wide range of mixed-shape nematics involving supramolecular rods templated by discs and highlight the possibility of multiple liquid symmetries (both isotropic and anisotropic) coexisting in mixtures of anisotropic colloids with reversible and thermoresponsive shape-asymmetry without cohesive interparticle forces. Future explorations should aim at a more careful assessment of biaxial nematic order, ignored in the present study, which could develop in near-equimolar rod-disc mixtures provided they are stable against global demixing (see Appendix 2.A for tentative discussion). Polymerizing rods and discs with finite particle thickness and low shape asymmetry may favor the emergence of liquid crystals possessing lamellar, columnar or fully crystalline signatures [131] which may be addressed using computer simulation models along the lines of Refs. [69, 70, 90]. Inspiration for such mixed-shape lamellar structures could be drawn from bio-inspired supramolecular liquid crystals [132] such as, for example, the ‘sliding columnar phase’ and similar stacked architectures observed in cationic liposome-DNA complexes [133, 134] which are essentially made up of mixed planar and rod-shaped architectures.

Appendices

Appendix 2.A Renormalized \mathcal{P}_2 approximation for slightly flexible polymers

We seek a simple perturbation theory for the one-body density Eq. (2.12) of near-rigid polymers characterized by a finite persistence length ℓ_p . Let us attempt the following generalization of the probability density distribution for the polymers:

$$\rho_r(\ell, \hat{\mathbf{u}}) = \ell e^{\varepsilon_b + \lambda_r \ell} e^{\ell(a_r + \xi) \mathcal{P}_2(\hat{\mathbf{u}})} \quad (2.53)$$

with ξ representing a correction induced by the *internal* orientational entropy of the polymer due to a small degree of worm-like chain flexibility. Inserting this expression into the worm-like chain contribution (last term) in the EL equation Eq. (2.12), substituting $\nabla^2 = \partial_t(1-t^2)\partial_t$ and $t = \cos \theta$, we find that for the uniaxial symmetry:

$$\frac{\nabla^2 \rho_r^{1/2}}{\rho_r^{1/2}} = \frac{3}{4} \tilde{a}_r^2 + \left(\frac{3}{2} \tilde{a}_r^2 - 3\tilde{a}_r \right) \mathcal{P}_2(t) + \mathcal{O}(t^4) \quad (2.54)$$

where $\tilde{a}_r = a_r + \xi$ denotes a rescaled alignment amplitude for the polymer.

Anti-nematic polymers

We expect that neglecting the fourth-order term will be fairly harmless in a strongly anti-nematic state where t is generally very small (since $\theta \sim \pi/2$ for most polymers). This situation is naturally encountered in the N^- phase where $a_r \ell \ll 0$ in particular for the long polymers. The constant in Eq. (2.54) is unimportant for the EL equation where it can be subsumed into the normalization factor λ , but must be retained when computing the worm-like chain free energy. Then, consistency requires that

$$\xi \approx \frac{1}{3\ell_p} \left(\frac{3}{2} \tilde{a}_r^2 - 3\tilde{a}_r \right) \quad (2.55)$$

where the chain persistence length ℓ_p should be interpreted in units of the segment length L_r . From the above the dependence of ξ on the bare alignment amplitude a_r is easily resolved and we find:

$$\xi \approx 1 + \ell_p + |a_r| - \sqrt{(1 + \ell_p)^2 + 2|a_r|\ell_p}, \quad (a_r \ll 0) \quad (2.56)$$

The correction factor vanishes in the rigid rod limit, $\lim_{\ell_p \rightarrow \infty} \xi = 0$, as it should.

Nematic polymers

We may repeat the analysis for the case of conventional nematic polymers as encountered in the polymer-dominated N^+ phase using a slightly different route. For $a_r \gg 1$ the average polar deflection angle will be small and we may expand the worm-like chain term up to quadratic order in θ . Using the asymptotic relation $\mathcal{P}_2(t) \sim 1 - 3\theta^2/2$ and ignoring any constant factors we find a simple approximation valid for $|t|$ close to unity (strong alignment):

$$\frac{\nabla^2 \rho_r^{1/2}}{\rho_r^{1/2}} \sim -\frac{3}{2}(\tilde{a}_r^2 + 2\tilde{a}_r)\mathcal{P}_2(t) \quad (2.57)$$

Then, in analogy with the preceding case we find an expression identical to Eq. (2.56) except for a minus sign:

$$-\xi \approx 1 + \ell_p + |a_r| - \sqrt{(1 + \ell_p)^2 + 2|a_r|\ell_p}, \quad (a_r \gg 0) \quad (2.58)$$

This simple scaling result confirms our expectation, namely that a small degree of backbone flexibility leads to a reduction of the alignment propensity of the polymers, since $|a_r + \xi|$ is always smaller than $|a_r|$. For strongly aligned systems, this effect turns out to be of equal strength for both nematic and anti-nematically ordered polymers.

Appendix 2.B Stability of biaxial nematic order

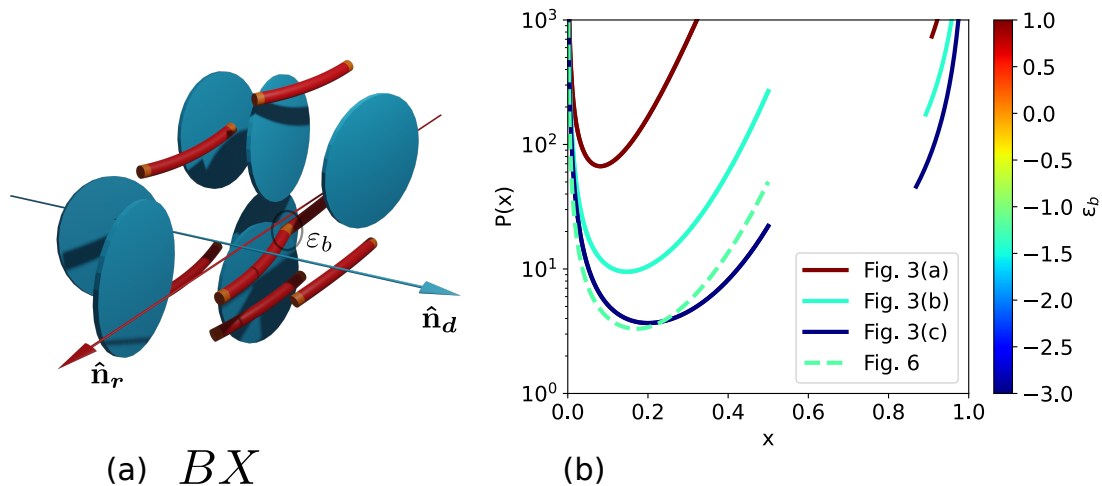


Figure 2.B.1: (a) Schematic representation of the biaxial nematic phase BX with orthorhombic (D_{2h}) point-group symmetry, characterized by mutually perpendicular nematic directors for each species (\hat{n}_r for the polymers and \hat{n}_d for discs). (b) Bifurcation curves locating the transition from uniaxial (U) order at low osmotic pressure P to biaxial (BX) nematic order at high pressure for a number of relevant cases studied in the main text. Here, x denotes the disc mole fraction.

So far, we have overlooked the possibility of biaxial nematic order in which both polymers and discs order along mutually perpendicular directors (see Fig. 2.B.1(a)). In order to tentatively locate the transition toward biaxial (BX) nematic order, we apply a simple bifurcation analysis in which we probe the stability of a uniaxial (U) fluid against weakly biaxial fluctuations [111,

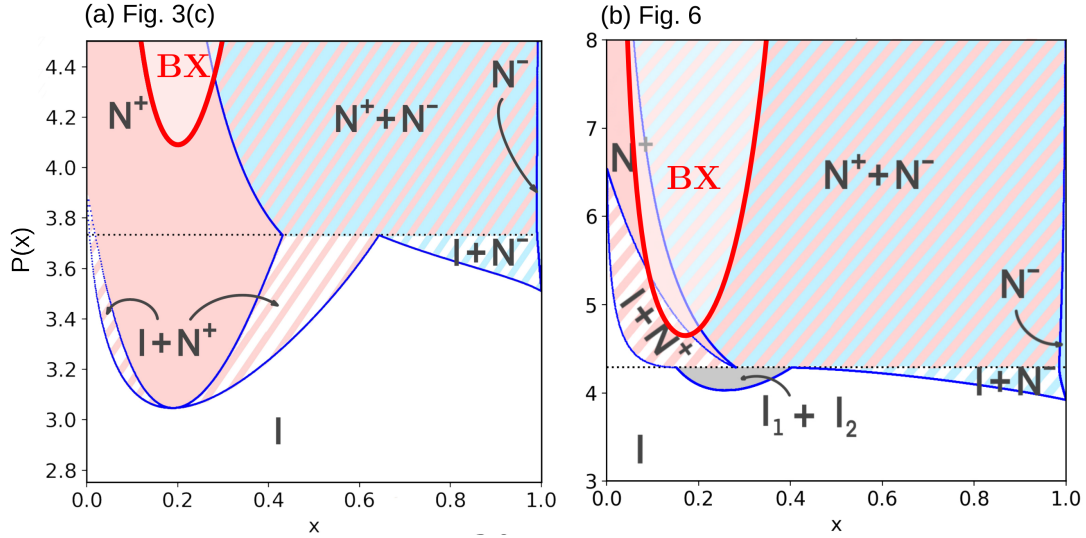


Figure 2.B.2: Bifurcation curves locating the transition from uniaxial (U) order at low osmotic pressure P to biaxial (BX) nematic order at high pressure superposed to their corresponding situation discussed in the main text. (a) Case depicted in Fig. 2.3(c). (b) Case depicted in Fig. 2.6

74]. If the U - BX transition is of second order, the bifurcation point at which biaxial solution emerges from the EL equations should pinpoint the actual phase transition. We begin by generalizing the second-polynomial expansion Eq. (2.7) to include biaxial nematic order using the addition theorem for spherical harmonics:

$$\begin{aligned} \mathcal{P}_2(\cos \gamma) &= \mathcal{P}_2(\cos \theta)\mathcal{P}_2(\cos \theta') \\ &+ \frac{1}{12}\mathcal{P}_2^2(\cos \theta)\mathcal{P}_2^2(\cos \theta')\cos 2(\varphi - \varphi') \end{aligned} \quad (2.59)$$

where φ is the azimuthal angle describing the particle orientation with respect to a secondary director $\hat{\mathbf{n}}_{\perp} \perp \hat{\mathbf{n}}$. The coupled EL equations then attain an additional term that accounts for biaxiality:

$$\begin{aligned} \ell^{-1} \ln[\rho_r(\ell, \hat{\mathbf{u}})\ell^{-1}] &= \lambda_r + \varepsilon_b + \alpha_r \mathcal{P}_2(\hat{\mathbf{u}}) \\ &+ \beta_r D(\hat{\mathbf{u}}) + \frac{L_r}{3\ell_p} \frac{\nabla^2[\rho_r(\ell, \hat{\mathbf{u}})]^{1/2}}{[\rho_r(\ell, \hat{\mathbf{u}})]^{1/2}} \end{aligned} \quad (2.60)$$

and

$$\ln[\rho_d(\hat{\mathbf{u}})] = \lambda_d + \alpha_d \mathcal{P}_2(\hat{\mathbf{u}}) + \beta_d D(\hat{\mathbf{u}}) \quad (2.61)$$

in terms of the weight function $D(\hat{\mathbf{u}}) = \sin^2 \theta \cos 2\varphi$ and amplitudes:

$$\begin{aligned} \beta_r &= \frac{15}{16}(\rho_{r0}\bar{\Delta}_r - 2q\rho_{d0}\Delta_d) \\ \beta_d &= \frac{15}{16}(z\rho_{d0}\Delta_d - 2q\rho_{r0}\bar{\Delta}_r) \end{aligned} \quad (2.62)$$

which feature the biaxial nematic order parameter of each species:

$$\begin{aligned}\Delta_{r\ell} &= \rho_{r\ell}^{-1} \int d\hat{\mathbf{u}} \rho_r(\ell, \hat{\mathbf{u}}) D(\hat{\mathbf{u}}) \\ \Delta_d &= \rho_{d0}^{-1} \int d\hat{\mathbf{u}} \rho_d(\hat{\mathbf{u}}) D(\hat{\mathbf{u}})\end{aligned}\quad (2.63)$$

Similar to the uniaxial case the bar denotes a molecular-weight average according to $\bar{\Delta}_r = \rho_{r0}^{-1} \sum_{\ell} \rho_{r\ell} \Delta_{r\ell}$. Substituting the EL equations into the biaxial nematic order parameters and linearizing for weakly biaxial amplitudes $|\beta| \ll 1$ we establish the condition under which a biaxial solution for the orientation distribution bifurcates from the uniaxial one:

$$\begin{aligned}\Delta_{r\ell} &= \rho_{r\ell}^{-1} \ell \beta_r \int d\hat{\mathbf{u}} \rho_r^{(U)}(\ell, \hat{\mathbf{u}}) D^2(\hat{\mathbf{u}}) \\ \Delta_d &= \rho_{d0}^{-1} \beta_d \int d\hat{\mathbf{u}} \rho_d^{(U)}(\hat{\mathbf{u}}) D^2(\hat{\mathbf{u}})\end{aligned}\quad (2.64)$$

This linear criterion basically stipulates the conditions (overall particle concentration, composition and effective temperature) at which the uniaxial nematic state is no longer guaranteed to be a local minimum in the free energy. Within the factorization Ansatz Eq. (2.27) for the uniaxial molecular-weight distributions the condition simplifies into:

$$\begin{aligned}\bar{\Delta}_r &= \beta_r (2m - 1) \langle D^2(\hat{\mathbf{u}}) \rangle_{f_G} \\ \Delta_d &= \beta_d \langle D^2(\hat{\mathbf{u}}) \rangle_{f_G}\end{aligned}\quad (2.65)$$

The brackets denote an average according to the nematic or anti-nematic Gaussians f_G specified in Eq. (2.28). Similarly, m denotes the mean aggregation number of either the N^+ or the N^- phase. The averages are easily obtained in the asymptotic angular limits ($\theta \ll 1$ or $\psi \ll 1$) and the leading order contributions read:

$$\langle D^2(\hat{\mathbf{u}}) \rangle_{f_G} \sim \begin{cases} 4/[\alpha^{(1)}]^2 & \text{nematic} \\ 1/2 & \text{anti-nematic} \end{cases}\quad (2.66)$$

The U - BX bifurcation condition Eq. (2.65) is equivalent to the matrix equation $\mathbf{M} \cdot \mathbf{\Delta} = \lambda_e \mathbf{\Delta}$ with $\mathbf{\Delta} = (\bar{\Delta}_r, \Delta_d)$ and \mathbf{M} given by the prefactors. The eigenvalues λ_e of the matrix \mathbf{M} are required to be unity ($\lambda_e = 1$). The solution is:

$$1 = -\frac{15}{32} c w_1 [(1-x) + xzW - \sqrt{(1-x)^2 + 2Wx(1-x)(8q^2 - z) + W^2 x^2 z^2}]\quad (2.67)$$

with

$$w_1 = \begin{cases} (2m_{N^+} - 1)4/\alpha_r^2 & N^+ - BX \\ (2m_{N^-} - 1)/2 & N^- - BX \end{cases}\quad (2.68)$$

and

$$W = \begin{cases} (2m_{N^+} - 1)^{-1} \alpha_r^2 / 8 & N^+ - BX \\ (2m_{N^-} - 1)^{-1} 8 / \alpha_d^2 & N^- - BX \end{cases} \quad (2.69)$$

The numerical solutions are shown in Fig. 2.B.1(b). The N^- - BX solutions cease to be internally consistent with the Gaussian approximation at $x < 0.8$ given that the nematic order parameter α_d of the discs tends to get too low. No such inconsistency occurs for the N^+ - BX branches. In general, we find that the transition occurs at pressures that are beyond the ranges explored in the phase diagrams of the main text. The only exceptions are Fig. 2.3(c) and Fig. 2.6 where the N^+ phase remains stable up to fairly large disc mole fractions and the N^+ - BX bifurcations are located within the monophasic N^+ regions (in red), as shown in Fig. 2.B.2. The tentative conclusion from this analysis is in line with previous reports in the literature [128], namely that the stability of BX nematic order is intimately linked to the excluded-volume asymmetry of the constituents which, in our case, is temperature-controlled. Lowering the temperature reduces the typical asymmetry which then stabilizes well-mixed rod-disc nematics that subsequently may develop BX order. We further note that disc-rich BX phases seem much harder to stabilize than polymer-dominated ones as the N^- - BX branches generally do not intersect the small monophasic N^- domains in the phase diagrams shown in the main text.

Chapter 3

Emergent biaxial order in hybrid chiral LCs

Abstract

Cholesteric liquid crystals (LCs) are classic examples of complex chiral mesophases with long-ranged periodicity but lack positional order at large length scales. Doping molecular cholesterics LCs with thin colloidal rods or disks with a large length-to-width ratio adds a further level of complexity due to the interplay between weak surface anchoring forces and elastic distortions around the rod-LC interface. We demonstrate that the rods have a strong tendency to orient perpendicular to the helix axis and local director, thus imparting strong local biaxiality on the hybrid cholesteric structure. We theoretically argue that the splay-bend elastic anisotropy plays a key role in stabilizing local orthorhombic order along the helix. Our predictions are corroborated by experimental results obtained in the group of I. Smalyukh (University of Colorado, USA) that we briefly review. We also discuss the case of discs and find a similar scenario of anomalous biaxial order along the helical director for discs with homeotropic anchoring immersed in short-pitch cholesteric hosts LCs.

3.1 Introduction

Since the experimental discovery of chiral nematic liquid crystals (LCs) over 150 years ago [135, 3], LC mesophases featuring chirality and long-range orientational order have been the focus of many research studies. The fundamental studies of geometry and topology of chiral nematic LCs as model systems provide extensive insights into physics principles associated with experimentally less accessible systems like particle physics or cosmology [136], in addition to their technological application in electro-optics and displays. On the other hand, biaxial nematic mesophases have been highly sought-after in soft matter systems since their first theoretical consideration in 1970 [137]. However, even in a soft-matter system with strongly biaxial building blocks such as brick-shaped molecules, biaxiality was experimentally elusive and hard to unambiguously demonstrate in equilibrium states. Recent reports of the experimental discovery of biaxial nematic order include observations in micellar and molecular LCs formed by amphiphilic and bent-core molecules, respectively [138, 139], and also colloidal dispersion of

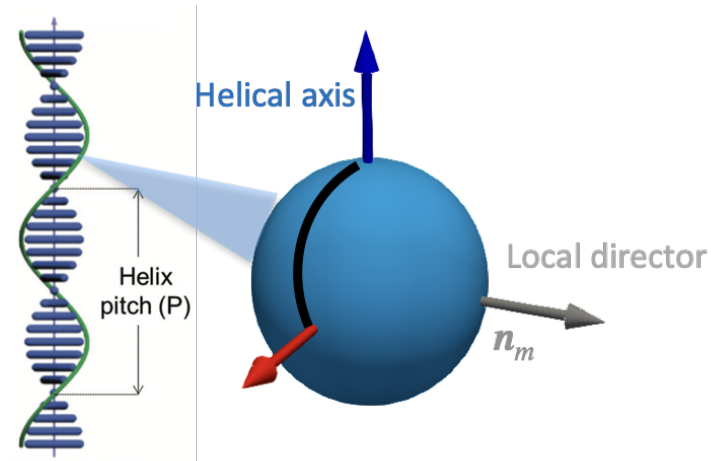


Figure 3.1.1: Illustration of alignment opportunities for an anisotropic colloidal particles immersed in a cholesteric host LC. Depending on the surface anchoring properties of the colloid and pitch of the cholesteric host, the colloid may preferentially align along either of the three main directions of the tripod. Alignment along the red arrow leads to strong emergent local biaxial order of a hybrid colloidal-molecular LC.

highly anisotropic particles immersed in molecular LC hosts, so-called hybrid nematics [140, 27, 86]. The interplay between chirality and biaxiality in orientational order has been intensively studied for LC systems [141, 142, 143, 144, 145, 146, 147, 148]. It has been concluded that cholesteric twisted alignment and biaxial order of LC molecules amplify each other and that a chiral twist configuration cannot be observed without building blocks featuring a certain degree of biaxiality in their orientational distributions at the molecular level. However, for purely molecular systems, the chirality-enhanced biaxiality of the molecular distribution was predicted and experimentally found to be rather weak [141, 142, 143, 144, 145, 146, 147, 148], scaling as $(qL_m)^2$ according to the prediction by Priest and Lubensky for single-component molecular LCs [141] (here $q = 2\pi/p$, p is the pitch of the chiral nematic and L_m the molecular length). To date, to the best of our knowledge, there are no experimental or theoretical considerations of how the biaxiality of the orientational distribution of anisotropic colloidal particles could interplay with the chirality of the nematic host in hybrid molecular-colloidal LC systems.

In this chapter we present a theoretical survey of ordering properties of colloidal particles immersed in a low-molecular weight liquid crystal. Based on a simple mean-field theory that accounts for the surface anchoring energy of a single colloid we explore the alignment properties of thin elongated rods and flat discs with respect to the helical director field of the molecular host fluid (see Fig. 3.1.1). A key element is the preferred surface anchoring properties of the molecular LC at the colloid surface which opens up several distinctly different ordering scenarios. Specific symmetries that we explore here are homeotropic, planar (see Fig. 3.2.1) as well as conically degenerate surface anchoring for the case of discs. Comparing with recent experimental results obtained in the group of I. Smalyukh (University of Colorado, USA) we conclude that our theory accounts for most of the experimental observations, but for one case. We demonstrate that the alignment of rodlike colloid with homeotropic anchoring is not driven by weak surface

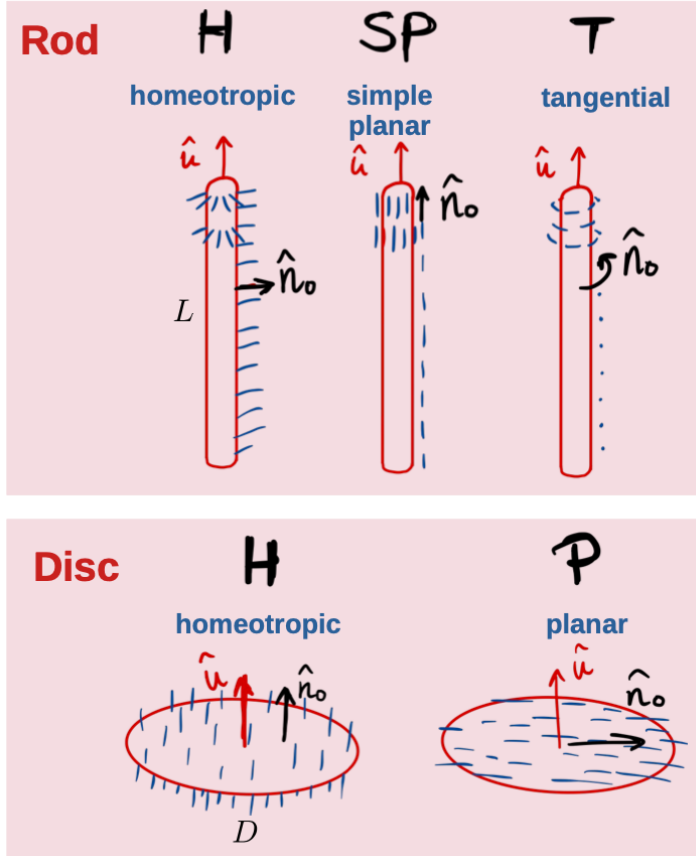


Figure 3.2.1: Illustration of the different surface anchoring scenarios for a colloidal rod with length L (top) and disc with diameter D (bottom).

anchoring forces, but rather by a twisted surface disclination effect. We address the weak elastic deformations around the colloids and demonstrate that the twisted disclination wrapped around a thin rod is the main driving force between homeotropic rods aligning perpendicular to the local host director and helical axis, thus imparting strong biaxial order onto the hybrid LC. A similar scenario is envisaged for homeotropic discs, but only in strongly cholesteric hosts with a pitch comparable to the disc diameter.

3.2 Surface anchoring of a cylindrical rod immersed in a cholesteric host

Let us consider a low-molecular-weight chiral liquid crystal (such as 5CB with chiral dopants) with a director field $\hat{\mathbf{n}}(z)$ twisted along Z -axis of a Cartesian laboratory frame. The director field of the cholesteric solvent, denoted by “ s ”, may be parameterized as:

$$\hat{\mathbf{n}}_s(z) = \hat{\mathbf{x}} \cos qZ + \hat{\mathbf{y}} \sin qZ \quad (3.1)$$

in terms of the pitch $p = 2\pi/q$ and handedness $q > 0$ that we assume right-handed without loss of generality. Next, we immerse an infinitely thin cylindrical rod with aspect ratio $L/D \rightarrow \infty$ into the chiral nematic phase. The main axis of each rod can be parameterized as $\hat{\mathbf{u}} = \hat{\mathbf{x}} \sin \theta \sin \varphi + \hat{\mathbf{y}} \sin \theta \cos \varphi + \hat{\mathbf{z}} \cos \theta$ in terms of a polar θ and azimuthal angle φ with respect to the helical axis $\hat{\mathbf{z}}$. The presence of the rod will generate elastic distortions of the uniform director field $\hat{\mathbf{n}}_s(\mathbf{r})$

due to the specific anchoring of the molecules at the surface of the rod, quantified by the surface anchoring energy $W_0 > 0$ (units energy surface area). The extent of elastic deformation around the colloid surface is commonly indicated by the surface extrapolation length $\ell_s = K/W_0$ where K designates the typical elastic constant of the thermotropic liquid crystal. In this project we focus on the regime of large surface extrapolation length ($\ell_s \rightarrow \infty$), in which case the elastic distortions are infinitesimally weak and the main energetic contribution imparted by the rod inclusions stems from the surface anchoring energy. Elastic corrections will be accounted for later on. If we assume the molecular director field $\hat{\mathbf{n}}$ to remain completely undistorted, the surface anchoring free energy can be obtained from a simple Rapini-Papoular integral of Eq. (3.1) over the colloid surface denoted by \mathcal{S} :

$$F_s = -\frac{1}{2}W_0 \oint d\mathcal{S} (\hat{\mathbf{n}}_s \cdot \hat{\mathbf{n}}_0(\mathcal{S}))^2 \quad (3.2)$$

with $\hat{\mathbf{n}}_0$ representing a unit vector normal to the colloid surface in case of *homeotropic* anchoring and tangential to the surface if the anchoring is *planar*.

For the particular case of a thin cylinder, we shall neglect small contributions associated with the ends of the cylinder so we only need to parameterize the cylindrical surface of magnitude πLD following the principal contour $\mathbf{r}_S(t) = \mathbf{r}_0 + \frac{L}{2}t\hat{\mathbf{u}}$ with $-1 < t < 1$ of a cylinder with centre-of-mass \mathbf{r}_0 . The surface anchoring free energy then becomes:

$$F_s = -\frac{1}{8}LDW_0 \int_0^{2\pi} d\phi \int_{-1}^1 dt [\hat{\mathbf{n}}_s(\mathbf{r}_S \cdot \hat{\mathbf{z}}) \cdot \hat{\mathbf{n}}_0]^2 \quad (3.3)$$

In order to describe various anchoring situations we define two unit vectors $\hat{\mathbf{e}}_{1,2}$ orthogonal to $\hat{\mathbf{u}}$ and parameterize:

$$\hat{\mathbf{n}}_0 = \begin{cases} \hat{\mathbf{e}}_1 \cos \phi + \hat{\mathbf{e}}_2 \sin \phi & \text{H} \\ -\hat{\mathbf{e}}_1 \sin \phi + \hat{\mathbf{e}}_2 \cos \phi & \text{T} \\ \hat{\mathbf{u}} & \text{SP} \end{cases} \quad (3.4)$$

In the case of homeotropic (H) anchoring the molecular director favors perpendicular alignment to the cylindrical surface, whereas for tangential (T) anchoring the easy axis follows the circular perimeter of the cylindrical cross section. The simple planar (SP) case corresponds to the easy axis $\hat{\mathbf{n}}_0$ pointing along main rod direction. We obtain the following generic expression:

$$F_s = -\frac{\pi}{8}LDW_0 \left(w_1 + w_2 \cos(2\delta) \frac{\sin(qL \cos \theta)}{qL} \right) \quad (3.5)$$

with $\delta = \varphi - qZ$ the azimuthal angle along a particle frame co-rotating with the helical director so that $\int d\hat{\mathbf{u}} = \int_0^{2\pi} d\delta \int_{-1}^1 d(\cos \theta)$ and w_1 and w_2 are angle-dependent coefficients that depend on the particular anchoring situation:

$$w_1 = \begin{cases} (1 + \cos^2 \theta) & \text{H/T} \\ 2 \sin^2 \theta & \text{SP} \end{cases} \quad (3.6)$$

and

$$w_2 = \begin{cases} -\sin\theta \tan\theta & \text{H/T} \\ 2\sin\theta \tan\theta & \text{SP} \end{cases} \quad (3.7)$$

in terms of the polar θ and azimuthal rod angle φ with respect to the helical axis. Note that the surface anchoring free energy is the same for the homeotropic and tangential anchoring scenarios.

For the homeotropic (H) case the free energy is minimal when $\theta^* = 0$ (with the azimuthal angle φ randomly distributed) which corresponds to the rod being aligned along the helical axis. However, there is a second, degenerate minimum at $\theta^* = \pi/2$ and $\delta^* = \pi/2$, that describes a rod pointing perpendicular both to the helical axis *and* the local director. The minimum surface anchoring energy is $F_s = -(\pi/4)LDW_0$ for both cases. The energy barrier between the two minima is only about $0.2 k_B T$ per rod so thermal fluctuations should easily make the colloids switch from one state to the other. For simple planar (SP) anchoring we only find a single minimum at $\theta^* = \pi/2$ and $\delta^* = 0$, i.e., the rod preferentially aligns along the revolving local nematic director.

3.2.1 Non-interacting rods

By balancing the surface anchoring free energy with the orientational entropy of the individual rods we easily establish the angular probability through the Boltzmann distribution:

$$f(\hat{\mathbf{u}}) = \mathcal{N} \exp(-\beta F_s(\delta, \theta)) \quad (3.8)$$

with $\beta^{-1} = k_B T$ the thermal energy in terms of temperature T and Boltzmann's constant k_B and \mathcal{N} a normalization constant ensuring that $\int d\hat{\mathbf{u}} f(\hat{\mathbf{u}}) = 1$. The surface anchoring strength is expressed in dimensionless form by $\bar{w} = \beta LDW_0$. The distributions are visualized in Fig. 3.2.2. It is easy to infer from Eq. (3.5) that the polar and azimuthal angles are strongly coupled. This indicates that the local distribution of rod orientations around the principal alignment directions (blue, red or white arrow in Fig. 3.2.2) is rendered *biaxial* by the chiral twist, as expected. The most interesting situation arises for the H/T case where there is a subpopulation of rods aligned along the helical axis ($qL = 1$). In order to gain further insight into the orientational symmetry of those rods, we perform a small-angle expansion around $\theta_e = 0$ and retain the leading order coupling term between the two principal angles θ and δ . The angular fluctuations about the helical axis (blue) are then described by the following free energy

$$F_s \approx \frac{\pi}{8} LDW_0 j_0(qL) \cos(2\delta) \theta^2 \quad (3.9)$$

with $j_0(x) = \sin(x)/x$. It suggests that the subpopulation of rods aligned along the helical axis in fact adopt a *twist-bend*-type organization with a pitch q identical to that of the molecular host. Contrary to cholesterics, these phases are characterized by a nematic director co-aligning with the helical axis. However, the situation here is more subtle given that chirality is only manifested at the level of orientational fluctuations around a mean director “backbone” that itself is not chiral. We identify a further interesting feature; depending on the sign of $j_0(qL)$

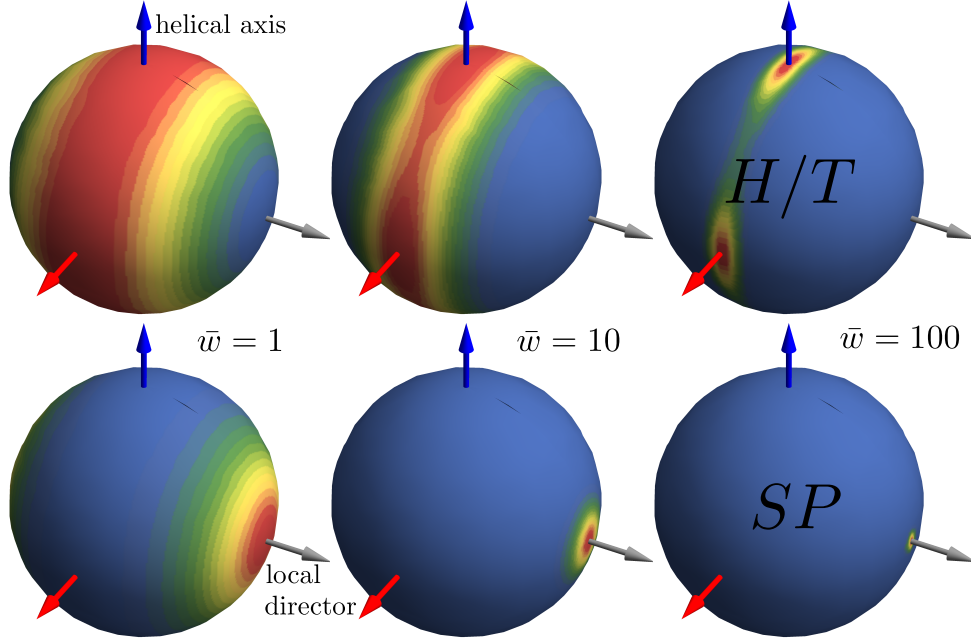


Figure 3.2.2: Unit-sphere projections of the local orientational probability of a rod immersed in a low molecular-weight cholesteric phase at different surface anchoring strengths $\bar{w} = \beta W_0 L D$. Zones of high orientational probability are in red. A bistable distribution is found for the homeotropic/tangential (H/T) anchoring case at elevated anchoring strength. For all distributions, the rod-length-to-pitch is $qL = 1$.

the twist-bend helix may be either in phase with the molecular helix ($\delta^* = 0$ for $qL = 4$) or out-of-phase ($\delta^* = \pi/2$ for $qL = 2$).

3.2.2 Non-interacting discs

We may now explore the case of a thin disc with $L \ll D$ immersed in a cholesteric LC. Let us denote its normal by $\hat{\mathbf{u}}$ and ignore anchoring at the rim. Similar to the case of rods we consider homeotropic (H) and planar (P) anchoring symmetries that we may express as follows:

$$\hat{\mathbf{n}}_0 = \begin{cases} \hat{\mathbf{u}} & \text{H} \\ \hat{\mathbf{e}}_1 \cos \xi + \hat{\mathbf{e}}_2 \sin \xi & \text{P} \end{cases} \quad (3.10)$$

The angle $0 < \xi < 2\pi$ must be chosen randomly in the case when planar anchoring is degenerate across all directions on the disc surface. Ignoring finite-thickness effects for $L \ll D$ we parameterize the face of the disc as follows:

$$\mathbf{r}_S = \mathbf{r}_0 + \frac{D}{2} t [\hat{\mathbf{e}}_1 \sin \phi + \hat{\mathbf{e}}_2 \cos \phi] \quad (3.11)$$

with $0 < t < 1$ and $0 < \phi < 2\pi$. The surface anchoring energy per disc face is expressed analogous to Eq. (3.3):

$$F_s = -\frac{1}{4} W_0 D^2 \int_0^{2\pi} d\phi \int_0^1 dt t \int_0^{2\pi} \frac{d\xi}{2\pi} [\hat{\mathbf{n}}_s(\mathbf{r}_S \cdot \mathbf{z}) \cdot \hat{\mathbf{n}}_0]^2 \quad (3.12)$$

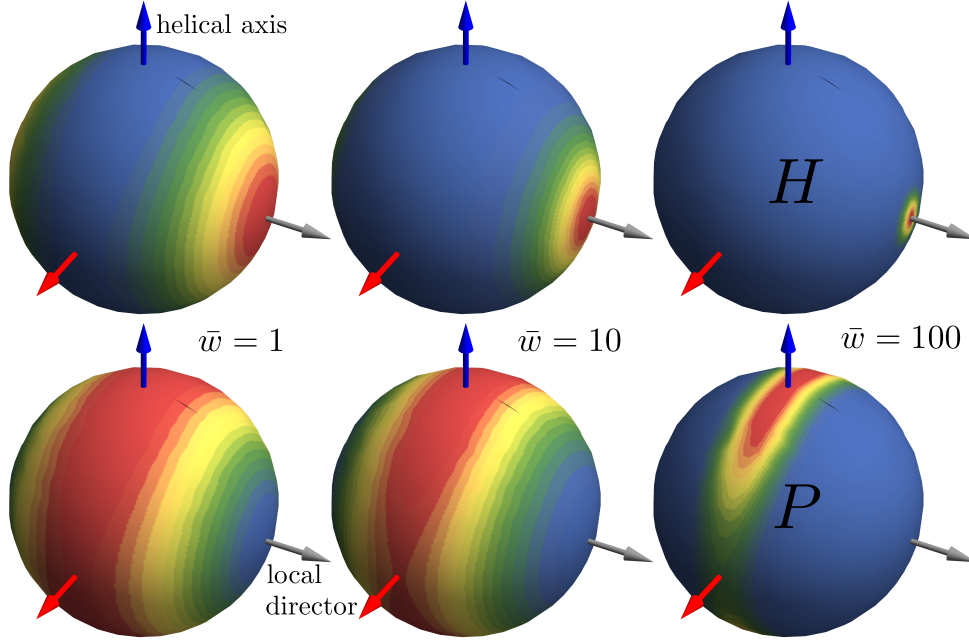


Figure 3.2.3: Unit-sphere projections of the local orientational probability of a disc immersed in a low molecular-weight cholesteric phase at different surface anchoring strengths $\bar{w} = \beta W_0 D^2$. For all distributions, the disc-diameter-to-pitch is $qD = 1$.

Leading to the following generic expression:

$$F_s = -\frac{\pi}{4} W_0 D^2 \left(w_1 + w_2 \cos(2\delta) \frac{J_1(qD|\sin\theta|)}{qD|\sin\theta|} \right) \quad (3.13)$$

with $J_1(x)$ a Bessel function of the first kind, $\delta = \varphi - qz$ the azimuthal angle with respect to the local cholesteric director, and coefficients:

$$w_1 = \begin{cases} \frac{1}{2} \sin^2 \theta & \text{H} \\ \frac{1}{8} (3 + \cos(2\theta)) & \text{P} \end{cases} \quad (3.14)$$

and

$$w_2 = \begin{cases} \sin^2 \theta & \text{H} \\ -\frac{1}{2} \sin^2 \theta & \text{P} \end{cases} \quad (3.15)$$

Similar to the rods the surface anchoring strength is expressed in dimensionless form by $\bar{w} = \beta W_0 D^2$. Taking discs with diameter $D \approx 2\mu\text{m}$ and $W_0 \approx 10^{-6} - 10^{-5} \text{J/m}^2$ we find an even higher value than for the rods, namely $\bar{w} \sim 10^3 - 10^4$ indicating that surface anchoring realignment is robust against thermal fluctuations.

3.2.3 Conically degenerate surface anchoring

The presented surface anchoring model is suitable for a vast selection of geometrical junctions between the cholesteric solvent and the particles. Another experimentally relevant scenario, and a generalization of the previously evaluated situations, would consist of a preferred anchoring direction $\hat{\mathbf{n}}_0$ forming an angle α (and thus drawing a degenerate conical surface with apex

angle $\alpha/2$) with respect to the vector normal to the colloid surface. Let ξ be the integration angle around such a cone.

For rod-like particles, the anchoring free energy is expressed analogous to Eq. (3.3):

$$F_s = -\frac{1}{8}LDW_0 \int_0^{2\pi} d\phi \int_{-1}^1 dt \int_0^{2\pi} \frac{d\xi}{2\pi} [\hat{\mathbf{n}}_s(\mathbf{r}_S \cdot \mathbf{z}) \cdot \hat{\mathbf{n}}_0]^2 \quad (3.16)$$

We may express $\hat{\mathbf{n}}_0$ in terms of the angles α , ϕ and ξ :

$$\begin{aligned} \hat{\mathbf{n}}_0 &= \hat{\mathbf{e}}_1(\cos \phi \cos \alpha - \sin \phi \sin \alpha \cos \xi) \\ &\quad + \hat{\mathbf{e}}_2(\sin \phi \cos \alpha + \cos \phi \sin \alpha \cos \xi) \\ &\quad + \hat{\mathbf{u}} \sin \alpha \sin \xi \end{aligned} \quad (3.17)$$

Leading to an expression equivalent to Eq. (3.5) with coefficients:

$$w_1 = \frac{1}{2}(3 - \cos^2 \alpha + (3 \cos^2 \alpha - 1) \cos^2 \theta) \quad (3.18)$$

and

$$w_2 = -\frac{1}{2}(3 \cos^2 \alpha - 1) \sin \theta \tan \theta \quad (3.19)$$

We can similarly take Eq. (3.12) for discs. In this case we define $\hat{\mathbf{n}}_0$ as follows:

$$\hat{\mathbf{n}}_0 = (\hat{\mathbf{e}}_1 \cos \xi + \hat{\mathbf{e}}_2 \sin \xi) \sin \alpha + \hat{\mathbf{u}} \cos \alpha \quad (3.20)$$

Leading to an expression equivalent to Eq. (3.13) with coefficients:

$$w_1 = \frac{1}{4}(2 - 2 \cos^2 \alpha + (3 \cos^2 \alpha - 1) \sin^2 \theta) \quad (3.21)$$

and

$$w_2 = \frac{1}{2}(3 \cos^2 \alpha - 1) \sin^2 \theta \quad (3.22)$$

The corresponding distributions are given in Fig. 3.2.4.

3.2.4 Order parameters

In order to facilitate comparison with experimental results, we define orientational order with respect to $\hat{\mathbf{n}}_s$ which defines the principal direction of molecular alignment along the cholesteric helix. Taking the local host director $\hat{\mathbf{n}}_s$ as a reference we define a uniaxial order parameter:

$$S = \langle \mathcal{P}_2(\hat{\mathbf{u}} \cdot \hat{\mathbf{n}}_s) \rangle_{f_q} \quad (3.23)$$

A biaxial nematic order parameter measures the relative orientational order with respect to the principal directions orthogonal to $\hat{\mathbf{n}}_s$:

$$\Delta = \langle a^2 - b^2 \rangle_{f_q} \quad (3.24)$$

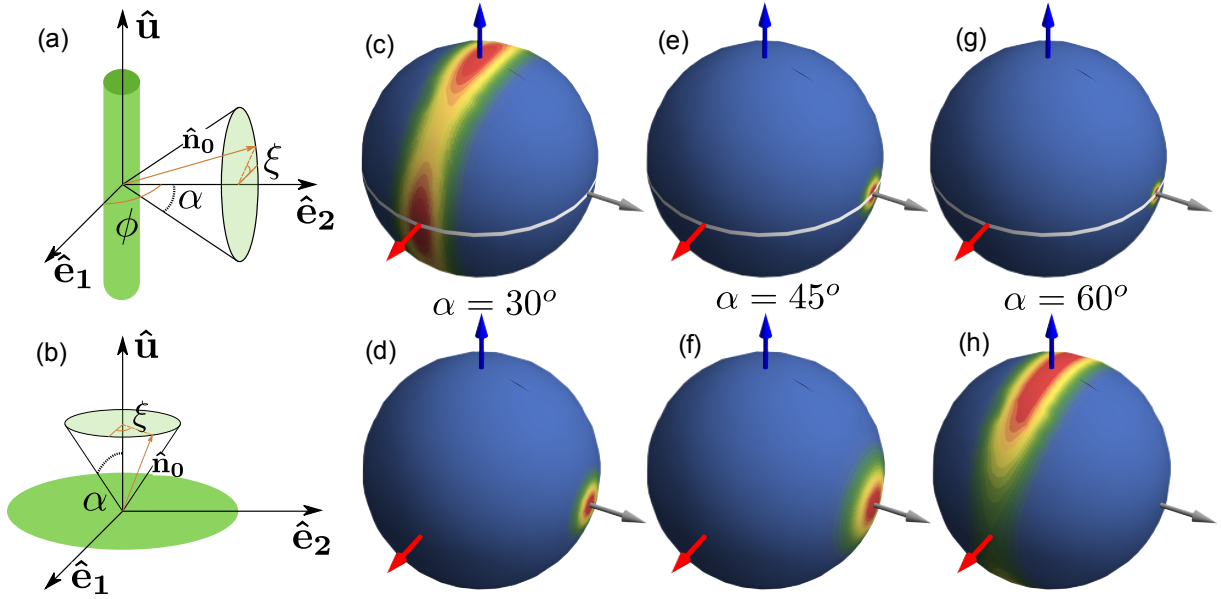


Figure 3.2.4: (a) (and (b)) Schemes to illustrate the conically degenerate surface anchoring with a fixed anchoring angle α on rods (and discs). (c-h) Unit-sphere projections of the local orientational probability of a rod (top panels c, e, g) or a disc (bottom panels d, f, h) immersed in a low molecular-weight cholesteric phase at different anchoring angles. For all distributions, the particle-length-to-pitch is $qL(D) = 1$ and the surface anchoring strength is $\bar{w} = 100$.

in terms of the projections $a = \hat{\mathbf{u}} \cdot (\hat{\mathbf{n}}_s \times \hat{\mathbf{z}})$ and $b = \hat{\mathbf{u}} \cdot \hat{\mathbf{z}}$. We stress that this convention is by no means unique and one could also define orientational order from the tensor $\mathbf{Q}_c = \frac{3}{2} \langle \hat{\mathbf{u}} \otimes \hat{\mathbf{u}} \rangle_{f_q} - \frac{\mathbf{I}}{2}$ which measures the orientational order parameters (S_c and Δ_c) with respect to the principal colloidal alignment direction $\hat{\mathbf{n}}$, independent from the chosen reference frame.

3.3 Experimental model system

The experiments performed in the group of I. Smalyukh are based on disk or rod-shaped $\beta - \text{NaYF}_4 : \text{Yb/Er}$ particles are synthesized following the hydrothermal synthesis methods described in detail in Refs. [86, 27]. Homeotropic anchoring with 5CB (pentyl-cyanobiphenyl or 4-cyano-4'-pentylbiphenyl) molecules on the $\beta - \text{NaYF}_4 : \text{Yb/Er}$ disk surfaces is controlled through surface-functionalization with a thin layer of silica and polyethylene glycol.

The colloidal rods have length $L \approx 1.6 \mu\text{m}$, thickness $D \approx 25 \text{nm}$ and *homeotropic* (H) surface anchoring with amplitude $W_0 \approx 10^{-5} \text{J/m}^2$. From this we find that $\bar{w} \approx 97$ indicating that the realigning forces generated by surface anchoring strongly exceed thermal fluctuation forces. The pitch of the cholesteric host is about $p \approx 30 \mu\text{m}$ so that $qL \approx 0.335$. The discs have a diameter of about $D \sim 2 \mu\text{m}$ and thickness of $L \sim 20 \text{nm}$. In view of their large diameter the surface anchoring amplitude $\bar{w} \sim 10^3 - 10^4$ each disk experiences strongly exceeds the thermal energy. The results of the experiments are summarized in the table below. In addition, numerical works have been performed based on minimizing the Landau-de Gennes free energy around a colloidal particle immersed. The numerical results fully account for the elastic anisotropy of the cholesteric host with input parameters based on the experimentally measured elastic moduli

for 5CB. The surface anchoring amplitude and symmetry was varied in similar ways as in our theoretical approach. Full details of the experiments and Landau-de Gennes computations will be disclosed in an upcoming joint publication with the group of I. Smalyukh.

	S	Δ	S_c	Δ_c
homeotropic disk	0.6564	0.0673	0.6564	0.0673
planar rod	0.9360	0.0140	0.9360	0.0140
homeotropic rod ($L = 1.7\mu m$)	-0.2561	0.7594	0.6976	0.1236
homeotropic rod ($L = 3\mu m$)	-0.3818	0.8935	0.8610	0.0650

Table 3.3.1: Colloidal order parameters measured in the local molecular frame and colloidal frame (with subscript ‘c’) for each set of experiments.

From the measured order parameters we infer that both planar rods and homeotropic discs tend to align along the cholesteric director, whereas homeotropic rods strongly prefer to orient towards the perpendicular axis indicated in red in Fig. 3.4.1. These observations are in line with the distributions depicted in Fig. 3.2.2 for the rods and Fig. 3.2.3 for the discs. However, Fig. 3.2.2 suggests that homeotropic rods with strong surface-anchoring coupling $\bar{w} = 100$ should have an equal probability to the red and blue arrows. This degeneracy is not observed in experiment where the subpopulation of rods pointing along the helix axis (blue) is estimated to be negligible. Clearly, the Rapini-Papoular surface anchoring energy does not suffice to explain the experimental observation which suggests that elastic deformations incurred by the weak surface anchoring forces must play a subtle role. This we will analyze next.

3.4 Comparison with experiments: role of elastic distortions

In our analysis so far we have completely ignored elastic deformations of the host director ($\ell_s = K/W_0 \rightarrow \infty$) so that rod realignment is dominated entirely by surface anchoring. The latter dictates that rods should point along the blue and red axis with equal probability (see Fig. 3.2.2). The experimental reality, however, is that the surface anchoring extrapolation length is large but finite ($\ell_s \approx 600nm \gg D$). Observations point at a scenario in which rods orienting along the red axis is largely preferred over the helical axis (blue). The reason why the latter is unfavorable is that it involves a twisting of the surface disclination that runs along the rod contour which presumably costs energy. This is illustrated in Fig. 3.4.1. No such twisting is necessary if the rod points along the red axis. Clearly, the discrepancy between experiment and theory must be attributed to the elastic distortions running along the rod surface (and their subsequent twisting) which was ignored in our model considerations thus far. In principle, weak director distortions may also lead to a minute decrease of the bulk nematic order parameter, in particular in regions where the director curvature is strong. In our analysis, we will assume that the scalar order parameter of the host is preserved even close to the rod surface where director distortions are expected to be the strongest.

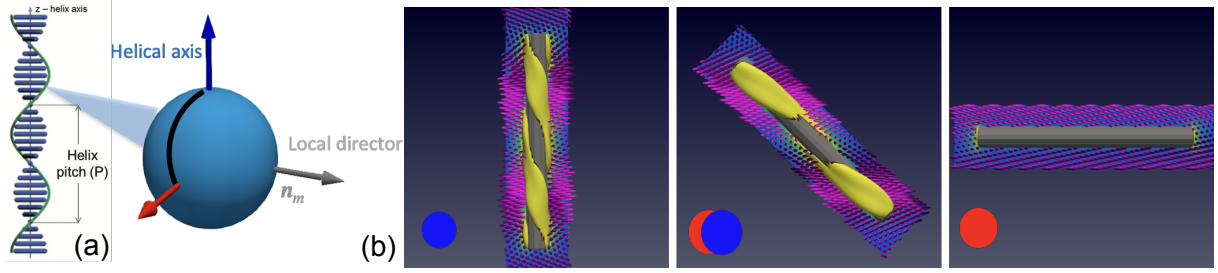


Figure 3.4.1: (a) Local tripod of directions along the molecular helix. (b) Illustrations of a helical surface defect emerging around a colloidal cylinder at various orientations along the tripod, indicated by the colored dots. When the rod aligns along the blue helical axis a helically twisted disclination occurs. It is absent when the rod points along the red arrow. Picture courtesy of Jason Wu (University of Colorado, USA).

3.4.1 Elastic energy of a twisted disclination wrapped around a thin rod

We will now attempt to quantify the twisted disclination effect by introducing an angular deviation $\Phi(\mathbf{r})$ and express the helical host director as follows:

$$\hat{\mathbf{n}}_s(\mathbf{r}) = \hat{\mathbf{x}} \cos(qz + \Phi(\mathbf{r}_\perp)) + \hat{\mathbf{y}} \sin(qz + \Phi(\mathbf{r}_\perp)) \quad (3.25)$$

with \mathbf{r} denoting a 3D distance vector and \mathbf{r}_\perp the lateral distance perpendicular to the helical axis $\hat{\mathbf{z}}$. The total free energy of a colloidal rod inclusion aligned along the helical axis is given by the Rapini-Papoular surface anchoring term Eq. (3.2) combined with the Frank elastic free energy in the presence of chirality:

$$F = \frac{1}{2} \int d\mathbf{r} [K_1(\nabla \cdot \hat{\mathbf{n}}_s)^2 + K_2(\hat{\mathbf{n}}_s \cdot \nabla \times \hat{\mathbf{n}}_s + q)^2 + K_3(\hat{\mathbf{n}}_s \times \nabla \times \hat{\mathbf{n}}_s)^2] - \frac{1}{2} W_0 \oint dS (\hat{\mathbf{n}}_s \cdot \hat{\mathbf{n}}_0(S))^2 \quad (3.26)$$

with K_1 , K_2 and K_3 respectively denoting the splay, twist and bend elastic modulus. The saddle-splay term surface elasticity reads:

$$F_{se} = -\frac{K_{24}}{2} \oint dS \cdot (\hat{\mathbf{n}}_s \nabla \cdot \hat{\mathbf{n}}_s + \hat{\mathbf{n}}_s \times \nabla \times \hat{\mathbf{n}}_s) \quad (3.27)$$

and is expected to have very little impact in the current geometry (cf. spherical colloidal inclusion). The director twist is very weak on the typical range of the director deformations which should be comparable to the rod diameter D rather than the rod length $L \gg D$. For simplicity, we assume the rod to be infinitely long and elastic distortions to occur only along the radial direction \mathbf{r}_\perp . Employing cylindrical coordinates $\Phi(\mathbf{r}_\perp) = \Phi(r, \vartheta)$, expanding up to second

order in q and integrating over z we obtain for the free energy F_{el} per unit rod length:

$$\begin{aligned} \frac{F_{el}}{L} = \frac{1}{2} \int d\mathbf{r}_\perp \left\{ \frac{K_1}{r^2} (1 + \partial_\vartheta \Phi)^2 + K_3 (\partial_r \Phi)^2 \right. \\ \left. + \frac{(qL)^2}{12} \Delta K \left[\frac{1}{r^2} (1 + \partial_\vartheta \Phi)^2 - (\partial_r \Phi)^2 \right] \right\} \end{aligned} \quad (3.28)$$

where $\Delta K = K_3 - K_1 > 0$ denotes the difference between the bend and splay moduli. The elastic anisotropy turns out to be of crucial importance since the twist correction $\mathcal{O}(q^2)$ vanishes in case of the one-constant approximation $K_1 = K_3 = K_2 = K$. Similarly, the surface anchoring free energy reads up to quadratic order in $qL \ll 1$:

$$\frac{F_s}{L} = -\frac{W_0}{2} \oint_{\mathcal{C}} d\vartheta \left\{ \cos^2(\vartheta - \Phi) - \frac{(qL)^2}{12} \cos[2(\vartheta - \Phi)] \right\} \quad (3.29)$$

where \mathcal{C} denotes the circular contour of the rod cross section with diameter D . For weak distortions $\Phi \ll 1$ we linearize for Φ and obtain:

$$\frac{F_s}{L} \approx \frac{F_s^{(0)}}{L} - \frac{W_0}{2} (1 - \frac{1}{6}(qL)^2) \oint_{\mathcal{C}} d\vartheta \sin 2\vartheta \Phi \quad (3.30)$$

The first term is the contribution for the *undistorted* director field previously analysed:

$$\begin{aligned} F_s^{(0)} &= -\frac{LW_0}{2} \oint_{\mathcal{C}} d\vartheta \left\{ \cos^2 \vartheta - \frac{(qL)^2}{12} \cos 2\vartheta \right\} \\ &\sim -\frac{\pi}{4} W_0 L D \end{aligned} \quad (3.31)$$

which corresponds to Eq. (3.3) for a homeotropic rod aligned perpendicular to the helical axis ($\theta = \delta = \pi/2$) in the large pitch limit $qL \ll 1$. The second term in Eq. (3.30) accounts for the change of surface anchoring free energy generated by the elastic distortions. The change of elastic free energy induced by the twist follows from:

$$\Delta F_{\text{twist}}^{(el)} \approx \frac{1}{24} (qL)^2 L \Delta K \mathcal{F}[\Phi_0] \quad (3.32)$$

where Φ_0 denotes the distortion angle for the *untwisted* system, and:

$$\mathcal{F}[\Phi_0] = \int d\mathbf{r}_\perp \left[\frac{1}{r^2} (1 + \partial_\vartheta \Phi_0)^2 - (\partial_r \Phi_0)^2 \right] \quad (3.33)$$

is a dimensionless quantity measuring the extent of the surface disclination surrounding the cylinder. Applying the one-constant approximation which does not lead to qualitative changes in this context, we determine Φ_0 from minimizing:

$$\frac{F_{el}(q=0)}{KL} = \frac{1}{2} \int d\mathbf{r}_\perp \left\{ \frac{1}{r^2} (1 + \partial_\vartheta \Phi)^2 + (\partial_r \Phi)^2 \right\} \quad (3.34)$$

so that $(\delta F_{el}/\delta \Phi)_{\Phi=\Phi_0} = 0$ and $\ell_s = K/W_0$ defines the (finite) surface anchoring extrapolation length. Functional minimization of the free energy we obtain the Laplace equation in polar

coordinates:

$$\partial_r^2 \Phi_0 + \frac{1}{r} \partial_r \Phi_0 + \frac{1}{r^2} \partial_\vartheta^2 \Phi_0 = 0 \quad (3.35)$$

subject to the boundary conditions:

$$\begin{aligned} \Phi_0(\infty, \vartheta) &= 0 \\ \ell_s \partial_r \Phi_0(D/2, \vartheta) &= \frac{1}{2} \sin 2\vartheta \end{aligned} \quad (3.36)$$

with the latter denoting a Neumann boundary condition at the colloid surface imparted by surface anchoring contribution Eq. (3.30). The result is a simple dipolar field:

$$\Phi_0(r, \vartheta) = -\frac{D}{16\ell_s} \left(\frac{D}{2r}\right)^2 \sin 2\vartheta \quad (3.37)$$

Plugging this back into Eq. (3.33) and integrating we find that the difference in elastic energy between the twisted (blue) and untwisted (red) case is independent of the surface anchoring extrapolation length ℓ_s and increases logarithmically with system size ℓ_{\max} :

$$\Delta F_{\text{twist}}^{(el)} \sim \frac{2\pi}{24} (qL)^2 L \Delta K \ln \left(\frac{2\ell_{\max}}{D} \right) \quad (3.38)$$

Taking $\ell_{\max} = L$ as typical size cut-off, $\Delta K \approx 4pN$ we find that $\Delta F_{\text{twist}} \approx 280k_B T$. The change in surface anchoring free energy associated with a twist of the director distortions reads:

$$\Delta F_{\text{twist}}^{(s)} \sim -\frac{\pi W_0 L D}{92} \frac{D}{\ell_s} (qL)^2 \quad (3.39)$$

which is negligible compared to the elastic contribution above so that the total distortion-induced free energy change reads $\Delta F_{\text{twist}} \approx \Delta F_{\text{twist}}^{(el)}$.

3.4.2 Elastic distortions around a rod tilted away from the host director

In order to complete our understanding of the strength of the elastic distortions surrounding the main section of the rod we now look at the case where the rod remains perpendicular to the helix axis but makes an oblique angle with respect to the host director (see Fig. 3.4.2). Ignoring chiral twist we parameterize the host director field case within a Cartesian reference frame with the rod aligned along $\hat{\mathbf{z}}$:

$$\hat{\mathbf{n}}_s(\mathbf{r}) = \begin{pmatrix} \cos \Phi(\mathbf{r}) \cos \chi(\mathbf{r}) \\ \sin \Phi(\mathbf{r}) \cos \chi(\mathbf{r}) \\ \sin \chi(\mathbf{r}) \end{pmatrix} \quad (3.40)$$

As before, we ignore end effects and express the spatial variation of the distortion angles in polar coordinates, i.e. $\Phi(r, \vartheta)$ and $\chi(r, \theta)$. In principle, the Euler-Lagrange expressions emerging from minimizing the elastic free energy are strongly coupled and cannot be solved analytically even in the case of weak surface anchoring. We expect, however, that a tilted rod will mostly experience distortions along its main axis $\hat{\mathbf{z}}$, expressed by a non-zero χ , while the director deviations Φ

surrounding the lateral cross-section of the rod remain far less affected by the rotation. Then, we can pursue a hybrid route by constraining $\Phi = \Phi_0$ to its solution for the perpendicular case Eq. (3.36) and minimize the free energy only with respect to χ . Working out the one-constant elastic free energy and taking the functional derivative we find that χ satisfies the following non-linear partial differential equation:

$$\partial_r^2 \chi + \frac{1}{r} \partial_r \chi + \frac{1}{r^2} \partial_\vartheta^2 \chi = -\frac{\sin 2\chi}{2r^2} \quad (3.41)$$

Corrections to the right-hand term are of order $\mathcal{O}(1/r\ell_s)$ and can be neglected for weak surface anchoring $\ell_s \gg D$. In order to accommodate a rotation of the rod axis with respect to the far field host director we define a rotation matrix:

$$\mathcal{R}(\delta) = \begin{pmatrix} \sin \delta & 0 & -\cos \delta \\ 0 & 1 & 0 \\ \cos \delta & 0 & \sin \delta \end{pmatrix} \quad (3.42)$$

such that $\delta = \pi/2$ reverts to the case where the far-field host director is perpendicular to the rod axis. The boundary conditions then follow from the Rapini-Papoular surface anchoring energy where the surface normal $\hat{\mathbf{n}}_0$ is subject to rotation:

$$\begin{aligned} F_s &= -\frac{W_0}{2} \oint d\mathcal{S} [\hat{\mathbf{n}}_s \cdot (\mathcal{R}(\delta) \cdot \hat{\mathbf{n}}_0(\mathcal{S}))]^2 \\ &= -\frac{W_0 L}{2} \oint d\vartheta \cos^2 \vartheta \sin^2(\delta - \chi(D/2, \vartheta)) \end{aligned} \quad (3.43)$$

from which we infer that at $\delta = \pi/2$ (red arrow) optimal surface anchoring is achieved when the distortion angle χ is zero, which leads back to Eq. (3.31). For oblique orientations $0 < \delta < \pi/2$, severe distortions are generated since the optimal anchoring angle at the rod surface $\chi_{\text{surf}} \sim \delta - \pi/2$ is incompatible with the far-field condition $\chi(r \rightarrow \infty) = 0$. The boundary condition for χ are the following:

$$\begin{aligned} \chi(\infty, \vartheta) &= 0 \\ \ell_s \partial_r \chi(D/2, \vartheta) &= -\frac{1}{2} \cos^2 \vartheta \sin[2(\delta - \chi(D/2, \vartheta))] \\ &\quad + D^{-1} \sin 2\chi(D/2, \vartheta) \end{aligned} \quad (3.44)$$

The latter condition tells us that the distortions will be independent of the tilt angle δ at infinitely weak surface anchoring ($\ell_s \rightarrow \infty$), as we expect. Clearly, the non-linear nature of the above differential equation and the complicated boundary conditions do not allow for an analytical solution of the problem.

Curvature-free rod cross-section

A more tractable way forward is to transform the above expressions into a Cartesian coordinate system, so that $\chi(x, y)$ with the far-field host director pointing along the x -axis. Basically, we assume that the rod cross-section along which the director distortions are expected to occur

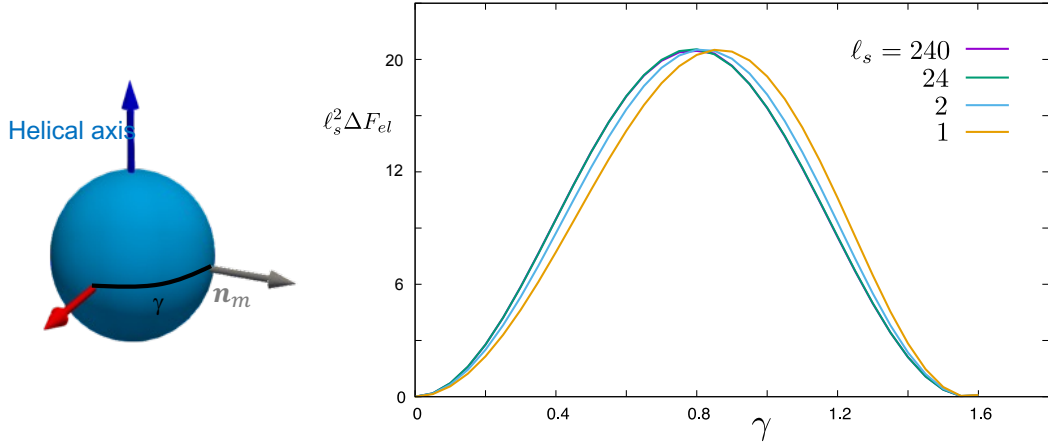


Figure 3.4.2: Free energy associated with elastic distortions around a homeotropic rod tilted at an angle γ away from the red arrow towards the molecular director (grey) at different surface anchoring extrapolation lengths ℓ_s (expressed in units of the rod diameter D).

can be described by a strip of length L and $D \ll L$. Further, we define a tilt angle $\gamma = \delta - \frac{\pi}{2}$ (with $0 < \gamma < \pi/2$) so that $\gamma = 0$ corresponds to the most favorable case where the rod points perpendicular along the red arrow. All distances are normalized in terms of D . The distortions are then described by the 2D Laplacian:

$$(\partial_x^2 + \partial_y^2)\chi = 0 \quad (3.45)$$

of which the general solution reads:

$$\chi(x, y) = \sum_{n=1}^{\infty} e^{-n\pi x} [a_n \cos(n\pi y) + b_n \sin(n\pi y)] \quad (3.46)$$

which vanishes in the far-field limit $\chi(x \rightarrow \infty) = 0$. The (Rapini-Papoular) surface anchoring free energy reads:

$$\frac{F_s}{KL} = -\frac{1}{2\ell_s} \int_0^1 dy \cos^2(\gamma - \chi(0, y)) \quad (3.47)$$

which translates into the following boundary condition at the surface of the strip located at $x = 0$:

$$\ell_s \partial_x \chi(0, y) = \frac{1}{2} \sin[2(\gamma - \chi(0, y))] \quad (3.48)$$

Further, for symmetry reasons we require the distortion angle to be vanishing at both sides of the strip:

$$\chi(0, 0) = \chi(0, 1) = 0 \quad (3.49)$$

which implies that $a_n = 0$. The coefficients b_n need to be resolved from:

$$n\pi b_n = \frac{1}{\ell_s} \int_0^1 dy \sin(n\pi y) \sin \left[2 \left(\gamma - \sum_{k=1}^{\infty} b_k \sin(k\pi y) \right) \right] \quad (3.50)$$

For small tilt angles $\gamma \ll 1$ distortions are expected to be weak $\chi \ll 1$ so that we linearize $\sin 2(\gamma - \chi) \approx 2(\gamma - \chi)$. This enables us to resolve the coefficients analytically:

$$b_n = \left(\frac{1 - (-1)^n}{(n\pi)^2} \right) \frac{\gamma}{\ell_s} \quad (3.51)$$

The free energy increase induced by the elastic distortions is given by:

$$\Delta F_{el} = \frac{\pi KL}{4} \sum_{n=1}^{\infty} n b_n^2 \quad (3.52)$$

which in the linearized regime for small γ gives a simple analytical result:

$$\Delta F_{el} = \frac{7KL}{8\pi^3} \zeta(3) \left(\frac{\gamma}{\ell_s} \right)^2 \quad (3.53)$$

with $\zeta(3) \approx 1.2$ a constant from the Riemann-Zeta function $\zeta(x)$. The surface anchoring free energy reads:

$$F_s = -LDW_0 \int_0^1 dy \cos^2(\gamma - \chi(0, y)) \quad (3.54)$$

Then, in the absence of elastic distortions and no tilt ($\gamma = 0$) the surface anchoring free energy would simply be $F_s = -LDW_0$ which only marginally differs from the result for the cylindrical case $F_s = -(\pi/4)LDW_0$. Within the linearized regime for small tilt angles $\gamma \ll 1$ the change in surface anchoring free energy imparted by the elastic distortions is given by:

$$\begin{aligned} \Delta F_s &\approx LDW_0 \int_0^1 dy (\gamma - \chi(0, y))^2 \\ &\approx W_0 LD \left(1 + \frac{1}{48\ell_s^2} - \frac{7\zeta(3)}{\pi^3 \ell_s} \right) \gamma^2 \end{aligned} \quad (3.55)$$

This expression along with Eq. (3.53) clearly reflects the basic trade-off between surface anchoring and elasticity in which the cost in elastic free energy is in part compensated by a reduction of the surface anchoring free energy (last term). The total free energy change for small tilt angles now reads:

$$\Delta F_{\text{tot}} \sim W_0 LD \left(1 - \frac{49\zeta(3)}{8\pi^3 \ell_s} \right) \gamma^2 + \mathcal{O}(\gamma^2/\ell_s^2) \quad (3.56)$$

Let us now compare our results with the simple Rapini-Papoular expression Eq. (3.3) in the *absence* of elastic distortions. Taking $\theta = \pi/2$ and expanding for small γ we find:

$$\Delta F_{\text{tot}}^{(RP)} \sim \frac{\pi}{4} W_0 LD \gamma^2 \quad (3.57)$$

Disregarding the trivial curvature prefactor $\pi/4$ in the last expression, we find that the impact of the elastic distortions is rather marginal, since the correction term in Eq. (3.56) is less than $1 k_B T$. Numerical resolution of Eq. (3.50) reveals that weak elastic distortions occur mostly when the rod is at an oblique angle $\gamma = \pi/4$. This is illustrated in Fig. 3.4.2 for a number of different anchoring strengths expressed by the extrapolation length ℓ_s .

Now that we have established that distortions remain weak at any angle γ for large enough extrapolation length $\ell_s \gg 1$ we may explore an alternative route to quantifying χ by linearizing the boundary condition Eq. (3.58) for $\chi \ll 1$:

$$\ell_s \partial_x \chi(0, y) \approx \frac{1}{2} \sin(2\gamma) - \chi(0, y) \cos(2\gamma) \quad (3.58)$$

From which the coefficients are easily established:

$$b_n = \frac{\sin(2\gamma)}{\cos(2\gamma) - n\pi\ell_s} \left(\frac{1 - (-1)^n}{n\pi} \right) \quad (3.59)$$

The corresponding elastic free energy then follows from the summation in Eq. (3.52) and the results agree with the ones shown in Fig. 3.4.2.

3.4.3 Effective orientational potential of a LC rod

Gathering the findings of the previous paragraphs we revisit the realigning potential acting on each rod. The total external potential is given by the bare Rapini-Papoular contribution Eq. (3.3) for the undistorted host director plus the free energy contributions from elastic distortions:

$$U_{\text{rod}}(\theta, \delta) \sim F_s(\theta, \delta) + \Delta F_{\text{dist}}(\theta, \delta) \quad (3.60)$$

Since the distortion term cannot be resolved for any rod orientation but only for cases when the rod is aligned along the principal Cartesian axes of the host frame we use the following interpolation form:

$$\Delta F_{\text{dist}}(\theta, \delta) \sim \Delta F_{\text{twist}} \cos^2 \theta + \Delta F_{\text{tilt}} \sin^2 \theta \cos^2 \delta \quad (3.61)$$

in terms of the two principal elastic contributions; $\Delta F_{\text{tilt}} = F(\text{grey}) - F(\text{red})$ associated with tilting the rod away from the red arrow and ΔF_{twist} [Eq. (3.38)] the energy cost associated with twisting of the surface disclination wrapped along the main part of the cylinder. From the analysis in the previous paragraphs we found that $\Delta F_{\text{twist}} = \mathcal{O}(10^2 k_B T)$ whereas elastic distortions due to tilting are very weak $\Delta F_{\text{tilt}} < k_B T$ and may, in fact, be neglected all together for the weak anchoring regime. The elastic energy is minimal (zero) when the rods align along the red arrow ($\theta = \pi/2$ and $\delta = \pi/2$) as observed in experiment.

At infinitely low rod concentrations, the order parameters S and Δ defined within the frame of the molecular host (Eq. (3.23) and Eq. (3.24)) are readily computed from the Boltzmann factor $f(\hat{\mathbf{u}}) = \mathcal{N} \exp(-\beta U_{\text{rod}}(\delta, \theta))$. An overview of the results as a function of the anchoring strength $\bar{w} = \beta W_0 L D$ is given in Fig. 3.4.3. The best correspondence with experimental data for homeotropic rods listed in Table 3.1 is found for $\bar{w} \sim 6 k_B T$ which corresponds to a surface anchoring amplitude of about $W_0 \sim 6 \times 10^{-7} \text{ J/m}^2$.

The typical energy scale related to the twisted disclination effect can be gleaned from the orientational distribution of the colloidal particles that have been measured in experiment. From these, we can identify a standard Gaussian FWHM $= 2.355/\sqrt{2\Delta F_{\text{twist}}}$. This subsequently gives $\Delta F_{\text{twist}} \approx 22 k_B T$ for homeotropic rods with $L = 1.7 \mu\text{m}$ and $\Delta F_{\text{twist}} \approx 76 k_B T$ for the longer

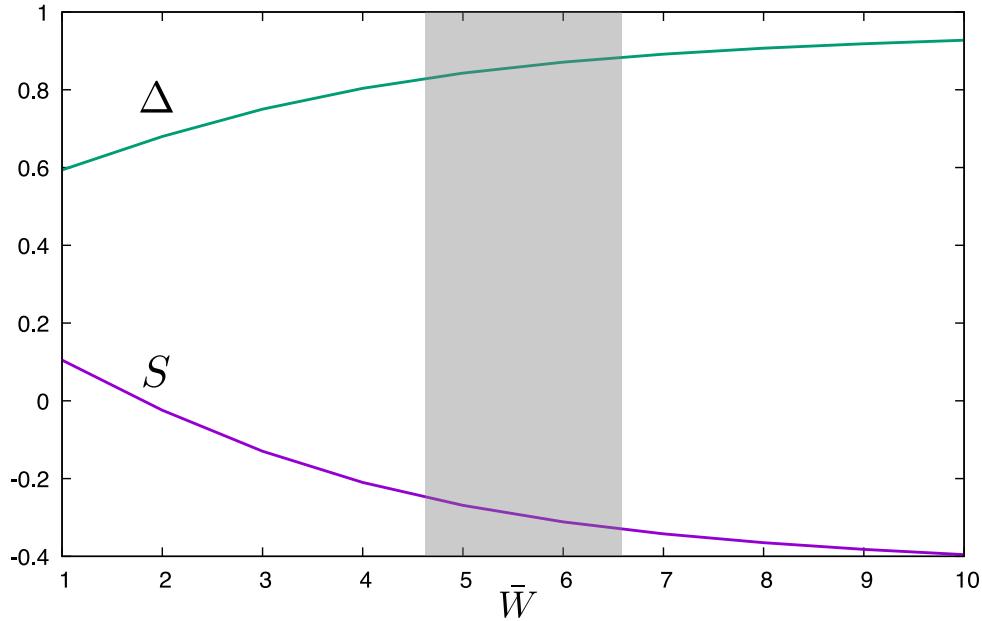


Figure 3.4.3: Colloidal nematic order parameters measured within the molecular frame as a function of the surface anchoring amplitude $\bar{w} = W_0LD$. The experimentally relevant region is indicated in grey.

rods with $L = 3\mu\text{m}$ suggesting that, in both cases, the thermal motion of the rods is assuredly insufficient to overcome the energy barrier between the τ and χ alignment directions. The values are in qualitative agreement with the prediction from our analytical model Eq. (3.38) where $\Delta F_{\text{twist}} \propto L^3$ suggests the energy to indeed be quite sensitive to the colloidal rod length. The actual values from Eq. (3.38), however, should be considered as an upper bound for ΔF_{twist} mainly because in our model the local nematic order parameter of the host is constrained at its far-field bulk value and is not allowed to relax in regions where director distortions are the largest, as observed in the experiment and numerical computations of the elastic energy.

3.4.4 Short-pitch cholesteric hosts

At much shorter pitches, comparable to the disc diameter, fluctuations in δ are greatly facilitated and the local minimum of U_{disc} eventually switches over to $\delta = \pi/2$ suggesting discs preferentially aligning perpendicular to the director and helical axis. Taking the Rapini-Papoular contribution Eq. (3.13) as the main contribution for the weak surface anchoring regimes considered here we can extract nematic order parameters associated with such a crossover. The results, shown in Fig. 3.4.4, clearly exhibit a sharp transition from uniaxial to biaxial order at a critical pitch of about $qD \approx 3.8$ which, taking $D = 2\mu\text{m}$ would correspond to cholesteric pitch of about $p \approx 3.3\mu\text{m}$.

3.4.5 Elastic distortions around a disc

Ignoring elastic distortions we find that discs with homeotropic surface anchoring tend to orient along the grey axis, as observed in experiment (see Table 3.1). This is the obvious optimal situation that incurs the least amount of elastic distortions, compared to the other principal di-

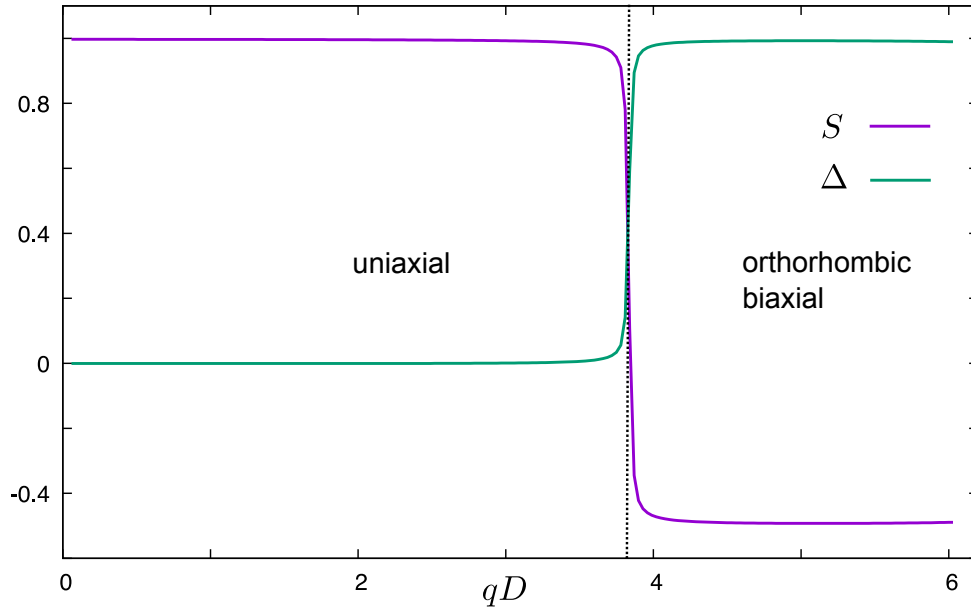


Figure 3.4.4: Nematic order parameters of discs with weakly homeotropic surface anchoring immersed in a cholesteric host with variable pitch qD . A crossover from uniaxial to orthorhombic biaxial local order occurs at around $qD \approx 3.8$.

rections in which cases the disc surface would experience strongly unfavorable tangential surface ordering. However, even when the disc normal is aligned along the local nematic director, there are local mismatches between the far-field and preferred surface director due to the weak twisting of the host director perpendicular to the disc normal (which occurs along the red axis) and when the disc normal fluctuates away from this axis. The elastic distortions are expected to be weak but they will become more outspoken at shorter pitches. It is instructive to compute the extent of these distortions along the lines of our previous analysis for rods. Let us consider an infinitely thin disc with its normal restricted to lie in the xy -plane at an angle δ away from the optimal direction indicated by the grey arrow (x -axis). The principal directions are indicated by the tripod in Fig. 3.4.5 with the xy -plane corresponding to the one spanned by the red and grey arrows. We assume weak elastic distortions χ developing in the xy -plane. Defining a host director $\hat{\mathbf{n}}_s = (\cos \Phi(x, y), \sin \Phi(x, y), 0)$ we find, assuming elastic isotropy, that the distortions are described by the Laplace equation:

$$(\partial_x^2 + \partial_y^2)\Phi = 0 \quad (3.62)$$

The effect of a twisting host director is accounted for in the surface anchoring free energy:

$$F_s = -\frac{W_0}{2} \oint d\mathcal{S} [\hat{\mathbf{n}}_s \cdot (\mathcal{R}(qz + \psi) \cdot \hat{\mathbf{n}}_0(\mathcal{S}))]^2 \quad (3.63)$$

where \mathcal{S} parameterizes the face of the disc (as previously we ignore finite thickness effects for discs with $D \gg L$) and $\hat{\mathbf{n}}_0 = (1, 0, 0)$ indicating homeotropic anchoring along the surface normal.

The rotation matrix reads:

$$\mathcal{R}(qz) = \begin{pmatrix} \cos qz & -\sin qz & 0 \\ \sin qz & \cos qz & 0 \\ 0 & 0 & 1 \end{pmatrix} \quad (3.64)$$

A key distinction with the rod case is that the distortions are not uniform across the disc surface but depend on the location of the surface element with respect to the helical axis. It is convenient to divide the disc surface into infinitely thin strips, with each surface element on the strip being equidistant from the centre-of-mass along the twist direction (z -axis) thus experiencing the same degree of elastic distortions.

For notational brevity, we implicitly normalize all lengths in units of the disc diameter D and parameterize the disc surface in terms of $y = \frac{1}{2} \cos \alpha$ and $z = \frac{1}{2} \sin \alpha$ with $-\pi < \alpha < \pi$. Each strip then has length $L_s = \cos \alpha$ and thickness $D_s = \frac{1}{2} \cos \alpha d\alpha$ and surface $ds = L_s D_s$. The surface anchoring free energy of an arbitrary strip with surface ds and centre-of-mass distance z then reads:

$$F_s^{\text{strip}} = -W_0 [\cos(\Phi(0, y) - qz - \delta)]^2 ds \quad (3.65)$$

The boundary condition at the strip located at the disc equator ($\alpha = 0$) reads:

$$\begin{aligned} \Phi(\infty, 0) &= 0 \\ \ell_s \partial_x \Phi(0, y) &= -\frac{1}{2} \sin[2(\Phi(0, y) - qz - \delta)] \\ &\approx \frac{1}{2} \sin[2(qz + \delta)] - \cos[2(qz + \delta)] \Phi(0, y) \end{aligned} \quad (3.66)$$

where we take $0 < y < 1$ for convenience. The distortions should be symmetric at the edges ($\Phi(0, 0) = \Phi(0, 1)$) and the solution of the Laplace equation is the same as for the rod considered in Section 3.4.2:

$$\Phi(x, y) = \sum_{n=1}^{\infty} e^{-n\pi x} b_n \sin(n\pi y) \quad (3.67)$$

Fortunately, the boundary condition Eq. (3.66) is the same as the linearized one for the rod (Eq. (3.58)) upon replacing $\gamma \rightarrow qz + \psi$. The same goes for the coefficients which now read:

$$b_n = \frac{\sin[2(qz + \delta)]}{\cos[2(qz + \delta)] - n\pi \ell_s} \left(\frac{1 - (-1)^n}{n\pi} \right) \quad (3.68)$$

Given that q and $-q$ do not give equivalent results we conclude that the distortions created near the disc surface carry a distinct *chiral signature* imparted by the chirality of the host LC, in agreement with the Landau-de Gennes calculations from the group of I. Smalyukh depicted in Fig. 3.4.6. The nature of the imprint depends on the twist angle ψ between the disc normal and the grey axis. We further deduce that the distortions vanish at infinitely weak surface anchoring ($\ell_s \rightarrow \infty$) and in the absence of twist and tilting ($q = 0$ and $\psi = 0$), as we expect. The elastic free energy for the total disc is given by:

$$\Delta F_{el} = \frac{\pi K D}{4} \int_{-\pi/2}^{\pi/2} d\alpha \cos \alpha \sum_n n b_n^2 \quad (3.69)$$

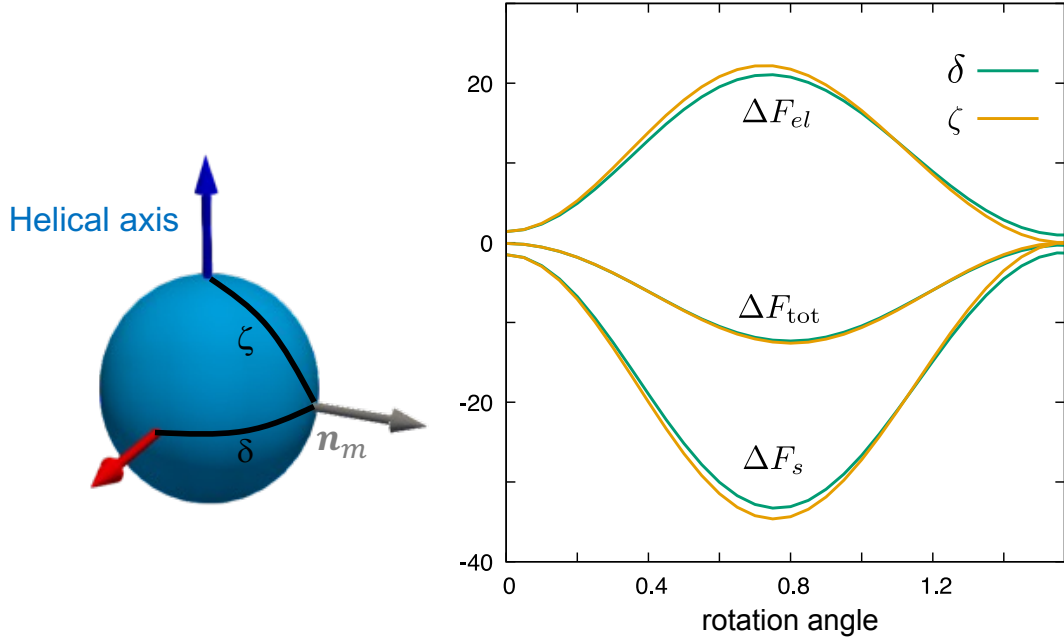


Figure 3.4.5: Distortion free energies (in units $k_B T$) around a disc immersed at an angle δ or ζ with the local host director. The distortion free energies remain relatively weak for all δ , but are most pronounced at oblique angles $\delta \sim \pi/4$. Parameters are based on the experimentally relevant situation: $qD = 0.4$ and $\ell_s/D = 3$ ($W_0 = 10^{-6} \text{ J/m}^2$).

which may be evaluated as a function of the angle ψ between the disc normal and the grey axis taking the surface anchoring extrapolation length (in units D) to be about $\ell_s \approx 3$. The change in surface anchoring free energy induced by the distortions follows from linearizing Eq. (3.65) and integrating over all strips:

$$\begin{aligned} \Delta F_s &= \frac{W_0 D^2}{2} \int_{-\pi/2}^{\pi/2} d\alpha \cos^2 \alpha \sin[2(qz + \delta)] \\ &\times \sum_n b_n \left(\frac{1 - (-1)^n}{n\pi} \right) \end{aligned} \quad (3.70)$$

We reiterate that z depends on the angle α via $z = \frac{D}{2} \sin \alpha$.

We finish our analysis by considering the case where the disc normal rotates within the xz -plane over an angle $\zeta = \frac{\pi}{2} - \theta$ away from the molecular director (grey) as indicated in Fig. 3.4.5. In this situation, the tilting will generate additional weak distortions across the z -direction that we denote by the angle χ . The spatially-dependent host director now reads:

$$\hat{\mathbf{n}}_s(\mathbf{r}) = \begin{pmatrix} \cos \Phi(\mathbf{r}) \cos \chi(\mathbf{r}) \\ \sin \Phi(\mathbf{r}) \cos \chi(\mathbf{r}) \\ \sin \chi(\mathbf{r}) \end{pmatrix} \quad (3.71)$$

with $\mathbf{r} = (x, y)$. As before each distortion angle obeys the Laplace equation in the xy -plane:

$$\begin{aligned} (\partial_x^2 + \partial_y^2) \Phi &= 0 \\ (\partial_x^2 + \partial_y^2) \chi &= 0 \end{aligned} \quad (3.72)$$

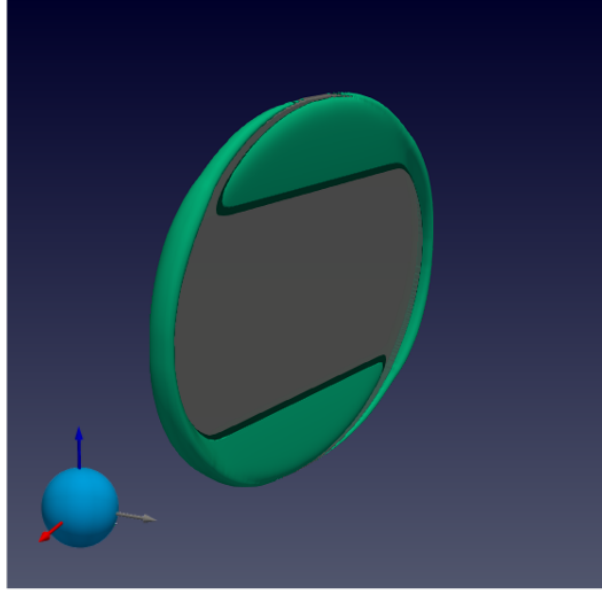


Figure 3.4.6: Computer simulation snapshot demonstrating the chiral defect structure (colored in green) around a disc with homeotropic surface anchoring immersed in a molecular cholesteric host LC. Picture courtesy of Jason Wu (University of Colorado, USA).

The surface anchoring free energy now takes the following form:

$$F_s = -\frac{W_0}{2} \oint d\mathcal{S} [\hat{\mathbf{n}}_s \cdot (\mathcal{R}_\zeta \mathcal{R}(qz) \cdot \hat{\mathbf{n}}_0(\mathcal{S}))]^2 \quad (3.73)$$

where the matrix \mathcal{R}_ζ describes a rotation of the disc normal within the xz -plane:

$$\mathcal{R}_\zeta = \begin{pmatrix} \cos \zeta & 0 & \sin \zeta \\ 0 & 1 & 0 \\ -\sin \zeta & 0 & \cos \zeta \end{pmatrix} \quad (3.74)$$

Analogous to the previous case, we may derive boundary conditions from linearizing F_s for weak distortions $\Phi \ll 1$ and $\chi \ll 1$. Plugging in the general solution [Eq. (3.67)] and defining b_n as the distortion modes pertaining to $\Phi(x, y)$ and d_n as those for $\chi(x, y)$ we find that both distortion angles are intricately coupled, as expected:

$$\begin{aligned} b_n &= c_n \cos \zeta \sin(2qz) \\ d_n &= c_n \sin(2\zeta) \cos^2(qz) \end{aligned} \quad (3.75)$$

From these we immediately assert the most basic scenarios; both distortions vanish for a disc in an achiral host ($q = 0$) at zero tilt ($\zeta = 0$), whereas at nonzero tilt angle only $\chi(d_n)$ is nonzero. For a disc immersed in a chiral host ($q \neq 0$) at zero tilt ($\zeta = 0$) we recover the previous scenario with $\Phi(b_n)$ given by Eq. (3.68) and $\chi(d_n) = 0$. Both distortion angles are expected to be nonzero in case the disc normal is tilted away from the local director of the chiral host. The

common prefactor reads:

$$c_n = \frac{2 \left(\frac{1 - (-1)^n}{n\pi} \right)}{1 + 2\ell_s n\pi - \cos(2\zeta) - 2 \cos^2 \zeta \cos(2qz)} \quad (3.76)$$

The change in elastic free energy is a simple superposition of amplitudes:

$$\Delta F_{el} = \frac{\pi KD}{4} \int_{-\pi/2}^{\pi/2} d\alpha \cos \alpha \sum_n n (b_n^2 + d_n^2) \quad (3.77)$$

The contribution arising from the host chirality turns out zero for symmetry reasons:

$$\Delta F_{chiral} = Kq \int d\mathbf{r} \partial_y \chi(x, y) = 0 \quad (3.78)$$

which is easily inferred from inserting the expansion Eq. (3.67) and integrating over y . The reduction in surface anchoring free energy caused by the distortions Φ is as follows:

$$\begin{aligned} \Delta F_{s,\Phi} &= W_0 D^2 \cos \zeta \int_{-\pi/2}^{\pi/2} d\alpha \cos^2 \alpha \sin(2qz) \\ &\quad \times \sum_n b_n \left(\frac{1 - (-1)^n}{n\pi} \right) \end{aligned} \quad (3.79)$$

supplemented with a similar contribution accounting for the distortions χ :

$$\begin{aligned} \Delta F_{s,\chi} &= W_0 D^2 \sin(2\zeta) \int_{-\pi/2}^{\pi/2} d\alpha \cos^2 \alpha \cos^2(qz) \\ &\quad \times \sum_n d_n \left(\frac{1 - (-1)^n}{n\pi} \right) \end{aligned} \quad (3.80)$$

Note the surface anchoring is always negative and should outweigh the cost in elastic free energy. The results in Fig. 3.4.5 demonstrate that elastic distortions are most developed at oblique orientations, and do not strongly depend on the direction along which the disc is tilted.

If we now reconsider the *total* alignment potential for discs accounting for corrections derived above we conclude that the ordering of the discs is hardly affected by the distortions. The free energy changes are typically several tens of $k_B T$ which is about two orders of magnitude smaller than the typical Rapini-Papoular surface anchoring free energy $W_0 D^2$ which is about $1500 k_B T$. Discs experiencing weak surface anchoring with a cholesteric host with large pitch ($qD < 1$) will therefore simply follow the local molecular director with thermal fluctuations around the optimum angle being strongly suppressed. The considerable penalty incurred by angular fluctuations away from the local cholesteric director is demonstrated in Fig. 3.4.7 for a number of different host pitches. The elastic distortions around the disc surface lead to a systematic reduction of the free energy, as expected, but their effect on the realigning properties is rather marginal. At short pitches, the disc takes on a preferred angle $\delta = \pi/2$ and aligns along the red arrow, leading to pronounced local biaxial order as highlighted in Fig. 3.4.4.

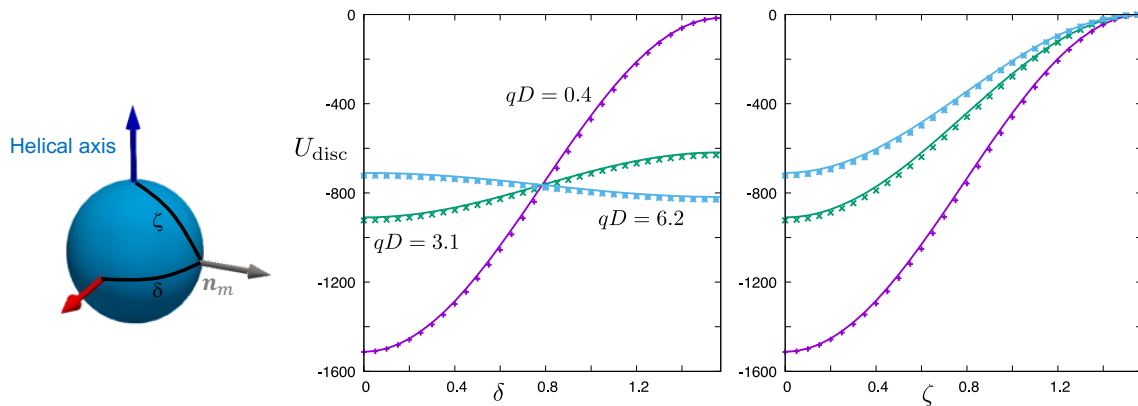


Figure 3.4.7: Free energy of a colloidal disc with weakly homeotropic surface anchoring immersed in a cholesteric host with pitch qD as a function of its orientation with respect to the local cholesteric director. Solid lines correspond to surface anchoring only [Eq. (3.13)], while the symbols denote the surface anchoring free energy including weak elastic distortions around the disc.

3.5 Conclusions

We have demonstrated that immersing uniaxial, non-chiral colloidal rods and disks into a low-molecular-weight cholesteric liquid crystal host leads to emergent biaxial order that we identify by combining experiment with numerical calculations and analytical theory. Unlike the previously studied case of hybrid molecular-colloidal biaxial phases [140, 27, 86], we observe multi-level biaxial symmetry-breaking at ultralow colloidal content where colloid-colloid interactions are negligible. By exploring a variety of colloidal shapes and surface anchoring symmetries we report biaxial order emerging at two distinct levels. First, molecular director distortions develop around each colloid which, although being of marginal extent because of weak surface anchoring conditions, display a distinct two-fold signature imparted by the cholesteric host. Second, the orientational distribution of the colloids around the local cholesteric director is demonstrated to adopt a clear biaxial signature, and the response of the corresponding biaxial order parameter is found to depend non-trivially upon the surface anchoring strength as well as the ratio of the cholesteric pitch and the principal colloidal dimension (rod length or disk diameter).

A particularly striking manifestation of biaxial symmetry-breaking is encountered for thermotropic cholesterics doped with colloidal rods with homeotropic surface anchoring. Driven by a combination of surface anchoring forces and an energy penalty incurred by twisting a weakly developed surface disclination along the rod main axis, these rods have a strong tendency to align perpendicular to both the helical axis and the local cholesteric director, thus imparting a two-fold D_{2h} orientational symmetry onto the hybrid system at each point along the cholesteric helix. By means of a simple mean-field theory based on the Rapini-Papoular surface anchoring energy combined with an analytical elasticity theory addressing the corresponding elastic distortions incurred by the presence of the colloids, we have revealed that the multi-level expression of emergent biaxiality in our systems is essentially a single-colloid effect that can be achieved in a wide variety of cholesteric systems doped with non-isotropic colloids. The next chapter will deal with possible scenarios that could arise when the colloid concentration is no longer negligible,

and direct correlations between the colloids interfere with the surface anchoring effects discussed in this chapter.

Chapter 4

Bi-helical order and demixing in hybrid chiral LCs

Abstract

We extend Onsager's theory to the case of hybrid molecular liquid crystals (LC) composed of colloidal particles immersed in thermotropic host. This framework enables us to explore colloid concentrations that are no longer infinitely small. Correlations between the colloids cause additional entropic and elastic contributions that interfere with surface anchoring effects explored in the previous chapter. We consider two distinct regimes, namely weak coupling where surface anchoring only marginally impacts the colloid orientations and strong coupling where the typical realignments energy strongly exceeds the thermal energy. We demonstrate at weak coupling that collective colloidal effects driven by steric colloid-colloid interaction may lead to liquid-liquid phase separation between two biaxial fluid phases. In the strong coupling regime, we argue that elastic force may facilitate the formation of bi-helical states where the helical organization of the colloidal and molecular components is unequal in pitch and even in handedness.

4.1 Introduction

In the previous chapter we have studied ordering of colloidal particles in so-called hybrid chiral liquid crystals composed of colloidal particles immersed in a low-molecular-weight cholesteric LC. Inspired by experimental work, we restricted our attention to the regime of low colloidal content where the principal ordering effect stems from single colloid properties related to surface anchoring and elastic distortions formed around the colloid surface. In this regime, the average interparticle distance remains sufficiently large to guarantee that direct interactions between colloids, mediated by steric collisions or guided by some interference of surface defects, are unimportant. Raising the concentrations of colloids, which has not been pursued in experiment thus far, offers interesting perspectives to explore the interplay between surface anchoring and alignment driven by colloid-colloid interactions as well as the role of (twist) elastic forces imparted by steric correlations between the colloids. In this chapter we generalize Onsager's theory suitably adapted to treat spatially non-uniform director field such as in a cholesteric, to explore

the ordering of colloids at large concentrations where entropic and elastic contributions imparted by the colloids play a role. In doing so we consider two extreme cases, namely weak coupling where colloid realignment caused by surface anchoring forces is weak, and strong coupling where such realignment is strong compared to the typical thermal fluctuations the colloid experiences. We highlight two main effects: (i) surface-anchoring-driven phase separation between two orthorhombic liquids at weak surface anchoring coupling and (ii) the formation of bi-helical chiral hybrid liquid crystals at large coupling strength. Since the latter case should occur for both rods and discs alike, exploring mixed molecular-colloidal LCs with inherent chirality opens up ways to create chiral fluids composed of discotic mesogens [149, 150].

4.2 Second-virial density functional

With the single-colloid properties fully specified in the previous chapter, we now proceed towards describing the many-particle system by invoking a simple Onsager-type density functional theory [15]. The grand potential Ω of an assembly of colloids in the presence of an external potential reads in general form [30]:

$$\begin{aligned} \Omega[\rho] = & \int d\mathbf{r}d\hat{\mathbf{u}}\rho(\mathbf{r}, \hat{\mathbf{u}}) [k_B T \ln \mathcal{V}\rho(\mathbf{r}, \hat{\mathbf{u}}) + U_{\text{ext}}(\mathbf{r}, \hat{\mathbf{u}}) - \mu] \\ & - \frac{k_B T}{2} \int d\mathbf{r}d\hat{\mathbf{u}} \int d\mathbf{r}'d\hat{\mathbf{u}}' \rho(\mathbf{r}, \hat{\mathbf{u}})\rho(\mathbf{r}', \hat{\mathbf{u}}') \Phi(|\mathbf{r} - \mathbf{r}'|, \hat{\mathbf{u}}, \hat{\mathbf{u}}') \end{aligned} \quad (4.1)$$

with \mathcal{V} denoting an effective thermal volume comprising contributions from rotational momenta and μ a chemical potential that controls the overall colloid concentration. The first contribution describes an ideal gas of non-interacting colloids while the second accounts for colloid-colloid interaction on the second-virial level. Here, the key input is the Mayer function Φ that, assuming the colloid interactions to be purely hard, renders minus unity if the cores of two colloids overlap and zero if they do not.

We assume that the colloid positions remain randomly distributed. The orientational probability, however, will be affected by a helical rotation of the colloidal director field $\hat{\mathbf{n}}(z)$. Since the cholesteric pitch $\lambda \approx 30\mu m$ is about an order of magnitude larger than the typical colloidal size (a few μm), the colloidal director is completely enslaved to the rotation of the local cholesteric director and adopts the same pitch length λ . A $\pi/2$ phase shift between the colloidal director $\hat{\mathbf{n}}(z)$ and the cholesteric one $\hat{\mathbf{n}}_s(z)$ may occur under certain anchoring conditions as we observe in Figs. 1 and 2. This scenario may no longer hold at larger colloid concentrations and/or shorter cholesteric pitches where the twist elasticity of the colloids becomes considerable, as we will contemplate in a later section. Let us proceed by parameterizing the one-body density in terms of an overall density $\rho = N/V$ and an orientational probability that explicitly depends on the position z along the helix:

$$\rho(\mathbf{r}, \hat{\mathbf{u}}) = \rho f_q(\hat{\mathbf{u}} \cdot \hat{\mathbf{n}}(z)) \quad (4.2)$$

In order to elaborate the grand potential we parameterize the system volume in cylindrical coordinates $d\mathbf{r} = d\mathbf{r}_\perp dz$ with $0 < |r_\perp| < \infty$ and $0 < z < 2\pi/q$. Given that the overall rod density is prescribed, the grand potential becomes a Helmholtz free energy F . The ideal

(translation plus orientation) entropy free energy per unit volume follows from:

$$\frac{\beta F_{\text{id}}}{V} = \int d\hat{\mathbf{u}} \int_0^{2\pi} \frac{d(qz)}{2\pi} f_q(\hat{\mathbf{u}} \cdot \hat{\mathbf{n}}(z)) \ln[\mathcal{V}\rho f_q(\hat{\mathbf{u}} \cdot \hat{\mathbf{n}}(z))] \quad (4.3)$$

Since the orientational distribution does not change along the cholesteric director the ideal free energy density simplifies into the conventional form:

$$\frac{\beta F_{\text{id}}}{V} = \rho \int d\hat{\mathbf{u}} \ln[\mathcal{V}\rho f_q(\hat{\mathbf{u}} \cdot \hat{\mathbf{n}})] f_q(\hat{\mathbf{u}} \cdot \hat{\mathbf{n}}) \quad (4.4)$$

with $\hat{\mathbf{n}}$ denoting the local director along the helix. Similarly, the external potential in Eq. (4.1) is associated to the surface anchoring free energy obtained from the Rapini-Papoular expression Eq. (3.3). It is defined in the angular coordinates $\hat{\mathbf{u}}(\theta, \delta)$ that co-rotate with the helical director so that:

$$\frac{F_s}{V} = \rho \int d\hat{\mathbf{u}} f_q(\hat{\mathbf{u}} \cdot \hat{\mathbf{n}}) F_s(\hat{\mathbf{u}}) \quad (4.5)$$

Next, we introduce a linear coordinate transformation $z' = z + \Delta z$ and write the excess free energy as follows:

$$\begin{aligned} \frac{\beta F_{\text{ex}}}{V} &= \frac{\rho^2}{2} \int_0^{2\pi} \frac{d(qz)}{2\pi} \int d\hat{\mathbf{u}} \int d\hat{\mathbf{u}}' f_q(\hat{\mathbf{u}} \cdot \hat{\mathbf{n}}(z)) \\ &\quad \times \int_{-\lambda}^{\lambda} d\Delta z \mathcal{A}(|\Delta z|, \hat{\mathbf{u}}, \hat{\mathbf{u}}') f_q(\hat{\mathbf{u}}' \cdot \hat{\mathbf{n}}(z + \Delta z)) \end{aligned} \quad (4.6)$$

where \mathcal{A} is an orientation-dependent excluded *area* of rod or disc. The excess free energy is non-local since it depends on volume exclusion between a reference particle at z and test particle at $z + \Delta z$ over which the local director will have rotated. It is therefore expedient to apply a transformation $\hat{\mathbf{u}}' \rightarrow \mathcal{R}(q\Delta z)\hat{\mathbf{u}}'$ which projects the orientation of the test colloid into the director frame of the reference one located at z via the rotation matrix:

$$\mathcal{R}(q\Delta z) = \begin{bmatrix} \cos(q\Delta z) & \sin(q\Delta z) & 0 \\ -\sin(q\Delta z) & \cos(q\Delta z) & 0 \\ 0 & 0 & 1 \end{bmatrix}$$

This renders the excess free energy local so that it may be simplified into a compact form:

$$\frac{\beta F_{\text{ex}}}{V} = \frac{\rho^2}{2} \int d\hat{\mathbf{u}} \int d\hat{\mathbf{u}}' f_q(\hat{\mathbf{u}} \cdot \hat{\mathbf{n}}) f_q(\hat{\mathbf{u}}' \cdot \hat{\mathbf{n}}) \mathcal{K}_q(\hat{\mathbf{u}}, \hat{\mathbf{u}}') \quad (4.7)$$

in terms of an excluded volume that takes into account the helical rotation of the director field:

$$\mathcal{K}_q(\hat{\mathbf{u}}, \hat{\mathbf{u}}') = \int_{-\lambda}^{\lambda} d\Delta z \mathcal{A}(|\Delta z|, \hat{\mathbf{u}}, \mathcal{R}(q\Delta z)\hat{\mathbf{u}}') \quad (4.8)$$

This clearly represents a highly convoluted object that we were only able to analyze analytically for thin hard rods, as discussed in the Appendix. As alluded to before, in the experimental situation the director twist is weak on the scale of the typical colloid size and it is justified to

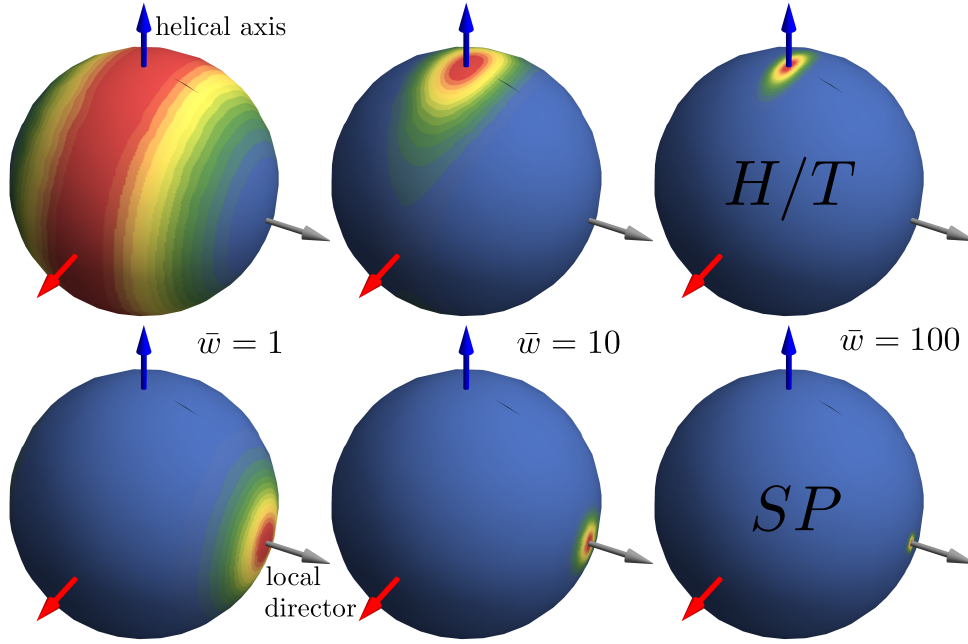


Figure 4.2.1: Unit-sphere projections of the local orientational probability of rods immersed in a low molecular-weight cholesteric phase at different surface anchoring strengths $\bar{w} = \beta W_0 L D$, in the presence of a low-correlated colloidal liquid crystal composed by particles of the same kind. The rod concentration represented here is $c = \rho L^2 D = 3$ which corresponds to an isotropic bulk system in the absence of surface anchoring. For all distributions, the rod-length-to-pitch is $qL = 1$.

assume

$$\mathcal{K}_q(\hat{\mathbf{u}}, \hat{\mathbf{u}}') \approx \mathcal{K}_0(\hat{\mathbf{u}}, \hat{\mathbf{u}}') = v_0 |\sin \gamma| \quad (4.9)$$

which corresponds to the conventional excluded volume between two (infinitely) thin hard rods ($v_0 = 2L^2 D$) or discs ($v_0 = \frac{\pi}{2} D^3$), as per Onsager's original theory [15]. This approximation ignores any twist elastic resistance imparted by the colloids and should hold only for low to moderate colloid concentrations and weak director twist ($\lambda \gg L$ or D). The effect of finite twist elasticity will be considered in an upcoming Section.

Combining all free energy contributions and formally minimizing the Helmholtz free energy with respect to f_q yields a Boltzmann distribution similar to Eq. (3.8):

$$f_q(\hat{\mathbf{u}}) = \mathcal{N} \exp \left(-\beta F_s(\hat{\mathbf{u}}) - \rho \int d\hat{\mathbf{u}}' f_q(\hat{\mathbf{u}}') \mathcal{K}_0(\hat{\mathbf{u}}, \hat{\mathbf{u}}') \right) \quad (4.10)$$

which reduces to the ideal gas probability Eq. (3.8) for vanishing rod density $\rho = 0$ as it should. The above condition needs to be solved iteratively for a given combination of dimensionless parameters pertaining to the rods (discs), namely the cholesteric pitch qL (qD), surface anchoring strength $\beta W_0 L D$ ($\beta W_0 D^2$) and colloid concentration $c = \rho L^2 D$ (ρD^3). Possible phase transitions can be probed from the osmotic pressure $\Pi \equiv \partial F / \partial V|_{N,T}$ and chemical potential

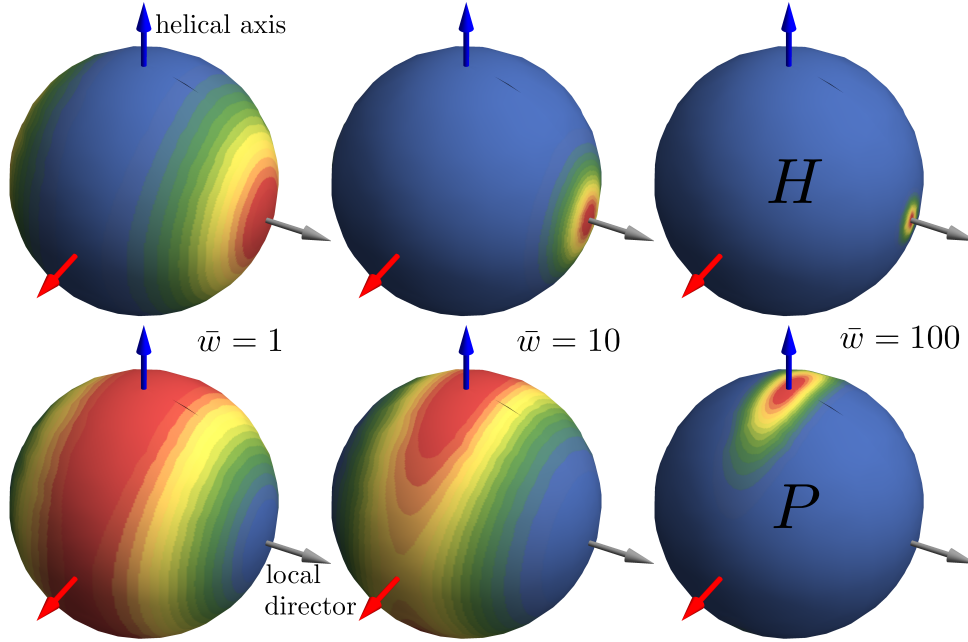


Figure 4.2.2: Unit-sphere projections of the local orientational probability of discs immersed in a low molecular-weight cholesteric phase at different surface anchoring strengths $\bar{w} = \beta W_0 D^2$, in the presence of a low-correlated colloidal liquid crystal composed by particles of the same kind. The disc concentration represented here is $c = \rho D^3 = 3$ which corresponds to an isotropic bulk system in the absence of surface anchoring. For all distributions, the disc-size-to-pitch is $qD = 1$.

$\mu \equiv \partial F / \partial N|_{V,T}$ which read:

$$\begin{aligned} \beta \Pi &= \rho + \frac{\rho^2}{2} \langle \langle \mathcal{K}_0(\hat{\mathbf{u}}, \hat{\mathbf{u}}') \rangle \rangle_{f_q} \\ \beta \mu &= \ln[\rho v_0] + \langle \ln[f_q(\hat{\mathbf{u}})] + \beta F_s(\hat{\mathbf{u}}) \rangle_{f_q} + \rho \langle \langle \mathcal{K}_0(\hat{\mathbf{u}}, \hat{\mathbf{u}}') \rangle \rangle_{f_q} \end{aligned} \quad (4.11)$$

The brackets are shorthand for an orientational average $\langle \cdot \rangle_{f_q} = \int d\hat{\mathbf{u}} f_q(\hat{\mathbf{u}}) (\cdot)$ measured with respect to the local director.

4.3 Orthorhombic liquid-liquid phase separation

In the absence of surface anchoring realignment ($\bar{w} = 0$) the colloids undergo a conventional isotropic-uniaxial nematic transition. This is the classic Onsager scenario where an isotropic (I) phase ($c_I = 4.19$, $S_I = 0$) coexists with a (uniaxial) nematic phase ($c_N = 5.34$, $S_N = 0.792$). For $\bar{w} > 0$ the $O(3)$ symmetry of the isotropic phase and the uniaxial $D_{\infty h}$ symmetry of the nematic will both be broken in favour of a biaxial, orthorhombic symmetry (D_{2h}), and a coexistence between two orthorhombic phases with different overall colloidal concentrations is expected. Resolving the coexistence conditions by imposing equality of chemical potential μ and pressure Π in both phases we may explore phase diagrams in the surface anchoring amplitude - colloid concentration ($\bar{w} - c$) plane. The results are shown in Fig. 4.3.1 and demonstrate that a phase coexistence between two orthorhombic nematic phases is indeed possible in the weak coupling

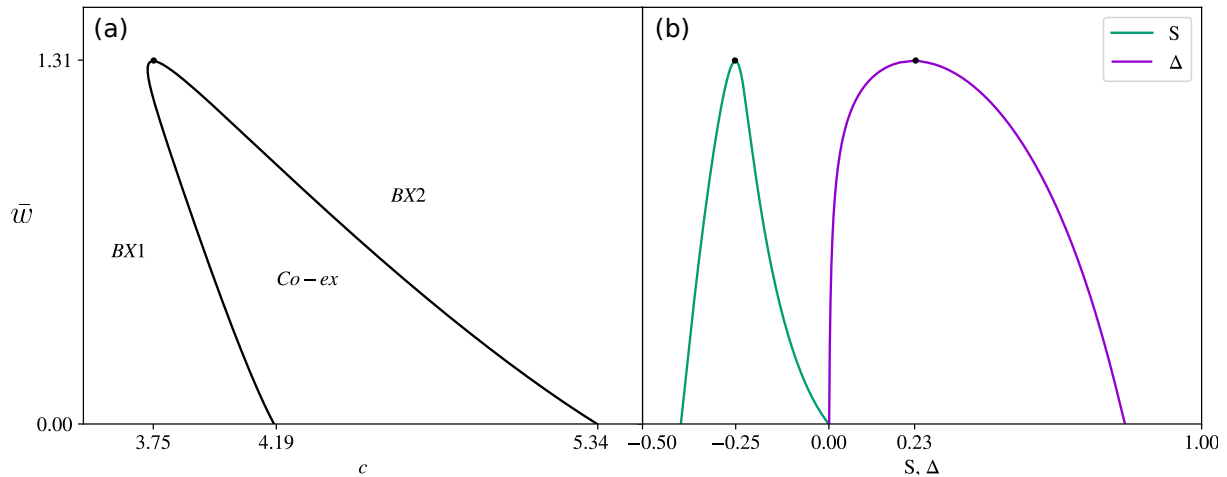


Figure 4.3.1: (a) $\bar{w} - c$ phase diagram for rods with homeotropic or tangential surface anchoring, $qL = 0.335$. (b) Corresponding uniaxial (green) and biaxial (purple) nematic order. A qualitatively equivalent scenario can be found for discs with planar surface anchoring.

regime ($\bar{w} < 1$). A critical point beyond which no phase transition is possible is located at a surface anchoring energy equivalent to a few times the thermal energy.

The scenario depicted in Fig. 4.3.1 is qualitatively similar to the paranematic-nematic transition proposed by Khokhlov and Semenov [151] and analyzed in subsequent studies on nematic fluids exposed to external orientational fields [152, 153, 154, 155]. In our situation, however, both states have a distinct biaxial symmetry rather than uniaxial. Furthermore, the external field is represented by a temperature-controlled surface anchoring contribution represented by the surface anchoring energy F_s in Eq. (4.10), which is different from the diamagnetic response of the colloids when subjected to an external magnetic field [154, 155]. A key condition for experimental realization of the demixing phenomenon is that the surface anchoring remains ultraweak such that the effective realignment strength \bar{w} imparted by the surface anchoring forces does not exceed a few times the thermal energy. Given that $\bar{w} = W_0LD$ scales with the bare colloidal dimensions (length L and diameter D) this could be achieved simply by reducing the length of the colloid rod at fixed (bare) surface anchoring strength W_0 .

4.4 Effect of colloid-induced elasticity

At certain conditions such as strong surface-anchoring coupling and large colloid concentration ρ and short cholesteric pitches the twist elastic resistance generated by the anisotropic colloid-colloid repulsions will prevent the colloidal director from keeping pace with the rotation of the cholesteric director. This may give rise to hybrid systems in which the colloidal director locally deviates from the cholesteric helix. Let us attempt to explore this scenario in more detail starting from the cholesteric director field Eq. (3.1) that we keep fixed in the laboratory frame. In doing so, we rely on three further basic assumptions; (i) the colloids remain uniformly distributed throughout the system and do not affect the cholesteric helix whose pitch q remains unaffected, (ii) the colloids are perfectly aligned and exhibit negligible thermal fluctuations around their main orientation, and (iii) the colloidal director remains perpendicular to

the helical axis $\hat{\mathbf{z}}$ but we allow the degree of local twist to be non-uniform along the z -direction. We then parameterize the colloidal director as follows:

$$\hat{\mathbf{n}}(z) = \hat{\mathbf{x}} \cos \phi(z) + \hat{\mathbf{y}} \sin \phi(z) \quad (4.12)$$

in terms of a local twist angle $\phi(z)$. Since the system is apolar, the director $\hat{\mathbf{n}}$ is equivalent to $-\hat{\mathbf{n}}$ so that $\phi(z)$ is equivalent to $\phi(z) + \pi$. For the cases discussed thus far, the colloidal director is simply co-helical with the cholesteric so that $\phi(z) = qz \pmod{\pi}$.

4.4.1 Rods

Let us focus first on the case of rods. The fraction of rods aligned along the helical axis $\hat{\mathbf{z}}$ (as observed in Fig. 4.2.1) may be disregarded as they contribute very little to the twist elastic resistance imparted by the colloids. Since we assume that the rods are perfectly aligned along the above director we write the rod contour $\mathbf{r}_S(t) = \mathbf{r}_0 + \frac{L}{2}t\hat{\mathbf{n}}(z)$ and applying this in the Rapini-Papoular expression Eq. (3.3) along with the above parameterization we find:

$$F_s[\phi(z)] = -\frac{1}{8}W_0LD \begin{cases} 2\pi \sin^2[\phi(z) - qz] & \text{H/T} \\ 4\pi \cos^2[\phi(z) - qz] & \text{SP} \end{cases} \quad (4.13)$$

In the absence of twist elastic effects the surface anchoring energy is indeed minimized along a uniform twist profile $\phi(z) = qz + \phi_0$ with phase shifts $\phi_0 = \pi/2$ (H/T) and $\phi_0 = 0$ (SP) as evident from the result in Fig. 4.2.1 and Fig. 4.2.2.

The (continuum) free energy per unit area reflects a competition between the surface anchoring energy, and a restoring (twist) elastic energy:

$$\frac{F}{A} = \int dz \left\{ \rho F_s[\phi(z)] + \frac{K_2}{2} (\hat{\mathbf{n}}(z) \cdot \partial \times \hat{\mathbf{n}}(z))^2 \right\} \quad (4.14)$$

with K_2 the twist elastic modulus of a colloidal nematic system. Removing the trivial phase angle by rescaling $\phi(z) \rightarrow \phi(z) - \phi_0$ and some further basic manipulation we obtain a universal expression for both anchoring scenarios:

$$\frac{F}{A} = \int dz \left\{ -\sigma \cos^2[\phi(z) - qz] + \frac{K_2}{2} (\partial \phi(z))^2 \right\} \quad (4.15)$$

in terms of surface anchoring energy density $\sigma_{\text{HT}} = \frac{\pi}{4}\rho W_0LD$ and $\sigma_{\text{SP}} = 2\sigma_{\text{HT}}$ for the SP case. The corresponding Euler-Lagrange equations reads:

$$K_2\phi''(z) - \sigma \sin[2(\phi(z) - qz)] = 0 \quad (4.16)$$

subject to the boundary conditions $\phi(0) = 0$ and $\phi'(0) = 0$, i.e., the colloids are kept non-chiral. The effect of chirality will be considered in a subsequent paragraph. It is convenient to introduce a non-linear twist angle $\varepsilon(z) = \phi(z) - qz$ which measures the local deviation of the colloidal director from the cholesteric one. Both anchoring situations can then be described by

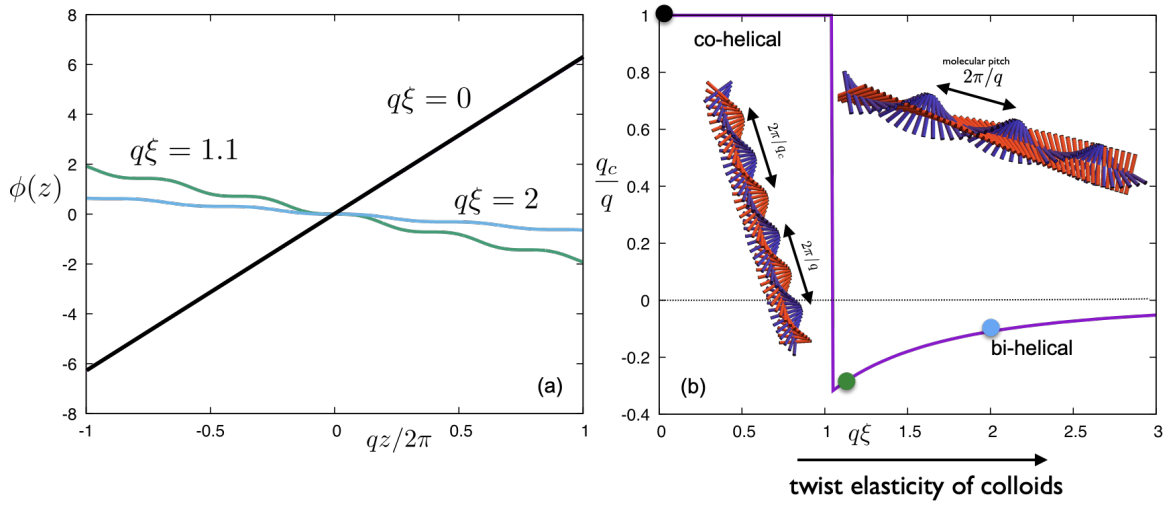


Figure 4.4.1: (a) Twist angle $\phi(z)$ of the colloidal director along the helical direction for different strengths of the twist elasticity of the colloids. At weak twist elasticity ($q\xi < 1$) the colloidal director remains co-helical with the cholesteric helix. At $q\xi > 1$ unwinding of the colloidal helix occurs with “breathing” instabilities. (b) Evolution of the pitch q_c of the colloidal helix with respect to the cholesteric pitch q . Note that in the bi-helical regime the cholesteric and colloidal helices have opposite handedness. The colloidal helix is shown in red, the molecular one in blue. Colored dots indicate the state-point corresponding to the breathing profiles in (a).

a sine-Gordon equation:

$$\xi^2 \varepsilon''(z) = \sin[2\varepsilon(z)] \quad (4.17)$$

It features the following length scale:

$$\xi = \sqrt{\frac{K_2}{\sigma}} \quad (4.18)$$

The solution under is non-analytical and can be written in terms of (inverse) elliptic functions:

$$\phi(z) = qz - \text{am}(qz, -2/(q\xi)^2) \quad (4.19)$$

with $\text{am}(x, k)$ denoting the Jacobi amplitude function which has the known limit $\text{am}(x, 0) = x$. From this we conclude that an untwisted director profile $\phi(z) = 0$ is found at infinite elasticity $q\xi \rightarrow \infty$, as should be the case. At large but finite $q\xi$ the colloidal helix unwinds with respect to the cholesteric and adopts an (average) pitch $q_c < q$, leading to a bi-helical hybrid system. This scenario is depicted in Fig. 4.4.1. Interestingly, at $q\xi > 1$ the colloidal helix not only unwinds, it also adopts a handedness that is opposite that of the cholesteric helix. Associated with the unwound colloidal director are periodic “breathing” fluctuations whose amplitude and period are shown in Fig. 4.4.2. These fluctuations are easily fitted to a periodic profile so that (for $q\xi > 1$):

$$\phi(z) - q_c z \approx \delta\phi e^{iq_b z} \quad (4.20)$$

in terms of an amplitude $\delta\phi$ and periodicity q_b . The amplitude slowly decays as $q\xi \rightarrow \infty$ while the breathing periodicity attains a constant value $q_b/q \rightarrow 2$.

Another common solution that is associated with the sine-Gordon equation is the soliton.

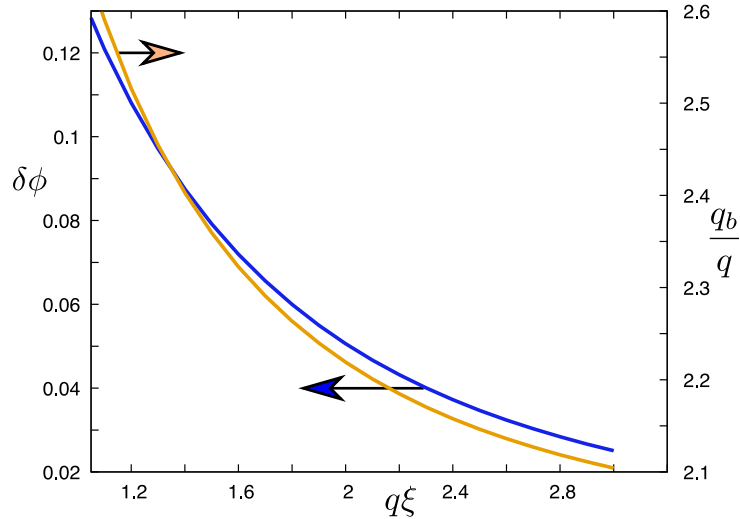


Figure 4.4.2: Amplitude $\delta\phi$ and periodicity q_b of the “breathing” instabilities encountered in the bi-helical state in Fig. 4.4.1b as a function of the twist elastic strength $q\xi$.

Taking the boundary conditions $\varepsilon'(\pm\infty) = 0$ and $\varepsilon(\infty) - \varepsilon(-\infty) = \pi$. The solution for the single soliton can be obtained in analytical form [156]:

$$\phi(z) = qz \pm \frac{\pi}{2} \pm 2 \arctan \left[\tanh \left(\frac{z - z_0}{R_s} \right) \right] \quad (4.21)$$

where $R_s = 2^{1/2}\xi$ defines the soliton width and z_0 the arbitrary position of its centre along the cholesteric helix. The $-$ solution refers to an anti-soliton. In achiral liquid crystals such as our colloidal subsystem, the (anti-)solitons are unstable with respect to the uniform background (i.e. the co-helical state). The dimensionless free energy difference between the soliton and the co-helical state is $\frac{\Delta F q}{A\sigma} = q\xi(2^{3/2} + \pi q\xi)$. However, once they are formed the solitons are metastable and cannot simply relax to the co-helical state without locally destroying nematic order.

From the scaling expression Eq. (4.31) for the twist elastic constant of rods proposed in the Appendix we find that the soliton width $\sim \xi$ is independent of rod concentration. However, the solitons would be unrealistically small as ξ turns out to be of the same scale as the width of the individual rods, namely $\xi \sim 70\text{nm}$ for long rods ($L \sim 3\mu\text{m}$ and $D \sim 30\text{nm}$ and $W_0 = 10^{-5}\text{J/m}^2$).

4.4.2 Effect of rod chirality

It is well known that conventional (non-hybrid) chiral liquid crystals subject to a uniform electromagnetic field perpendicular to the helical axis may form stable solitons provided that the nematogens are sufficiently chiral [157, 158, 136]. In fact, our rods must have some intrinsic chirality in view of the decoration of helical disclinations imparted by the cholesteric environment, as demonstrated in the previous chapter. The effect of chirality is easily accounted for by an additional free energy [39]:

$$\frac{F_{\text{chiral}}}{A} = K_t \int dz (\hat{\mathbf{n}}(z) \cdot \partial \times \hat{\mathbf{n}}(z)) = K_t \int dz (\partial\phi(z)) \quad (4.22)$$

with K_t denoting the strength of the chiral interactions between the rods. It is customary to identify $K_t = q_r K_2$ where q_r would be the pitch of a chiral nematic formed by the rods *alone*. In general, q_r differs from the pitch q of the cholesteric helix q although a subtle coupling between the two is expected. We stress that q_r is a purely hypothetical variable since the rods would not be chiral in the absence of surface anchoring effects imparted by the cholesteric solvent. Since the chiral contribution is linear in the gradient of ϕ , the Euler-Lagrange equation Eq. (4.16) associated with the total free energy remains unchanged. The boundary conditions now read $\phi(0) = 0$ and $\phi'(0) = q_r$. If we assume the handedness of the rods to be the same as that of the cholesteric environment, then the main effect of colloid chirality is that the co- to bi-helical transition shifts towards larger $q\xi$. This is a natural consequence of the fact that chirality favors the twisted co-helical state over the (partially) untwisted bi-helical one. Of course, the reverse effect occurs if the rods adopt a handedness that is opposite to that of the cholesteric state ($q_r < 0$). Then, the transition to the bi-helical state in Fig. 4.4.1b systematically shifts to smaller $q\xi$ upon increasing the chiral strength $|q_r|$.

The free energy between the soliton and the co-helical state now reads $\frac{\Delta F q}{A\sigma} = q\xi[2^{3/2} + \pi q\xi(1 - \frac{q_r}{q})]$. This means that solitons may eventually become stable within the co-helical regime if $\frac{q_r}{q} > 1 + \frac{2^{3/2}}{\pi q\xi}$ which implies that the rods must be very strongly chiral indeed. However, the soliton width is not affected by chirality and remains of the order of the colloid thickness which means that the solitons remain a purely hypothetical scenario, at least within our simple coarse-grained model.

4.4.3 Discs

The case of discs proceeds in an analogous way. If we assume the same set of basic approximations to hold for the colloidal discs as well, we may start with computing the surface anchoring free energy which takes a simple form (ignoring irrelevant constants):

$$F_s[\phi(z)] = \begin{cases} -\sigma_H \cos^2[\phi(z) - qz] & \text{H} \\ -\sigma_P \sin^2[\phi(z) - qz] & \text{P} \end{cases} \quad (4.23)$$

with $\sigma_H = \frac{\pi}{4}\rho W_0 D^2 \frac{J_1(qD)}{qD}$ and $\sigma_P = \frac{1}{2}\sigma_H$ describing the two basic anchoring symmetries we consider. Comparing with Fig. 3.2.3 we immediately identify the optimal profile $\phi(z) = qz + \phi_0$ with $\phi_0 = 0$ (H) and $\phi_0 = \frac{\pi}{2}$ (P) at least for weak to moderate cholesteric pitch $qD < 2$. Clearly, since the surface anchoring energy has the same basic form as those previously discussed in Eq. (4.13) for rods, the director profiles are identical too, provided the lengthscale $\xi = \sqrt{K_2/|\sigma|}$ is taken to be the one appropriate for discs. Using the scaling expression from the Appendix, we find:

$$\xi \sim 0.87c \sqrt{\frac{|q|D}{J_1(|q|D)}} \sqrt{\frac{k_B T}{W_0}} \quad (4.24)$$

which yields about $\xi \approx 80nm$ for $D = 2\mu m$ sized discs studied experimentally at a concentration $c = \rho D^3 = 3$, $W_0 = 10^{-5} J/m^2$ and a cholesteric pitch length of $30\mu m$ corresponding to $qD \approx 0.6$.

For certain values of qD the surface anchoring amplitude σ may become negative ($\sigma < 0$).

In those cases, the phase angles associated with the two anchoring scenarios are simply swapped so that $\phi = \frac{\pi}{2}$ (P) and $\phi_0 = 0$ (P). By rescaling $\phi(z) \rightarrow \phi(z) - \phi_0$ we obtain the same Euler-Lagrange equation Eq. (4.16) with $\sigma \rightarrow |\sigma|$.

4.5 Conclusions and outlook

In this chapter we have theoretically addressed the implications of finite colloid concentration in self-organization of hybrid colloidal-molecular liquid crystals. While at low colloid content the orientation of each colloid is mainly driven by single-particle effect related to surface anchoring and possible surface defects, the phenomenology becomes richer and exciting when colloid-colloid interactions are taken into account. We argue that steric combined with weakly aligning surface anchoring forces may drive liquid-liquid phase separation between two orthorhombic fluids, each with a different colloid concentration and orientational order parameters. This scenario bears some resemblance to the paranematic-nematic phase transition of elongated colloids in external fields put forward decades ago by Khokhlov and Semenov [151]. In the strong coupling regime, when surface-anchoring-mediated particle realignment are no longer overcome by thermal energy, the colloids impart non-negligible twist elasticity that may stabilize a variety of different bi-helical hybrid LCs in which both molecular and colloidal self-organize along distinctly different helical mesostructures. We also predict the typical colloidal concentration needed to stabilize these structures in experiment.

At elevated colloid concentration additional interactions could become more prominent, for instance those imparted by surface defects and long-range electrostatic forces owing to surface charges residing on the colloids, which will have an impact on the elastic properties generated by the colloids. In fact, one could naively argue that these could give rise to a significant stiffening of the elastic moduli of the colloidal subcomponent which could lead to a stabilization of bi-helical structures at much lower colloid concentrations than anticipated here. Clearly, any further quantitative prediction requires a considerable refinement of our analysis beyond the simple steric model considered here.

Appendices

Appendix 4.A Twist elastic resistance of thin hard needles and discs

For hard rods a tractable analytical expression for the z -resolved excluded area is available in the needle limit $L/D \rightarrow \infty$ [159, 160]:

$$\begin{aligned} \mathcal{A}(|\Delta z|, \hat{\mathbf{u}}, \hat{\mathbf{u}}') &= - \int d\Delta \mathbf{r}_\perp \Phi(|\Delta \mathbf{r}|, \hat{\mathbf{u}}, \hat{\mathbf{u}}') \\ &= 2L^2 D |\sin \gamma| \begin{cases} 0 & |\Delta z| > A + B \\ \frac{A+B-|\Delta z|}{4AB} & A - B \leq |\Delta z| \leq A + B \\ \frac{1}{2A} & |\Delta z| < A - B \end{cases} \end{aligned} \quad (4.25)$$

with $A = \frac{L}{2} |\max(u_z, u'_z)|$ and $B = \frac{L}{2} |\min(u_z, u'_z)|$. We can make headway by realizing that a rotation of the reference director only affects the azimuthal angle φ . More specifically we have $\mathcal{R}(q\Delta z) |\sin \gamma| = \sqrt{1 - (\cos \theta \cos \theta' - \sin \theta \sin \theta' \cos(\Delta\varphi - q\Delta z))^2}$ with $\Delta\varphi = \varphi - \varphi'$. Performing the integration over Δz we can cast the kernel as a Taylor series in terms of even powers of the colloidal pitch qL :

$$\mathcal{K}_q(\hat{\mathbf{u}}, \hat{\mathbf{u}}') = 2L^2 D \sum_{n=0}^{\infty} \frac{(qL)^{2n}}{2n!} a_{2n}(\hat{\mathbf{u}}, \hat{\mathbf{u}}') \quad (4.26)$$

Note that odd powers in q must vanish since the rods are considered to be achiral. We note that the immersed rods induce weak distortions of the solvent director which are known to adopt a helical signature that could render the rod-rod interaction chiral. The angle-dependent factor reads in explicit form:

$$\begin{aligned} a_{2n}(\hat{\mathbf{u}}, \hat{\mathbf{u}}') &= \frac{(\frac{1}{2}u_z + \frac{1}{2}u'_z)^{2n+2} - (\frac{1}{2}u_z - \frac{1}{2}u'_z)^{2n+2}}{u_z u'_z (2n+1)(n+1)} \\ &\quad \times \frac{\partial^{(2n)} |\sin \gamma|_{q=0}}{\partial \Delta\varphi^{(2n)}} \end{aligned} \quad (4.27)$$

and it is easily verified that $a_0 = |\sin \gamma|$ as required. It is insightful to express the excess free energy per unit volume in the following way:

$$\frac{F_{ex}}{V} = k_B T \frac{\rho^2}{2} \langle \langle \mathcal{K}_0(\hat{\mathbf{u}}_1, \hat{\mathbf{u}}_2) \rangle \rangle_{f_q} + \sum_{n=1}^{\infty} \frac{q^{2n}}{2n!} K_2^{(2n)} \quad (4.28)$$

The quantities $K_2^{(2n)}$ could be interpreted as *generalized* twist elastic constants defined as:

$$K_2^{(2n)} = k_B T \rho^2 L^{2n+2} D \langle \langle a_{2n}(\hat{\mathbf{u}}_1, \hat{\mathbf{u}}_2) \rangle \rangle_{f_q} \quad (4.29)$$

for most conventional cholesteric phases the director twist is weak on the scale of the rod ($qL < 1$) and the expansion may be truncated after the second term. Furthermore, the orientation distribution is unaffected by any director twist so that f_q can be approximated by the orientation distribution f_0 of a non-chiral uniaxial nematic phase. The quantity $K_2^{(2)}$ is then identified as the conventional twist elastic constant for which the microscopic definition reads:

$$K_2 = K_2^{(2)} = k_B T \rho^2 L^4 D \langle \langle a_2(\hat{\mathbf{u}}, \hat{\mathbf{u}}') \rangle \rangle_{f_0} \quad (4.30)$$

For conventional uniaxial nematic order scaling results exist that relate K_2 to the total rod concentration. Using Gaussian theory Odijk [161] found that for asymptotically strong nematic alignment:

$$\beta K_2 D \sim \frac{7}{96} c \quad (4.31)$$

For infinitely thin hard discs a much steeper increase with colloid concentration was found [162]:

$$\beta K_2 D \sim 0.606 c^3 \quad (4.32)$$

which suggests that lyotropic discotic nematic phases are far more difficult to twist than their rod-based counterparts at equivalent particle concentration (note that $c \gg 1$ for most stable nematics).

Chapter 5

Twisted membranes versus ribbons in colloidal rod-polymer mixtures

Abstract

At the mesoscopic level, rigid rodlike colloids with chiral features such as fd virus rods mixed with non-adsorbing polymer form a variety of different liquid crystalline droplets with varying shape and internal twisted structure. Inspired by recent experiment work on the droplet morphology of these rod-polymer mixtures, we use extensive Monte Carlo simulations supplemented with theory to explore two prominent droplet shapes, namely the twisted membrane and the ribbon. In experiment, the elongated ribbon structure is found to dominate at elevated chiral strength. In our simulations, however, we demonstrate that upon increasing chirality the membranes tend to transition into multi-domain structures consisting of multiple twisted near-circular units separated by π -walls, while the transition into twisted ribbons is impeded by the strong surface tension experienced by the droplet. We supplement our simulations with simple microscopic theoretical descriptions for both droplet morphologies which enable us to predict the evolution of the twist angle across the membranes. For the ribbons, our simple theory provides generic predictions for the typical ribbon width, internal twist and edge tilt angle that are in broad agreement with experimental observations of twisted ribbons composed of fd virus rods mixed with dextran.

5.1 Introduction

Rodlike colloidal particles are capable of assembling into a variety of liquid crystalline mesostructures whose bulk properties depend primarily on the topology of the director field indicating the average direction of rod alignment [7, 163]. In general, site-specific attractive forces between non-spherical nanoparticles may affect the self-assembly properties and lead to a wealth of different superstructures [164] such as twisted ribbons of semi-conducting rods [165] or platelets [166]. Mixing rodlike colloids with non-adsorbing polymers or other small depletant particles induces a short-ranged attractive ('sticky') effective potential between the rods that can be exploited to control the self-assembly morphology [167, 168].

The size and concentration of the added polymer can be exploited to tune the morphology

and internal structure of the droplets. Tactoids with nematic-type order have been observed experimentally in mixtures of rods and big depletants (typically bigger than the diameter of the colloidal rods), as well as smectic-like single layer droplets, named colloidal membranes, when significantly increasing polymer concentration. The morphology of these membranes is further controlled by strong electrostatic and chiral twist interactions between the individual rods. Though these interactions are not well understood yet, it has been empirically observed that, in close contact with one another, fd rods tend to twist preferentially clockwise, instead of arrange following a global nematic direction. When both depletion effect and chirality are strong, twisted colloidal membranes tend to destabilize to give way to twisted ribbons. The additional effect of intrinsic particle chirality strongly impinges onto the self-assembled mesostructure and drives a vast range of different twisted or chiral structures ranging from smectic membranes to chiral ribbons [28] and hexagonal nanocrystals displaying screw-dislocations [169]. These twisted structures have been observed experimentally, but reproducing the various mesophases with distinctly different twisted morphologies in computer simulation has been elusive so far. Modelling efforts have focused almost exclusively on twisted membranes [170, 171, 172] or conventional LC tactoids exhibiting full three-dimensional fluidity [173, 174, 175]. Resembling the local fluid structure of a smectic monolayer these membranes provide a convenient platform to address the typical length scale, called penetration length, over which twist is expelled from the edges of a colloidal smectic phase [176]. The concept of twist-expulsion was introduced by De Gennes in the 1970s who established an analogy between the smectic A phase and superconductors. It follows that smectic layers expel twist deformations in the same way that superconductors expel magnetic field [39].

In a recent study Kuhnhold et al. [172] have reported an extensive simulation study of the properties of twisted membranes comparing numerical results with theoretical predictions. In order to facilitate membrane stabilization, the rod centres-of-mass were constrained to reside on the smectic plane, thereby suppressing out-of-plane fluctuations. While the constraint should be reasonably harmless for the flat membranes it does preclude the system from engaging in further morphological transitions such as the formation of ribbons and other filamentous structures observed in experiment [28] and conjectured in continuum theory [177, 170]. The aim of this study is to re-address the stability and microstructure of membranes by exploring the full degrees of freedom of the rods. To describe rod-polymer mixtures we use large-scale Monte Carlo simulations of the well-known Asukara-Oosawa model comprising hard-spherocylinders mixed with penetrable hard spheres. The latter represent small polymers that are excluded from the spherocylinder surface but do not feel each other (ideal polymer). This model is at the core of a range of free-volume theories that address the bulk thermodynamic properties and phase behavior of colloidal particles of various shapes mixed with non-adsorbing polymers [37]. The spherocylinder interactions are rendered chiral by means of a simple pseudo-scalar potential that finds widespread use in computer simulation. Thus, we have a model system where chiral twist competes with short-ranged attractive depletion interactions and surface tension in driving mesoscopic liquid crystalline droplets of various internal structure and shape. In our simulations based on the semi-grand ensemble we fix the polymer chemical potential in the hypothetical reservoir containing polymeric spheres at a high enough value to prevent the droplets from dissolving and systematically vary the chiral interactions between the rods.

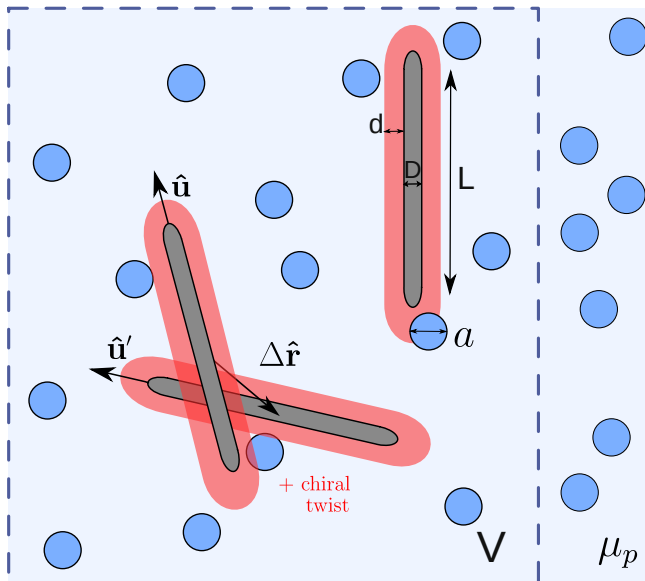


Figure 5.2.1: Sketch of the simulation model: hard spherocylinders (grey) mixed with non-adsorbing polymers modeled as penetrable hard spheres (blue) with diameter $a = 2D$ (as depicted here). Overlap of the cores (grey) gives infinite repulsion while overlapping coronae (red zones) favors a twisted pair configuration representing the (chiral) electrostatic forces between fd rods. The system has a fixed volume V with periodic boundary conditions and connected to a polymer reservoir at constant chemical potential μ_p .

We supplement our simulations with a minimalist theory for the membranes and ribbon based on the Frank elastic energy combined with contributions that incorporate the effect of polymer depletion on local director distortions as well as the surface tension the droplets experience with the surrounding polymer fluid. Whereas our membrane theory is inspired by a previous model by Kang et al. [170, 178] we develop a similar nematic-elasticity-based approach for the ribbons with predictions for the longitudinal and transverse pitch as well as the typical edge width of the ribbon. We also propose a tentative state diagram outlining the different membrane morphologies and their conditions for stability.

5.2 Simulation model

We consider a system of N hard-core rigid spherocylinders of length L , thickness D and aspect ratio $L/D = 10$. The spherocylinders are a simplified representation of fd rods that are much thinner ($L/D > 100$) and carry a small degree of backbone flexibility with persistence length $\ell_p \gg L$. Since the large particle aspect ratio in combination with backbone flexibility poses considerable limitations on the numerical efficiency of our simulations we only consider rigid rods with a relatively short length assuming that the key features of the mesoscopic structures evaluated in this work do not critically depend on the rod aspect ratio or flexibility. We study these systems by means of Monte Carlo simulations in the semi-grand canonical ensemble (N, V, μ_p, T) consisting of a system of N rods in a volume V at constant temperature T in osmotic equilibrium with a polymer reservoir at constant chemical potential μ_p . The number of polymers in the system is then a fluctuating quantity with the average polymer concentration controlled by μ_p .

5.2.1 Depletion interactions

The spherocylinders are mixed with non-adsorbing polymers that in our model act as penetrable hard spheres. Polymer-polymer interactions are neglected, while the interactions between polymers and spherocylinders are treated as being strictly hard; the potential energy is infinitely large when a sphere and spherocylinder overlap and zero otherwise. The polymer diameter a is chosen to equal twice that of the spherocylinder ($a = 2D$) because, in that regime, depletants are small enough to realistically reproduce the depletion effect and big enough to generate long-ranged attraction interactions between the spherocylinders and thus be able to observe intra-lamellar liquid-like order in the resulting smectic compounds. Depletants are treated in an implicit way by means of the algorithm proposed by Glaser *et al.* [50]. More details on the implementation of this algorithm are developed in Section 1.4.3.

The simulation box is assigned a fixed volume V and is subjected to periodic boundary conditions (PBC). However, the effective volume of the simulation box is not a critical parameter due to the application of the implicit depletant algorithm, which renders the volume irrelevant as long as it is sufficiently large to avoid any boundary effects affecting the mesogen edges. In practical terms, the depletants are characterized, rather than by their chemical potential μ_p , by their average packing fraction ϕ_p ; which is defined as the volume fraction in the reservoir fully occupied by spheres. The chemical potential is trivially connected to the polymer packing fraction via:

$$\phi_P = \frac{\pi a^3}{6\Lambda_p} e^{\beta\mu_P} \quad (5.1)$$

where Λ_P denotes the thermal (de Broglie) volume.

The typical attraction energy between two rods due to polymer depletion can be estimated from free-volume theory [37] and reads:

$$U_{r,\text{dep}} \sim -\Pi_P V_{r,\text{ov}} \quad (5.2)$$

with $\Pi_P = k_B T N_P / V$ the (van't Hoff) osmotic pressure of the polymer reservoir and $V_{r,\text{ov}}$ the overlap volume of the depletion layers surrounding each rod which depends on the orientation of each rod.

5.2.2 Chiral interactions

In order to account for both entropic ordering and chiral features, the pair interaction U_r between two spherocylinders with solid angles $\hat{\mathbf{u}}$ and $\hat{\mathbf{u}}'$ and centre-of-mass distance $\Delta\mathbf{r}$ follows from a combination of short-range steric forces (treated as strictly hard) and electrostatic forces at larger distance. The interaction potential between a pair of rods depends on centre-of-mass distance vector $\Delta\mathbf{r}$ and orientation vector $\hat{\mathbf{u}}$ of both rods. In our model, the interactions are encapsulated in the following core-shell potential:

$$U_r(\Delta\mathbf{r}, \hat{\mathbf{u}}, \hat{\mathbf{u}}') = \begin{cases} \infty & \text{if hard cores overlap} \\ U_{\text{twist}} & \text{otherwise} \end{cases} \quad (5.3)$$

The electrostatic interactions between fd rods give rise to so-called electrostatic twist which is intimately linked to the chirality surface architecture of fd virus rods. The chiral potential is commonly expressed in terms of a pseudoscalar form initially put forward by Goossens [38]:

$$U_{\text{twist}}(\Delta\mathbf{r}, \hat{\mathbf{u}}, \hat{\mathbf{u}}') = -\varepsilon_c \left(\frac{D}{\Delta r}\right)^7 (\hat{\mathbf{u}} \cdot \hat{\mathbf{u}}')(\hat{\mathbf{u}} \times \hat{\mathbf{u}}' \cdot \Delta\hat{\mathbf{r}}) \quad (5.4)$$

where $\Delta\hat{\mathbf{r}}$ denotes a unit vector for the centre-of-mass distance. The sign of ε_c defines the microscopic handedness of the rods. Without loss of generality we take $\varepsilon_c > 0$ reflecting the right-handedness of fd rods. The chiral symmetry of the potential is expressed by the pseudoscalar that imparts a sign change upon inversion $\Delta\hat{\mathbf{r}} \rightarrow -\Delta\hat{\mathbf{r}}$. In view of its rapid decay with Δr the potential is very short-ranged and the rods need to be very close together in order to feel the chiral twist. Thanks to this fast decay, we are able to truncate the interaction range in order to avoid chiral potential calculations between rods that are very far away from each other without affecting the total energy felt by the simulated rods. This truncated range is defined by d in Fig. 5.2.1. We choose $d = D$ so that the neglected contributions do not possibly exceed $\sim 0.05\varepsilon_c$.

Alternative possibilities for the chiral interaction can be chosen. Some preliminary results are shown in Appendix 5.A for the case of a long-ranged square potential.

5.2.3 Simulation details

Monte Carlo steps conceived from the specifications of the previous sections are performed as follows:

In the initial setup, all rods point along the z direction, their centres of mass are fixed to the XY plane centered in height ($z = L_z/2$) and they are arranged on a hexagonal lattice in a circular domain. During the relaxation from the initial configuration, we randomly apply single-particle moves: translations within the volume and rotations around arbitrary axes. To decide if a trial move is accepted, we first check for overlaps with other colloids and with depletants. If no overlap takes place, the variation in the chiral energy is computed and the Metropolis acceptance criterion is used to decide whether the move is energetically favorable. If the move induces a loss in energy, it is accepted; otherwise it will be accepted with probability $\sim \exp[-\beta(U_{\text{new}} - U_{\text{old}})]$.

The step size for the spherocylinder translations and rotations are chosen adaptively such as to maintain an average acceptance ratio of about 30 %. The MC code is optimized using cell-linked list routines that significantly reduce the number of overlap checks between rod-rod and rod-polymer pairs involved in each MC step. We keep a square box shape with $L_x = L_y = L_z$ and periodic boundary conditions (PBC) in all directions. The polymer concentration is chosen to be high enough to favor the equilibration of a smectic droplet, and low enough to avoid crystallinity.

At intervals of 1000 MC cycles, we monitor two quantities, namely the total overlap volume of the depletion layers (V_{ov}) and the total twist energy ($\mathcal{U} = \sum_i \sum_{j < i} U_{\text{twist}}$), to gauge whether the drop has reached its equilibrium state (one MC cycle correspond to N trial moves, so that each rod has been tried to be moved once on average). The equilibration takes at least 10^6 MC cycles. Notably, for larger systems (larger N) and intermediate to high values of ε_c , long-

range effects due to chirality may emerge later in the equilibration process and result in an increase in the equilibration time. The relaxed system configurations also serve as initial states for conducting subsequent simulations with different parameter sets.

5.3 Results

We conducted a series of simulation runs for different values of the number of rods $N = 500, 1000$ and the chiral strength $\varepsilon_c = 0, 1, 2, \dots, 20$. Furthermore, simulations were carried out for analogous parameter sets but avoiding displacements along the z -axis i. e. without vertical fluctuations, thereby allowing a comparison to the findings of [172], where rods are pinned to a horizontal plane, and facilitating an examination of the impact of vertical fluctuations on the observed structures. The value of the polymer packing fraction ϕ_p is equal for all simulation runs of the same type (with and without vertical fluctuations), and it is slightly lower for the case without vertical fluctuations. The reason for this is that, due to the loss of degrees of freedom, the depletion pressure needed to stabilize the droplets in the latter case is lower, and high depletant concentrations can promote the appearance of intra-lamellar crystalline order more easily. We then lower the depletant concentration in order to find a better qualitative consistency between the two scenarios. However, we have not conducted a comprehensive study to determine the optimal value for achieving the best correspondence, and the selected values ($\phi_p = 0.25$ for the case with vertical fluctuations and $\phi_p = 0.175$ for the case without vertical fluctuations) should be considered qualitatively reliable.

Membrane morphologies for different values of ε_c are shown in Fig. 5.3.1 for systems with $N = 500$. For comparison, we show each snapshot along with its equivalent in the case without vertical fluctuations. Chirality affects the shape of the membrane in different ways depending on whether the rods are pinned to the horizontal plane or not. In the pinned case, where the rods centers of mass are confined within a plane, the membrane shape tends to present a circular shape with slightly fluctuating boundaries. As for the unpinned case, rods are allowed to escape the horizontal plane, and thus can be found with a higher probability in the isotropic phase or adsorbed onto the membrane surface; and membranes tend to present a more elongated shape, rather than circular. The presence of surface ripples and fluctuations suggests that the (effective) surface tension of the membrane is affected by the pinning, and appears to be smaller for membranes composed of unpinned rods despite the higher polymer content and the depletion attractions being more pronounced. These elongated structures, although they do not give way to elongated twisted ribbons, may sometimes show indications of a ribbon instability, e. g. for $\varepsilon_c = 4$ in the unpinned case in Fig. 5.3.1. However, these instabilities are never observed in the pinned case. One significant difference between the two cases is that multi-domain membranes appear at stronger chiral forces in the pinned case ($\varepsilon_c = 16$) than in the unpinned case ($\varepsilon_c = 12$), which lead us to think that vertical positional order hinders the apparition of multi-domain structures in favor of single domain membranes with stronger twist at the edges. We note, however, that this critical value of ε_c also depends on the size of the system: it increases for the unpinned case when $N = 1000$ (in this case, the smectic membrane configuration becomes unstable at $\varepsilon_c = 15$, not shown).

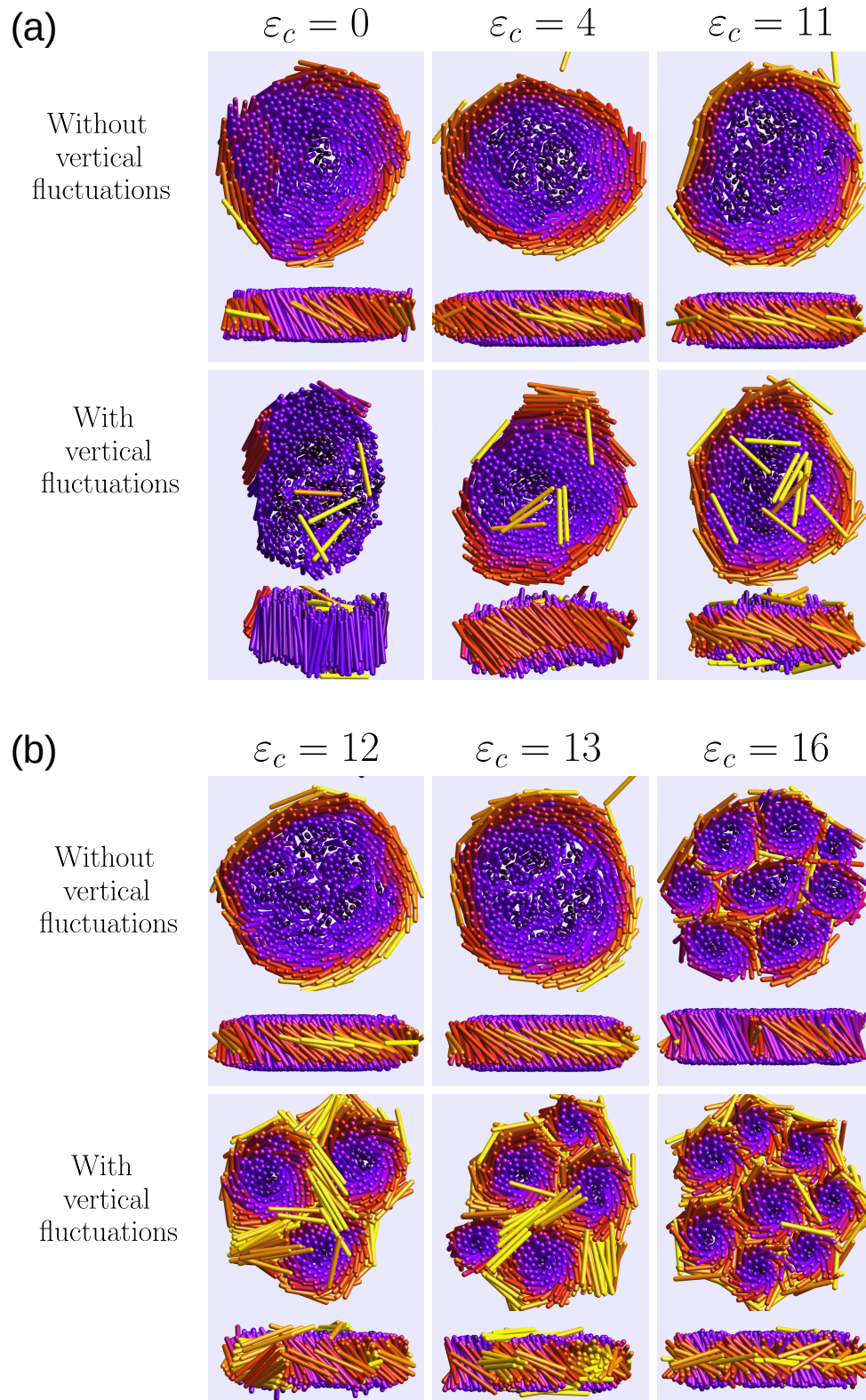


Figure 5.3.1: Top and front views of membrane-shaped tactoids of chiral rods mixed with non-adsorbing polymer (not shown). Color indicates the enclosed angle between each individual rod and membrane normal, from black $\varphi = 0$ to yellow $\varphi = \frac{\pi}{2}$. Shared parameters are $a = 2D$, $\ell = 10$ and $N = 500$. For the cases where vertical fluctuations are (not) allowed, $\phi_p = 0.25$ ($\phi_p = 0.175$). (a) Low chirality regime. (b) Strong chirality regime showing a cascade of multi-core membranes.

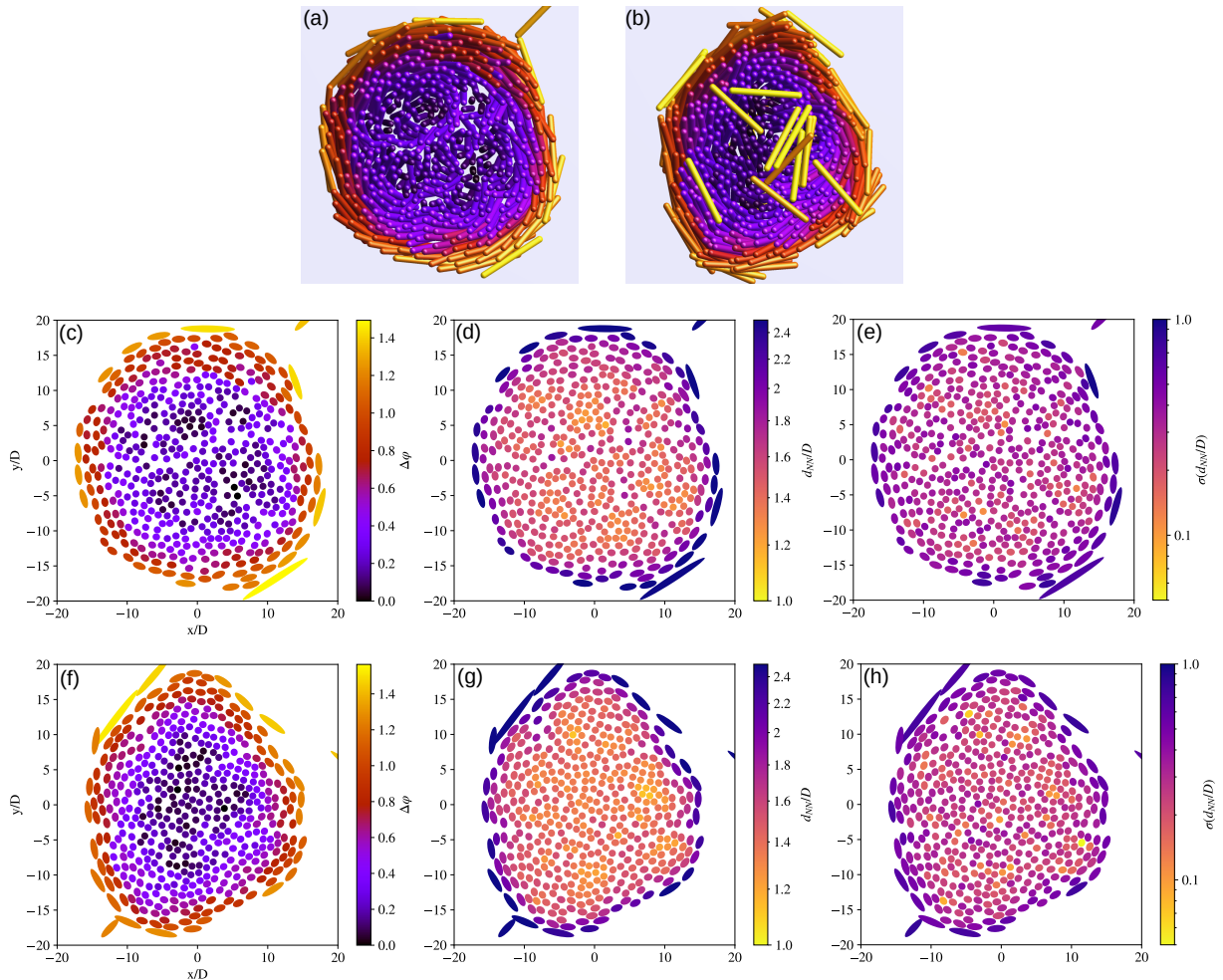


Figure 5.3.2: Crystallinity of membrane-shaped tactoids of chiral rods mixed with non-adsorbing polymer formed in bulk. Top row: rendered snapshots (a) without vertical fluctuations and (b) with vertical fluctuations. Middle and bottom rows: cuts through the plane generated from a 2D linear regression of the centers of mass of the rods, so that tilted rods appear as ellipses. Color scales indicate: (a)-(c), (f): enclosed angle between each rod's direction and the global nematic director; (d), (g): average distance between each rod and its six nearest neighbours; and (e), (h): nearest neighbour distance's standard deviation. Shared parameters are $a = 2D$, $\ell = 10$, $N = 500$ and $\varepsilon_c = 11$. For the case where vertical fluctuations are (not) allowed, $\phi_p = 0.25$ ($\phi_p = 0.175$).

To gain further insight into the influence of vertical fluctuations on membrane shape, we computed various quantities related to the internal structure of the membranes. These quantities are intended to provide the reader with an intuitive overview of local density and crystallinity in both the pinned and unpinned cases. Fig. 5.3.2 (intermediate chirality regime) and Fig. 5.3.3 (strong chirality regime) display the relative orientation, average nearest neighbor distance (which is related to the local density), and standard deviation of the nearest neighbor distance for each individual rod (as a direct but simplistic way of showing the local crystallinity). Rather than using 3D rendering, additional spatial information can be extracted by plotting horizontal sections along the central plane of the membrane. By doing so, out-of-plane noise can be reduced, and the relative distances between rods can be better observed. In the case without vertical fluctuations, the horizontal section is straightforward: we cut the system through the plane that contains the centers of mass of the rods. However, in the case with vertical fluctuations, we need to adopt a procedure to select the best fitting cut. We chose to generate a plane from a 2D linear regression of the centers of mass of the rods. Since mesogens are allowed to rotate, this plane may not be entirely horizontal with respect to the system coordinates. After the plane is selected, we project the rod position into it. Because the center of mass of the rod may be out of plane, we need to determine the intersection between the rod axis and the plane. The intersection point is then the center of an ellipse, and its edges define the horizontal section of the rod. Thus, upright (untwisted) rods appear as disks in this view, while tilted rods appear as ellipses.

In Fig. 5.3.2, we observe stabilized twisted membranes in the intermediate chirality regime. We see that ellipses are more separated from each other in the case without vertical fluctuations, whereas in the unpinned case rods tend to occupy a smaller surface and remain closer to their neighbours. The higher local density in the unpinned case induces a higher level of crystalline order as can be observed by comparing subpanels (e) and (h); yellow regions in these panels present smaller fluctuations in the relative distance between rods. In contrast, rods in the pinned case present a more liquid-like ordering. This effect may be due to the difference in the depletant concentration which, as explained previously, is different for each case. However, for lower depletant concentrations, a smectic droplet is hard to stabilize in the unpinned case, and thus we state that a more liquid-like internal ordering is unlikely to be found in membranes of these characteristics.

Fig. 5.3.3 shows multi-domain structures that have formed in the strong chirality regime. The subdomains are separated by domain walls where the rods perform a π turn going from one domain to the other (a so-called π -wall). We observe from the horizontal section depictions that the distance between rods located at the edges of these domains is considerably bigger compared to the distance between rods located inside the domains. The drop of the local rod density within the domain walls seems greater than the reduction of rod density for the single-core membranes. Consequently, in view if the additional free volume available polymer spheres are allowed to partially accumulate within the domains while being strongly depleted away from the dense core zones. The multi-domain membranes, therefore, are complex non-radially symmetric structures in which both rod and polymer densities are strongly non-uniform across the membrane surface.

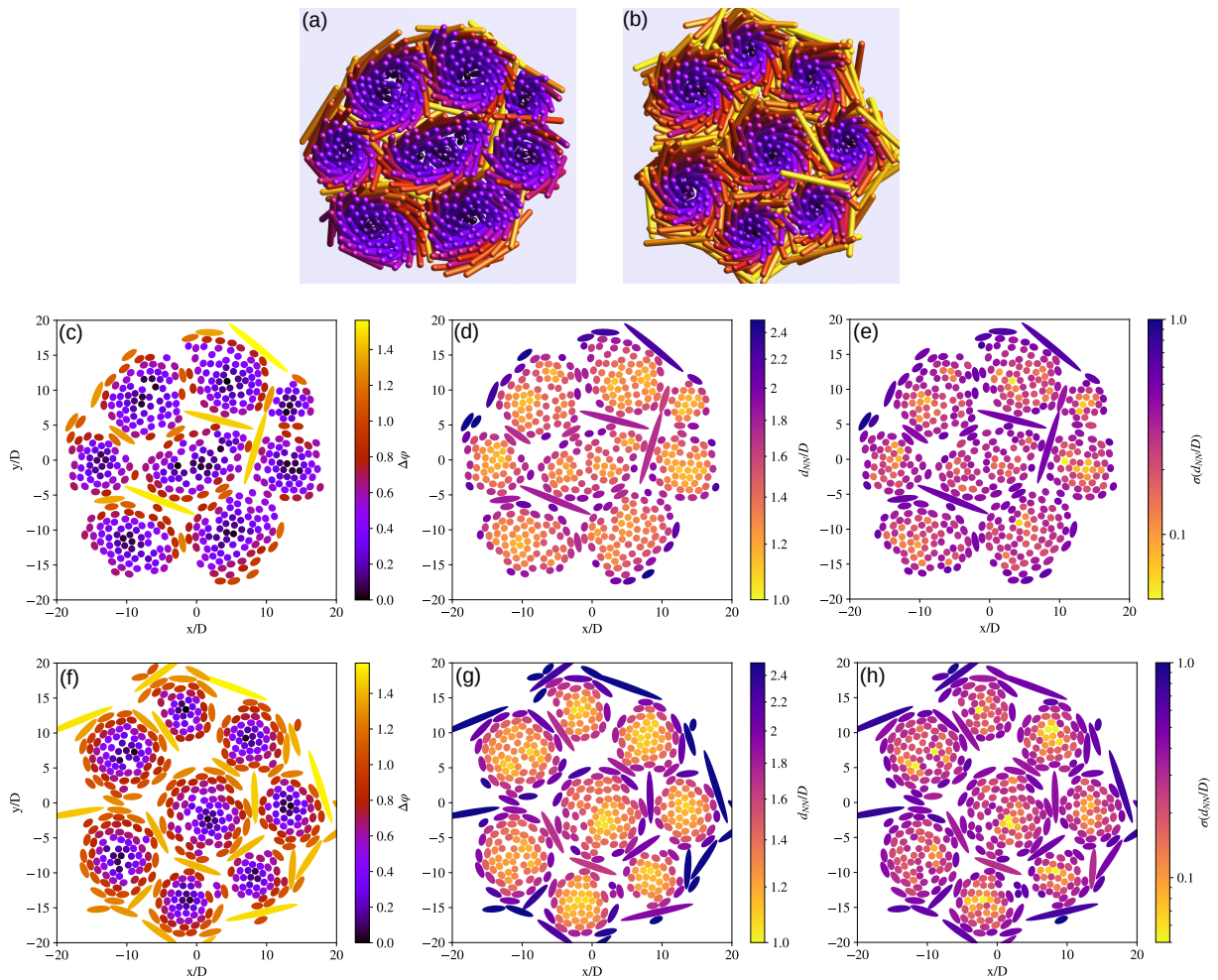


Figure 5.3.3: Crystallinity of multi-domain membrane-shaped tactoids of strongly chiral rods mixed with non-adsorbing polymer formed in bulk. (a),(c-e) without vertical fluctuations and (b),(f-h) with vertical fluctuations. What is illustrated in this figure is equivalent to Fig. 5.3.2 except for the chosen chirality regime ($\varepsilon_c = 11$ in Fig. 5.3.2, $\varepsilon_c = 16$ in this figure).

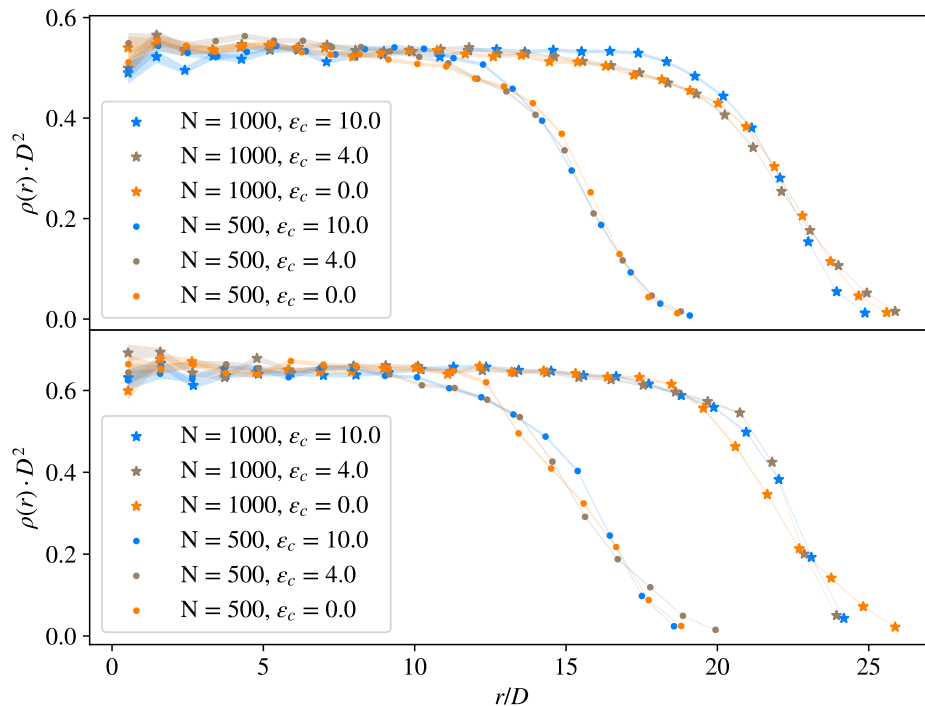


Figure 5.3.4: Rod number density profile of membrane-shaped tactoids of chiral rods mixed with non-adsorbing polymer formed in bulk. Top: without vertical fluctuations. Bottom: with vertical fluctuations. For all cases, $a = 2D$. For the cases where vertical fluctuations are (not) allowed, $\phi_p = 0.25$ ($\phi_p = 0.175$).

For the single-core membranes the evolution of the local rod concentrations is measured in terms of the radial density profile. This is done for both cases (pinned and unpinned) by taking the projected rod positions in the horizontal plane (as shown in middle and bottom rows of Fig. 5.3.2 and Fig. 5.3.3) in order to obtain the two-dimensional coordinates at the horizontal section. We compute the distance between each rod and the center of mass of the system and we numerically integrate the profile by binning the space in concentric cylindrical rings with radii r_b and width $\Delta r_b = D$. Finally, we count the number of rods residing in each bin and plot $N_r(r_b)/A_r(r_b)$, where $N_r(r_b)$ is the reduced number of rods with distance in $[r_b - \Delta r_b/2, r_b + \Delta r_b/2)$ and $A_r(r_b)$ is the area of the cylindrical bin. Results are shown in Fig. 5.3.4 for the pinned and unpinned case, for the two values of N and several values of ϵ_c that cover the whole low to intermediate chirality regime (where multi-domain membranes are not found for any of the simulations). Results are averaged over 100 configurations at different MC cycles of the same equilibrated simulation run. We clearly observe a significant drop of the local density near the membrane edges which confirms that the membrane density and the associated elastic moduli are not uniform throughout the membrane as is commonly assumed in the theoretical models developed thus far [171, 170, 177] including the one we will be discussing in Section 5.4.

The twist angle profile can be obtained in an analogous way, by averaging the enclosed angle between each rod and the main system director, and numerically integrating by bins defined as for the density profile. Computed profiles are shown in Fig. 5.3.5 for the two cases

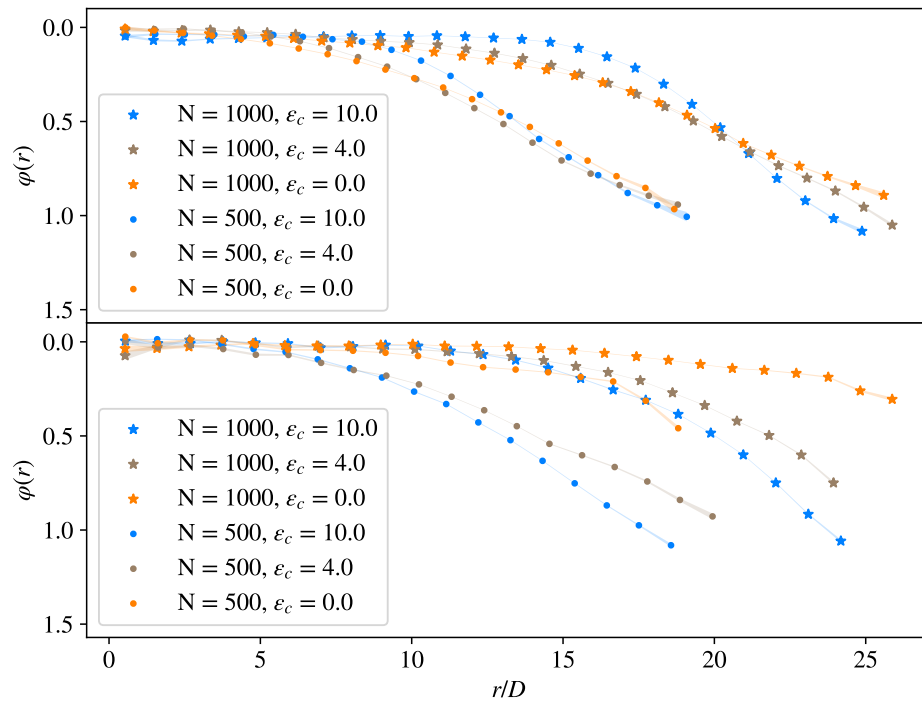


Figure 5.3.5: Twist angle profile of membrane-shaped tactoids of chiral rods mixed with non-adsorbing polymer formed in bulk. Top: without vertical fluctuations. Bottom: with vertical fluctuations. For all cases, $a = 2D$. For the cases where vertical fluctuations are (not) allowed, $\phi_p = 0.25$ ($\phi_p = 0.175$).

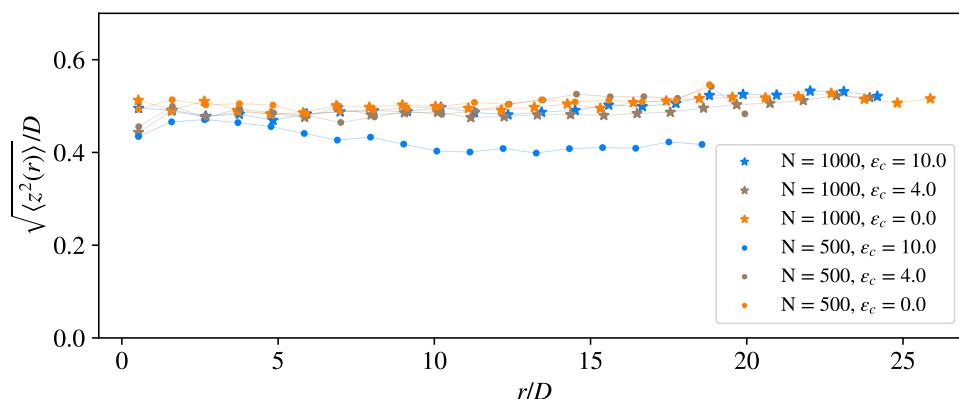


Figure 5.3.6: Vertical fluctuations as a function of the distance to the center of 3D membrane-shaped tactoids of chiral rods mixed with non-adsorbing polymer formed in bulk, $a = 2D$, $\phi_p = 0.25$.

considered in simulations. Differences between the pinned and unpinned rods are relatively minor which suggests that the pinned rod model is a very reliable one to study local effects in twisted membranes through computer simulation [172]. In both cases, we observe that twist expulsion towards the edge is more effective for the larger membranes ($N = 1000$) while the smaller membranes exhibit a smoother decay. This is in agreement with the original theory of De Gennes [39] and with more specific theoretical predictions for depletion-stabilized membranes [171, 170]. We also see that the twist at the membrane edge increases with chiral strength ε_c although much less so for the pinned rods than for the unconstrained rods. Note that the difference in polymer concentration between the pinned and unpinned rods precludes one-to-one comparison between the two cases.

Finally, we show fluctuations along the z direction for the unpinned case in Fig. 5.3.6. It can be seen that the typical positional fluctuations exerted by the rods are quite weak, being only a fraction of the rod diameter, and are uniform across the membrane; they do not depend on the distance to the center. The fluctuations do not strongly depend on the membrane size either, although they seem slightly weaker for $\varepsilon_c = 10$ and $N = 500$. As discussed above, in this case the system is very close to the strong chirality regime where multi-domains start to appear, which may affect the amount of out-of-plane fluctuations that are mostly dominated by entropic depletion forces in all the other cases.

5.4 Theory for twisted membranes

To complement our simulation results we now develop a theory for twisted membranes by focussing on two distinct morphologies that have been observed in experiment, namely half-skyrmion-type membranes and twisted ribbons. Later on, we will include the multi-domain membranes in our discussion. In both cases, the twisting of the rods occurs in both principal directions of the membrane (double twist), whereas the cholesteric phase exhibits unidirectional twist. Somewhat confusingly, double twist may also refer to the case of *chiral ribbons* in which the membrane itself is wrapped in a helical fashion thus exhibiting non-zero mean curvature [179, 180]. Although these chiral ribbons have also been observed in *fd* polymer mixtures under certain conditions [28], we will not consider this particular case in our model.

Let us begin by recalling the well-known Frank-Oseen elastic energy of the general case of a bulk chiral liquid crystal for an arbitrary nematic director field $\hat{\mathbf{n}}$ in three spatial dimensions:

$$F = \frac{1}{2} \int d\mathbf{r} [K_1(\nabla \cdot \hat{\mathbf{n}})^2 + K_2(\hat{\mathbf{n}} \cdot \nabla \times \hat{\mathbf{n}} + q_0)^2 + K_3(\hat{\mathbf{n}} \times \nabla \times \hat{\mathbf{n}})^2] \quad (5.5)$$

with K_1 , K_2 and K_3 respectively denoting the splay, twist and bend elastic moduli. The inverse pitch q_0 quantifies the chiral strength of the particles in the liquid crystal.

For the specific case of a cylindrically symmetric, twisted membrane depicted in Fig. 5.4.1 with radius R_m we may invoke a cylindrical geometry with radial coordinate $0 < R < R_m$ and angle α . Deformations from a uniform director field ($\hat{\mathbf{n}} = \hat{\mathbf{z}}$) are assumed to be concentric and

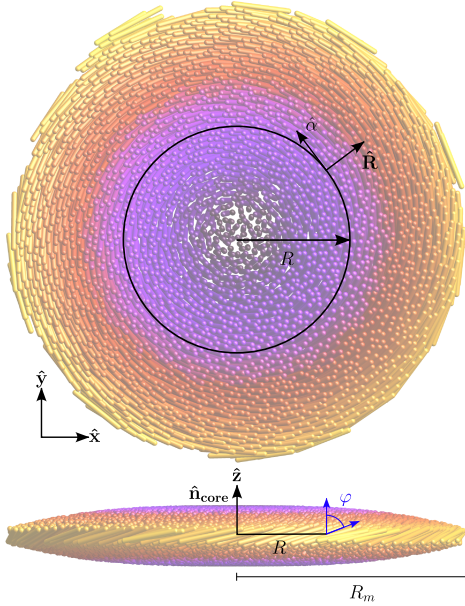


Figure 5.4.1: Schematic structure (top and front view) of a twisted smectic membrane of radius R_m composed of strongly chiral spherocylinders with aspect ratio $\ell = 10$ mixed with non-adsorbing polymers (not shown) providing strong side-to-side depletion attraction between the rods. The top graph depicts the top view, the lower one a side view of the membrane. The director twist, expressed by the twist angle φ , is zero at the membrane core $\hat{\mathbf{n}}_{\text{core}} = \hat{\mathbf{z}}$ and increases concentrically with radius R .

can be described as:

$$\hat{\mathbf{n}} = \cos \psi(R) \cos \varphi(R) \hat{\mathbf{z}} + \cos \psi(R) \sin \varphi(R) \hat{\boldsymbol{\alpha}} + \sin \psi(R) \hat{\mathbf{R}} \quad (5.6)$$

in terms of a twist angle φ denoting a twist deflection of the rods with respect to the membrane normal and ψ a splay deformation along the membrane radial vector (see Fig. 5.4.1). We take the local rod density within the membrane to be uniform so that the one-body density reads $\rho(R, \hat{\mathbf{w}}) = \rho_0 f(R, \hat{\mathbf{w}})$, in terms of the rod number density ρ_0 denoting the number of rods per area unit, and a three-dimensional rod unit vector $\hat{\mathbf{w}}$ distributed along the local director obeying an a priori unknown distribution f . The twist-bend elastic free energy takes the following form [176, 171]:

$$F_{el} = \int d\mathbf{R} \left[K_2 \left(\partial_R \varphi + \frac{\sin 2\varphi}{2R} + q_0 \right)^2 + K_3 \frac{(\sin \varphi)^4}{R^2} \right] \quad (5.7)$$

with $\int d\mathbf{R} = 2\pi \int_0^{R_m} R dR$ in circular coordinates for a membrane with radius R_m . The elastic moduli for the membrane are distinctly different from those of a bulk liquid crystal and will be specified in the next section. We remark that these elastic moduli are strictly 2D quantities with dimension energy.

In an earlier version of our theory [171] the effect of depletion attraction due to the non-adsorbing polymer can be described in terms of a simple free energy

$$F_{dep} \sim U_0 \int d\mathbf{R} (\sin \varphi)^2 + \text{cst} \quad (5.8)$$

where U_0 is a tilt energy density (per unit area) related to the osmotic pressure of the polymer reservoir and polymer radius of gyration. The simple sine squared contribution is chosen here for simplicity and is in line with de Gennes' original treatment of twist expulsion towards the edges or around defects of smectic layers in analogy with superconductors [39, 176]. It captures

the basic trend that the local director tilting away from the membrane normal compromises the free volume experienced by the non-adsorbing polymer thereby inducing a free energy penalty. In our theory, out-of-plane fluctuations of the rod centre-of-mass away from the 2D plane are not included, but this can be done on a simple mean-field level [170]. Ignoring the curvature terms $R \rightarrow \infty$ and considering a smectic layer on an infinite half-plane enables an analytical minimisation of the free energy in terms of the twist penetration depth $\lambda_t = \sqrt{K_2/a}$ [39, 176]. For the circular membrane, a simple simulated-annealing Monte Carlo algorithm can be employed to minimise the free energy with respect to the twist angle $\varphi(R)$ for any given triplet of length scales, namely the bulk cholesteric pitch q_0^{-1} , twist penetration depth λ_t and membrane radius R_m . With the twist elastic modulus and chiral amplitude being microscopically defined Eq. (5.9) a simple one-parameter fitting procedure can be used to determine the depletion strength a and the twist penetration depth λ_t .

The main features we established from the numerical results [171] are the following: (i) the twisting becomes more pronounced toward the membrane edge when the twist penetration depth becomes shorter, as expected, but also when membrane size grows larger. (ii) Increasing the pitch q_0 enhances the maximum twist angle while keeping the overall shape of the twist angle profile largely unchanged. (iii) The local splay angle remains negligibly small across the membrane so that the omission of splay effects seems fully justified.

5.4.1 Scaling results for the elastic moduli for a fluid membrane

Using second-virial theory combined with a Gaussian approximation for the orientation probability of the rods within the membrane one can estimate the leading-order contributions of the torque-field, splay, twist and bend elastic constants of a membrane, respectively:

$$\begin{aligned} K_1 &\sim \frac{17\rho_0\ell^2}{24} = \frac{17}{2}K_2 \\ K_2 &\sim \frac{\rho_0\ell^2}{12} \\ K_3 &\sim \frac{1}{4}K_2 \end{aligned} \tag{5.9}$$

Note that the membrane moduli have units $\text{N} \cdot \text{m}$ (the 3D moduli would be expressed in Newtons) and $\rho_0 = ND^2/A$ refers to planar density of rods with diameter D , aspect ratio $\ell = L/D$ and membrane area A . The results suggest that the moduli of rodlike particle confined to a membrane are quite different from those of 3D bulk nematic fluid, at least for strongly elongated rods experiencing strong nematic order. In the limit of asymptotic alignment, the splay-to-twist ratio of a bulk fluid [161] was predicted to scale as $K_1/K_2 \sim 3$ whereas a much higher ratio $K_1/K_2 \sim 17/2$ is found for the membrane. The bend-to-twist ratio for a hard rod nematic fluid was found to be proportional to the degree of nematic alignment $K_3/K_2 \sim \sigma \gg 1$ [161] where σ is steered by the rod concentration. The curvature-to-twist elasticity of a membrane turns out to be smaller than unity $K_3/K_2 \sim 1/4$ and independent of the rod concentration. In other words, rods confined to a membrane experience a much stronger resistance to splay fluctuations whereas bend fluctuations are far less penalised compared to a 3D nematic fluid. Since the splay modulus is about an order of magnitude larger than the twist elasticity, we

expect director deformations whereby rods tilt along the radial vector of the membrane to be of marginal importance and will be ignored.

5.4.2 Chiral twist

The pitch q_0 of a twisted membrane can be estimated by considering a weakly chiral pair potential U_c described by some arbitrary but short-ranged spatial decay function $g(r)$ describing the range over which chiral forces interact and chiral amplitude ε_c much smaller than the thermal energy. This potential takes the following generic form [38]:

$$U_c \sim \varepsilon_c g(r) (\hat{\omega}_1 \times \hat{\omega}_2 \cdot \hat{\mathbf{x}}) (\hat{\omega}_1 \cdot \hat{\omega}_2) \quad (5.10)$$

From this, we may compute the so-called torque-field constant exerted by the chiral potential [171]:

$$K_t \sim -\rho_0^2 \bar{\varepsilon}_c \quad (5.11)$$

in terms of an integrated chiral amplitude $\bar{\varepsilon}_c$ which is *different* from that of a 3D cholesteric system as it implicitly encodes the geometric confinement given that \mathbf{r} is a 2D vector:

$$\bar{\varepsilon}_c = \varepsilon_c \int d\mathbf{r} |\mathbf{r} \cdot \hat{\mathbf{x}}| g(r) \quad (5.12)$$

which has units energy times volume ($k_B T \times D^3$). The chiral potential drives the twisting of the membrane and K_t provides an explicit link between the effective torque-field and the range and amplitude of the chiral pair potential between a pair of rods. We remark that the above mean-field treatment will be less adequate for strongly chiral amplitudes $\varepsilon_c \gg k_B T$. A common choice for $g(r)$ is a short-ranged power law $g(r) = 1/r^7$ but long-ranged forms such as a square-well (SW) potential could be conceivable as well [181]. Taking the power law featuring in Eq. (5.4) we obtain $\bar{\varepsilon}_c = \varepsilon_c D^3$. From this we find a *microscopic* expression for the typical equilibrium pitch of the membrane $q_0 = K_t/K_2$ that further depends on the in-plane rod density ρ_0 and rod aspect ratio $\ell = L/D$:

$$q_0 \sim \frac{12\rho_0 \bar{\varepsilon}_c}{\ell^2} \quad (5.13)$$

While for the single-twisted cholesteric phase the twist angle increases linearly $\varphi(z) = q_0 z$ at each position z along the helix axis, the angle will be strongly non-linear with radius R in case of the twisted membrane, in particular if the twist penetration length λ_t is small [171].

5.4.3 Effect of depletants and twist penetration length

Kang et al. [170] have proposed a more sophisticated expression for the effect of the depletion attraction on the twist angle via the local membrane height $h = (L/2) \cos \varphi$:

$$F_{dep} \sim 2n_p a k_B T \left[\int d\mathbf{R} \sqrt{1 + (\nabla h)^2} + \oint dl h \right] \quad (5.14)$$

with n_p the polymer reservoir pressure and a the polymer radius of gyration. The last contribution is identified as a line tension generated by depletion forces between rods. Combining this with the elastic part of the Eq. (5.7) we find the following free energy for a membrane with radius R_m :

$$\begin{aligned} \frac{F}{K_2} \sim \int d\mathbf{R} \left[\left(\partial_R \varphi + \frac{\sin 2\varphi}{2R} + q_0 \right)^2 + \frac{K_3 (\sin \varphi)^4}{K_2 R^2} \right. \\ \left. + \lambda_t^{-2} \sqrt{1 + (\partial_R h)^2} \right] + 2\pi \lambda_t^{-2} R_m h(R_m) \end{aligned} \quad (5.15)$$

with $\int d\mathbf{R} = 2\pi \int_0^{R_m} R dR$ in circular coordinates. The line tension contribution drops with increasing twist at the edges and becomes zero if the rods are twisted perpendicular to the membrane normal $\varphi(R_m) = \pi/2$. The twist penetration length is given by $\lambda_t = \sqrt{K_2/2n_p a k_B T}$ which, using Eq. (5.9) leads to a compact expression depending on quantities known from experiment such as the in-plane rod density (assumed uniform across the membrane), rod-polymer size ratio D/a , rod aspect ratio ℓ and the reservoir polymer concentration n_p :

$$\frac{\lambda_t}{D} = \sqrt{\frac{\rho_0 \ell^2}{24(n_p a^3)(D/a)^2}} \quad (5.16)$$

Taking typical numbers from our simulation ($\ell \sim 10$, $\rho_0 \sim 0.5$, $D/a = 2$ and $n_p a^3 \sim 0.2$) we find that the twist penetration length is only a few times the rod diameter, i.e. $\lambda_t \sim 2D$. This is broadly in line with the twist angle profiles in Fig. 5.3.5 where the twist expulsion at the edge was found to extend over a typical distance of about $\sim 5D$. For *fd* rods a much larger value is found primarily because they are longer than our rods ($\ell \sim 130$). The predicted value $\lambda_t \sim 20D$ is roughly in line with the experimentally measured value of about half a rod length depending on the polymer concentration that was used to stabilize the membranes [176].

In Ref. [172] a simple trial form was used to fit the simulation data:

$$\varphi(R) = \varphi_0 \left(\frac{R}{R_m} \right)^\alpha \quad (5.17)$$

with φ_0 the twist angle at the membrane edge and α a variational parameter governing the degree of twist near the edge. It is tempting to insert the trial form into the free energy Eq. (5.15) and seek an algebraic minimization route through the variational parameters φ_0 and α . However, such an approach turns out to be unfeasible because the free energy is strongly non-linear in φ . As in Ref. [171] we therefore employ a simulated-annealing Monte Carlo algorithm to obtain the angular profile as a function of the distance from the membrane core.

5.5 Starfish instability and twisted ribbon

At elevated chiral strength the circular membranes are known to transition into twisted ribbons [28]. These were identified as quasi-1D twisted protrusions growing out of the perimeter of the membrane, through a mechanism termed ‘starfish’ instability.

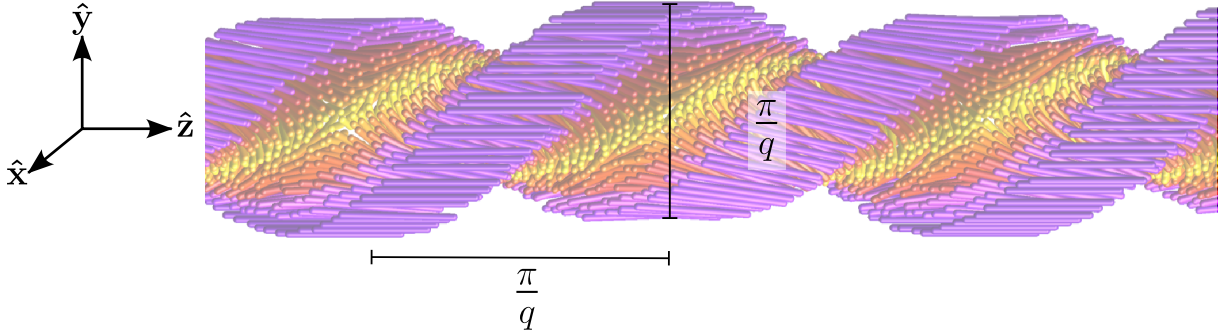


Figure 5.5.1: Schematic structure of a twisted ribbon of width $s_y = 2\ell$ composed of strongly chiral spherocylinders with aspect ratio $\ell = 15$ mixed with non-adsorbing polymers (not shown) providing strong depletion attraction between the rods. The rods are color coded by orientation. The typical ribbon dimensions are indicated by the pitch q with π/q corresponding to a half pitch length.

Lowering the temperature strengthens the chiral forces between the rods, which raises the free energy of the interior untwisted rods while lowering the free energy of edge-bound twisted rods. This enables chiral control of edge line tension which, when the edge tension approaches zero, leads to spontaneous transitions of the membrane into an array of 1D twisted ribbons, called a “starfish” [28]. A phenomenological model aimed at capturing the onset of the surface-driven instability was presented in Ref. [170]. So far, no minimalist theory along the spirit of the one discussed for the membrane has been contemplated for the ribbon whose intricately twisted structure is depicted in Fig. 5.5.1 based on a nematic director parameterization we are about to present. While the membrane exhibits double twist in a circularly symmetric fashion, the rods within the ribbon are twisted in two mutually perpendicular directions along the short and long axes of the ribbon. Then, the director field of a twisted ribbon may be constructed from a combination of two rotation matrices, each corresponding to a twist along mutually perpendicular Cartesian axes. Without loss of generality we fix the director field of the untwisted ribbon along the x -axis of the frame $\hat{\mathbf{n}}_0 = (1, 0, 0)$ so that the director field of the ribbon reads:

$$\hat{\mathbf{n}}_r[\Phi, \chi] = \mathcal{R}_{xz}[\Phi] \cdot \mathcal{R}_{xy}[\chi] \cdot \hat{\mathbf{n}}_0 \quad (5.18)$$

in terms of the rotation matrices

$$\mathcal{R}_{xz}[\Phi] = \begin{bmatrix} \cos \Phi(y) & 0 & \sin \Phi(y) \\ 0 & 1 & 0 \\ -\sin \Phi(y) & 0 & \cos \Phi(y) \end{bmatrix}$$

and

$$\mathcal{R}_{xy}[\chi] = \begin{bmatrix} \cos \chi(z) & \sin \chi(z) & 0 \\ -\sin \chi(z) & \cos \chi(z) & 0 \\ 0 & 0 & 1 \end{bmatrix}$$

Here, Φ and χ denote two angles describing the twist along the short and long (ribbon) axes that we parameterize via the coordinates $-s_y/2 < y < s_y/2$ and $-s_z/2 < z < s_z/2$, respectively. The ribbon area $A = s_y s_z$ is conserved. We further define the local thickness of the ribbon:

$$h = \frac{L}{2} |\hat{\mathbf{n}}_0 \cdot \hat{\mathbf{n}}| = \frac{L}{2} |\cos \chi(y) \cos \Phi(y)| \quad (5.19)$$

We now simplify matters by assuming linear twist in both directions so that $\chi = qz$ and $\Phi = qy$ where q denotes the principal pitch of the ribbon quantifying the degree of twist along the long and short ribbon axes. We remark that the ribbon pitch is likely to be different from the value q_0 that we defined in Eq. (5.13) which quantifies the chiral strength between the rods. Henceforth, we will use the ribbon width as our length unit and render all pitches dimensionless via $q \rightarrow qs_y$. We assume the ribbon to be long enough so we can ignore surface effects imparted by the short edge of the ribbon. Using the parameterization of the director Eq. (5.18) we find that the contributions corresponding to bend, splay and twist elasticity *per unit ribbon length* reads:

$$\begin{aligned} F_{bend} &= \frac{K_3}{16} [3q^2 - q \sin q (\cos q - 2)] \\ F_{splay} &= \frac{K_1}{8} (q^2 - q \sin q) \\ F_{twist} &= \frac{K_2}{16} [8q_0(q_0 - q - \sin q) + q \sin q (\cos q + 4) + 7q^2] \end{aligned} \quad (5.20)$$

Note that the bulk elastic energies are all *even* functions of the pitch q , except for the first term in the twist contribution which encodes chirality and vanishes for achiral rods ($q_0 = 0$). We must also consider the effect of saddle-splay, which is nonzero due to the curvature of the ribbon (it does not play a role for the flat membranes). It can be defined in terms of the following bulk contribution to the Frank elastic energy:

$$F_{saddle} = -\frac{K_{24}}{2} \int d\mathbf{r} [\nabla \cdot (\hat{\mathbf{n}} \nabla \cdot \hat{\mathbf{n}} + \hat{\mathbf{n}} \times \nabla \times \hat{\mathbf{n}})] \quad (5.21)$$

which gives:

$$F_{saddle} = -\frac{K_{24}}{4} q \sin q \quad (5.22)$$

The depletion contribution Eq. (5.14) can be derived in a similar way. Ignoring factors independent of the pitch, we find:

$$F_{dep} \sim 2n_p a k_B T \left[\frac{(qL)^2}{16} + \oint dlh \right] \quad (5.23)$$

Twisting a rectangular slab into a ribbon enhances the contour length of the object, which is reflected in the line integral in Eq. (5.14) that we express as $\oint dlh = (q/2\pi) \sqrt{1 + (q/2)^2} \int_{-\pi/q}^{\pi/q} dz h$. With this we find a simple expression:

$$\oint dlh = \frac{2L}{\pi} |\cos(\frac{1}{2}q)| \sqrt{1 + \frac{1}{4}q^2} \quad (5.24)$$

which suggests that the tension contribution is minimal at maximum tilt at the ribbon edge when

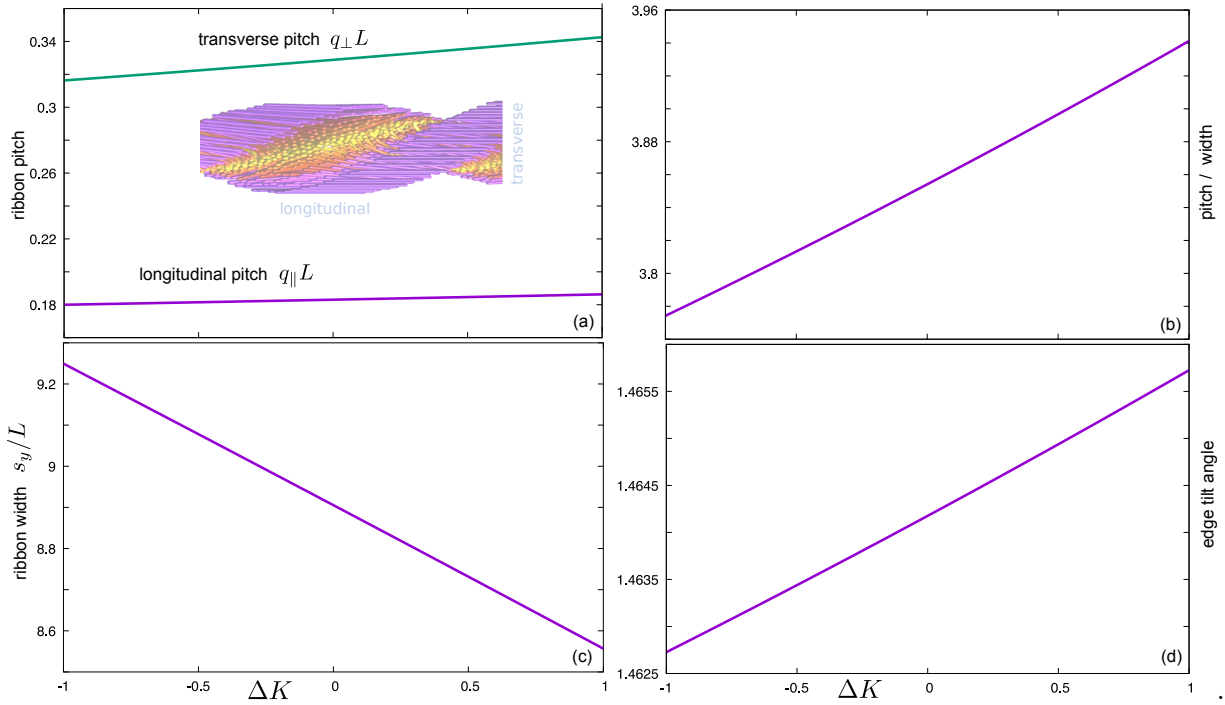


Figure 5.5.2: Overview of the ribbon properties as a function of the elastic anisotropy ΔK [Eq. (5.26)] of the LC material. Parameters $\lambda_t = 0.5L$ and $q_0 = 0.4L^{-1}$. Shown are (a) the longitudinal and transverse ribbon pitches. (b) The equilibrium ribbon width in units rod length L . (c) The typical ribbon aspect ratio in terms of the longitudinal pitch versus ribbon width. (d) The tilt angle at the ribbon edge.

$q = \pm\pi$. Simultaneously, it penalizes large pitches as the perimeter-to-area ratio of the ribbon increases with the degree of longitudinal twist, although this effect is of minor importance.

Although the expressions obtained are entirely algebraic, minimization of the total free energy can only be performed numerically. To make progress, we expand the free energy contributions up to quadratic order in q . Combining terms and reintroducing the twist penetration length λ_t we arrive at a compact expression for the total free energy per unit length of a weakly twisted ribbon ($q \ll 1/s_y$):

$$\frac{F}{K_2} \sim -qq_0 + \frac{1}{2} \left(\frac{\Delta K}{2} + \frac{L^2}{8\lambda_t^2} \right) q^2 + \frac{2L}{\pi\lambda_t^2} \quad (5.25)$$

The first two terms encode the free energy change due to (chiral) twist, the second the effect of splay, bend and saddle-splay elasticity along with depletion, whereas the last term denotes the line tension which up to leading order does not depend on the pitch. The constant ΔK represents a combination of the bend-twist and saddle-twist elastic anisotropies:

$$\Delta K = \frac{K_3}{K_2} - \frac{K_{24}}{K_2} + 3 \quad (5.26)$$

The equilibrium ribbon pitch follows from minimizing Eq. (5.25) and is related to q_0 via:

$$q \sim q_0 \left(\frac{\Delta K}{2} + \frac{L^2}{8\lambda_t^2} \right)^{-1} \quad (5.27)$$

Inserting this back into the quadratic free energy and reexpressing all variables in bare units we find:

$$\frac{F}{K_2} \sim -\frac{1}{2} \left(\frac{\Delta K}{2} + \frac{L^2}{8\lambda_t^2} \right) (q_0 s_y)^2 + \frac{2Ls_y}{\pi\lambda_t^2} \quad (5.28)$$

which combines a bulk term proportional to s_y^2 and a surface contribution linear in s_y . Minimization yield for the typical ribbon width:

$$s_y \sim \frac{2L}{\pi\lambda_t^2 q_0^2} \left(\frac{\Delta K}{2} + \frac{L^2}{8\lambda_t^2} \right) \quad (5.29)$$

Finally, we deduce the ribbon pitch versus width:

$$\frac{\text{ribbon pitch}}{\text{ribbon width}} = \frac{2\pi}{qs_y} \sim \frac{\pi^2 q_0 \lambda_t^2}{L} \quad (5.30)$$

and the tilt angle at the ribbon edge:

$$\bar{\Phi}(y = s_y/2) = \frac{1}{2} q s_y \sim \frac{L}{\pi q_0 \lambda_t^2} \quad (5.31)$$

The predictions above should be qualitatively correct and give valuable insight into how the ribbon properties depend on, for instance, the intrinsic chirality and elasticity of the LC material. A potential caveat of the low- q expansion, however, is that ribbons form at elevated chirality where the ribbon pitch qL is not necessarily a small parameter ($qL \ll 1$). Because deviations from the simple quadratic free energy Eq. (5.25) are to be expected, we chose to minimize the free energy numerically which is an easy task given that all free energy contributions are in algebraic form.

In doing so, we may also probe a more general scenario where the twist along the principal ribbon directions is *anisotropic*. To this end, we characterize the twist angles via $\chi = q_{\parallel}z$ and $\Phi = q_{\perp}y$ in terms of a longitudinal and transverse pitch, q_{\parallel} and q_{\perp} , respectively. Typical input values for the case of *fd* rods can be obtained by fixing the twist penetration length $\lambda_t = L/2$ [176] and taking a typical (cholesteric) pitch $q_0 = 0.4L^{-1}$. The elastic anisotropy ΔK is much harder to specify as it depends quite sensitively on the saddle-splay modulus K_{24} which is unknown for *fd* rods. The numerical results are shown in Fig. 5.5.2. The dependence of the quantities on the elastic anisotropy ΔK is evident but turns out rather weak, indicating that the predictions should be robust against a wide range of elastic properties of the LC material. We further observe that the twist is indeed considerably anisotropic with the transverse ribbon pitch being larger than the longitudinal pitch, while both are *smaller* than the typical cholesteric pitch q_0 that quantifies the chiral strength at the rod level. We further infer that the ribbon width is always a few times the rod length, suggesting that ribbons are indeed very slender quasi-1D objects. The ribbon pitch-to-width ratio is predicted to be about 3, which is in agreement with experimental observations reported in Ref. [28]. A typical value of 5 was quoted in Kaplan *et*

al. [177] for ribbons of fd rods mixed with non-adsorbing polymer. Finally, the edge tilt angle is virtually insensitive to ΔK and is predicted to be about 84° , confirming that the rods make a near $\pi/2$ -twist at the ribbon edge.

The membrane-ribbon transition could, in principle, be analyzed by comparing the free energies for both twisted morphologies for a given droplet volume. This however is technically very demanding given that the circular symmetry of the membrane, as encoded in the strongly non-linear elastic free energy Eq. (5.7), precludes a tractable analytical solution of the twist angle unlike for the ribbon. Below, we resort to a hand-waving argument as to why a membrane-ribbon transition should or should not take place.

5.6 Membrane or ribbon ?

Having established a minimal theoretical description for the membranes and ribbons we now wish to explore under which conditions the various droplet morphologies are favored. It is instructive to consider the main energetic effects involved in shaping the droplets, namely a surface energy and a (bulk) chiral energy that is contained in the twisting of the rods within the droplet. The preference for one state or the other can be argued as resulting from a trade-off between these two energies. On the one hand, for any finite membrane volume (or area) flat circular membranes have a minimal surface free energy but are able to accommodate only a limited amount of twist as the result of twist being expelled from the core and confined into a narrow zone of length λ_t near the membrane edges. Twisted ribbons, in view of their elongated shape, have an unfavorable perimeter-to-area ratio but are much more efficient at accommodating chirality because the twist is *uniform* throughout the main section of the object. Using these arguments, a membrane-to-ribbon transition can be understood as a natural consequence of a controlled experiment in which enforced chirality driven by cooling the system (a mixture of fd rods with dextran) was found to lead to a simultaneous reduction of the line tension of the membrane [28].

We now propose a heuristic argument for the stability of the membrane by balancing the bulk chiral and interfacial energetic contributions. First, the chiral free energy contained in the twisted rim of the membrane can be estimated from:

$$\frac{F_{\text{chiral}}}{K_2} \sim 2\pi \int_{R_m - \lambda_t}^{R_m} dR R [(\partial_R \varphi(R))^2 + q_0 \partial_R \varphi(R)] \quad (5.32)$$

ignoring the depletion and curvature contributions for large membranes ($R_m \rightarrow \infty$). Minimization of the free energy yields an analytical solution for the twist angle versus radius, namely $\varphi(R) = -\frac{q_0}{2}R + C_1 \ln R + C_2$. The constants C_1 and C_2 can be specified from the following boundary conditions:

$$\begin{aligned} \varphi(R_m - \lambda_t) &= 0 \\ \lambda_t^2 \partial_R \varphi(R_m) &= \frac{L}{2} \sin \varphi(R_m) \end{aligned} \quad (5.33)$$

The first refers to the untwisted core at $R < R_m - \lambda_t$ while the second follows from the inter-

facial tension at the membrane edge at $R = R_m$. To simplify matters further we fix the twist penetration length at half the rod length $\lambda_t = L/2$ [176] and linearize the boundary condition via $\sin \varphi(R_m) \approx \varphi(R_m)$. The chiral free energy stored in the membrane rim then reads:

$$\frac{F_{\text{chiral}}}{K_2} \sim \frac{\pi}{16}(q_0 L)^2 \left(1 - \frac{4R_m}{L}\right) \quad (5.34)$$

which is negative for large membranes. This free energy must be balanced against the interfacial contribution which in our minimalist approach reads:

$$\frac{F_{\text{interface}}}{K_2} \sim \frac{4\pi R_m}{L} \cos \varphi(R_m) \quad (5.35)$$

with the edge tilt angle being proportional to the chiral strength via $\varphi(R_m) = q_0/4$. Equating the two expressions and taking an infinitely large membrane $R_m \rightarrow \infty$ we find a critical pitch of $q_0^* L = 3.296$. This means that below this value the interfacial energy outweighs the gain in chiral energy ($F_{\text{interface}} + F_{\text{chiral}} > 0$) and the membrane is stable. At strong chirality, $q_0 > q_0^*$ the rim contribution dominates and transitions towards elongated twisted structures such as the ribbon can be expected. The critical pitch increases for finite-sized membranes given that smaller membranes have a relatively larger rim to surface proportion. The membrane-ribbon transition line based on the non-linearized boundary condition Eq. (5.33) is easily obtained numerically and is given by the purple curve in Fig. 5.6.1. We remark that quantitative predictions from the current expressions have to be taken with care because of our simplistic description of the membrane surface tension which does not account for the effect of chirality and does not include curvature corrections that will play a more prominent role for small droplets [182]. A more general expression for the surface tension σ of the droplet should therefore read:

$$\sigma(R_m) \sim 2n_p a k_B T \left(1 - \frac{2\delta}{R_m}\right) + \sigma_{\text{chiral}} \quad (5.36)$$

in terms of the Tolman length δ , which could be positive or negative, and a chirality-dependent correction as conjectured in Ref. [28] for the case of *fd*. However, both contributions are unknown for our particular simulation model. It is probable that the chirality contribution is very distinct from the one proposed for the experimental case such that the surface tension is little sensitive or even decreases with chirality. Also, the Tolman length could be negative resulting in σ rising for smaller membrane radii [183, 182]. We may therefore assert that the small membranes simulated in our study are likely to experience a considerable surface tension that constrains the droplets to remain more or less circular. An alternative strategy to cope with high levels of chirality is then to increase the perimeter of twisted zones at the interior of the membranes by splitting into multiple cores with shared interfaces, reminiscent of domain walls. Within the interfacial zones between the cores the rods display a $\pi/2$ twist from the local core (see Fig. 5.3.1). This enables adjacent cores to share an interface with no incommensurability in the edge twist. The interfacial cost imparted by the domain walls is likely to be much smaller than that of the membrane and its surrounding polymer fluid.

A naive estimate of the transition from the single to a multi-core membrane can be established by comparing the chiral energy of the two states. Let us focus on the simplest case,

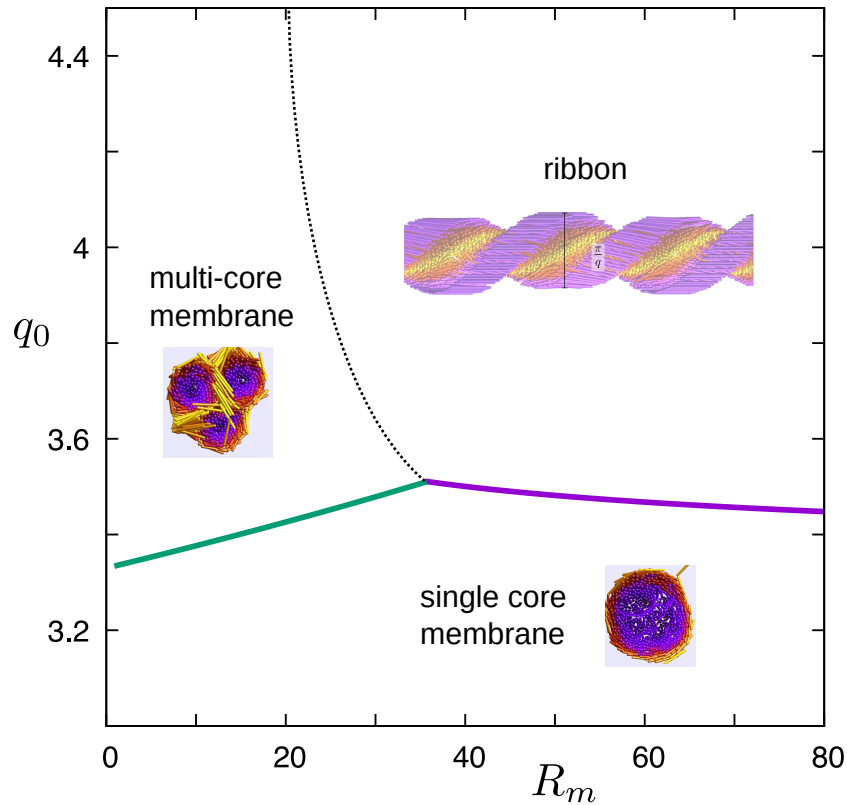


Figure 5.6.1: Overview of the various membrane morphologies predicted for chiral colloidal rods mixed with non-adsorbing polymer as a function of the membrane radius R_m and pitch q_0 (both expressed in units of the rod length L). Depending on the membrane radius, weakly chiral rods tend to self-assemble into single-core twisted membranes but may transition into elongated twisted ribbons beyond a critical chiral strength. Small droplets tend to be curved by surface tension and are precluded from forming ribbons, developing into multi-core membranes instead (see also Fig. 5.3.1).

namely the one composed of three cores [Fig. 5.3.1(b) for $\varepsilon_c = 12$] and denote the radius of each core by $R_s = R_m/\sqrt{3}$ which guarantees conservation of the total membrane area. Furthermore, we assume that the twist angle at the subcore edge is $\pi/2$ so that the second boundary condition in Eq. (5.33) should be replaced by $\varphi(R_s) = \pi/2$. Then, the chiral energy contained in each subcore rim reads:

$$\frac{F_{\text{chiral}}^{(s)}}{K_2} \sim \frac{\pi}{4} q_0^2 (\lambda_t^2 - 2\lambda_t R_s) + 2(\pi + \lambda_t q_0)^2 \ln \left(\frac{R_s - \lambda_t}{R_s} \right) \quad (5.37)$$

Balancing this against the single-core free energy $F_{\text{chiral}} = 3F_{\text{chiral}}^{(s)}$ and assuming the interfacial contribution to be the same for both states we find a simple criterion for the onset of multi-domain order. The result is given by the green curve in Fig. 5.6.1. In our simulations, we find the single-to-triple core transition to occur around $\varepsilon_c = 12$. According to Eq. (5.13) for $\rho_0 \sim 0.5D^{-2}$ this corresponds to about $q_0 \approx 0.9$ which is considerably smaller than the value predicted from our naive free energy balance. Combined with the prediction for the (single core) membrane-ribbon transition we construct a tentative state diagram stipulating the conditions for the different morphologies as shown in Fig. 5.6.1. We speculate that the multi-domain structures, in view of their enhanced capacity to harbour strong twists, retain their morphology and do not transition into ribbons even at elevated chiral strength. This is tentatively indicated by the dotted black curve. The key conclusion to be drawn from the diagram is that ribbons are more likely to appear from large membranes (say $R_m > 50L$) than from small ones. Taking a typical membrane density of $0.5D^{-2}$ [cf. Fig. 5.3.4] we find that the required system size far exceeds the ones probed in our study, $N > 25\pi(L/D)^2 \sim 8000$ for $L/D = 10$. This clearly poses a significant challenge for future simulation efforts that should be directed towards modelling rod-polymer mixtures using high-performance Molecular Dynamics computations [184, 185] that are capable of handling system sizes of about an order of magnitude larger than ours.

5.7 Conclusions and outlook

Inspired by recent experimental observations of morphological transitions of LC membranes of colloidal rods mixed with non-adsorbing polymers we use extensive Monte Carlo simulations combined with liquid crystal continuum theory to explore the shape and internal structure of droplets of rod-depletant mixtures.

In our model, we focus in particular on the effect of chiral strength between the rods which drives the formation of a variety of twisted structures, analogous to the classical cholesteric liquid crystals in bulk. Chief among them is the double-twisted membrane in which strong side-by-side attractions between the rods creates a monolayer of aligned colloids with weak to moderate out-of-plane fluctuations. These attractions, mediated by polymer depletion, force the colloidal rods to assemble into quasi-2d circular membranes with a double twist prevalent at the edges of the membrane. We are able to reproduce these structures in our simulations and find evidence for typical twist expulsion length introduced by De Gennes [39] that was found to be in good agreement with the predictions from a fit-free theoretical model [171]. When the chiral strength between rods exceeds a certain threshold we observe that the double-twisted membrane

forms multi-core domains that contain a tunable number of half-skyrmion-type twisted subunits separated by domain walls (π -walls). Owing to the considerable surface tension our membranes experience we do not find evidence of so-called twisted ribbons that have been observed in experiment [28]. We propose a simple continuum theory based on minimization of the Frank elastic free energy of a LC membrane combined with a depletion-mediated surface contribution that predicts the conditions under which the various states, namely single versus multi-core membranes and twisted ribbons, could be expected. Also emerging from our theory are first-time predictions for the internal twist along the longitudinal and transverse directions of the ribbon as well as the typical ribbon width which are all in broad agreement with experimental observations in *fd*-dextran mixtures [28, 170]. More detailed experimental studies are however required to put our predictions to a more stringent test in particular regarding the degree of rod twist along the longitudinal and transverse directions of the ribbon which we predict to be distinctly different.

Future studies could be aimed at numerically exploring much larger membrane sizes that are less enslaved to surface-effects and are therefore more likely to transition into ribbons. Conversely, it would be intriguing to see if the multi-core domains could be observed in experiment, for instance by seeking to independently control the chiral strength between the colloidal rods and the surface tension of the droplets. This could be achieved, for instance, using chiral dopants that boost the internal chirality of the membrane. In this vein, depletion-induced droplet formation of other colloidal particles could be explored such as cellulose nanocrystals (CNC) which are also chiral but whose shape and chirality transfer mechanism is quite different from *fd* [186, 187, 188]. The exploration of CNC-polymer mixtures may necessitate appropriate surface treatments of the CNCs that reduce the tendency for polymers to adsorb onto the colloid surface. Another interesting avenue for future simulation work could be to explore droplet shapes and their internal structure in strong planar confinement. Experimental work in this direction has already been undertaken in the group of E. Grelet (CRPP, Bordeaux) where *fd*-dextran mixtures have been confined in slit-like microfluidic chambers of about one rod length in width [189]. Clearly, confinement adds another level of complexity to the physics of LC tactoids given that the introduction of walls gives rise to (partial) wetting between the droplet and the solid substrate. The presence of geometric confinement thus further complicates the subtle balance between bulk and surface effects that dominates the shape and LC director structure of colloid-polymer based tactoids [175].

Appendices

Appendix 5.A Preliminary results using a square-well chiral potential

The system presented in this chapter accepts further modifications that can help us explore a variety of possibilities. One possible direction is to consider chiral interactions with larger ranges. At the time of publication of this thesis, simulations have been performed for the following square-well (SW) version of the chiral potential:

$$U_r(\Delta\mathbf{r}, \hat{\mathbf{u}}, \hat{\mathbf{u}}') = \begin{cases} 0 & \text{if } \Delta\mathbf{r} \geq L + D \\ -\varepsilon_c(\hat{\mathbf{u}} \cdot \hat{\mathbf{u}}')(\hat{\mathbf{u}} \times \hat{\mathbf{u}}' \cdot \Delta\hat{\mathbf{r}}) & \text{if } \Delta\mathbf{r} < L + D \text{ and no overlap} \\ \infty & \text{if overlap} \end{cases} \quad (5.38)$$

in the spirit of the theory proposed by [181]. This potential, applied to spherocylinders, covers a wider radial distance since its range scales with the total spherocylinder length $L + D$ and may be used to encapsulate chiral forces transmitted through electrostatic interactions, in contrast to the original Goossens potential used in the main text which is designed to address chiral forces arising from short-range phenomena such as chiral decorations present on the surface of the rods or mesogens possessing chiral shapes.

The preliminary snapshots displayed in Fig. 5.A.1 are formed from the same initial conditions as those employed in the main text. The figure indicates that double twisted membranes can also be stabilized using this SW potential. However, when using an elongated slab configuration, there are strong indications of the emergence of twisted ribbons. The resulting configurations for such initial conditions are presented in Fig. 5.A.2, though subpanels (e) and (f) demonstrate that these configurations may not be at equilibrium yet. Nevertheless, using this approach, the stabilization of twisted ribbons appears to be more promising than for the original Goossens potential employed in the main text, in which case the elongated slab configuration was also tested, and resulted in either the rearrangement of the slab into a membrane or the fractionation into smaller domains.

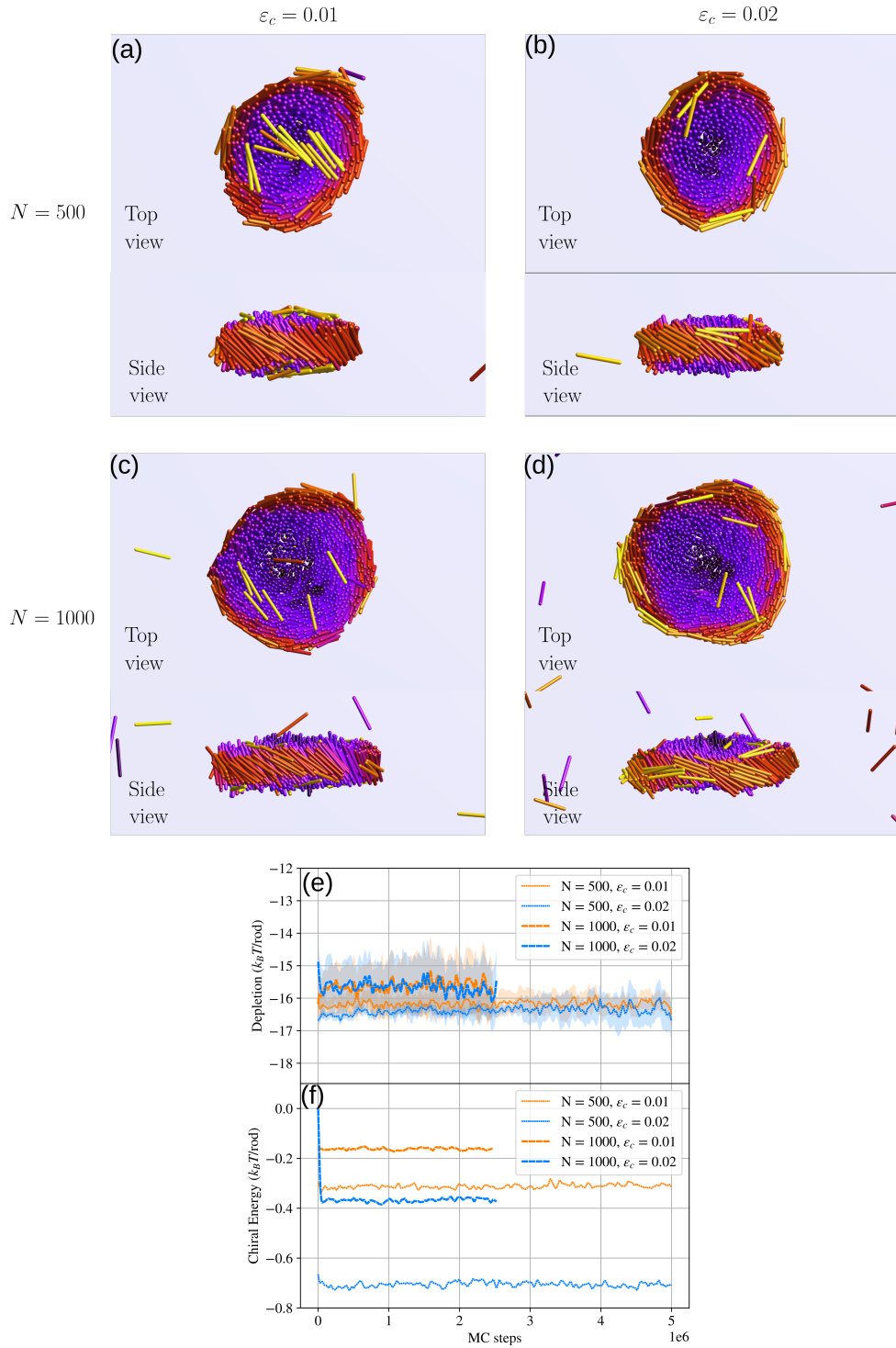


Figure 5.A.1: (a)-(d) Snapshots obtained from simulations using the SW potential described by Eq. (5.38) for $N = 500$ and $N = 1000$ and for $\varepsilon_c = 0.01$ and $\varepsilon_c = 0.02$. Initial conditions were chosen as in the main text (described in Section 5.2.3). (e) Depletion potential as a function of MC time estimated by integrating the total overlap volume between depletion layers. (f) Computed chiral energy as a function of MC time. Shared parameters are $a = 2D$, $\ell = 10$ and $\phi_p = 0.25$.

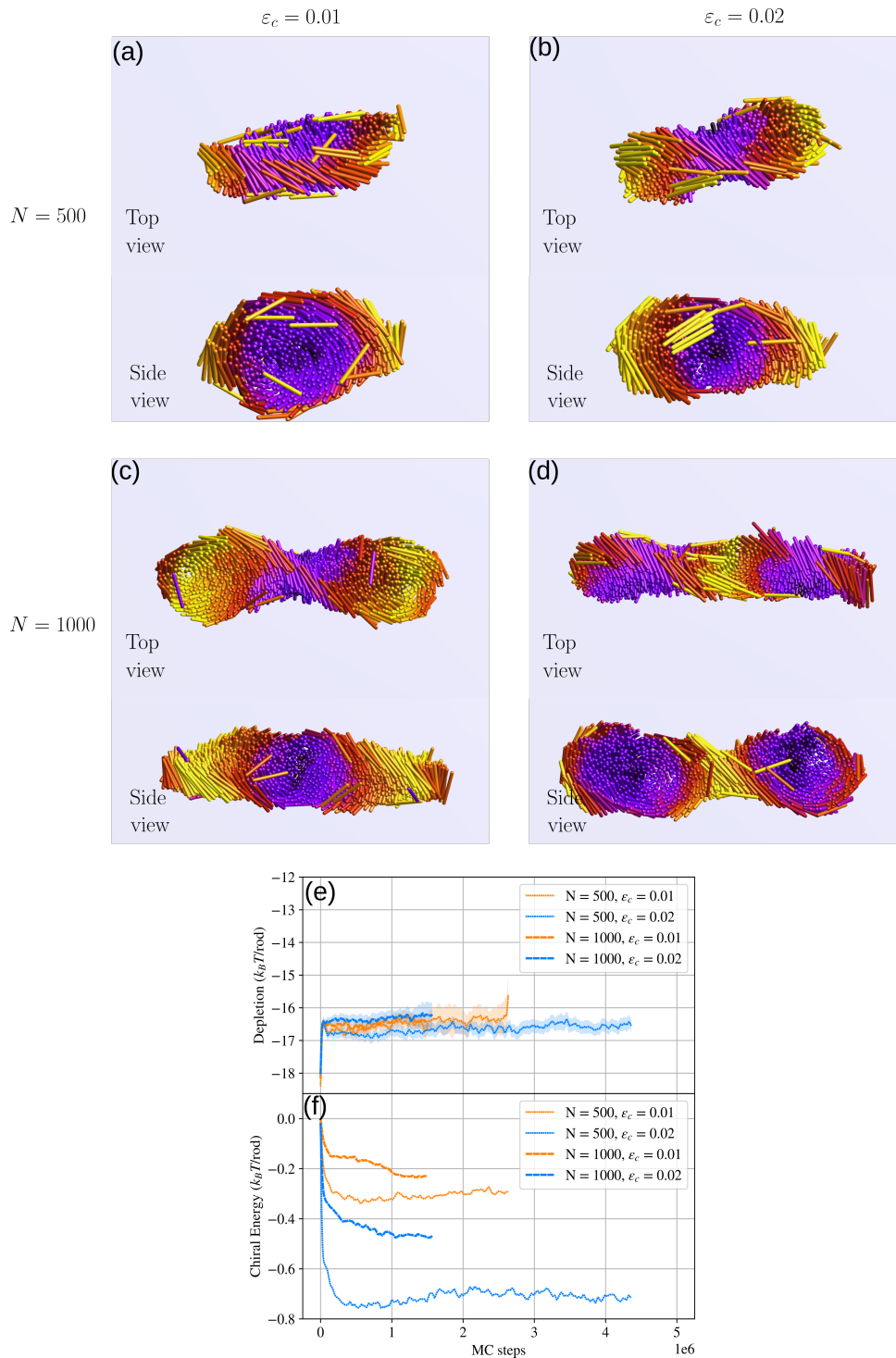


Figure 5.A.2: (a)-(d) Snapshots obtained from simulations using the SW potential described by Eq. (5.38) for $N = 500$ and $N = 1000$ and for $\epsilon_c = 0.01$ and $\epsilon_c = 0.02$. Initial conditions correspond to a rectangular slab where rods were oriented towards the y axis and arranged in a hexagonal lattice. (e) Depletion potential as a function of MC time estimated by integrating the total overlap volume between depletion layers. (f) Computed chiral energy as a function of MC time. Shared parameters are $a = 2D$, $\ell = 10$ and $\phi_p = 0.25$.

Bibliography

- [1] R. Borsali and R. Pecora, eds. Springer, 2008.
- [2] J. Perrin. Alcan (Paris), 1913. ISBN: 9782271082916.
- [3] F. Reinitzer. In: *Monatshefte für Chemie* 9.1 (1888), pp. 421–441.
- [4] Q. Li, ed. John Wiley & Sons, Inc., May 2012.
- [5] T. Gibaud. Nov. 2017.
- [6] A. Sonin. In: *Journal of Materials Chemistry* 8.12 (1998), pp. 2557–2574.
- [7] Z. Dogic and S. Fraden. In: *Curr. Opin. Colloid Interface Sci.* 11 (2006), p. 47.
- [8] F. Livolant and A. Leforestier. In: *Prog. Polym. Sci.* 21 (1996), p. 1115.
- [9] K. Fontell. In: *Molecular Crystals and Liquid Crystals* 63.1 (1981), pp. 59–82.
- [10] F. C. Bawden et al. In: *Nature* 138 (1936), p. 1051.
- [11] J. D. Bernal and I. Fankuchen. In: *J. Gen. Physiol.* 25 (1941), pp. 111–146.
- [12] H. Zocher. In: *Z. Anorg. Allg. Chem.* 147 (1925), p. 91.
- [13] I. Langmuir. In: *J. Chem. Phys.* 6 (1938), p. 873.
- [14] I. Dierking and A. Martins Figueiredo Neto. In: *Crystals* 10.7 (July 2020), p. 604. ISSN: 2073-4352.
- [15] L. Onsager. In: *Annals of the New York Academy of Sciences* 51.6 (1949), pp. 627–659.
- [16] B. Alder and T. Wainwright. In: *J. Chem. Phys.* 27 (1957), p. 1208.
- [17] W. W. Wood and J. D. Jacobson. In: *J. Chem. Phys.* 27 (1957), p. 1207.
- [18] D. Frenkel, H. N. W. Lekkerkerker, and A. Stroobants. In: *Nature* 332 (1988), p. 822.
- [19] D. Frenkel. In: *Liq. Cryst.* 5 (1989), p. 929.
- [20] J. A. C. Veerman and D. Frenkel. In: *Phys. Rev. A* 45 (1992), p. 5632.
- [21] Á. González García et al. In: *Chemical Physics Letters* 709 (2018), pp. 16–20. ISSN: 0009-2614.
- [22] S. Asakura and F. Oosawa. In: *J. Chem. Phys.* 22 (1954), p. 1255.
- [23] S. Asakura and F. Oosawa. In: *J. Pol. Sci.* 33 (1958), p. 183.
- [24] A. Vrij. In: *Pure Appl. Chem.* 48 (1976), p. 471.
- [25] E. Grelet. In: *Physical Review X* 4.2 (June 2014).

- [26] B. Senyuk et al. In: *Phys. Rev. E* 104.1 (2021), p. 014703.
- [27] H. Mundoor et al. In: *Nature* 590 (2021), p. 268.
- [28] T. Gibaud et al. In: *Nature* 481 (2012), pp. 348–351.
- [29] G. J. Vroege and H. N. W. Lekkerkerker. In: *Rep. Prog. Phys.* 55 (1992), p. 1241.
- [30] M. P. Allen et al. In: *Adv. Chem. Phys.* 86 (1993), p. 1.
- [31] J. -P. Hansen and I. R. McDonald. London: Academic Press, 1986.
- [32] D. Frenkel. In: *J. Phys. Chem.* 91 (1987), p. 4912.
- [33] D. Frenkel. In: *J. Phys. Chem.* 92 (1988), p. 5314.
- [34] M. A. Cotter and D. E. Martire. In: *J. Chem. Phys.* 53 (1970), p. 4500.
- [35] M. A. Cotter. In: *The molecular physics of liquid crystals*. Ed. by G. R. Luckhurst and G. W. Gray. New York, 1979: Academic Press.
- [36] H. Löwen et al. In: *J. Phys; Condens. Matt.* 14 (2002), p. 11897.
- [37] H. N. W. Lekkerkerker and R. Tuinier. Vol. 833. Lecture Notes in Physics. Springer, 2011.
- [38] W. J. A. Goossens. In: *Mol. Cryst. Liq. Cryst.* 12 (1971), p. 237.
- [39] P. G. de Gennes and J. Prost. Oxford: Clarendon Press, 1993.
- [40] A. Rapini and M. Papoular. In: *J. Phys. Colloq. (France)* 30.C4 (1969), pp. C4–54.
- [41] G. Barbero and G. Durand. In: *J. de Phys.* 47.12 (1986), pp. 2129–2134.
- [42] D. Frenkel and B. Smit. Second. Vol. 1. Computational Science Series. San Diego: Academic Press, 2002.
- [43] N. Metropolis et al. In: *The Journal of Chemical Physics* 21.6 (June 1953), pp. 1087–1092.
- [44] H. N. W. Lekkerkerker et al. In: *Europhys Lett.* 20 (1992), p. 559.
- [45] P. Bolhuis and D. Frenkel. In: *The Journal of Chemical Physics* 101.11 (Dec. 1994), pp. 9869–9875.
- [46] R. L. C. Vink and J. Horbach. In: *The Journal of Chemical Physics* 121.7 (Aug. 2004), pp. 3253–3258.
- [47] P. G. Bolhuis et al. In: *J. Chem. Phys.* 5 (1997), p. 1551.
- [48] M. Dijkstra et al. In: *Phys. Rev. E* 73 (4 Apr. 2006), p. 041404.
- [49] J. Henzie et al. In: *Nature Materials* 11.2 (Nov. 2011), pp. 131–137.
- [50] J. Glaser, A. S. Karas, and S. C. Glotzer. In: *J. Chem. Phys.* 143.18 (2015), p. 184110.
- [51] M. T. Lázaro, R. Aliabadi, and H. H. Wensink. In: *Phys. Rev. E* 104 (5 Nov. 2021), p. 054505.
- [52] M. E. Cates. In: *Macromolecules* 20.9 (1987), p. 2289.
- [53] M. E. Cates. In: *J. Phys. France* 49 (1988), p. 1593.
- [54] G. Riess. In: *Prog. Polym. Sci.* 28.7 (2003), pp. 1107–1170.

- [55] A. Blanzas, S. P. Armes, and A. J. Ryan. In: *Macromol. Rapid Commun.* 30 (2009), pp. 267–277.
- [56] C. De Michele et al. In: *Soft Matter* 8.32 (2012), pp. 8388–8398.
- [57] C. De Michele et al. In: *ACS Macro Lett.* 5.2 (2016), pp. 208–212.
- [58] J. Lydon. In: *J. Mat. Chem.* 20.45 (2010), p. 10071.
- [59] S.-W. Tam-Chang and L. Huang. In: *Chem. Commun.* 17 (2008), pp. 1957–1967.
- [60] T. P. J. Knowles and M. J. Buehler. In: *Nat. Nanotechnol.* 6.8 (2011), p. 469.
- [61] E. Fuchs and D. W. Cleveland. In: *Science* 279.5350 (1998), pp. 514–519.
- [62] F. Gittes et al. In: *J. Cell Biol.* 120 (1993), pp. 923–934.
- [63] J. F. Berret et al. In: *EPL* 25 (1994), p. 521.
- [64] M. Nakata et al. In: *Science* 318 (2007), p. 1276.
- [65] A. Matsuyama and T. Kato. In: *J. Phys. Soc. Jpn.* 67.1 (1998), p. 204.
- [66] T. Odijk. In: *Macromolecules* 19 (1986), p. 2313.
- [67] P. van der Schoot and M. E. Cates. In: *Langmuir* 10.3 (1994), pp. 670–679.
- [68] J. T. Kindt and W. M. Gelbart. In: *J. Chem. Phys.* 114.3 (2001), pp. 1432–1439.
- [69] T. Kuriabova, M. D. Betterton, and M. A. Glaser. In: *J. Mater. Chem.* 20 (2010), pp. 10366–10383.
- [70] K. T. Nguyen, F. Sciortino, and C. De Michele. In: *Langmuir* 30.16 (2014), pp. 4814–4819.
- [71] L. Tortora et al. In: *Soft Matter* 6.17 (2010), p. 4157.
- [72] R. Kato et al. In: *ACS Omega* 3.11 (2018), p. 14869.
- [73] R. Alben. In: *J. Chem. Phys.* 59 (1973), p. 4299.
- [74] A. Stroobants and H. N. W. Lekkerkerker. In: *J. Phys. Chem.* 88 (1984), p. 3669.
- [75] P. J. Camp et al. In: *J. Chem. Phys.* 106 (1997), p. 9270.
- [76] E. Sokolova and A. Vlasov. In: *J. Phys. Condes. Matter* 9 (1997), p. 4089.
- [77] A. G. Vanakaras et al. In: *Mol. Cryst. Liq. Cryst.* 323 (1998), p. 199.
- [78] A. G. Vanakaras, A. F. Terzis, and D. J. Photinos. In: *Mol. Cryst. Liq. Cryst.* 362 (2001), p. 67.
- [79] H. Matsuda et al. In: *J. Phys. Soc. Jpn.* 72.9 (2003), p. 2243.
- [80] S. Varga, A. Galindo, and G. Jackson. In: *J. Chem. Phys.* 117 (2002), p. 10412.
- [81] S. Varga, A. Galindo, and G. Jackson. In: *J. Chem. Phys.* 117.15 (2002), p. 7207.
- [82] A. Galindo et al. In: *J. Chem. Phys.* 119 (2003), p. 5216.
- [83] H. H. Wensink, G. J. Vroege, and H. N. W. Lekkerkerker. In: *J. Chem. Phys.* 115 (2001), p. 7319.
- [84] H. H. Wensink, G. J. Vroege, and H. N. W. Lekkerkerker. In: *Phys. Rev. E* 66 (2002), p. 041704.

- [85] A. Matsuyama. In: *J. Chem. Phys.* 132 (2010), p. 214902.
- [86] H. Mundoor et al. In: *Science* 360 (2018), p. 768.
- [87] C. Avendaño et al. In: *Proc. Natl. Acad. Sci. (USA)* 113.35 (2016), p. 9699.
- [88] H. H. Wensink and C. Avendaño. In: *Phys. Rev. E* 94 (6 2016), p. 062704.
- [89] I. Dozov et al. In: *J. Phys. Chem. B* 115.24 (2011), p. 7751.
- [90] S. D. Peroukidis, S. H. L. Klapp, and A. G. Vanakaras. In: *Soft Matter* 16 (47 2020), p. 10667.
- [91] Y. Lyatskaya and A. C. Balazs. In: *Macromolecules* 31.19 (1998), p. 6676.
- [92] V. V. Ginzburg, C. Singh, and A. C. Balazs. In: *Macromolecules* 33.3 (2000), p. 1089.
- [93] F. M. van der Kooij and H. N. W. Lekkerkerker. In: *J. Phys. Chem. B* 102 (1998), p. 7829.
- [94] J. C. P. Gabriel, C. Sanchez, and P. Davidson. In: *J. Phys. Chem.* 100 (1996), p. 11139.
- [95] L. J. Michot et al. In: *Proc. Natl. Acad. Sci. (USA)* 103.44 (2006), p. 16101.
- [96] E. Paineau et al. In: *J. Phys. Chem. B* 113.48 (2009), p. 15858.
- [97] P. van der Asdonk and P. H. J. Kouwer. In: *Chem. Soc. Rev.* 46 (19 2017), p. 5935.
- [98] M. P. Taylor and J. Herzfeld. In: *Phys. Rev. A* 43 (1991), p. 1892.
- [99] P. van der Schoot and M. E. Cates. In: *EPL* 25.7 (1994), pp. 515–520.
- [100] S. Varga, A. Galindo, and G. Jackson. In: *Phys. Rev. E* 66 (2002), p. 011707.
- [101] P. van der Schoot. In: *J. Chem. Phys.* 104 (1996), p. 1130.
- [102] J. A. C. Veerman and D. Frenkel. In: *Phys. Rev. A* 45 (1992), p. 5632.
- [103] F. M. van der Kooij, K. Kassapidou, and H. N. W. Lekkerkerker. In: *Nature* 406 (2000), p. 868.
- [104] F. M. van der Kooij and H. N. W. Lekkerkerker. In: *Langmuir* 16 (2000), p. 10144.
- [105] F. M. van der Kooij and H. N. W. Lekkerkerker. In: *Phys. Rev. Lett.* 84 (2000), p. 781.
- [106] P. Woolston and J. S. van Duijneveldt. In: *Langmuir* 31.34 (2015), pp. 9290–9295.
- [107] A. Galindo, G. Jackson, and D. J. Photinos. In: *Chem. Phys. Lett.* 325 (2000), p. 631.
- [108] H. H. Wensink. In: *Macromolecules* 52 (2019), p. 7994.
- [109] A. R. Khokhlov and A. N. Semenov. In: *Phys. A* 112 (1982), p. 605.
- [110] K. Lakatos. In: *J. Stat. Phys.* 2 (1970), p. 121.
- [111] R. F. Kayser and H. J. Raveché. In: *Phys. Rev. A* 17 (1978), p. 2067.
- [112] H. N. W. Lekkerkerker et al. In: *J. Chem. Phys.* 80 (1984), p. 3427.
- [113] A. Speranza and P. Sollich. In: *J. Chem. Phys.* 117 (2002), p. 5421.
- [114] M. Abramowitz and I. A. Stegun. New York: Dover, 1973.
- [115] S. Fraden. In: *Observation, prediction and simulation of phase transitions in complex fluids*. Ed. by M. Baus. Kluwer, 1995.
- [116] P. Davidson and J. C. P. Gabriel. In: *Curr. Opin. Colloid Interface Sci.* 9 (2005), p. 377.

- [117] H. H. Wensink, G. J. Vroege, and H. N. W. Lekkerkerker. In: *J. Phys. Chem. B* 105 (2001), p. 10610.
- [118] M. Dijkstra, D. Frenkel, and J.-P. Hansen. In: *J. Chem. Phys.* 101 (1994), pp. 3179–3189.
- [119] M. Dijkstra and R. van Roij. In: *Phys. Rev. E* 56 (1997), p. 5594.
- [120] M. Chen et al. In: *Soft Matter* 11 (28 2015), p. 5775.
- [121] R. Aliabadi, M. Moradi, and S. Varga. In: *J. Chem. Phys.* 144.7 (2016), p. 074902.
- [122] J. Phillips and M. Schmidt. In: *Phys. Rev. E* 81 (2010), p. 041401.
- [123] A. Matsuyama and T. Kato. In: *J. Chem. Phys.* 105 (1996), p. 1654.
- [124] C. G. Reyes et al. In: *Soft Matter* 15.30 (2019), p. 6044.
- [125] V. F. D. Peters, M. Vis, and R. Tuinier. In: *J. Polym. Sci.* 59 (2021), p. 1175.
- [126] V. F. D. Peters et al. In: *Phys. Rev. Lett.* 125 (12 2020), p. 127803.
- [127] Á. González García et al. In: *Sci. Rep.* 7 (2017), p. 17058.
- [128] L. Mederos, E. Velasco, and Y. Martinez-Raton. In: *J. Phys. Condens. Matter* 26.46 (2014), p. 463101.
- [129] A. A. Hyman, C. A. Weber, and F. Jülicher. In: *Annu. Rev. Cell Dev. Biol.* 30 (2014), p. 39.
- [130] Y. Shin and C. P. Brangwynne. In: *Science* 357 (2017), eaaf4382.
- [131] S. D. Peroukidis, A. G. Vanakaras, and D. J. Photinos. In: *J. Mat. Chem.* 20.46 (2010), p. 10495.
- [132] C. R. Safinya et al. In: *Liq. Cryst.* 40 (2013), p. 1748.
- [133] G. C. L. Wong et al. In: *Science* 288 (2000), p. 2035.
- [134] C. S. O'Hern and T. C. Lubensky. In: *Phys. Rev. Lett.* 80.19 (1998), p. 4345.
- [135] J. Planer. In: *Annalen der Chemie und Pharmacie* 118 (1861), pp. 25–27.
- [136] J.-S. Wu and I. I. Smalyukh. In: *Liquid Crystals Reviews* (2022), pp. 1–35.
- [137] M. J. Freiser. In: *Physical Review Letters* 24.19 (1970), p. 1041.
- [138] L. J. Yu and A. Saupe. In: *Physical Review Letters* 45.12 (1980), p. 1000.
- [139] C. Tschierske and D. J. Photinos. In: *Journal of Materials Chemistry* 20.21 (2010), pp. 4263–4294.
- [140] Q. Liu et al. In: *Proc. Natl. Acad. Sci. U.S.A.* 113.38 (2016), p. 10479.
- [141] R. G. Priest and T. C. Lubensky. In: *Physical Review A* 9.2 (1974), p. 893.
- [142] T. Kroin et al. In: *Physical Review A* 40.8 (1989), p. 4647.
- [143] J. D. Bunning, D. A. Crellin, and T. E. Faber. In: *Liquid crystals* 1.1 (1986), pp. 37–51.
- [144] A. B. Harris, R. D. Kamien, and T. C. Lubensky. In: *Physical review letters* 78.8 (1997), p. 1476.
- [145] S. Dussi and M. Dijkstra. In: *Nature Communications* 7.1 (2016), pp. 1–10.

- [146] S. Dhakal and J. V. Selinger. In: *Physical Review E* 83.2 (2011), p. 020702.
- [147] L. Longa, W. Fink, and H.-R. Trebin. In: *Physical Review E* 50.5 (1994), p. 3841.
- [148] G. Canevari. In: *ESAIM: Control, Optimisation and Calculus of Variations* 21.1 (2015), pp. 101–137.
- [149] H. K. Bisoyi and S. Kumar. In: *Chemical Society Reviews* 39.1 (2010), pp. 264–285.
- [150] R. J. Bushby and O. R. Lozman. In: *Current opinion in colloid & interface science* 7.5-6 (2002), pp. 343–354.
- [151] A. R. Khokhlov and A. N. Semenov. In: *Macromolecules* 15.5 (1982), pp. 1272–1277.
- [152] I. Szalai, S. Varga, and G. Jackson. In: *Mol. Phys.* 93.3 (1998), pp. 377–387.
- [153] S. Varga, G. Kronome, and I. Szalai. In: *Mol. Phys.* 98.14 (2000), pp. 911–915.
- [154] H. H. Wensink and G. J. Vroege. In: *Phys. Rev. E* 72.3 (2005), p. 031708.
- [155] D. Van der Beek et al. In: *Phys. Rev. E* 77.3 (2008), p. 031708.
- [156] R. D. Kamien and J. V. Selinger. In: *Journal of Physics: Condensed Matter* 13.3 (2001), R1.
- [157] L. Lam and J. Prost. Springer Science & Business Media, 2012.
- [158] P. J. Ackerman et al. In: *Physical Review E* 90.1 (2014), p. 012505.
- [159] A. Poniewierski and R. Holyst. In: *Phys. Rev. A* 38.7 (1988), p. 3721.
- [160] K. Shundyak and R. van Roij. In: *J. Phys.: Condens. Matter* 13.21 (2001), p. 4789.
- [161] T. Odijk. In: *Liq. Cryst.* 1 (1986), p. 553.
- [162] H. H. Wensink. In: *Soft Matter* 14 (44 2018), pp. 8935–8944.
- [163] O. Ikkala and G. ten Brinke. In: *Science* 295.5564 (2002), pp. 2407–2409.
- [164] T. Wang et al. In: *Science* 338.6105 (2012), pp. 358–363.
- [165] S. Srivastava et al. In: *Science* 327.5971 (2010), pp. 1355–1359.
- [166] S. Jana et al. In: *Sci. Adv.* 3.9 (2017).
- [167] D. Baranov et al. In: *Nano Letters* 10.2 (2010), pp. 743–749.
- [168] P. Sharma et al. In: *Nature* 513 (2014), pp. 77–80.
- [169] E. Grelet and B. Sung. personal communication. 2016.
- [170] L. Kang et al. In: *Soft Matter* 12 (2 2016), pp. 386–401.
- [171] H. H. Wensink and L. Morales Anda. In: *Journal of Physics: Condensed Matter* 30.7 (2018), p. 075101.
- [172] A. Kuhnhold, N. Göth, and N. Helmer. In: *Soft Matter* 18.4 (2022), pp. 905–921.
- [173] P. Prinsen and P. van der Schoot. In: *Phys. Rev. E* 68.2 (2003), p. 021701.
- [174] P. Prinsen and P. van der Schoot. In: *J. Phys.: Condens. Matt.* 16.49 (2004), p. 8835.
- [175] A. Kuhnhold and P. van der Schoot. In: *J. Chem. Phys.* 156.10 (2022), p. 104501.
- [176] E. Barry et al. In: *J. Phys. Chem. B* 113 (2009), pp. 3910–3913.

-
- [177] C. N. Kaplan et al. In: *Phys. Rev. E* 82.2 (2010), p. 021701.
- [178] L. Kang and T. C. Lubensky. In: *PNAS* 114.1 (2017), E19–E27.
- [179] A. E. Green. In: *Proc. Math. Phys. Eng.* 154.882 (1936), pp. 430–455.
- [180] J. Chopin, V. Démery, and B. Davidovitch. In: *The Mechanics of Ribbons and Möbius Bands* (2016), pp. 137–189.
- [181] H. H. Wensink and G. Jackson. In: *The Journal of Chemical Physics* 130.23 (June 2009), p. 234911.
- [182] A. Malijevský and G. Jackson. In: *J. Phys. Condens. Matter* 24.46 (2012), p. 464121.
- [183] Y. A. Lei et al. In: *J. Am. Chem. Soc.* 127.44 (2005), pp. 15346–15347.
- [184] A. P. Thompson et al. In: *Comp. Phys. Comm.* 271 (2022), p. 108171.
- [185] W. S. Fall and H. H. Wensink. in preparation.
- [186] J. P. Lagerwall et al. In: *NPG Asia Materials* 6.1 (2014), e80–e80.
- [187] C. Schutz et al. In: *Langmuir* 31.23 (2015), pp. 6507–6513.
- [188] I. Usov et al. In: *Nature Comm.* 6.1 (2015), p. 7564.
- [189] E. Grelet. personal communication. 2023.

List of Figures

1.1	Examples of basic liquid crystals formed by rod-like molecules or nanoparticles. . .	2
1.2	The presence of non-adsorbing polymers or other depletion agents (whose size is usually smaller than the colloidal nanoparticles)	6
1.3	Illustration of the excluded volume of two spherocylinders of length L and diameter D at mutual orientation γ	11
1.4	Elastic deformations and surface anchoring types	15
1.5	Depletant positions (spheres) considered for rejection of a colloid move (orange spherocylinders)	21
2.1	Schematic representation of the various liquid crystal phases emerging for discs mixed with polymerizing rods	27
2.2	Polymer molecular-weight distributions $\rho_{r\ell}$ and corresponding uniaxial nematic order parameter $S_{r\ell}$ as a function of the polymer length ℓ	35
2.3	Overview of the isotropic I (white) - polymer nematic N^+ (red) - discotic nematic N^- (blue) phase diagrams for a mixture of	41
2.4	Nematic order of the polymers (α_r) and discs (α_d) and polymer mean aggregation number (m) of the nematic N^+ phase	43
2.5	Phase diagram in the osmotic pressure-composition ($P - x$) representation with the following parameters:	44
2.6	Phase diagram in the osmotic pressure-composition showing a quadruple point	45
2.B.1	Schematic representation of the biaxial nematic phase BX with orthorhombic (D_{2h}) point-group symmetry	48
2.B.2	Bifurcation curves superposed to their corresponding phase diagram	49
3.1.1	Illustration of alignment opportunities for an anisotropic colloidal particles immersed in a cholesteric host LC.	53
3.2.1	Illustration of the different surface anchoring scenarios for a colloid rod with length L (top) and disc with diameter D (bottom).	54

3.2.2 Unit-sphere projections of the local orientational probability of a rod immersed in a low molecular-weight cholesteric	57
3.2.3 Unit-sphere projections of the local orientational probability of a disc immersed in a low molecular-weight cholesteric	58
3.2.4 Schemes to illustrate the conically degenerate surface anchoring	60
3.4.1 Illustrations of a helical surface defect emerging around a colloidal cylinder at various orientations	62
3.4.2 Free energy associated with elastic distortions around a homeotropic rod tilted at an angle γ	66
3.4.3 Colloidal nematic order parameters measured within the molecular frame as a function of the surface anchoring	69
3.4.4 Nematic order parameters of discs with weakly homeotropic surface anchoring immersed in a cholesteric host	70
3.4.5 Distortion free energies (in units $k_B T$) around a disc immersed at an angle δ or ζ with the local host director	72
3.4.6 Computer simulation snapshot demonstrating the chiral defect structure (colored in green)	73
3.4.7 Free energy of a colloidal disc with weakly homeotropic surface anchoring immersed in a cholesteric host	75
4.2.1 Unit-sphere projections of a rod in the presence of a low-correlated colloidal liquid crystal	80
4.2.2 Unit-sphere projections of a disc in the presence of a low-correlated colloidal liquid crystal	81
4.3.1 $\bar{w} - c$ phase diagram for rods with homeotropic or tangential surface anchoring	82
4.4.1 Evolution of the pitch q_c of the colloidal helix with respect to the cholesteric pitch q	84
4.4.2 Amplitude $\delta\phi$ and periodicity q_b of the “breathing” instabilities encountered in the bi-helical state in Fig. 4.4.1b as a function of the twist elastic strength $q\xi$	85
5.2.1 Sketch of the simulation model	92
5.3.1 Top and front views of membrane-shaped tactoids of chiral rods mixed with non-adsorbing polymer	96
5.3.2 Crystallinity of membrane-shaped tactoids of chiral rods mixed with non-adsorbing polymer formed in bulk $\varepsilon_c = 11$	97
5.3.3 Crystallinity of membrane-shaped tactoids of chiral rods mixed with non-adsorbing polymer formed in bulk $\varepsilon_c = 16$	99
5.3.4 Rod number density profile	100
5.3.5 Twist angle profile	101

5.3.6 Vertical fluctuations	101
5.4.1 Schematic structure (top and front view) of a twisted smectic membrane	103
5.5.1 Schematic structure of of twisted ribbon	107
5.5.2 Overview of the ribbon properties as a function of the elastic anisotropy	109
5.6.1 Overview of the various membrane morphologies predicted for chiral colloidal rods mixed with non-adsorbing polymer	113
5.A.1 Snapshots obtained from simulations using the SW potential, circular initial con- ditions	117
5.A.2 Snapshots obtained from simulations using the SW potential, rectangular initial conditions	118
5.1.3 Exemples de cristaux liquides basiques formés par des molécules ou des nanopar- ticules en forme de bâtonnets	131

Résumé

Les systèmes en matière molle présentent, dans la plupart des cas, des échelles de longueur structurelle allant du nanomètre au micromètre, et sont donc classés dans le domaine de la "nanotechnologie". Les systèmes colloïdaux sont des exemples bien connus pour lesquels cette caractéristique est essentielle pour définir la plage dans laquelle un type de comportement très spécifique se produit. Les colloïdes sont des substances supramoléculaires et submicroniques dispersées dans un milieu qui peut être un liquide ou un gaz. Ils sont beaucoup plus gros que les molécules et, par conséquent, le milieu d'une suspension colloïdale peut souvent être considéré comme un "arrière-plan" en ce qui concerne la gamme de tailles des colloïdes : ce milieu peut être approximé comme un continuum. En même temps, les colloïdes sont suffisamment petits pour présenter une agitation thermique considérable par rapport à l'effet de sédimentation (qui est causé par des forces gravitationnelles qui deviendraient plus importantes pour des particules de taille plus élevée). Les colloïdes ont été découverts pour la première fois par Perrin, qui a détecté le mouvement brownien comme une manifestation visible de l'agitation thermique dans des dispersions de colloïdes de résine dans l'eau [2].

Lorsque les particules colloïdales présentent des formes anisotropes, elles peuvent se trouver dans des phases cristallines liquides. Les cristaux liquides sont des substances qui ont l'apparence d'un liquide mais qui possèdent certains niveaux d'arrangement moléculaire semblables à des cristaux. Les cristaux liquides ont été découverts pour la première fois en 1888 par Friedrich Reinitzer, qui a remarqué qu'une substance à base de cholestérol avait deux points de fusion à des températures différentes, chacun d'eux donnant lieu à une phase liquide aux propriétés optiques différentes [3]. À l'époque de Reinitzer, seules trois phases étaient connues (gaz, liquide et solide). Au fil des ans, on a découvert qu'un grand nombre de substances présentaient de nombreux états de la matière, y compris des phases cristallines liquides qui sont aujourd'hui largement utilisées dans les avancées technologiques telles que les écrans et les thermomètres à cristal liquide [4].

La principale différence entre un cristal liquide et les états gazeux, liquide et solide couramment observés est que les propriétés du premier sont anisotropes et varient en fonction de la direction, même si la substance elle-même reste fluide. Ces propriétés uniques sont dues à la forme allongée de ses éléments constitutifs, qui favorisent l'alignement collectif dans une certaine direction. En d'autres termes, les phases cristallines liquides sont des états supplémentaires de la matière, intermédiaires entre le liquide usuel et le solide cristallin, dont l'existence est liée aux degrés de liberté supplémentaires que possèdent les particules anisométriques par rapport aux particules sphériques.

Parmi les nombreuses phases cristallines liquides, on peut trouver différents degrés d'ordre, mis en évidence par exemple par la diffraction des rayons X et de la lumière. Les mesures de ce type permettent de classer ces systèmes en fonction de leur similitude avec la phase liquide ou la phase solide. Considérons, entre autres, les phases cristallines liquides suivantes, représentées dans Fig. 5.1.3 :

La phase fluide *isotrope* (I) est très similaire aux phases gazeuse et liquide pour les particules sphériques et se caractérise par une absence totale d'ordre positionnel et orientationnel. Au stade immédiatement suivant, nous trouvons la phase *nématique* (N), dans laquelle les particules sont réparties de manière homogène sans ordre de position comme dans une phase liquide, mais sont ordonnées dans leur orientation suivant une direction moyenne : le directeur nématique \hat{n} . Comme nous le voyons à plusieurs reprises tout au long de cette thèse, les particules, en plus d'être anisotropes, peuvent être chirales. Cela peut être dû à l'arrangement des atomes dans un composé moléculaire, à une forme de particule (hélicoïdale) dans certains systèmes colloïdaux ou à une distribution chirale des charges à la surface des particules, observée par exemple dans les virus en forme de filament *fd* [5]. Lorsque les particules chirales sont en phase nématique, elles s'organisent en une structure fortement torsadée. Ce cas particulier de phase nématique chirale est souvent appelé *cholestérique*.

La phase *smectique* (Sm) est plus proche de la phase solide. Dans les cristaux liquides smectiques, les particules sont ordonnées en couches et ne peuvent pas se déplacer librement d'une couche à l'autre. La phase smectique est à son tour divisée en plusieurs types aux propriétés différentes. Par exemple, la phase smectique A (SmA), où les particules peuvent se déplacer librement à l'intérieur des couches comme dans un liquide bidimensionnel, ou la phase smectique B (SmB), où il existe un ordre positionnel à longue distance : à des concentrations plus élevées ou à des températures plus basses, les molécules ont tendance à s'arranger de manière de plus en plus proche d'un réseau cristallin.

Une autre classification des matériaux cristaux liquides est basée sur le mécanisme par lequel ils passent d'un état à l'autre. Les systèmes *thermotropes*, principalement formés par des constituants de faible poids moléculaire - et aussi certains polymères -, subissent des transitions de phase dues à des changements de température, puisque les propriétés thermodynamiques de ces espèces dépendent des forces d'attraction entre les molécules. Dans cette thèse, nous nous concentrons principalement sur les cristaux liquides *lyotropes*, qui se forment en augmentant la concentration des particules de soluté. C'est le cas des systèmes formés par des nanoparticules synthétiques et biologiques de haut poids moléculaire [6, 7], des polymères tels que l'ADN [8] ou des surfactants dans un solvant [9]. Le premier cas est celui étudié dans cette thèse, où le fait que la forme ne soit pas sujette à des fluctuations dues à des changements dans la composition du solvant est une simplification avantageuse par rapport à ses homologues amphiphiles et polymériques.

Les premiers rapports expérimentaux sur les cristaux liquides lyotropes à base de nanoparticules remontent à la description du comportement cristal liquide du virus de la mosaïque du tabac et de la tomate (TMV) [10, 11] et du pentoxyde de vanadium (V_2O_5) [12] au début du 20e siècle. Outre ces systèmes de particules en forme de bâtonnets, on a découvert que les particules colloïdales chargées en forme de plaquettes et les particules d'argile présentaient

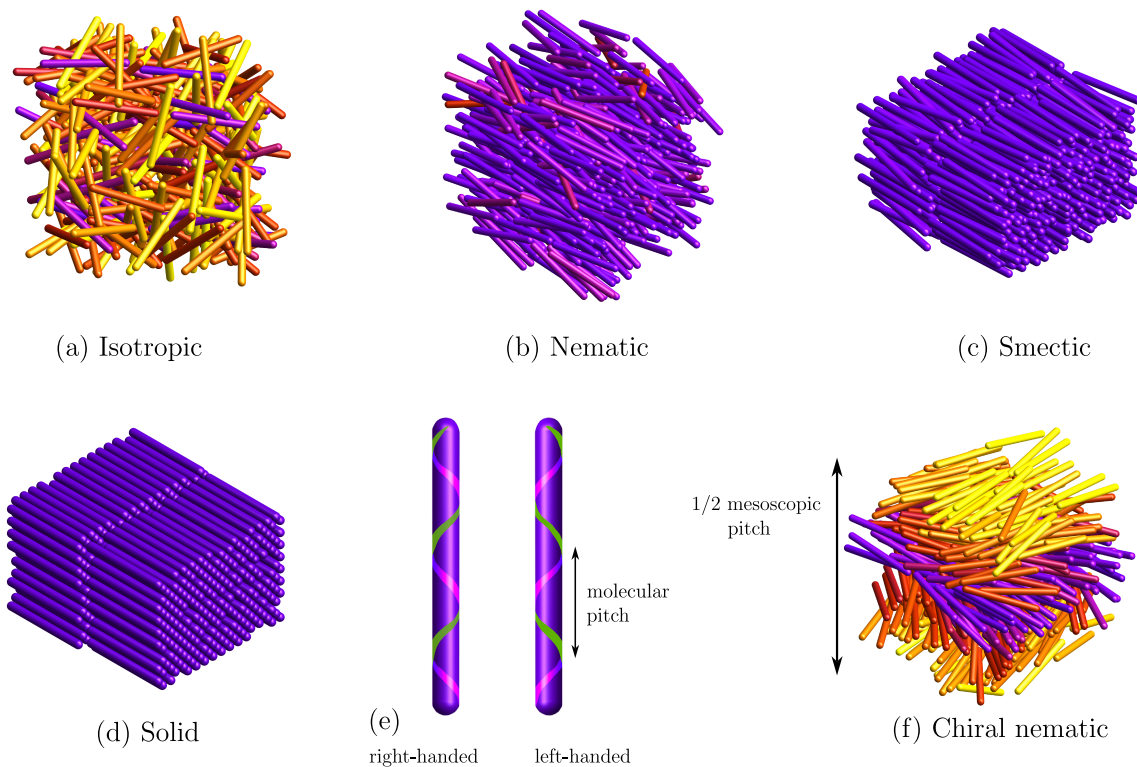


Figure 5.1.3: (a)-(d) Exemples de cristaux liquides de base formés par des molécules ou des nanoparticules en forme de bâtonnets. (e) Les cristaux liquides peuvent être formés par des constituant chiraux; (f) ces particules génèrent un type particulier de phase nématique : le nématique chiral. Les implications de la chiralité moléculaire sur la mésostructure hélicoïdale (en particulier, le *pitch* mésoscopique) des phases nématiques chirales restent une question difficile.

un comportement cristal liquide [13]. Actuellement, il existe de nombreux autres exemples de cristaux liquides lyotropes dans une grande variété de dispersions de particules colloïdales (principalement en forme de bâtonnets) et de solutions de polymères rigides (voir par exemple [14] pour une vue d'ensemble).

Ce travail de recherche se concentre sur les approches théoriques et numériques pour l'exploration du comportement de phase dans les composés colloïdaux anisotropes, avec un intérêt particulier pour la transition de phase isotrope-nématique de nature *entropique*. Cette transition est bien décrite par la théorie d'Onsager, proposée en 1949, qui suppose une similitude entre un gaz et une solution de particules [15] ; et sera utilisée à plusieurs reprises dans ce manuscrit (plus particulièrement dans les chapitres 2 et 4) avec d'autres outils théoriques et numériques pour étudier l'auto-organisation liquide-cristalline de bâtonnets ou de plaquettes colloïdales dans des environnements complexes. Grâce à nos recherches, nous espérons mieux comprendre le comportement de ce type de systèmes et contribuer au domaine plus large de la recherche sur les cristaux liquides.

Le chapitre 1 de cette thèse fournit une introduction au contexte et à la portée de la recherche présentée. Il couvre le contexte de mécanique statistique appliquée aux fluides de particules anisométriques *dures*. Nous discutons ensuite de l'utilisation des simulations de Monte Carlo de

particules dures, en mettant en évidence certaines particularités de telles simulations pour le cas de particules anisométriques. Dans l'ensemble, le chapitre sert de fondement pour le reste de la thèse, en exposant les concepts et les méthodes pertinents pour la recherche présentée dans les chapitres suivants.

Dans le chapitre 2, un modèle théorique est proposé pour explorer le comportement de phase à faible concentration d'un système composé de bâtonnets peu flexibles liés de manière non covalente et traités comme des *living polymers* mélangés à des disques colloïdaux rigides non adsorbants. En utilisant une théorie du second coefficient du viriel qui corrèle les différentes entropies associées aux polymères et aux disques, nous démontrons que de faibles fractions d'additifs discotiques favorisent la formation d'une phase nématique de polymère. À des concentrations plus élevées de disques, cependant, la phase est perturbée par l'alignement collectif des disques en faveur d'un fluide nématique discotique dans lequel les polymères sont dispersés de manière *antinématique*. Nous montrons que l'arrangement antinématique des polymères génère une distribution de poids moléculaires non exponentielle et stimule la formation d'espèces oligomériques. À des concentrations suffisantes, les disques facilitent une séparation de phase liquide-liquide qui peut être mise en coexistence simultanée avec les deux phases nématiques fractionnées, fournissant ainsi des preuves d'une coexistence à quatre fluides dans un mélange de particules dures de formes différentes sans forces interparticulaires cohésives. Nous stipulons les conditions dans lesquelles un tel phénomène pourrait être observé expérimentalement.

Les chapitres 3 et 4 abordent des problèmes liés aux cristaux liquides nématiques moléculaires hybrides. Dans cette partie du travail, nous considérons un système dans lequel les cristaux liquides cholestériques moléculaires sont dopés avec de fines particules colloïdales ayant de grands rapports longueur-largeur. Dans le chapitre 3, nous considérons des insertions individuelles de colloïdes. Nous démontrons que les tiges ont une forte tendance à s'orienter perpendiculairement à l'axe hélicoïdal et au directeur local, conférant ainsi une forte biaxialité locale à la structure cholestérique hybride. Nous argumentons théoriquement que l'anisotropie élastique et l'étalement de la courbure joue un rôle clé dans la stabilisation de l'ordre orthorhombique local le long de l'hélice. Nos prévisions sont corroborées par des résultats expérimentaux obtenus dans le groupe de I. Smalyukh (Université du Colorado, États-Unis) que nous examinons brièvement. Nous discutons également le cas des disques et trouvons un scénario similaire d'ordre biaxial anormal le long du directeur hélicoïdal pour des disques à ancrage homéotrope immergés dans des hôtes cholestériques à pas court.

Dans le chapitre 4, nous utilisons la théorie d'Onsager pour rendre compte des effets collectifs dans le cas hypothétique où de nombreuses particules colloïdales sont insérées dans le LC hybride. Ce cadre nous permet d'explorer des concentrations de colloïdes qui ne sont plus infiniment petites. Les corrélations entre les colloïdes entraînent des contributions élastiques et entropiques supplémentaires qui interfèrent avec les effets d'ancrage de surface explorés dans le chapitre précédent. Nous considérons deux régimes distincts, à savoir le couplage faible où l'ancrage de surface n'a qu'un impact marginal sur les orientations des colloïdes et le couplage fort où l'énergie de réalignement typique dépasse largement l'énergie thermique. Nous démontrons en couplage faible que les effets collectifs colloïdaux induits par l'interaction stérique colloïde-colloïde peuvent conduire à une séparation de phase liquide-liquide entre deux phases fluides

biaxes. Dans le régime de couplage fort, nous soutenons que la force élastique peut faciliter la formation d'états bi-hélicoïdaux où l'organisation hélicoïdale des composants colloïdaux et moléculaires est inégale en pas et même en chiralité.

Finalement, dans le chapitre 5, nous utilisons des simulations de Monte Carlo approfondies, complétées par la théorie, pour explorer deux formes de gouttelettes importantes dans la littérature, à savoir la membrane torsadée et le ruban colloïdaux. Dans les expériences, la structure de ruban allongée domine à force chirale élevée. Cependant, dans nos simulations, nous démontrons qu'en augmentant la chiralité, les membranes ont tendance à se transformer en structures à plusieurs domaines composées de plusieurs unités presque circulaires torsadées séparées par des parois π , tandis que la transition en rubans torsadés est entravée par la forte tension de surface subie par la gouttelette. Nous complétons nos simulations avec des descriptions théoriques microscopiques simples pour les deux morphologies de gouttelettes, ce qui nous permet de prédire l'évolution de l'angle de torsion à travers les membranes. Pour les rubans, notre théorie simple fournit des prévisions génériques pour la largeur de ruban typique, la torsion interne et l'angle d'inclinaison des bords qui sont en accord avec les observations expérimentales de rubans torsadés composés de bâtonnets de virus *fd* mélangés avec du dextran.

Mots clés: cristal liquide; colloïde; théorie d'Onsager; Hard Particle Monte Carlo

